Insight into the Mechanism of [NiFe] Hydrogenase by means of Magnetic Resonance Experiments and DFT Calculations

vorgelegt von
Diplom-Chemiker, Master of Science
Matthias Stein
aus Berlin

Vom Fachbereich 5 – Chemie –
der Technischen Universität Berlin
zur Erlangung des akademischen Grades
Doktor der Naturwissenschaften
– Dr. rer. nat. –
genehmigte Dissertation

Promotionsausschuß:

Vorsitzender: Prof. Dr. Schoen
Berichter: Prof. Dr. Lubitz
Berichter: Prof. Dr. Koch
Tag der mündlichen Prüfung: 02. Februar 2001

Berlin 2001
D 83

Abstract

Stein, Matthias

Insight into the Mechanism of [NiFe] Hydrogenase by means of Magnetic Resonance Experiments and DFT Calculations

Hydrogenasen katalysieren die reversible heterolytische Dissoziation von molekularem Wasserstoff. Die Untersuchung dieses Elementarprozesses übergangsmetallhaltiger Enzymkatalyse ist der zentrale Aspekt dieser Arbeit. [NiFe]-Hydrogenasen besitzen ein heterobimetallisches aktives Zentrum, an dem die Umsetzung des Wasserstoffs erfolgt. EPR und verwandte experimentelle magnetische Resonanzmethoden lassen sich auf die paramagnetischen Redoxzustände des Nickelzentrums anwenden und liefern Aussagen über die elektronische Struktur und Ligandenumgebung der Metalle. Diese werden ergänzt durch theoretische Berechnung im Rahmen der Dichtefunktionaltheorie (DFT).

Im Rahmen dieser Doktorarbeit wurde die Berechnung von Observablen der magnetischen Resonanz ($\mathbf{g}$- und $\mathbf{A}$-Tensoren) mit der relativistischen DFT und dem ZORA (zero-order regular approximation) Hamiltonoperator an zwei Nickelmodellkomplexen etabliert und evaluiert. Beide Verbindungen wiesen strukturelle und elektronische Ähnlichkeiten mit dem aktiven Zentrum der [NiFe]-Hydrogenase auf. Der Einfluß relativistischer Effekte auf die geometrische und elektronische Struktur wurde kritisch diskutiert.

Der Einfluß verschiedener möglicher verbrückender Liganden X im aktiven Zentrum auf die geometrische Struktur und die Verteilung der ungepaarten Spindichte wurde mit DFT Rechnungen untersucht. Sauerstoffverbrückte Strukturen erscheinen plausibel für die oxidierten Ni-A und Ni-B Zustände, während im reduzierten Ni-C Zustand die Position wahrscheinlich durch ein Hydridanion besetzt wird.

In Proteineinkristallen der [NiFe]-Hydrogenase aus *Desulfovibrio vulgaris* Stamm Miyazaki F wurde die Protonenumgebung des Ni-Zentrums mit gepulster ENDOR Spektroskopie in den Zuständen Ni-A und Ni-B charaketrisiert. Drei Hyperfeintensoren konnten β-CH_2 Protonen von Cysteinaminosäuren in der Umgebung des Nickels zugeordnet werden. Die Meßergebnisse wurden unterstützt von DFT berechneten Hyperfeintensoren. Ni-A und Ni-B unterscheiden sich im Protonierungsgrad des Brückenliganden. Ein μ-Oxo-Ligand im Ni-A Zustand und eine μ-Hydroxo-Brücke im Ni-B Zustand führten zu einer leicht unterschiedlichen Spindichteverteilung. Diese wirkte sich auch auf die Hyperfeinwechselwirkung der β-CH_2 Protonen der terminalen Cysteine aus. Eine Protonenkopplung des terminalen Cysteines 81 konnte im Ni-B, aber nicht im Ni-A Zustand gemessen werden.

Relativistische DFT Rechnungen lieferten atomare Vorstellungen von den paramagnetischen Zuständen Ni-A, Ni-B, Ni-C, Ni-L und Ni-CO. Die berechneten $\mathbf{g}$-Tensoren sind in guter Übereinstimmung mit experimentellen Ergebnissen, soweit vorhanden. Ni-A und Ni-B sind μ-Oxo- und μ-Hydroxo verbrückt. Ni-L geht aus dem Ni-C Zustand durch Photodissoziation des verbrückenden Liganden hervor. Die berechneten Hyperfeintensoren für alle Kerne sind ebenfalls in guter Übereinstimmung mit experimentellen Werten. Kohlenmonoxid als Inhibitor des Enzyms bindet im Ni-L Zustand in axialer Position an das Ni Atom und kann so diese Koordinationsstelle blockieren.

Der Ni-C Zustand der regulatorischen Hydrogenase (RH) aus *Ralstonia eutropha* wurde in gefrorener Lösung mit Hilfe der orientierungsselektierten ENDOR Spektroskopie untersucht. Mit Hilfe der theoretisch berechnete $\mathbf{g}$-Tensororientierung und der Größe und Orientierung der Protonenhyperfeintensoren konnten fünf Hyperfeintensoren zu Protonen in der molekularen Struktur zugeordnet werden. Die Struktur des aktiven Zentrums im Ni-C Zustand ist der der Standardhydrogenasen sehr ähnlich.

Auf der Grundlage der gewonnenen experimentellen und theoretischen Ergebnisse wird ein Reaktionsmechanismus für die [NiFe]-Hydrogenase vorgeschlagen. Dieser deutet auf eine Beteiligung der Proteinumgebung hin. Das terminale Cystein 530 könnte die heterolytische Spaltung des Wasserstoffs als Base unterstützten. Während das Hydrid in der Brücke verbleibt, kann das Proton vom Brückenliganden aufgenommen werden und das aktive Zentrum als H_3O^+ oder über einen Protonentransferkanal verlassen.

Teile der vorliegenden Arbeit wurden bereits veröffentlicht

Wissenschaftliche Publikationen

1. M. Brecht, M. Stein, O. Trofanchuk, F. Lendzian, R. Bittl Y. Higuchi, W. Lubitz
   Catalytic Center of the [NiFe] Hydrogenase: A Pulse ENDOR and ESEEM Study
   In: *Magnetic Resonance and Related Phenomena* Vol.II Technische Universität Berlin, pp. 818-819, (1998).
2. M. Stein and W. Lubitz
   Electronic Structure of the Active Center [NiFe] Hydrogenase
   In: *Magnetic Resonance and Related Phenomena* Vol. II, Technische Universität Berlin, pp. 820-821, (1998).
3. O. Trofanchuk, M. Stein, Ch. Gessner, F. Lendzian, Y. Higuchi, W. Lubitz
   Single Crystal EPR Studies of the Oxidized Active Site of [NiFe] Hydrogenase from *Desulfovibrio vulgaris* Miyazaki F
   J. Biol. Inorg. Chem., **5**, 36-44 (2000).
4. W. Lubitz, M. Stein, M. Brecht, O. Trofanchuk, S. Foerster, Y. Higuchi, E. van Lenthe, F. Lendzian
   Single Crystal EPR and DFT Studies of the Paramagnetic States of [NiFe] Hydrogenase from *Desulfovibrio vulgaris*
   Biophys. J., **78 A**, 1660 (2000).
5. M. Stein, E. van Lenthe, E. J. Baerends, W. Lubitz
   G- and A-Tensor Calculations in the Zero-Order Approximation for Relativistic Effects of Ni-Complexes $Ni(mnt)_2^-$ and $Ni(CO)_3H$ as Model Complexes for the Active Center of [NiFe]-Hydrogenase
   J. Phys. Chem. A, **105**, 416-425 (2001).
6. M. Stein, E. van Lenthe, E. J. Baerends, W. Lubitz
   Relativistic DFT Calculations of the Paramagnetic Intermediates of [NiFe] Hydrogenase. Implications for the Enzymatic Mechanism.
   J. Am. Chem. Soc., in press (2001).
7. M. Stein, W. Lubitz
   DFT Calculations of the Electronic Structure of the Paramagnetic States of [NiFe] Hydrogenase
   PCCP, submitted (2001).
8. M. Stein, O. Trofanchuk, M. Brecht, F. Lendzian, R. Bittl, Y. Higuchi, W. Lubitz
   Pulsed-ENDOR Crystallography of Oxidized Single Crystals of [NiFe] Hydrogenase from *Desulfovibrio vulgaris* Miyazaki F
   J. Am. Chem. Soc. manuscript in preparation.

Konferenzbeiträge

1. W. Lubitz, Ch. Gessner, F. Lendzian, O. Trofanchuk, Ch. Reichle, M. Stein, Y. Higuchi
   Single Crystal EPR and ENDOR of the Active Site of the [NiFe]-Hydrogenase From *Desulfovibrio vulgaris*
   Hydrogenases 97, Albertville, France, 12-17 July 1997.

2. M. Stein, W. Lubitz
   H_2-Evolving Complexes: A DFT Study of Nickelbisthiolenes as Model Complexes for NiFe-Hydrogenases
   DFT97, Vienna, Austria, 2-6 September 1997.

3. O. Trofanchuk, M. Stein, M. Brecht, W. Hofbauer, F. Lendzian Y. Higuchi, W. Lubitz
   Catalytic Center of [NiFe]-Hydrogenases: X- and W-Band EPR Studies
   RSC 31st EPR Annual International Meeting, Manchester, UK, 29 March-2 April 1998.

4. M. Brecht, M. Stein, O. Trofanchuk, F. Lendzian, R. Bittl, Y. Higuchi, W. Lubitz
   Catalytic Center of the [NiFe] Hydrogenase: ENDOR and ESEEM Studies RSC 31st EPR Annual International Meeting, Manchester, UK, 29 March-2 April 1998.

5. M. Stein, O. Trofanchuk, M. Brecht, F. Lendzian, Y. Higuchi, W. Lubitz
   Determination of Protons in the Environment of *D. vulgaris* Miyazaki F Single Crystals. Pulsed-ENDOR Spectroscopy and DFT Calculations.
   COST818 Workshop, Umea, Sweden, 11-14 June 1998.

6. M. Stein, O. Trofanchuk, M. Brecht, F. Lendzian, Y. Higuchi, W. Lubitz
   Determination of Proton Hyperfine Tensors in Single Crystals of
   D. vulgaris Miyazaki F [NiFe] Hydrogenase. Pulsed-ENDOR Spectroscopy
   and DFT Calculations.
   “Quantum Chemical Calculations of NMR and EPR Parameters”,
   Smolenice Castle, Slovakia, 14-18 September 1998.

7. M. Stein, O. Trofanchuk, M. Brecht, F. Lendzian, Y. Higuchi, W. Lubitz
   Determination of Proton Hyperfine Tensors in Single Crystals of *D. vulgaris* Miyazaki F [NiFe] Hydrogenase. Pulsed-ENDOR Spectroscopy and DFT Calculations.
   Jahrestagung der Deutschen Gesellschaft fuer Biophysik, Frankfurt/Main Germany, 21-23 September 1998.

8. W. Lubitz, M. Stein, M. Brecht, O. Trofanchuk, F. Lendzian, R. Bittl, Y. Higuchi
   EPR, ENDOR and ESEEM Studies of Hydrogenase Single Crystals from *Desulfovibrio vulgaris*
   COST818 Workshop, Sintra, Portugal, 9-13 December 1998.

9. W. Lubitz, M. Stein, S. Foerster, M. Brecht, O. Trofanchuk, F. Lendzian, Y. Higuchi
   Structure and Function of [NiFe] Hydrogenase - Advanced EPR and Theoretical Investigations
   5th European Biological Inorganic Chemistry Conference, Toulouse, France, 17-20 July 2000.

10. M. Stein, W. Lubitz
    A Quantum Chemical Description of the Paramagnetic States of [NiFe] Hydrogenases - Towards an Understanding of the Reaction Mechanism (Invited Lecture)
    6th International Conference on the Molecular Biology of Hydrogenases, Potsdam, Germany, 5-10 August 2000.

11. M. Brecht, M. Stein, T. Buhrke, S. Foerster, B. Friedrich, W. Lubitz
    Characterization of the Active Site of the Hydrogen Sensor from *Ralstonia eutropha* by ENDOR and ESEEM Spectroscopy
    6th International Conference on the Molecular Biology of Hydrogenases, Potsdam, Germany, 5-10 August 2000.

12. S. Foerster, O. Trofanchuk, M. Stein, Y. Higuchi , W. Lubitz
    On the Active Site of [NiFe]-Hydrogenase from *Desulfovibrio vulgaris* Miyazaki F: EPR Spectroscopic Investigation of Single Crystals and of the 61Ni Labeled Protein
    6th International Conference on the Molecular Biology of Hydrogenases, Potsdam, Germany, 5-10 August 2000.

13. S. Foerster, M. Brecht, M. Stein, O. Trofanchuk, Y. Higuchi, W. Lubitz
    EPR and ENDOR Spectroscopic Investigations of Single Crystals of the [NiFe]-Hydrogenase from *Desulfovibrio vulgaris* Miyazaki F
    DFG-Rundengespräch “Anwendungen der Magnetischen Resonanz in der Bio- und Materialwissenschaft” 17-22 September 2000, Hirschegg, Austria.

Weitere Publikationen

1. W. Byers Brown, I. H. Hillier, A. J. Masters, I. J. Palmer D. H. V. DosSantos, M. Stein, M. A. Vincent
   Modelling the Photonucleation of Water Vapour by UV in the Presence of Oxygen and the Absence of Pollutants
   Faraday Diss. **100** 253-267, (1995).

2. M. Stein, J. Sauer
   Formic Acid Tetramers: Structure Isomers in the Gas Phase
   Chem. Phys. Lett. **267**, 111-115, (1997).

3. Ch. Gessner, M. Stein, S. P. J. Albracht, W. Lubitz
   Orientation-Selected ENDOR of the Active Center in *C. vinosum* [NiFe]-Hydrogenase in the Oxidized,‘Ready‘ State
   J. Biol. Inorg. Chem., **4**, 379-389 (1999).

4. W. Koch, M. Stein
   Handbook of Computational Chemistry by D. B. Cook (book review)

Angew. Chem., **111**, 1059-1060, (1999);
Angew. Chem. Int. Ed. **38**, 1680-1681, (1999).

5. R. Isaacson, F. Lendzian, M. Stein, W. Lubitz, C. Boullais
   Identification of ENDOR Lines in Q_A^- and Q_B^- in RCs of *Rb. sphaeroides* by Selective Isotopic Labeling
   Biophys. J. , **78 A** , 2001 (2000).

6. M. Stein
   DFT - A Promising Tool for Studying Transition Metal Enzymes
   In: *Hydrogenases - What can we learn from Nature*, M. Frey, R. Cammack, Eds.; Academic Press, to appear 2001.

Weitere Konferenzbeiträge

1. M. Stein, D.H.V. DosSantos, W. Byers Brown, A. J. Masters
   Modelling the Water-Hydrogens Peroxide System
   “How to Derive Interatomic Potentials Needed for Computer Simulations”
   Oxford, UK, July 1994.

2. M. Stein, D.H.V. DosSantos, W. Byers Brown, A. J. Masters
   Modelling the Water-Hydrogens Peroxide System
   Annual Meeting of the RSC Statistical Mechanics and Thermodynamics Group,
   Manchester, UK, August 1994.

3. M. Stein, J. Sauer
   Formic Acid Gas Phase Structures
   CCP1 Study Weekend “Quantum Theory of Large Molecules”
   Daresbury, UK, September 1996.

Contents

Chapter 1

Introduction

Hydrogenases belong to the oldest bacteria and archae on Earth. Although the production and consumption of H_2 by microorganisms had been known since end of the 19^{th} [1] and the beginning of the 20^{th} century [2, 3], it was not until 1931 that the name 'hydrogenase' was proposed [4]. Hydrogenases are involved in the respiration of elemental sulphur and/or polysulphide. The ability to reduce sulphur using H_2 or organic substrates as electron donors is widespread among bacteria and archae. Some of the hypothermophilic organisms live in water-containing volcanic areas at up to 80° C. *In vivo* nearly all hydrogenases function in one way only, they catalyze an 'irreversible' reaction: either split or produce molecular hydrogen. Only in presence of an excess of electron donors or acceptors, they may reverse the preferred reaction

$$H_2 \rightleftharpoons H^+ + H^- \qquad . \tag{1.1}$$

The investigation of the heterolytic cleavage of the strongest single bond (436 kJ mol^{-1} at 298 K, pK_a = 35) at room or body temperature is the subject of this dissertation.

The combustion of fossil carbon compounds, which were accumulated for millions of years on earth, to carbon dioxide is going to disturb the sensitive equilibrium of our atmosphere. The 'green-house effect' and the global warming threaten to change our climate. When hydrogen were used as energy carrier for automobiles, no exhaust gases would be produced. The investigation of one of the major problems of today's world, related to the fossil fuel question, requires a combined interdisciplinary approach from various fields (for a perspective see i.e. [5]).

The direct combustion of hydrogen requires a controlled explosion of H_2 and O_2 (Knallgasreaktion). In fuel cells, hydrogen and oxygen react but not in a direct combustion which produces a lot of thermal energy but in a 'cold' process mediated by an electrolyte (for a review see [6]). Fuel cells are electrochemical cells which convert chemical energy from a reaction between a fuel and an oxidant directly into electrical energy. A schematic diagram of a fuel cell is given in Figure **1.1**. Fuel cells are open devices, unlike batteries. Fuel and oxidant are continuously supplied to the electrodes (fuel, i.e. H_2, to the anode side, air or oxygen to the cathode side). Anode and cathode are separated by a polymer electrolyte membrane (PEM) which also acts as a proton conductor. The electrochemical reactions at the anode and cathode are also displayed in Figure **1.1**. At the anode, hydrogen is oxidized to protons and electrons and at the cathode oxygen is reduced to oxide. As the electrons, produced by the electrochemical reaction, move through the external circuit (see Figure **1.1**) a current can be measured and used to drive an electric motor. Protons are transfered via the PEM to the cathode side. When pure hydrogen is used in fuel cells, the combustion product of a fuel cell is water - a true zero emission process. The thermal heat liberated by a fuel cell can be used to heat individual homes, co-generating steam for the reformer in a power plant or discarded as waste heat. Today, many large automobile manufacturers operate a fleet of fuel cell driven vehicles (for a review see [7]) [1].

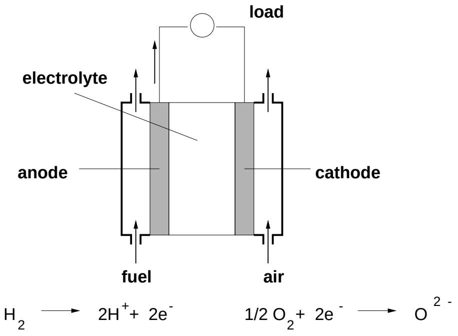

Figure 1.1: Schematic drawing of a fuel cell

Apart from the electrolysis of water, the biological production of hydrogen is the most promising route (“bio-hydrogen”). An efficient coupling of solar energy conversion and biological hydrogen production is achieved by combining photosystem II (PSII) and hydrogenases. PSII delivers oxygen and protons from the photolytically driven splitting of water (water oxidation). Hydrogenases can make use of the protons generated and yield H_2 (Figure **1.2**).

The activity of [Fe]-only hydrogenases is usually larger than that of [NiFe] hydrogenases. [NiFe] hydrogenases act mostly as ‘hydrogen-uptake’ hydrogenases and consume hydrogen whereas [Fe] hydrogenases most frequently produce hydrogen. The efficiency of hydrogenases is demonstrated in an example: 1 mole of the [Fe] hydrogenase from *D. desulfuricans* can fill the airship Graf Zeppelin in ten minutes (assuming a sufficient supply of reductants and protons) [8].

---

[1] A comprehensive list of fuel cell applications is given at the web site http://www.fuelcells.org

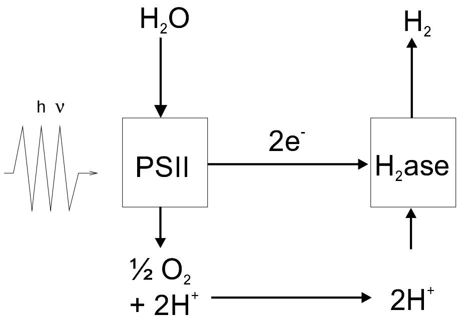

Figure 1.2: Photoproduction of biohydrogen

Nature's choice of Ni for the active site of enzymes is peculiar, given the modern distribution of soluble metals on Earth. Still, Ni plays a versatile role in enzymatic catalysis [9]. One possibility is that the choice of Ni reflects a selection that was made under different atmospheric conditions. Before O_2 became abundant, many transition metals would have been present as sulphides and nickel sulphides are among the more soluble transition metal sulphides [10]. [NiFe] hydrogenases are resistant to oxygen whereas [Fe]-only hydrogenases are destroyed in the presence of oxygen. This may indicate an adaption of the hydrogenases to an increase of oxygen in the atmosphere. Nature's choice of Ni as a redox active switch may be due to the following reasons [11]:

- Ni is a good catalyst for H_2 heterolytic cleavage
- A nickel hydride may serve as an electron storage device and guarantee reversibility
- Compared to Fe, Ni is resistant to oxidation (but at lower battery efficiency).

In order to contribute to the understanding of the heterolytic splitting of molecular hydrogen by [NiFe] hydrogenases, Electron Paramagnetic Resonance (EPR) and Electron Nuclear Double Resonance (ENDOR) spectroscopies and modern theoretical approaches, namely Density Functional Theory (DFT), are used in this thesis.

The EPR and pulsed-ENDOR spectra in Chapter 6 were recorded together with Dr. Olga Trofanchouk. The orientation-selected ENDOR spectra of the Ni-C state were measured together with Dipl.-Phys. Marc Brecht.

Chapter 2

Hydrogenases

Hydrogenases are a family of oxidoreductase enzymes of different constitution that catalyze the reversible oxidation of molecular hydrogen H_2 (enzyme classification EC 1.18.99.1). Hydrogenases have been classified according to the contents of their active sites as [NiFe] [12], [NiFeSe] [12], [Fe]-only [13] and transition metal-free [14] hydrogenases. Nickel-containing hydrogenases have been isolated from eubacteria (i.e. *Desulfovibrio*, *Azobacter*, *Rhodobacter*, *Ralstonia*) and archaebacteria (i.e. *Methanobacterium* and *Methanothermus*) [15]. The mesophilic sulphate-reducing bacteria *Desulfovibrio* live at an optimum of body-temperature (37°C) and pH 7.2 [16]. *Desulfovibrio* use H_2 as a source of energy by coupling its oxidation (electron flow) to the reduction of sulphate to sulphide [17]

$$4H_2 + SO_4^{2-} \rightarrow S^{2-} + 4H_2O \tag{2.1}$$

or H_2S (see Figure **2.1**).

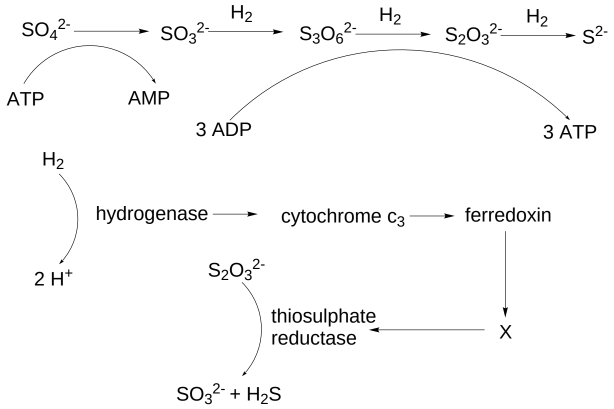

Figure 2.1: H_2 metabolism in *Desulfovibrio*, X denotes unknown electron carrier(s) [17].

Hydrogenases from the anaerobic bacteria of *Desulfovibrio* use cytochrome c_3 as the physiological electron carrier but may also employ artificial electron acceptors such as methyl viologen and benzyl viologen (see Figure **2.2.**). The heterolytic cleavage of molecular hydrogen into protons and electrons (or one proton and one hydride anion) has been shown by hydrogen-deuterium exchange reactions and the para/ortho conversion of H_2 [17].

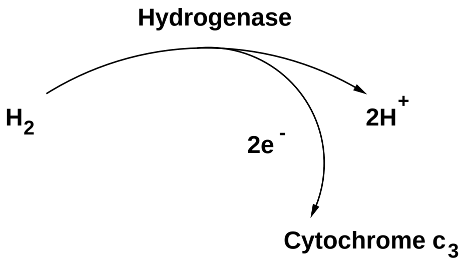

Figure 2.2: The heterolytic cleavage of H_2 by Hydrogenases from *Desulfovibrio*

2.1 Classification of [NiFe] Hydrogenases

The molecular biology of hydrogenases has been reviewed in [15, 18, 19]. Genetically, [NiFe] hydrogenases can be classified into five groups according to [15]. Group I is the [NiFeSe] hydrogenase from *Desulfovibrio (Desulfomicrobium) baculatum*, group II hydrogenases comprise *D. gigas*, *D. vulgaris* Miyazaki F and *D. fructosovorans*. Group III hydrogenases are slightly more divergent and display less homology (i.e. *Rhodobacter capsulatus*, *Azobacter vinelandii*). All enzymes in group I-III represent two-subunit enzymes, consisting of a small β (28-35 kDa) and a large α (56-68 kDa) subunit. Groups I and II are encoded by simple two-gene operons, group III by more complex operons. The “large” subunit binds the active site nickel, whereas the “small” subunit has an electron transfer function. This structural difference between group II and III [NiFe] hydrogenases is manifested in their mode of action: group II hydrogenases donate their electrons to a soluble, non-membrane-bound, periplasmic cytochrome while electrons from group III hydrogenases are delivered directly to a membrane-bound electron transport chain.

Enzymes in groups IV (i.e. *Ralstonia eutropha*, *Methanobacterium autotrophicum*) and V (*E. coli* hydrogenase-3) have a more complex subunit composition and fading homology with the group I-III hydrogenases.

It can be concluded that the [NiFe] hydrogenases from *D. gigas*, *D. vulgaris* Miyazaki F and *D. fructosovorans* genetically exhibit a high homology (65-70%) and represent a subclass of [NiFe] hydrogenases. The identity of the amino acid sequence in the large subunit of *D. vulgaris* with that from *D. gigas* is 69% (FASTA alignment), with that from *D. fructosovorans* 66% and with the [NiFeSe] hydrogenase from *D. baculatum* still 42%. These [NiFe] hydrogenases are sometimes referred to as ‘standard hydrogenases‘. Figure **2.3** shows the classification of hydrogenases according to a protein sequence comparison of the large (α) subunit.

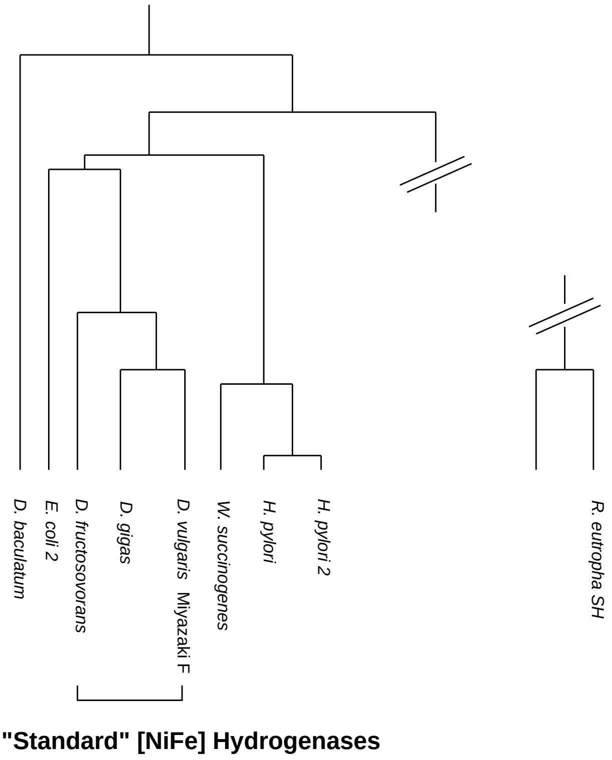

Figure 2.3: Dendogram of the [NiFe] hydrogenases based on a protein sequence homology of the large (α) subunit with the FASTA algorithm. The comparison was only done for hydrogenases for which the complete protein sequence is available.

The [NiFe] hydrogenases from *Allochromatium vinosum* (formerly *Chromatium vinosum*) and *Thiocapsa roseopersicina* may also be associated with group II hydrogenases due to their spectroscopic characteristics. These two bacteria belong to the group of purple-sulphate bacteria and still possess the ability to perform photosynthesis and grow phototrophically - an ability the usual class II hydrogenases have lost during evolution. Until now, there is no primary structure available for *A. vinosum.* The [NiFe] hydrogenase from *Th. roseopersicina* BBS has recently been sequenced for a 8000 base pair fragment [20]. The homology of the gene for the large subunit with that from *D. vulgaris* was 58% and justifies their assignment to a class II hydrogenase. The protein similarity between *A. vinosum* and *Th. roseopersicina* may also be fortuitous. The two organisms seem to have developed independently to perform dissimilar metabolic functions [21].

Nevertheless, all [NiFe] hydrogenases which have been sequenced so far, possess two highly conserved consensus Cys–X–X–Cys in the α subunit, one towards the N-terminus and one further down towards the C-terminus. In [NiFeSe] hydrogenases the first cysteine of the latter motif is replaced by a selenocysteine. Those cysteine amino acids can be shown to coordinate the heterobinuclear metal active site (see below). The conservation of amino acids is less pronounced in the β subunit which is responsible for the electron transfer. A varying number of Fe-S clusters of different composition may participate in the electron transfer chain.

Comparing [NiFe] and [Fe] hydrogenases, there is no significant homology between the polypeptides encoding the active sites of these enzymes. The two families must therefor have evolved independently. The [NiFe] hydrogenases with their high homology must have developed from a common ancestor. It appears plausible to assume that a cytoplasmic, nickel-containing hydrogenase existed before the evolutionary path towards a periplasmic enzyme left the nickel-binding site relatively conserved and invented a more variable electron-transferring subunit.

2.2 Molecular Structure

The arrangement of the conserved residues and the composition of the active sites became clear from X-ray crystallographic studies and from spectroscopic work. Since 1995, crystal structures at atomic resolution of several nickel-containing enzymes have been determined and contributed to the understanding of biological nickel in catalysis (see Table **2.1**). The progress in nickel bioinorganic structural chemistry has been described in some reviews [9, 22–25]. Recently, two X-ray structures of [Fe]-only hydrogenases from *Clostridium pasteurianum* [30] and *Desulfovibrio desulfuricans* [31] were independently published. Until now, there is no X-ray structure of the metal-free hydrogenase.

Table 2.1: Overview of Ni-containing protein X-ray structures

Protein	Resolution [Å]	Metal binding	References
Urease	2.1	Binuclear nickel	[26]
[NiFe] hydrogenase	1.8, 2.5	Binuclear nickel and iron	[27, 28]
Methyl-CoM reductase	1.45	Ni-porphinoid	[29]

A milestone in [NiFe] hydrogenase research was the first X-ray structure of the *D. gigas* enzyme at 2.85 Å resolution [32]. The crystal form was triclinic with two molecules in the unit cell. While the small subunit, containing 1 [3Fe-4S] and 2 [4Fe-4S] clusters, displayed similarities to the flavodoxin redox protein, the large subunit presented a new topological class of enzyme with an unusual Ni coordination sphere. Figure **2.4** shows the cofactor arrangement in the [NiFe] hydrogenase from *Desulfovibrio vulgaris* Miyazaki F [28]. The large subunit bears the active site, the small subunit contains three iron–sulphur clusters which are arranged in a chain and participate in electron transfer to and from the active site. The active centre contains a nickel and a second metal ion, the discovery of the latter came as a surprise. It was only tentatively assigned to a Fe atom [32]. Cysteines 68 and 533 serve as bridging ligands between the metals whereas Cys65 and Cys530 (in *D. gigas* enumeration of amino acids) are terminally bound to the nickel atom (see Figure **2.5**). Higher temperature factors of the Ni and its surrounding sulphur atoms were determined which could originate from disorder, X-ray damage to the crystal, only partial Ni occupancy of the active sites in the crystal or the presence of several Ni redox states. The latter was investigated by EPR spectroscopy and revealed that the X-ray structure corresponds primarily to that of the Ni-A form (see below) [32]. This was also supported by activation of the crystallized enzyme which required hours to recover full hydrogen uptake activity. The three non-protein ligands of the second metal were modelled as water molecules since a positive assignment of the electron density peaks

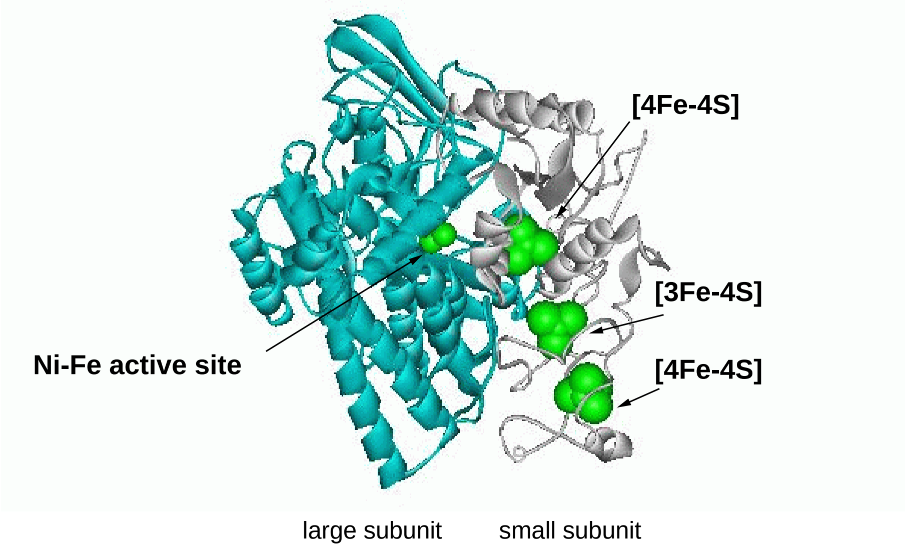

Figure 2.4: Cofactor arrangement in *Desulfovibrio vulgaris* Miyazaki F [28]. The large subunit (left) harbours the Ni-Fe active site, the small subunit (right) incorporates the proximal [4Fe-4S] cluster, the [3Fe-4S] cluster and the distal [4Fe-4S] cluster which may be involved in electron transfer.

was not possible. The heterobinuclear center then led the authors to a speculation of the CO inhibitor and H_2 substrate binding in the bridging position between the nickel and iron atoms. Speculations about possible electron and proton transfer pathways were also made. An electron transfer from the active site via two Fe-S cluster to the distal [4Fe-4S] cluster and then to cytochrome c_3 was proposed. A highly conserved His/Glu motif would represent a separate possible way of proton transfer. Table **2.2** gives details of the active site structural parameters from the refined X-ray analysis. The Ni $\cdots$ Fe distance was given as 2.69 Å, the Ni-S distances were 2.23 Å (Cys68), 2.04 Å (Cys65), 2.42 Å (Cys530), and 2.60 Å for Cys533. A non-protein ligand bridging the nickel and iron atoms (labelled 'X' in Table **2**) is not included in this model. This position was vacant in the initial structure.

In a later publication by the same authors, a new, pseudo-hexagonal crystal form was investigated [27]. This time the second metal atom was unambiguously identified to be iron by collecting data at wavelengths close to either side of the Fe absorption edge. The resolution was increased to 2.54 Å. The bridging cysteines (Cys68 and 533) refined to distances of 2.6 Å, that of the terminal cysteines were shorter (2.2 Å for Cys65 and 2.3 Å for Cys530) (see Table **2.2**). A strong peak in the electron density map indicated the presence of an additional ligand in a bridging position between the Ni and Fe centres. This peak was tentatively assigned to an oxygen species, leaving the nickel atom in a highly distorted square pyramidal coordination sphere with a vacant axial sixth ligand site. The iron atom has six ligands in a distorted octahedral environment (see Figure **2.5**).

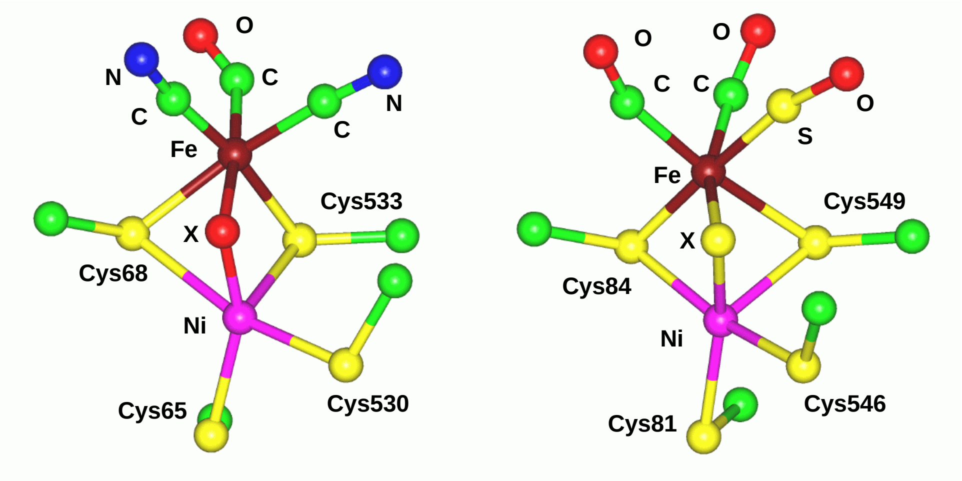

Figure 2.5: Details of the active centres of the [NiFe] hydrogenases from *D. gigas* [27] (left) and *D. vulgaris* Miyazaki F [28] (right). The bridging ligand *X* is supposed to be an oxygen or sulphur species in *D. gigas* and *D. vulgaris*, respectively.

Candidates for the bridging ligand are mono-oxygenated species derived from the reduction of O_2. Inclusion of a diatomic molecule would be sterically hindered according to the authors [27]. Higher temperature factors were only observed for the Ni ion, the S atom of Cys530 and the bridging species which were assigned to static disorder due to structural differences between the various active sites present in the crystal. The findings for the *D. gigas* [NiFe] hydrogenase together with a speculation about the mechanism have been reviewed in [11, 33–35].

Table 2.2: Selected structural parameters of the active centre of ‘as-isolated’ [NiFe] hydrogenases from different X-ray structures. Bond lengths in Å, bond angles (∠) in °.

	D. gigas	*D. gigas*	*D. vulgaris* Miyazaki F	*D. fructosovorans*
Å,°/res., ref.	2.85Å [32]	2.54Å [27]	1.8Å [28]	2.7Å [36]
Ni · · · Fe	2.69	2.90	2.52	3.23
Ni–SCys533	2.60	2.62	2.36	2.45
Ni–SCys68	2.23	2.58	2.15	1.62
Ni–SCys530	2.42	2.27	2.33	2.12
Ni–SCys65	2.04	2.16	2.22	2.16
Ni · · · X	not given	1.74	2.19	not given
Fe–SCys533	2.26	2.20	2.36	2.31
Fe–SCys68	2.62	2.23	2.15	2.22
Fe · · · X	not given	2.14	2.28	not given
∠ Ni-X-Fe	not given	96.5	68.4	not given
∠ Ni-SCys533-Fe	66.7	73.6	64.1	85.6
∠ Ni-SCys68-Fe	66.8	73.9	66.2	113.9

The [NiFe] hydrogenase from *D. vulgaris* Miyazaki F is highly related to that of *D. gigas* (see above). After first single crystals became available [37] the active site and the Fe-S clusters were localized at a resolution of 4 Å [38]. The membrane-bound hydrogenase is solubilized by trypsin digestion thus facilitating the crystallization. The hydrogenase from *D. vulgaris* crystallizes in the space group $P2_12_12_1$. The folding pattern of the protein and structural features of the metal centres are very similar to those of *D. gigas*. The two structures can be superimposed with a root mean square deviation of 0.82 Å for all main chain atoms [28]. The coordination of the Ni-Fe active centre is very similar to that of *D. gigas*. Ni is coordinated by four sulphur atoms of cysteines (amino acid residues 80, 84, 546 and 549). The Fe atom (as identified by anomalous dispersion difference maps) is coordinated by two bridging cysteines (Cys84 and Cys549) and exhibits three distinctive electron density peaks as terminal ligands. A comparison of the active centres of the [NiFe] hydrogenases from *D. gigas* and *D. vulgaris* Miyazaki F is done in Table **2.2** and depicted in Figure **2.5**. At closer inspection, however, differences in the structural parameters of the active site become apparent (see Table **2.2**). The Ni $\cdots$ Fe distance is 2.55 Å, the diatomic ligands to the Fe were refined to one S=O, and two CO or CN molecules (higher electron density peak for one non-protein ligand and pyrolysis MS experiments with an usual mass peak at 48 (S=O) [28]) and the bridging ligand is assigned to a sulphur atom based on a higher electron density although an oxygen species remained a possible second candidate. Unexpectedly, a magnesium ion was also discovered near the C terminus of the large subunit which might be involved in proton transfer reactions.

The [NiFe] hydrogenase from *D. fructosovorans* has been also crystallized and its structure was elucidated by X-ray crystallography. Until now, it has only been published in the context of a [3Fe-4S] → [4Fe-4S] cluster conversion by site-directed mutagenesis of a glycin into a cysteine residue after heterologuous expression in *D. gigas* [36]. The coordinates of the [NiFe] hydrogenase from *D. fructosovorans*, however, have been deposited at the Brookhaven Protein Data Bank (PDB) as a 'layer 1' file. This indicates that the structural parameters are still not definite and must be used with caution. They are also included in Table **2.2** .

Thus for all hydrogenases of the group II, X-ray structures have become available. The hydrogenases from *D. gigas* and *D. vulgaris* Miyazaki F are spectroscopically very similar [39]. It thus remains to be investigated whether an agreement about the composition of the active centre can be reached.

2.3 The Redox States of [NiFe] Hydrogenases

Hydrogenases are oxidoreductases which means that they oxidize a substrate, transport the electrons and reduce a reductant.

In particular, they oxidize H_2 to 2 H^+ and 2 electrons, pass the electrons to their physiological electron acceptor cytochrome c_3 and finally utilize them to reduce sulphur to sulphide.

During the course of the redox cycle, [NiFe] hydrogenases pass through a number of different redox states. Electron paramagnetic resonance spectroscopy (EPR) and related techniques (see below) are the method of choice to characterize the *paramagnetic* states involved in the redox cycle. Figure **2.6** gives a schematic picture of the complex redox states of the [NiFe] hydrogenase. There are potentially four paramagnetic centres in the [NiFe] hydrogenase: namely the heterobimetallic NiFe cluster in the large

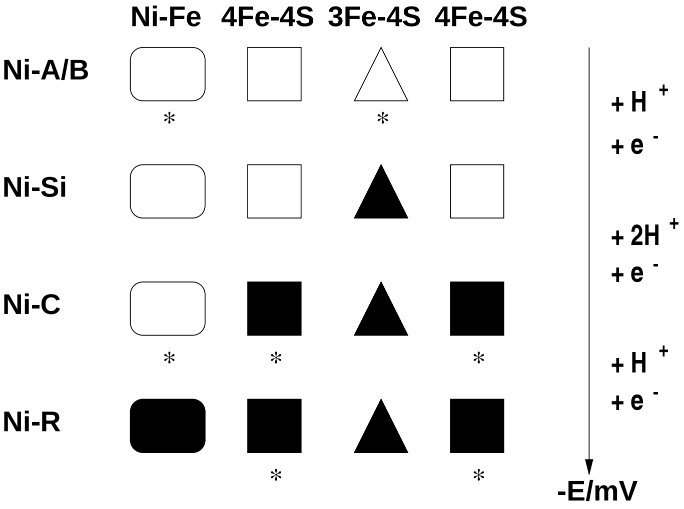

Figure 2.6: Redox-States of the [NiFe] Hydrogenase. Asterists denote paramagnetic (S = 1/2) states, squares symbolize the cubane [4Fe-4S] clusters, a triangle stands for the [3Fe-4S] cluster. The active centre is given by the rectangle with rounded corners. Open symbols stand for oxidized, filled symbols for completely reduced states. The redox potential of the protein in solution is lowered when going from the oxidized Ni-A/B states to the completely reduced Ni-R form. On the right hand side, the numbers of protons and electrons are given which are involved in each redox step. These were determined by redox titrations in the presence of dyes (see [40] and references therein). The number of protons are derived from the pH-dependence of the midpoint potentials.

subunit, the proximal [4Fe-4S] cluster in the small subunit, one [3Fe-4S] cluster, and the distal [4Fe-4S] cluster.

In the ‘as-isolated’ form the active site of the enzyme is in its oxidized, enzymatic inactive, paramagnetic states Ni-A or Ni-B. Ni-A displays EPR spectra with g-tensor principal values $g_{x,y,z}$ = 2.32, 2.24, 2.01 and Ni-B with $g_{x,y,z}$ = 2.33, 2.16, 2.02. In addition, at low temperatures ($\leq$ 60 K) a rather isotropic EPR signal at g = 2.01 is visible which is assigned to the oxidized $[3Fe\text{-}4S]^+$ cluster in the small subunit. EPR experiments with ^{61}Ni enriched protein samples [41, 42] and the observed ^{61}Ni hyperfine splitting therein unambiguously showed that the EPR signals originate from the Ni atom in the active centre. The correlation between the EPR signals and enzymatic activity was first established by Fernandez *et al.* [43]. They showed that Ni-A and Ni-B differ in their rates of activation. Whereas Ni-B is activated by incubation under an H_2 atmosphere within minutes (therefore sometimes referred to as ‘ready’ or Ni_r) Ni-A requires incubation for hours (sometimes called ‘unready’ Ni_u). During activation, the Ni-A and Ni-B EPR signals disappear and a diamagnetic, EPR-silent state Ni-SI is reached.

EPR analysis of the first protein crystals from *D. gigas* revealed a constitution of 85% Ni-A and

15% Ni-B [32], the amount of EPR-silent fraction was not determined. Later Dole *et al.* examined a polycrystalline powder sample of the *D. gigas* hydrogenase and obtained an EPR spectrum essentially identical to that of a frozen solution of Ni-A [44]. A constitution of 10% Ni-B, 40 % Ni-A and 50% Ni-SI was determined.

Upon reduction from the oxidized states to the EPR-silent form Ni-SI, the [3Fe-4S] cluster is reduced to its S = 2 $[3Fe\text{-}4S]^0$ form. Upon further reduction, a new rhombic EPR signal of the active site "Ni-C" with principal values $g_{x,y,z}$ = 2.20, 2.14, 2.02 appears. This state is believed to be two electrons more reduced than Ni-A/B and belong to a catalytic intermediate in the redox cycle. The relation between catalytic activity and the appearance of the Ni-C EPR signal was given by Moura *et al.* [45]. Here, EPR spectroscopy provides a direct spectroscopic assay of enzyme activity. The Ni-C state displays unusual features. The Ni-C state is light-sensitive and converts into a fourth paramagnetic state Ni-L with g-tensor principal values $g_{x,y,z}$ = 2.28, 2.11, 2.05. The reaction is carried out at low temperatures between 4 and 77 K. Upon further 'warming' the sample to 120 K in the dark, the Ni-L signal disappears and the Ni-C signal is recovered. In addition, in the Ni-C state, both the proximal and the distal [4Fe-4S] clusters become paramagnetic (S = 1/2) in their reduced $[4Fe\text{-}4S]^+$ forms. Magnetic interaction between the proximal $[4Fe\text{-}4S]^+$ cluster and the NiFe active site induces the appearance of a complex EPR spectrum (called "split Ni-C") at low temperatures and a significant enhancement of the relaxation rates of the Ni centre. The magnetic interaction between the two centres was analyzed by Guigliarelli *et al.* [46, 47]. Based on numerical simulations, they determined the parameters of exchange and dipolar interactions between the two closely spaced paramagnets and also obtained the relative orientations of the g-tensors with respect to each other. Furthermore, the g-values of the proximal [4Fe-4S] cluster, which are observed by the spin-coupling with the distal [4Fe-4S] cluster, were given. The study was later extended to the interaction of the Ni-L state and the proximal [4Fe-4S] (in the "split Ni-L" signal) and led the authors to the conclusion that the g-tensor orientations in Ni-C and Ni-L were very similar [48].

Finally, the fully reduced diamagnetic 'resting' state Ni-R is obtained for which hardly any spectroscopic data apart from Fourier-transformed infrared spectroscopy (FTIR) are available.

Whereas EPR suffers from the drawback of being applicable only to the *paramagnetic* states of the enzyme, FTIR covers the complete range of redox states. After the initial discovery of unusual high frequency bands in [NiFe] hydrogenases and their speculative assignment to non-protein CO and CN ligands at the Fe atoms in the active centre [27, 49, 50], they were unambiguously assigned to 2 CN and 1 CO ligand in *A. vinosum* upon cultivation with ^{15}N and ^{13}C enriched media and observing the respective isotope shifts of the IR bands [51]. The band around 1930-1940 cm^{-1} corresponds to the stretching frequency of the C=O bond. The two bands above 2040 cm^{-1} belong to the symmetric and antisymmetric stretching frequencies of the C≡N triple bonds (see Figure **2.7**).

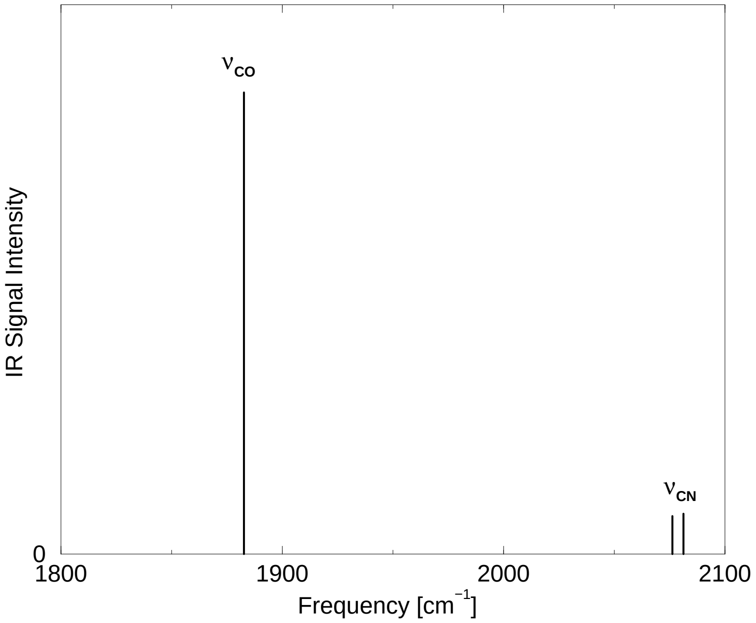

Figure 2.7: BLYP/DZVP calculated high frequency IR vibrational frequencies of a small cluster model of the Ni-B state. The positions of the vibrations approximately correspond to those observed experimentally (see text). B3LYP/6-311+G IR frequencies were also obtained for larger Ni-A, Ni-B, Ni-C and Ni-L model clusters. The respective frequencies were 1988, 1995, 1612 cm^{-1} (Ni-A), 2016, 2002, 1697 cm^{-1} (Ni-B), 2014, 2009, 1687 cm^{-1} (Ni-C), 1969, 1963, 1586 cm^{-1} (Ni-L). The magnitude of the deviations are a typical systematic error inherent in DFT methods in the calculation of IR frequencies (in particular for CO stretching vibrations [52]) and also originate from the drastic influence of spin-contamination on the calculated IR vibrations [53] ($\langle S^2 \rangle$ values are 0.94 for Ni-A, 0.80 for Ni-B, 0.79 for Ni-C, 1.18 for Ni-L).

The characterization of all redox states of [NiFe] hydrogenases by means of their IR spectra, the *in situ* following of their bands upon oxidation/reduction has matured to near perfection [50, 54, 55]. Table **2.3** collects FTIR data for the two most intensively investigated [NiFe] hydrogenases *D. gigas* and *A. vinosum.* In general, the shift in IR bands is rather small between the different redox states of the enzymes. FTIR spectroscopy probes the strength of the C=O and C≡N bonds. The force constant of the bond depends on the balance between σ ligand-metal bonding and π-back bonding. Metal-ligand π-back donation into anti-bonding π^* orbitals of the C≡N triple bond weakens the C-N bond. A decrease of 3-5 cm^{-1} in the CN IR bands upon reduction from Ni-B to Ni-C thus indicates a slight increase in the metal-ligand π-back donation caused by an increase of charge density at the Fe atom. The changes are all in the range of 30-35 cm^{-1} and smaller than that expected for a one electron change of the electron

Table 2.3: Characterization of the redox states of [NiFe] hydrogenases by their IR bands

Redox state	High frequency IR bands [cm^{-1}]					
	D. gigas [27]			*A. vinosum* [55]		
	ν_{CO}	ν_{CN}		ν_{CO}	ν_{CN}	
Ni-A	1947	2083	2093	1945	2083	2093
Ni-B	1946	2079	2090	1944	2079	2090
Ni-C	1952	2073	2086	1950	2074	2087
Ni-L				1898	2043	2058
Ni-R	1940	2060	2073	1936	2059	2073
Ni-SU	1950	2089	2099	1950	2089	2099
Ni-SI$_{I}$	1914	2055	2069	1910	2051	2067
Ni-SI$_{II}$	1934	2075	2086	1932	2074	2086

density on an iron atom (102 cm^{-1} [56]). The largest shifts are observed for the reduction Ni-B to Ni-SI (a concerted shift downwards by approx. 30 cm^{-1}) and the Ni-C to Ni-L conversion (30 cm^{-1} for the CN bands and 50 cm^{-1} for the CO band). These two processes must be accompanied by a larger change of electron density at the Fe metal site, i.e. an increase in electron density due to liberation or photodissociation of a ligand.

During the catalytic cycle, paramagnetic and diamagnetic states alternate. The appearance or disappearance of the corresponding EPR signal serves as an assay of the redox state of the Ni centre. Redox titrations of [NiFe] hydrogenases gave a midpoint potential for the Ni-A/B $\rightarrow$ Ni-SI (Ni(III)/Ni(II)) conversion between -410 and -110 mV [12,57] (see Figure **2.6**). The midpoint potential of Ni(III) was found to be pH-dependent by -60 mV per pH unit. The first reduction step can thus be written as

$$\mathrm{Ni(III)} + \mathrm{H}^{+} + \mathrm{e}^{-} \rightarrow \mathrm{Ni(II)H}^{+} \qquad . \tag{2.2}$$

The Ni-SI $\rightarrow$ Ni-C conversion exhibited a pH-dependence twice as large as that of the initial step which indicates that two protons might enter the active centre [40]. The Ni-C $\rightarrow$ Ni-R reduction, again, is a step associated with a single protonation ([58], see Figure **2.6**).

2.4 Specific Properties of the Paramagnetic States

Table **2.4** gives an overview about the measured hyperfine splittings in EPR and ENDOR spectra with nuclei which possess a nuclear spin I $\geq$ 1/2. Very often, the reported hyperfine splittings are only deduced from linewidth broadening effects in EPR spectra and are thus only crude estimates, often simulations were not performed. The given hyperfine interactions are also those measured along the g-tensor principal values. In the case where hyperfine tensor and g-tensor are not collinear, the true hyperfine tensor principal values might differ. After the first discovery of an EPR signal from [NiFe] hydrogenases [41], actual proof of it being a Ni signal was obtained from ^{61}Ni enrichment and subsequent detection of line broadening and hyperfine splitting [59, 64]. Moura *et al.* produced evidence that all three paramagnetic states Ni-A, Ni-B and Ni-C showed ^{61}Ni hyperfine broadening or splitting [45]. In the literature, however, only one complete ^{61}Ni hyperfine tensor is found which was obtained from simulations of the EPR spectra [59]. All other delivered only estimates from the line broadening effects. For an overview of ^{61}Ni hyperfine splittings in [NiFe] hydrogenases see [65].

Table 2.4: Collection of hyperfine data in MHz for [NiFe] hydrogenases

Nucleus	State	Organism^a	Hyperfine Coupling			Ref.	Remarks
			A$_x$	A$_y$	A$_z$		
^{61}Ni	Ni-A	M. t.	21	42	76	[59]	simulated
	Ni-A	D. g.	6-17	6-17	76	[45]	A$_x$, A$_y$ estd.
	Ni-C		–	–	76		A$_x$,A$_y$ not resolved
	Ni-C	R. a.	17	14	-	[60]	A$_z$ not resolved
	Ni-L		56	28	14		
^{57}Fe	Ni-A	D. g.		≈ 1		[61]	^{57}Fe-ENDOR
	Ni-B	D. d.		none			
	Ni-C	D. g.		none			
^{33}S	Ni-B	W. s.	27	39	–	[62]	
^{17}O	Ni-A	A. v.	14	11	13	[63]	
	Ni-B		0	11	20		
^{13}CO	Ni-CO	A. v.	81	85	90	[63]	g=2.12, 2.07, 2.02

a Abbreviations: M.t. *M. thermoautotrophicum*, D. g. *D. gigas*, R. a. *R. eutropha* (SH), D. d. *D. desulfuricans*, W. s. *W. succinogenes*, A. v. *A. vinosum*

The detection of a second metal ion (the Fe) in the active centre of then termed “[NiFe]”-hydrogenases in the X-ray structure analysis was a surprise to the magnetic resonance community. So far, a second metal situated close to the nickel had not been detected. There was no effect of ^{57}Fe enrichment on the EPR spectrum of Ni-A from *D. gigas* [66]. The absence of ^{57}Fe line broadening alone is not sufficient to demonstrate that the Ni-Fe binuclear centre is not a spin-coupled system. In case of an exchange-coupled system one would expect a deviation from Curie’s law at low temperatures. The very existence of a spin-coupled centre is ruled out by analysis of the temperature dependence of the Ni-A, Ni-B, Ni-C and Ni-L EPR signal intensities [44]. No deviation from Curie’s law was detected between 10K and 240K. Further support comes from recent ^{57}Fe-ENDOR experiments (see Table 2.5) in which no hyperfine interaction could be detected for Ni-B and Ni-C and only a very small one (approx. 1 MHz) for Ni-A [61]. The total spin multiplicities of the metals in the active centre necessarily must therefor be assumed to be S = 1/2 for the Ni and S = 0 for the Fe atom. The low spin Fe(II) 3d^6 state is plausible because of the CN and CO non-protein ligands (see above) which impose a strong ligand field on the iron atom.

The spectroscopic detection of spin density at a sulphur ligand to the Ni atom comes from ^{33}S enriched protein from the [NiFe] hydrogenase from *Wollinella succinogenes* [62]. Hyperfine splitting due to interaction between the I = 3/2 nuclear spin from ^{33}S and the electron spin of the Ni centre in Ni-B was detected (see Table 2.4). Simulations of the measured line broadening of the g_x-component and hyperfine splitting of the g_y-component assuming an enrichment of 70% and hyperfine interaction with *one* ^{33}S nucleus gave good agreement with the experimental spectrum. For Ni-C line broadening was also observed. A difference spectrum of the Ni-L minus Ni-C spectrum also revealed a ^{33}S hyperfine splitting of the g_z-component in Ni-L. The experiments are indicative of the fact that hyperfine interaction to *one* sulphur nucleus is present in Ni-B, Ni-C and Ni-L states. It cannot be said, however, whether this is the same sulphur atom in all these states.

In order to investigate the hypothesis of an oxygenic species present in the oxidized states of the [NiFe] hydrogenase, the effect of $^{17}O_2$ upon the EPR spectra in the oxidized states Ni-A/B was studied by van der Zwaan *et al.* [63]. They measured a nearly isotropic line broadening of all g-components in EPR spectra of Ni-A (see Table **2.4**) but also some detectable hyperfine broadening in the Ni-B state. It was concluded that either O_2 or a reduction adduct binds in the vicinity of the oxidized states. According to the authors, the difference between Ni-A and Ni-B species, therefore, cannot be explained by assuming that only in one state (the unready Ni-A) O_2 or one of its species is bound to the active site.

When Ni-C is treated with CO, its EPR signal transforms into a Ni-C_{CO} signal with $g_{x,y,z}$ = 2.12, 2.04, 2.02 [63]. The bound CO is photolabile and the Ni-C signal is recovered upon illumination. The effect of ^{13}CO (I = 1/2) on the EPR spectra of the CO-inhibited Ni-C$_{CO}$ was investigated [63] (see Table **2.4**). From the nearly isotropic hyperfine splitting from ^{13}C of ^{13}CO about 85 MHz along the g principal values, an axial bonding situation for the CO is discussed. Very recently, it was investigated whether it would be the Ni-C or the Ni-L state that actually binds the carbon monoxide molecule [58].

The investigation of ^{1}H hyperfine interactions in the different paramagnetic states of the [NiFe] hydrogenase is of particular relevance. Since the enzyme is involved in hydrogen metabolism, either substrate H$_2$, or the products H$^+$, H$^-$ or H$^\bullet$ are expected to be bound in the vicinity of the Ni atom in the active centre and thus should be detectable by EPR or ENDOR spectroscopies.

When the enzyme in the Ni-C form is solvent-exchanged with D$_2$O/D$_2$, a slight but significant reduction of line width of the g$_x$- and g$_y$ components was noticed (maximum effect on g$_y$ of 14 MHz (0.5 mT)) [67]. This indicates a solvent-exchangeable proton in the ligand surrounding of the Ni atom in the Ni-C state. The Ni-C to Ni-L conversion is six-fold slower when the enzyme is prepared in D$_2$O/D$_2$ solvent [67] which indicates that a hydrogen species (respectively a deuterium species) is lost upon illumination. Likewise the re-appearance of the Ni-C signal at high temperatures is also five-fold slower in D$_2$O/D$_2$ [68].

The ultimate detection of ^{1}H or ^{2}H nuclear hyperfine interaction in the vicinity of the Ni active site is complicated by the large EPR linewidth but can be resolved by double resonance experiments such as ENDOR and electron spin echo envelope modulation (ESEEM). Chapman *et al.* used two-pulse ESEEM spectroscopy to address the question of solvent accessibility of the Ni-A and Ni-C states by comparing spectra in H$_2$O and D$_2$O [68]. The Ni signal in Ni-A showed no modification upon solvent exchange. This indicates that there is no proton bound to the active centre which can be substituted by a deuteron. The [3Fe-4S]$^+$ signal, however, showed the presence of a solvent exchangeable proton. The Ni-C signal exhibited a significant modulation in D$_2$O due to a deuterium nucleus in the vicinity of the Ni. Table **2.5** collects ^{1}H- and ^{2}H-ENDOR data. Fan *et al.* investigated the active site of the [NiFe] hydrogenase from *D. gigas* in three paramagnetic states Ni-A, Ni-B, Ni-C by means of ENDOR spectroscopy [69]. Ni-A spectra were identical in H$_2$O and D$_2$O in agreement with the finding by Chapman (see above). Large hyperfine couplings of 12.8 MHz at g$_y$ were assigned to β-CH$_2$ protons. The ^{1}H-ENDOR spectrum of the Ni-C form displays an additional large hyperfine coupling of 16.8 MHz at g$_y$ which is lost upon solvent exchange with D$_2$O. The corresponding ^{2}H-ENDOR signal was also detected. The second signal which also showed a D$_2$O effect (4.4 MHz) was later shown to originate from the Ni-B form. The β-CH$_2$ proton couplings increase from 12.8 MHz in Ni-A to 15 MHz in Ni-B.

Whitehead *et al.* later repeated ENDOR experiments on a different organism, the [NiFe] hydrogenase from *Th. roseopersicina* [70]. Here, the Ni-C to Ni-L conversion was also investigated. In Ni-C, two

Table 2.5: Overview of ^{1}H-ENDOR Data of [NiFe] Hydrogenases

State	Organism^a	Hyperfine Coupling	Remark/Assignment	Ref.
Ni-A	D. g.	12.8 MHz at g_y	cysteinyl β-CH_2	[69]
			in D_2O identical	
Ni-B		15 MHz at g_y	cysteinyl β-CH_2	
		4.4 MHz at g_x	loss in intensity in D_2O/OH^- or H_2O	
Ni-C		16.8 MHz at g_x	solvent exchangeable A^H = [15, 22, 25]	
			line narrowing in D_2O (3, 7, 8 MHz)	
			^{2}H-ENDOR 2.4 MHz/in plane H^-	
Ni-C	T. r.	$A(^1H_1)$ 16-20 MHz	in D_2O $A(^2H_1) \approx 3.1$ MHz	[70]
			solvent exchangeable proton	
		$A(^1H_2) \approx 12$ MHz	isotropic, not exchangeable	
		$A(^1H_3) \leq 5$ MHz		
Ni-L		$A(^1H_1)$ lost	photololabile species	
		$A(^1H_2) \approx 10$ MHz	neither photolabile nor exchangeable	

a Abbreviations D.g. *D. gigas*, T. r. *Th. roseopersicina*

large ^{1}H hyperfine couplings were detected. The isotropic, non-exchangeable coupling of 12 MHz was assigned to β-CH_2 protons of a cysteine residue. The larger coupling of 16-20 MHz is D_2O exchangeable and lost upon photoillumination in the Ni-L state. Unresolved signals smaller than 5 MHz in the Ni-C state could not be assigned. The largest ^{1}H couplings in the Ni-L state are 8-10 MHz and thus smaller than in the Ni-A, Ni-B and Ni-C forms.

2.5 Motivation and Perspective of this Work

Albeit there was a large amount of very detailed spectroscopic data in the literature, their interpretation in the context of structural changes between the redox states was not possible before the work in this thesis was started. This was due to several complications.

The elucidation of the X-ray structure of a [NiFe] hydrogenase in 1995 revealed atomic details of the active Ni site in the enzyme for the first time. The detection of a heterobimetallic cluster with an additional Fe atom was unexpected. The unusual coordination sphere of the Ni raised more questions than it answered. Is Ni the catalytic site? Is there a bridging ligand in all states, what is its nature and role, do the cysteine ligands participate in the cleavage of the H–H bond, what is the role of the Fe atom, how do the different paramagnetic states differ from each other? How do the H_2 and proton channels look like? What is the influence of the protein environment?

Only in 1999, an X-ray structure of the reduced enzyme were published. Some of the information can be gained from EPR investigations of protein single crystals. The large and well-ordered protein single crystals of the [NiFe] hydrogenase from *D. vulgaris* Miyazaki F opened a new field. One can deduce the *spatial* arrangement of i.e. g-tensors with respect to the ligand environment, orientations of hyperfine interaction tensors of, for example ^{1}H nuclei, and possibly detect the binding situation of molecular hydrogen or its dissociation products in the active centre.

The correlation between magnetic resonance parameters and structural modifications is still difficult. Changes in EPR or ENDOR spectra can only indirectly be interpreted in terms of changes in the X-ray structure. It is not possible to perform a high-resolution collection of X-ray diffraction data of a crystal mounted in an EPR quartz tube. However, the determination of the unit cell parameters and the orientation of the crystal axes is feasible. Likewise, after massive X-ray diffraction data collection in a synchrotron beam, the protein single crystal suffers from X-ray damage and from the generation of additional radicals.

Here, a theoretical approach which yields hyperfine parameters and g-tensors for a given geometry may provide useful information. Is it possible to find a methodology that allows the prediction of magnetic resonance parameters for a system as complex as the active site of a metalloprotein with sufficient accuracy and affordable computing resources?

This combination of protein single crystal EPR and ENDOR and theoretical calculations in the frame of approximate Density Functional Theory (DFT) is the central aspect of this work.

When this work was started, there was no theoretical study of [NiFe] hydrogenases, neither on the electronic structure nor on the reaction mechanism published. This metalloenzyme recently gained attention and a number of publications based on *first principles* calculations appeared in the last years [71–76]. None of them, however, dealt with a theoretical description of the paramagnetic states of the enzyme for which many experimental data exist.

Until recently, there was also no rigorous approach to reliably deal with the magnetic resonance parameters of transition metal complexes, not to say that the treatment of systems as complex as the active centre of a metalloenzyme was out of reach with conventional post-Hartree Fock methods. Thus, a new relativistic DFT approach has been critically evaluated and was used here for the characterization of the paramagnetic intermediates of [NiFe] hydrogenase. Based upon the results obtained for the intermediates, a plausible enzymatic mechanism can be suggested which considers experimental findings.

Chapter 3

Theory and Fundamentals

3.1 EPR Spectroscopy

The basics and more sophisticated details of EPR spectroscopy are given in many text books [77, 78]. In the following only a very concise treatment of the aspects which are necessary for the understanding of this thesis is given. Electron Paramagnetic Resonance (EPR) spectroscopy detects the interaction of an unpaired electron spin with a magnetic field and with its environment. Paramagnetism of the sample thus is a prerequisite.

3.2 The Spin-Hamiltonian

The interaction of an electron spin with an external magnetic field $\mathbf{B_0}$ is described by the electron-Zeeman term

$$\mathcal{H}_{\mathrm{eZ}} = g\beta\mathbf{B_0}\hat{S} \tag{3.1}$$

where g is the electron g-factor, β is the Bohr magneton and $\hat{S}$ the electron spin operator (see Figure **3.1**).

The electron, however, does not sense the external magnetic field $\mathbf{B_0}$ but an effective field, weakened or enforced by shielding or deshielding.

$$\mathbf{B_{eff}} = \mathbf{B_0} + \mathbf{B_{local}} = (1-\sigma)\mathbf{B_0} = (g/g_e)\mathbf{B_0} \tag{3.2}$$

Thus any deviation from g_e is a measure of the chemical environment of the unpaired electron. In transition metal complexes it is not only the electron's angular momentum that contributes to the deviation from g_e. Some complexes (i.e. d-metal complexes) possess a resulting orbital angular momentum which

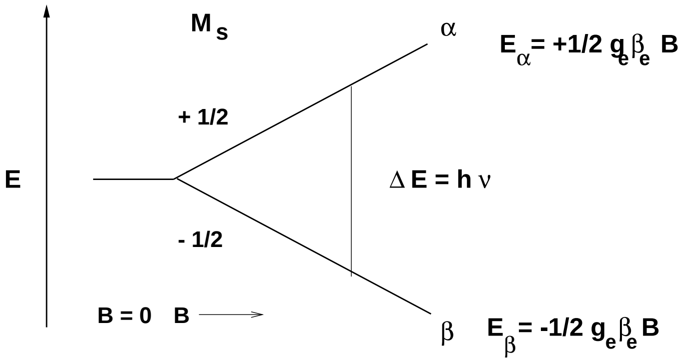

Figure 3.1: Electron-Zeeman Splitting in a Magnetic Field. In the presence of a homogeneous, time-independent magnetic field $\mathbf{B_0}$ the two degenerate energetic states split into a spin-up (α M$_s$ = +1/2) and a spin-down (β M$_s$ = -1/2) energy level. The energetic difference between the two states is $\Delta E = g_e \beta_e B$ and must be matched by the microwave radiation $\Delta E = h\nu$.

may cause a significant deviation from the free electron value due to spin-orbit coupling (LS coupling).

$$\mathcal{H}_{SO} = \lambda \mathbf{\hat{L}^T} \cdot \mathbf{\hat{S}} \tag{3.3}$$

Electronic ground states may also acquire orbital magnetic momentum due to spin-orbit coupling from higher states with $L \neq 0$ into the ground state wavefunction and display g-values different from g_e.

Due to the anisotropic surrounding, the local field also becomes orientation-dependent. This dependency can be taken into account in the spin-Hamiltonian by replacing the scalar g-factor by a matrix $\mathbf{g}$.

$$\mathcal{H}_{\mathrm{eZ}} = \beta \mathbf{B_0} \mathbf{g} \hat{S} \tag{3.4}$$

This matrix **g** is usually referred to as 'g-tensor'. [1] The g-tensor can be diagonalized to yield its principal values g_{xx}, g_{yy}, and g_{zz} in its principal axes system (x,y,z). The "g-tensor principal axes system" is related to the orbital axes system and thus to the molecular bonding situation of the complex.

The nuclear Zeeman-term describes the energy of a paramagnetic nucleus ($I \neq 0$) in the presence of a magnetic field in analogy to the electron-Zeeman term

$$\mathcal{H}_{\mathrm{nZ}} = \beta_{\mathrm{N}} \mathbf{B_0} g_{\mathrm{N}} \hat{I} \tag{3.5}$$

It is of the order of $g\beta/g_{\mathrm{N}}\beta_{\mathrm{N}} \approx 1000$ smaller than the electron-Zeeman term but often as large as the hyperfine interaction.

---

[1] Note that mathematically only the $\mathbf{G^2}$ matrix is a tensor.

The hyperfine term arises from the interaction of the electron spin $\hat{S}$ with the nuclear spin $\hat{I}$. I can be a ligand nucleus (i.e. ^{1}H, ^{14}N) or the metal nucleus itself.

$$\mathcal{H}_{\mathrm{hf}} = \hat{S}\mathbf{A}\hat{I} \tag{3.6}$$

The hyperfine tensor $\mathbf{A}$ describes the magnitude and orientation of the coupling in the molecule or complex.

The nuclear-quadrupole term originates from an additional interaction of the electric field gradient at the position of the nucleus with its nuclear spin ($I \geq 1$) exhibiting an electric quadrupole moment.

$$\mathcal{H}_{\mathrm{Q}} = \hat{I}\mathbf{P}\hat{I} \qquad . \tag{3.7}$$

The total spin Hamiltonian is of the form

$$\mathcal{H} = \mathcal{H}_{\mathrm{eZ}} + \mathcal{H}_{\mathrm{hf}} + \mathcal{H}_{\mathrm{nZ}} + \mathcal{H}_{\mathrm{Q}} = \beta\mathbf{B_0}\mathbf{g}\hat{S} + \hat{S}\mathbf{A}\hat{I} + \beta_{\mathrm{N}}\mathbf{B_0}g_{\mathrm{N}}\hat{I} + \hat{I}\mathbf{P}\hat{I} \qquad . \tag{3.8}$$

3.3 The g-Tensor

Depending on the orbital angular momentum of the electronic ground state and the nature of the coordinating ligands, transition metal complexes may exhibit EPR spectra with g-values different from g_e. For transition metal complexes, the g-tensor is mostly rhombic, e.g. $g_x \neq g_y \neq g_z$. That means that the interaction of the magnetic field is anisotropic and different along the x-, y-, and z-directions of the molecule. This is the most general case. Special cases e.g. axial ($g_x = g_y \neq g_z$) or isotropic ($g_x = g_y = g_z$) g-tensors arise from accidentally or orbital-symmetrically degenerate spin density distributions and spin-orbit couplings. The theory of EPR spectroscopy of transition metal ions is described in various text books [79–81]. The EPR-spectra of [NiFe] hydrogenases usually display such a rhombic EPR spectrum (see Figure **3.2**). The g-anisotropy, nevertheless, is still modest with a $\Delta(g_x - g_z) < 0.4$ compared to e.g. low-spin ferric (Fe(III)) haem with $\Delta(g_x - g_z) \approx 3$. For Ni, there is no simple model which can predict the g-values of a Ni complex. The variations in nature and number of coordinating ligands, ligand strengths and coordination geometries make it impossible to suggest an instructive way to predict g-values.

3.4 The Hyperfine Tensor

When the hyperfine interaction $\mathbf{A}$ is larger than the EPR linewidth, a splitting of the EPR lines by this hyperfine interaction can be observed. In [NiFe]-hydrogenases, the EPR linewidth is so large (usually of

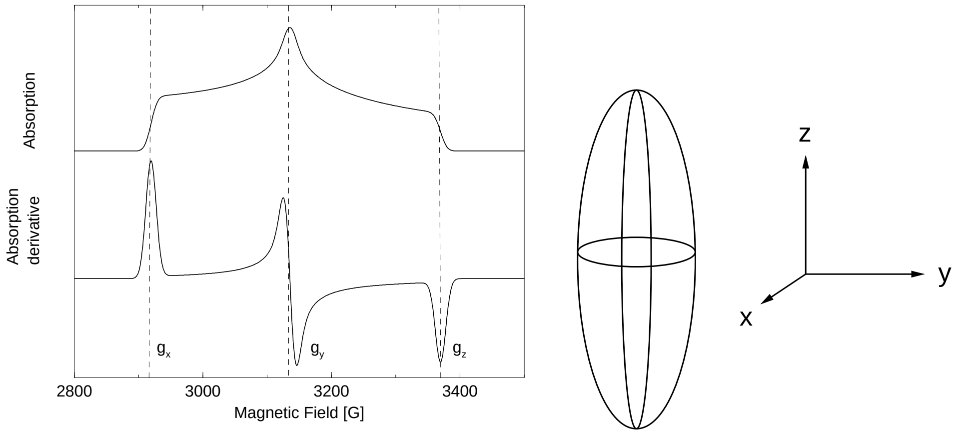

Figure 3.2: Rhombic EPR spectrum: Left: Simulated EPR spectrum with parameters typical for the Ni-B EPR signal of [NiFe] hydrogenase: g_x = 2.32, g_y = 2.16 , g_z = 2.01; linewidth 19 G, microwave frequency 9.480 GHz, centre field 3150 G, sweep width 700 G. Top: absorption spectrum, bottom: derivative spectrum. Right: Geometrical shape associated with a rhombic g-tensor.

the order of 10-20 G) that only very large hyperfine interactions can be detected, in favourable cases. The electron-nuclear double resonance (ENDOR) spectroscopy allows the measurement of small hyperfine interaction by means of a high-resolution double resonance experiment [82]. In ENDOR spectroscopy, the influence of a second swept radiation frequency, in the radio-frequency (RF) range, on the microwave absorption of an EPR transition is observed. When the RF field matches one of the NMR transitions with ΔM_S = 0, ΔM_I = 1 in Figure **3.3** (corresponding to two transitions between hyperfine levels), the effective relaxation rates of the systems are changed and so is the EPR absorption. This change of EPR absorption is detected while sweeping the RF field. The higher resolution of ENDOR is obtained at the expense of experimental sensitivity (the ENDOR effect is only of the order of a few percent). However, ENDOR is much more sensitive than the respective NMR experiment. Further details of ENDOR spectroscopy are given in [81, 83–85].

The two NMR transitions correspond to two ENDOR transition frequencies ν_+ and ν_- which are detected in an ENDOR experiment. They are obtained as two lines

$$\nu_\pm = \left| \nu_\mathrm{N} \pm \frac{A}{2} \right| \tag{3.9}$$

around the nuclear Larmor frequency ν_N. The splitting of the two ENDOR frequencies corresponds to the hyperfine coupling.

The hyperfine tensor $\mathbf{A}$ is the sum of an isotropic, scalar part (a_{iso}) and an anisotropic part ($\mathbf{A}_{aniso}$)

$$\mathbf{A}_{tot} = a_{iso}\mathbb{1} + \mathbf{A}_{aniso} \tag{3.10}$$

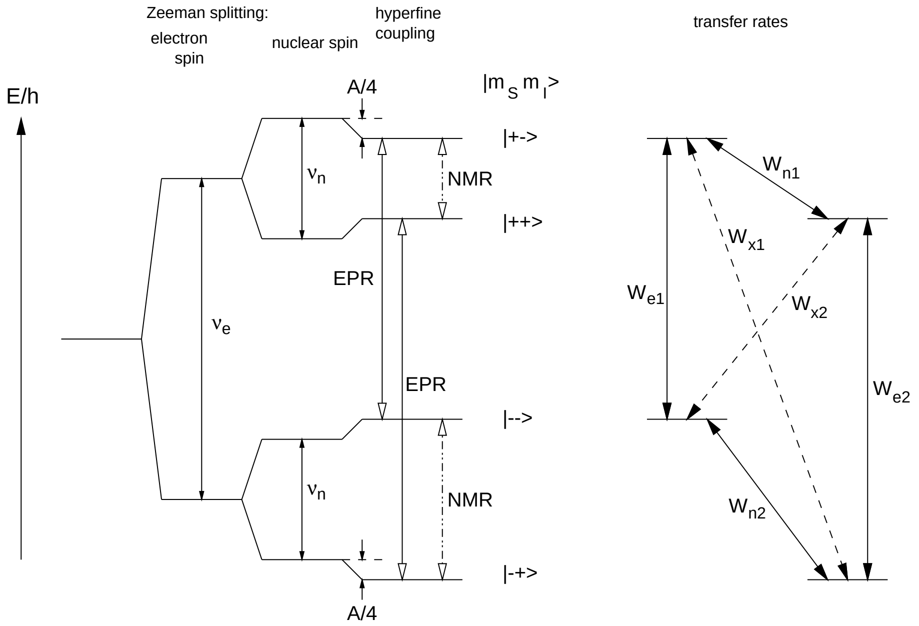

Figure 3.3: Four level diagram of a S=1/2 and I= 1/2 system. Schematic drawing of the energy levels of a S = 1/2 and I = 1/2 system in an external magnetic field due to electron Zeeman, nuclear Zeeman and hyperfine interaction. The allowed EPR and NMR transitions are marked with arrows (left). On the right hand side the transfer rates are given

.

where $\mathbb{1}$ is the unity matrix. The isotropic coupling (Fermi contact term) arises from the probability of finding the unpaired electron (or a fraction of the unpaired spin density) at the position of the nucleus.

$$a_{iso} = \frac{2}{3} g_e \beta_e g_N \beta_N |\Psi(0)|^2 \tag{3.11}$$

Only s-orbitals have a non-vanishing probability density at the nucleus; p-, d-, or f-orbitals all have nodes at the nucleus. The detection of an isotropic hyperfine interaction in d-metal complexes can either originate from a direct occupation of s-orbitals, from a polarization of s-orbitals by higher angular momentum orbitals (i.e. p- or d-orbitals) or from an admixture of excited states into the ground state wavefunction by spin-orbit coupling.

The anisotropic, or dipolar, contribution $\mathbf{A}_{aniso}$ is caused by the interaction of the magnetic dipoles of nucleus and unpaired electron. Its energy is given by the classical equation for the interaction of two dipoles.

$$\mathcal{H}_{\text{dip}} = \frac{\beta g \beta_{\text{N}} g_{\text{N}}}{h} \left(\frac{3(\hat{S} \cdot \mathbf{r})(\hat{I} \cdot \mathbf{r})}{r^5} - \frac{\hat{S} \cdot \hat{I}}{r^3} \right) \tag{3.12}$$

where $\mathbf{r}$ is the vector connecting the two dipoles and r its modulus. In matrix form

$$\mathcal{H}_{\text{dip}} = \hat{S} \cdot \mathbf{A}_{\text{dip}} \cdot \hat{I} \tag{3.13}$$

with

$$(\mathbf{A}_{\text{dip}})_{ij} = \frac{\beta g \beta_{\text{N}} g_{\text{N}}}{h} \left\langle \frac{3 r_i r_j - \delta_{ij} r^2}{r^5} \right\rangle \qquad , \tag{3.14}$$

with the angular brackets indicating the integration over the electron wavefunction in order to remove the explicit spatial dependence of the angle between the magnetic field and the $\mathbf{r}$-vector.

The analysis of isotropic hyperfine couplings for organic π-radicals is done by the McConnell equations and more sophisticated treatments of the same form [86]. It relates the measured isotropic ^{1}H hyperfine coupling to the p$_z$ spin density at the nucleus of the neighbouring sp^2 hybridized carbon atom by an empirical relation. For transition metal ions or complexes, a quantitative interpretation is not possible in the same way because more electrons are involved with a tendency to more variations in their bonding situations and no simple hybridization scheme is applicable. If a detailed and reliable interpretation of the electronic structure of transition metals is required, one should attempt a thorough analysis of the *total* hyperfine and g-tensors and their relative orientations.

Furthermore, there is an additional, second-order contribution to the hyperfine interaction in transition metal complexes [79, 87]. So far, the magnetic hyperfine interaction was assumed to originate from the interaction of nuclear magnetic moment and electron spin angular momentum. In systems, where the g-values differ appreciably from g_e there is a resulting orbital angular momentum which can interact with the one from the electron spin (‘spin-orbit coupling’) and contribute to the hyperfine tensor [79, 87]. This plays a role for central metal hyperfine coupling but also for ligand hyperfine interactions in transition metal complexes. It is described by

$$\mathbf{A}_{\mathbf{SO}} = \sum_j \sum_{\nu,\nu'} \frac{g_\nu g_e^{'}}{8} \frac{Z_{\nu'} k_0^2(r_{j,\nu})}{r_{j,\nu}^3 r_{j,\nu'}^3} \times [(\mathbf{r}_{j,\nu} \cdot \mathbf{r}_{j,\nu'})(\mathbf{S}_j \cdot \mathbf{I}_\nu) - (\mathbf{S}_j \cdot \mathbf{r}_{j,\nu'})(\mathbf{I}_\nu \cdot \mathbf{r}_{j,\nu})] \tag{3.15}$$

where j runs over the number of electrons, $\nu, \nu^{'}$ run over all nuclei.

The use of EPR and ENDOR techniques to study metalloproteins is extensively reviewed in [88].

3.5 DFT

Density Functional Theory (DFT) as a tool of electronic structure calculations has received recognition by the award of the 1998 Nobel Prize in Chemistry

> “to Walter Kohn for his development of the density-functional theory and to John Pople for his development of computational methods in quantum chemistry.”

The underlying principles of DFT are given in a series of monographs [89, 90]. Electronic structure calculations try to numerically solve the time-independent, electronic Schrödinger equation in the Born-Oppenheimer approximation

$$\mathcal{H}_{elec}\Psi_{elec} = E_{elec}\Psi_{elec} \tag{3.16}$$

with the electronic Hamiltonian

$$\begin{aligned} \mathcal{H}_{elec} &= -\frac{1}{2}\sum_{i=1}^{N}\nabla_i^2 - \sum_{i=1}^{N}\sum_{A=1}^{M}\frac{Z_A}{r_{iA}} + \sum_{i=1}^{N}\sum_{j>i}^{N}\frac{1}{r_{ij}} \\ &= \hat{T}_e + \hat{V}_{Ne} + \hat{V}_{ee} \end{aligned} \tag{3.17}$$

The nuclear-nuclear repulsion enters only parametrically

$$E_{nuc} = \sum_{A=1}^{M}\sum_{B>A}^{M}\frac{Z_A Z_B}{r_{AB}} \tag{3.18}$$

and the total energy of the system then is

$$E_{tot} = E_{elec} + E_{nuc} \qquad . \tag{3.19}$$

In DFT, unlike in Hartree-Fock theory, the electron density is the central quantity. The one-particle electron density is the probability of finding any of N electrons in a finite volume element

$$\rho(\vec{r}_1) = N\int\cdots\int|\Psi(\vec{x}_1,\vec{x}_2,\ldots\vec{x}_N)|^2 ds_1 d\vec{x}_2\ldots d\vec{x}_N \qquad . \tag{3.20}$$

Two conditions must be fulfilled by the electron density: It must vanish at infinity ($r \to \infty$) and integrate to the total number N of electrons in the system

$$\begin{aligned} \rho(r\to\infty) &= 0 \qquad , \\ \int\rho(\vec{r}_1)d\vec{r}_1 &= N \qquad . \end{aligned} \tag{3.21}$$

Two electrons do not move independently from each other. Rather, the probability of finding two electrons with spins σ_1 and σ_2 simultaneously within two volume elements $d\vec{r}_1$ and $d\vec{r}_2$ is diminished by the *exchange-correlation hole* $h_{XC}(\vec{x}_1;\vec{x}_2)$. The exchange-correlation hole has two contributions: the *Fermi hole* and the *Coulomb hole*. The first originates from the hole due to the Pauli principle and applies to two electrons with the same spin only. The latter results from the classic $1/\mathrm{r}_{12}$ electrostatic repulsion of two particles with the same charge.

The approach taken by DFT is not new. The first attempt to use the electron density rather than the wavefunction comes from the work by Thomas and Fermi in 1927. Further improvement was made by

Slater in 1951 (the so-called 'X_α' approximation). The theoretical justification of the use of DFT were later given by Hohenberg and Kohn in 1964.

The first Hohenberg-Kohn theorem proves that the complete ground state energy (and all other properties thereof) is a functional of the ground state electron density

$$\rho_0 \Rightarrow \{N, Z_A, R_A\} \Rightarrow \mathcal{H} \Rightarrow \Psi_0 \Rightarrow E_0 \tag{3.22}$$

albeit the functional itself is unknown. In the second Hohenberg-Kohn theorem they have shown that the variational principle applies to the Hohenberg-Kohn functional

$$E_0 \leq E[\tilde{\rho}] \tag{3.23}$$

and the best solution to the exact value (if the functional was known) is obtained by minimizing the energy of the trial density $\tilde{\rho}$.

Kohn and Sham in 1965 facilitated the practical use of DFT. They chose the kinetic energy of a non-interacting (T_{ni}) system as reference and all deviations thereof were put into the non-classical contributions to electron-electron repulsion (the *exchange-correlation energy* E_{XC})

$$F[\rho(\vec{r})] = T_{ni}[\rho(\vec{r})] + J[\rho(\vec{r})] + E_{XC}[\rho(\vec{r})] \tag{3.24}$$

with

$$E_{XC}[\rho(\vec{r})] \equiv (T[\rho] - T_{ni}[\rho]) + (E_{ee}[\rho] - J[\rho]) = T_i[\rho] + E_{ncl}[\rho] \tag{3.25}$$

T_i is the part of the true kinetic energy that is not covered by the non-interacting reference system T_{ni}. Finally, the energy of the true, interacting system is written as

$$\begin{aligned} E[\rho(\vec{r})] &= T_{ni}[\rho(\vec{r})] + J[\rho(\vec{r})] + E_{XC}[\rho(\vec{r})] + E_{Ne}[\rho] \\ &= -\frac{1}{2}\sum_i^N \langle\varphi_i|\nabla^2|\varphi_i\rangle + \frac{1}{2}\sum_i^N\sum_j^N \int\int |\varphi_i(\vec{r}_i)|^2 d\vec{r}_1 d\vec{r}_2 \\ &+ E_{XC}[\rho(\vec{r})] - \sum_i^N \int \sum_A^M |\varphi_i(\vec{r}_i)|^2 d\vec{r}_1 \qquad . \end{aligned} \tag{3.26}$$

The effective potential in which an electron moves is

$$V_{eff}(\vec{r}) = \int \frac{\rho(\vec{r}_2)}{r_{12}} d\vec{r}_2 + V_{XC}(\vec{r}_1) - V_{N1} \tag{3.27}$$

in which only V_{XC} is not known. The obtained Kohn-Sham orbitals are those of a non-interacting system with the same electron density as the interacting one.

There are a number of possibilities for approximating the exact an exchange-correlation functional. The simplest is the *local density approximation* (LDA)

$$E_{XC}^{LDA}[\rho] = \sum \rho(\vec{r})\epsilon_{XC}(\rho(\vec{r})d\vec{r} \tag{3.28}$$

which contains the exchange functional per particle from Slater

$$\epsilon_X = -\frac{3}{4}\sqrt{\frac{3\rho(\vec{r})}{\pi}} \tag{3.29}$$

and the correlation functional ϵ_C derived from numerical quantum Monte Carlo simulations of the homogeneous electron gas by Ceperly and Alder 1980. Surprisingly, already the LDA gives structural parameters comparable to or sometimes better than Hartree-Fock. The performance of LDA for energetics, however, is poor. DFT has received interest in the 1980's when improved functionals appeared and made a step from the solid-state physicists' community to those interested in calculations of chemical accuracy. These functionals make use of the *generalized gradient approximation* (GGA). The functionals do not only depend on the electron density $\rho(\vec{r})$ but also on the gradient of the density $\nabla\rho(\vec{r})$ in order to consider a non-homogeneous density distribution.

$$E_{XC}^{GGA}[\rho_\alpha, \rho_\beta] = \sum f(\rho_\alpha, \rho_\beta, \nabla\rho_\alpha, \nabla\rho_\beta)d\vec{r} \qquad . \tag{3.30}$$

There is an increasing number of separate exchange and correlation functionals. To mention only a few of the most popular ones Becke's exchange functional B88 [91], Lee-Yang-Parr's correlation functional (LYP) [92], Perdew's 1986 correlation functional [93]. More details can be found in the original references. Further work to improve current functionals is to also include the Laplacian of the electron density $\nabla^2\rho(\vec{r})$, use high-level electron densities for fitting new functionals (HCTH [94]) or use a hybrid density functional (see below).

In Hartree-Fock, the exchange energy of a Slater determinant can be computed exactly. The idea is to use this exchange energy in DFT calculations

$$E_{XC} = E_X^{exact} + E_C^{KS} \qquad . \tag{3.31}$$

This does not work well, because E_X^{exact} is not a good match with E_C^{KS}. Therefore a weighted mixture of E_X^{exact} and E_C^{KS} is required (adiabatic connection). The most successful approach along that line is Becke's empirical three parameter combination of Hartree-Fock exchange and PW91 correlation functional [95] which was later replaced [96] by the LYP correlation functional to yield the hybrid density functional B3LYP

$$E_{XC}^{B3LYP} = (1-a)E_X^{LSD} + aE_{XC}^{\lambda=0} + bE_X^{B88} + cE_X^{LYP} + (1-c)E_C^{LSD} \qquad . \tag{3.32}$$

Here, $\lambda = 0$ refers to the exact Hartree-Fock exchange. There are, recently, attempts to reduce the numbers of empirical parameters.

The success of DFT in the last 10-15 years originates from two facts. One, the implicit consideration of electron correlation in the exchange-correlation functionals. Two, the moderate computational costs for DFT. Hartree-Fock formally scales with the size of the treated system N of the order of the fourth power ($O(N^4)$) and DFT $O(N^3)$. When electron correlation is considered in post-Hartree-Fock approaches the computation time increases to $O(N^5)$ for second-order Møller-Plesset perturbation theory, and $O(N^7)$ for quadratic configuration interaction (QCI) with single and double excitations and perturbatively added triples (CISD(T)) and coupled-cluster (CCSD(T)). This formal scaling behaviour reduces quickly for larger systems. The last two methods are the most accurate ones but their demands make them hardly feasible for systems larger a few atoms.

One must bear in mind, however, that the results from DFT calculations have to be evaluated critically. There is no systematic route of improvement as opposed to wavefunction based methods. The accuracy of B3LYP is about 2-3 kcal/mol for atomization energies of the G2 training set of data, the *pure* GGA functionals like BLYP, BP86 are in error by about 5 kcal/mol. But, B3LYP gives up on the favourable scaling compared to HF calculations because HF exchange is explicitly included and two electron four-centre integrals must be evaluated.

3.6 DFT and Transition Metals

The field of transition metal complexes is a matter of the success story of DFT (for a review, see for example [97–99]). This fact originates from the difficulties associated with the nature of these complexes. A large number of energetically close lying states, often open-shell species and a large variability of bonding situations. The bonding situation is an interplay of donor and acceptor contributions from both the central metal and its ligands. The necessity of using electron correlation becomes obvious [100]. For a comparison of DFT and conventional quantum chemical methods see a review by Siegbahn [101] and references therein. For transition-metal complexes the BP86 functional proved to be most accurate of the pure functionals [102] and the B3LYP hybrid functional gives results of the same accuracy. Bond distances are often reproduced within 0.02Å and bond angles within 0.4° (for a collection of critical comparisons see [90]).

The feasibility of DFT to treat large bioinorganic system has recently been reviewed by Siegbahn and Blomberg [103].

3.7 Relativistic Quantum Chemistry

Relativistic effects manifest themselves in heavy atoms. The magnitude of the kinetic energy of the core electrons leads to a contraction and stabilization of atomic s- and p-orbitals. Increased shielding of the nuclear charge on the other hand causes an expansion and destabilization of d- and f-type orbitals. Relativistic bond length contraction, on the other hand, is mainly due to a reduction of the electronic kinetic energy (for a review see [104]).

Traditional relativistic quantum chemistry makes use of the four-component Dirac-Fock wavefunction. In its full implementation, very high system requirements with respect to memory, disk space and computing time have to be met [105, 106]. In relativistic density functional theory (RDFT) (see for example [107]) a "fully-relativistic" four-component Dirac-Kohn-Sham model is the reference. More approximate, two-component schemes project out the positronic states and give the "fully-relativistic" electronic states at a lower computational effort. The decomposition can go even further and introduce spin-free ("scalar relativistic") and spin-dependent ("spin-orbit") contributions. One-component methods treat mass-velocity and Darwin corrections but neglect spin-orbit coupling completely. One of the oldest approximate treatments of this kind is the quasi-relativistic (QR) scheme by Ziegler *et al.* which uses the Pauli operator self-consistently [108]. There is theoretical scepticism because the Pauli operator is not bounded from below and one may end up with non-physical low energies due to the variational treatment. The Douglas-Kroll-Hess (DK) approach transforms into a one- or two-component form [109]. Relativistic effective core potentials (RECP) (for a review see e.g. [110,111]) are an efficient way to treat scalar-relativistic effects. They represent an analytic fit of the core-close electron distribution to results from atomic four-component calculations.

3.7.1 The ZORA-Hamiltonian

The approach taken in this thesis to consider relativistic effects is the "zeroth-order regular approximation" (ZORA) which is a perturbational expansion of the Dirac equation [112, 113]. It was already presented by Chang, Pélissier and Durand as the CPD equation [114]. It follows the propositions by Harriman which he called 'modified partitioning of the Dirac equation' [87]. In the two-component ZORA calculations, spin-orbit coupling is treated self-consistently such that $\mathrm{p}_{1/2}$ and $\mathrm{p}_{3/2}$ have different radial extensions from the beginning. Here, stationary states are classified by the total momentum $J = L + S$. The two-component spinors transform in a special way under symmetry operations which require the introduction of double group symmetry in close relation and analogy to point group symmetry.

The total energy of a particle is

$$W = \sqrt{m_0^2 c^4 + p^2 c^2} + V \qquad . \tag{3.33}$$

In chemical applications, $|E| < (2m_0c^2 - V)$ which leads to

$$E = \sqrt{m_0^2 c^4 + p^2 c^2} - m_0 c^2 + V \tag{3.34}$$

The non-relativistic result

$$E_{NR} = V + \frac{p^2}{2m_0} \tag{3.35}$$

and the first-order Pauli energies are obtained

$$\begin{aligned} E_{Pauli} &= E_{NR} - (\frac{E_{NR} - V}{2m_0c^2})\frac{p^2}{2m_0} \\ &= V + \frac{p^2}{2m_0} - \frac{p^4}{8m_0^3 c^2} \end{aligned} \tag{3.36}$$

which correspond to an expansion in $(E - V)/(2m_0c^2)$. The Pauli-type Hamiltonian has problems when $r \to 0$ then $E - V > 2m_0^2$. The Hamiltonian of the ‘zero-order regular approximation´ (ZORA) for relativistic effects corresponds to an expansion in $(E - V)/(m_0c^2 - V)$ which gives

$$E^{ZORA} = \frac{p^2c^2}{2m_0c^2 - V} + V \qquad . \tag{3.37}$$

The scaled ZORA energy even contains certain higher order terms

$$E^{scaled} = \frac{E^{ZORA}}{1 + \frac{p^2c^2}{(2m_0c^2 - V)^2}} \tag{3.38}$$

The transformation from the four-component Dirac-Hamiltonian to a two-component form is defective for most traditional approaches. A more systematic approach is the Foldy-Wouthuysen transformation which eliminates the small component. The ZORA Hamiltonian incorporates relativistic effects that traditionally are only introduced at the level of the Pauli Hamiltonian. The great advantage of the ZORA Hamiltonian H^{ZORA} is that it can be used variationally and that it does not suffer from the singularities for $r \to 0$ like the Pauli Hamiltonian. One other approach, which is also regular for Coulomb potentials, is the Douglas-Kroll-Hess Hamiltonian which will not be discussed further here. In situations in quantum chemistry where spin-orbit coupling is not important, a pure ‘scalar-relativistic´ Hamiltonian may be advantageous

$$\begin{aligned} H_{SR}^{ZORA}\Phi_{SR}^{ZORA} &= (V + \vec{p}\frac{c^2}{2c^2 - V}\vec{p})\Phi_{SR}^{ZORA} \\ &= E_{SR}^{ZORA}\Phi_{SR}^{ZORA} \qquad . \end{aligned} \tag{3.39}$$

The full ZORA Hamiltonian leads to the eigenvalue equation

$$\begin{aligned} H^{ZORA}\Phi^{ZORA} &= (V + \vec{p}\frac{c^2}{2c^2 - V}\vec{p} + \frac{c^2}{(2c^2 - V)^2}\vec{\sigma}) \cdot (\vec{\nabla} \times \vec{p}) \\ &= E^{ZORA}\Phi^{ZORA} \end{aligned} \tag{3.40}$$

which is bounded from below.

3.8 Calculations of Magnetic Resonance Parameters

3.8.1 Hyperfine Tensors

Semi-empirical calculations like UHF-INDO [115] were used to calculate the isotropic hyperfine interaction of very large systems. The s-orbital occupancies from a spin-unrestricted wavefunction were converted into isotropic hyperfine coupling constants (hfcc) by means of empirical conversion factors. These empirical correlations were necessary because semi-empirical methods only consider the valence electrons and the isotropic hfcc is a property of electrons near the nucleus.

Hartree-Fock calculations at the UHF level suffer from the drawback of major spin contamination and the complete neglect of electron correlation and make it an unsuitable method for calculating hfccs. The RHF-INDO/SP approach tried to circumvent this deficiency by a perturbatively added spin-polarized calculation on top of a self-consistent spin-restricted INDO calculation [116].

Post-Hartree Fock (the explicite consideration of electron configuration by e.g. configuration interaction CI) approaches for the calculation of the hfccs of small molecules lead to very accurate results at the price of massively increasing computational requirements (see for example [117–119]).

The use of DFT methods in the calculation of hfccs was established in 1993 independently by two research groups [120, 121]. The results are non-relativistic and of first-order only, neglecting relativistic effects and spin-orbit coupling contributions to the isotropic and anisotropic hyperfine interactions. Accurate results were obtained for light elements but they still fall behind more expensive post-HF calculations. Since then an increasing number of publications using this approach appeared (for a review see [122–124]). For a comparison of CI and DFT calculated hfccs see [125]. Munzarova and Kaupp [126] and Hayes [127] used this first-order approach to calculate hfccs of transition metal complexes. Munzarova and Kaupp made a fortuitous choice of complexes for which spin-orbit coupling effects are expected to be small and obtained reasonable results. Hayes came, however, to a very pessimistic conclusion about the use of DFT to calculate the hyperfine interaction of transition metal complexes [127]. This was due to the complete neglect of higher-order effects.

A perturbative treatment of spin-orbit coupling on top of a non-relativistic calculation was introduced by Belanzoni *et al.* [128, 129] and later also used by Swann and Westmoreland [130]. The spin-orbit coupling parameters are either taken from experimental values or from relativistic atomic calculations. RECPs cannot be used in the context of hyperfine coupling constants. The isotropic hyperfine interaction is a property of electrons near the nucleus which are not explicitly considered in RECP calculations.

3.8.2 ZORA Calculations of Hyperfine Tensors

In this work, the ZORA Hamiltonian is used to evaluate hyperfine coupling constants for both light and heavy nuclei [131].

The Hamiltonian of Eq 3.40 can be used to calculate the interaction between an effective electronic spin and a magnetic nucleus. Spin-orbit coupling is already included variationally in the ZORA Hamiltonian which means that only a first order perturbation theory (FOPT) is necessary to evaluate the influence of spin-orbit coupling on the hyperfine tensors $\mathbf{A}$. If one includes spin-orbit coupling, the spin used in the effective spin Hamiltonian is in fact a fictitious spin. The hyperfine Hamiltonian can be formulated as

$$\begin{aligned} H^{hyperfine} &= \frac{g_e}{4c}[K\sigma\cdot\mathbf{B}^{\nu} + K\mathbf{A}^{\nu}\cdot\mathbf{p} + \mathbf{p}\cdot\mathbf{A}^{\nu}K \\ &+ \sigma\cdot(\nabla K\times\mathbf{A}^{\nu})] \end{aligned} \tag{3.41}$$

where $\mathbf{A}^{\nu}$ is the vector field of the magnetic dipole of the nucleus ν and the corresponding magnetic field $\mathbf{B}^{\nu} = \nabla\times\mathbf{A}^{\nu}$. $K = [1 + (E - V)/2c^2]^{-1}$. The first term is the electron spin hyperfine interaction and the last term is the spin-orbit hyperfine correction while the remaining terms (second and third) are the orbital hyperfine interaction. For reasons of simplicity, they can be rewritten as

electron spin hyperfine interaction

$$\frac{g_e g_\nu}{8Mc^2}\sigma\cdot(K(3\frac{\mathbf{r}_\nu(\mathbf{I}^\nu\cdot\mathbf{r}_\nu)}{r_\nu^5} - \frac{\mathbf{I}^\nu}{r_\nu^3} + \frac{8\pi}{3}\delta(\mathbf{r}_\nu)\mathbf{I}^\nu) \quad , \tag{3.42}$$

spin-orbit hyperfine correction

$$\frac{g_e g_\nu}{8Mc^2}\sigma\cdot(\nabla K\times(\frac{\mathbf{I}^\nu\times\mathbf{r}_\nu}{r_\nu^3})) \quad , \tag{3.43}$$

and orbital hyperfine interaction with $\mathbf{L}^\nu = \mathbf{r}_\nu\times\mathbf{p}$

$$\frac{g_e g_\nu}{8Mc^2 r_\nu^3}[K\mathbf{I}^\nu\cdot\mathbf{L}^\nu + \mathbf{I}^\nu\cdot\mathbf{L}^\nu K] \tag{3.44}$$

For spin-orbit coupling, the spin-restricted formalism is used since spin-polarization effects in spin-orbit coupled equations are difficult to calculate (see for example [132]). For the isotropic hyperfine interactions for which spin-polarization is dominant, one has to resort to spin-polarized scalar relativistic results.

3.8.3 g-Tensors

The electronic g-tensor can be obtained from any wavefunction by an *a posteriori* perturbation approach. Spin-orbit coupling is treated as a perturbation to the non-relativistic wavefunction.

Semi-empirical calculations are feasible for organic radicals because the g-tensor is a property of the valence electrons and core electrons are omitted from these calculations. Spin-orbit coupling is introduced via experimental spin-orbit coupling constants (for a recent application see for example [133]). The use of Hartree-Fock wavefunctions to evaluate the g-tensors of organic radicals is also possible [134, 135]. Generalized Hartree-Fock theory was also used and gave reasonable results [136].

The benchmarks for small molecules come from MRCI [137, 138], CI [139] and MCSCF calculations [140, 141]. These calculations yield very accurate results for smallest deviations from g_e. Their applicability, however, is limited to systems with only a few atoms.

DFT methods, certainly, cannot compete with those sophisticated approaches. Belanzoni *et al.* [128] treated spin-orbit coupling as a perturbation to a non-relativistic Kohn-Sham wavefunction. Later this approach was also used by Swann and Westmoreland [130]. Schreckenbach and Ziegler used a quasi-relativistic (QR) approach and calculated the g-tensor from a relativistic Pauli DFT wavefunction by means of perturbation theory [142–144]. For a review of DFT calculations of g-tensors see [145].

In this thesis, the g-tensor is calculated from a ZORA wavefunction in which spin-orbit coupling is treated variationally [146] and gauge-including atomic orbitals (GIAOs) are used. Until recently, there was no publication on g-tensor calculations from a Kohn-Sham wavefunction using RECPs although such a treatment of relativistic effects, in principle, would be possible. This method was only very recently presented by Malkina *et al.* in the treatment of systems containing heavy atoms [147].

3.8.4 ZORA Calculations of g-Tensors

The ZORA-Hamiltonian in the presence of a time-independent magnetic field $\vec{B}$ and with substitution

$$\vec{p} \to \vec{\Pi} = \vec{p} - \vec{A} \tag{3.45}$$

one arrives at

$$\begin{aligned} H^{ZORA} &= V + \vec{\sigma} \cdot \vec{\Pi} \frac{c^2}{2c^2 - V} \vec{\sigma} \cdot \vec{\Pi} \\ &= V + \vec{\Pi} \frac{c^2}{2c^2 - V} \vec{\Pi} - \frac{c^2}{2c^2 - V} \vec{\sigma} \cdot \vec{B} + \frac{c^2}{(2c^2 - V)^2} \vec{\sigma} \cdot (\vec{\nabla} \times \vec{\Pi}) \end{aligned} \tag{3.46}$$

where $\vec{A}$ is the vector potential (Maxwell equation) such that $\vec{B} = \vec{\nabla} \times \vec{A}$. The terms that arise from this Hamiltonian are similar to that in the Pauli approximation, namely the spin-Zeeman kinetic energy correction (relativistic mass correction to the spin-Zeeman term)

$$-\frac{1}{4c^3}p^2\sigma \cdot \mathbf{B} \tag{3.47}$$

and the one-electron spin-orbit Zeeman gauge correction

$$\frac{1}{4c^3}\sigma \cdot (\nabla V \times \mathbf{A}) \tag{3.48}$$

The Zeeman Hamiltonian H^Z is then ($\mathbf{L} = \mathbf{r} \times \mathbf{p}$)

$$H^Z = \frac{g_e}{2c}[\frac{K}{2}\sigma \cdot \mathbf{B} + \frac{K}{4}\mathbf{B}^0 \cdot \mathbf{L} + \mathbf{B}^0 \cdot \mathbf{L}\frac{K}{4} + \sigma(\nabla\frac{K}{2} \times \mathbf{A}^0)] \tag{3.49}$$

where $K = 1$ corresponds to the non-relativistic case and $K = [1 - V/2c^2]^{-1}$ to the ZORA equation. From the last term in Eq. 3.49, complex matrix elements arise which must be evaluated. For the energy in first order in the magnetic field, matrix elements of the derivative of the Zeeman-Hamiltonian with respect to the external magnetic field have to be calculated (see Abragam and Bleaney [79])

$$\begin{aligned} \frac{\partial}{\partial B_k^0}H^Z &= \frac{g_e}{2c}[\frac{1}{2}\sigma_k + \frac{K}{4}L_k + L_k\frac{K}{4} + \nabla \cdot (\frac{K-1}{4}\mathbf{r})\sigma_k \\ &- \nabla_k(\frac{K-1}{4}\sigma \cdot \mathbf{r})], \qquad k = x, y, z. \end{aligned} \tag{3.50}$$

Gauge-invariance is ensured using ‘gauge-including atomic orbitals´ (GIAOs).

Chapter 4

Nickel Model Complexes

4.1 Introduction

Transition metals are required for many biochemical processes, as catalysis, electron transfer or gene regulation [10]. Consequently, the investigation of biologically essential transition metals is a field of intense research. In recent years, six nickel-containing enzymes were discovered (for a review, see ref. [9, 23–25, 65]). A prominent example are the [NiFe] hydrogenases [12, 34]. Hydrogenases are enzymes that catalyze the reversible oxidation of molecular hydrogen into protons and electrons. There is considerable interest in understanding the electronic structure of [NiFe] hydrogenases which is available from a combined approach of EPR techniques and theoretical (DFT) calculations. However, before DFT methods can be applied to calculate magnetic resonance parameters of [NiFe] hydrogenase, their accuracy must be evaluated on simple model complexes, which is the aim of this chapter.

The bio-mimetic chemistry of inorganic nickel compounds has been extensively reviewed by Halcrow and Christou [148].

The choice of the model compounds (Fig. **4.1**) containing Ni as the central metal atom was made on the following grounds:
In bis(maleonitriledithiolato)nickelate(III) ($\mathrm{Ni(mnt)}_2^-$) (**I**) the nickel atom possesses a similar coordination sphere as in [NiFe] hydrogenases. In the hydrogenases, Ni in the active centre is coordinated in a distorted tetrahedron sphere by four cysteine amino acid residues [28, 32]. In $\mathrm{Ni(mnt)}_2^-$, nickel is also bound to four sulphur atoms in a square planar coordination sphere. The Ni(III) oxidation state present in $\mathrm{Ni(mnt)}_2^-$ is also discussed for the oxidized forms Ni-A and Ni-B of the [NiFe] hydrogenase. In the neutral complex $\mathrm{Ni(CO)_3H}$ (**II**) the nickel is formally in its +1 oxidation state and a hydride ion is axially bound to the Ni. This bonding situation resembles the one discussed for the catalytic intermediate Ni-C

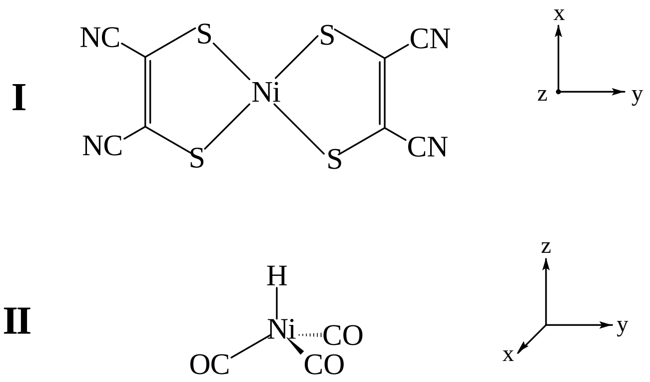

Figure 4.1: Schematic representation of the investigated Nickel complexes bis(maleonitriledithiolato)nickelate(III) Ni(mnt)$_2^-$ (**I**) and nickeltricarbonylhydride Ni(CO)$_3$H (**II**) with their local coordinate axes systems.

of the hydrogenase [12].

Ni(mnt)$_2^-$ has been very well characterized and the calculations performed on this complex may therefore serve as a benchmark for evaluating the methodology . The **g**-tensor orientation was obtained from single crystal measurements [149]. From ^{61}Ni enriched single crystals Maki and Edelstein obtained the Ni hyperfine tensor [149]. Furthermore, all ^{33}S hyperfine tensors were determined from angular dependent EPR spectra [150]. Recently, Ni(mnt)$_2^-$ regained interest as model cluster for [NiFe] hydrogenase and, in addition to the existing data, the ligand ^{13}C hyperfine tensor and ^{14}N hyperfine and quadrupole tensors and ^{15}N hyperfine tensor were determined by orientation selected pulsed-ENDOR and ESEEM spectroscopy [151].

X$_\alpha$ calculations [152] and recent BLYP calculations [151] only gave atomic spin populations. Very recently, a publication on the DFT calculation of hyperfine tensor of Ni(mnt)$_2^-$ appeared [127]. Discouraging results were obtained from various functionals. The calculated hyperfine tensors were of first-order only and no route of improvement was suggested. There are a number of quantum chemical investigations for the Ni complex with hydrogens replacing the CN groups. They range from Hückel [153] and Pariser-Parr-Pople [154] to Hartree-Fock [153, 155, 156], MP2 [157] and DFT calculations [158]. For Ni(CO)$_3$H there is only one DFT study to our knowledge that aimed to calculate the hyperfine interaction [126].

Very often, the analysis of experimental hyperfine splittings is limited to the discussion of atomic spin densities. The measured hyperfine couplings are related to theoretical values of singly occupied atomic orbitals [159] and the orbital occupation is obtained as the ratio of experimental to theoretical values. A more direct route to the comparison of experimental and calculated magnetic resonance parameters is given by the *first principles* calculations of the EPR parameters, e.g. as done in this paper from a density functional theory (DFT) wave function. Although the merit of DFT methods in the calculation of hyperfine parameters of organic radicals is unquestionable, its value for the description of paramagnetic resonance parameters of heavier elements, i.e. transition metal complexes, is still largely unexplored [127]. Belanzoni *et al.* demonstrated the importance of un-freezing core electrons in the calculation of **g**- and **A**-tensors [128, 129]. Swann and Westmoreland [130] investigated molybdenum(V) oxyhalide anions using a spin-polarized wave function without un-freezing the core. Schreckenbach and Ziegler [142, 145] used a Pauli-type relativistic Hamiltonian with the inclusion of spin-orbit coupling based on second order perturbation theory which was later also applied to study transition metal complexes [143]. Recently, Munzarova and Kaupp critically evaluated the use of various DFT functionals in the calculation of hyperfine parameters of a number of transition metal complexes [126]. They used a non-relativistic calculation of hyperfine parameters based on geometries that were optimized using a relativistic effective core potential (RECP). However, in this work no **g**-tensors were calculated.

With the zero-order regular approximation (ZORA) for relativistic effects [112, 113] one has a fast and powerful tool at hand to calculate the hyperfine tensor **A**, the quadrupole tensor **Q** and the **g**-tensor of systems containing heavy elements [131, 146]. Here the ZORA formalism is applied in order to validate its application for the calculation of magnetic resonance parameters for transition metal complexes, in particular [NiFe] hydrogenases. The ZORA formalism seems to overcome the shortcomings of the other approaches used so far. In addition, the influence of scalar-relativistic and variationally spin-orbit coupled DFT wave functions on the **g**- and **A**-tensors for light and heavy elements can be separately studied so that the influence of second order contributions to the hyperfine coupling can be rationalized. The computational efficiency of the ZORA method makes it an ideal tool for investigating the active centres of metalloenzymes.

4.2 Computational Details

The calculations reported here are based on the Amsterdam Density Functional program package [160] characterized by Slater-type orbital (STO) basis sets, the use of a density fitting procedure to obtain accurate Coulomb and exchange potentials in each SCF cycle and an accurate and efficient numerical integration of the effective one-electron Hamiltonian matrix elements [161]. All electrons were included in the calculations there were no frozen core electrons. The ZORA Hamiltonian [112, 113] was used for the inclusion of relativistic effects which will be referred to as scalar-relativistic (SR) effects and spin-orbit (SO) coupling. Both are treated variationally. Geometry optimizations were performed at the ZORA SR level for which gradients are available [162]. The **A**-tensors and **g**-tensor are obtained from the ZORA Hamiltonian in the presence of a homogeneous time-independent magnetic field which is then introduced via first-order perturbation theory [131, 146]. The **g**-tensor is obtained from a spin-non-polarized wave function since spin-polarization effects in spin-orbit coupled equations are difficult to calculate, see e.g. [132]. The effect of spin-polarization is assumed to be similar to that observed when going from a SR spin-restricted open shell Kohn-Sham (ROKS) calculation to a SR spin-unrestricted open shell Kohn-Sham (UKS) calculation. The **g**-tensor deviates from that of a free electron g_e due to spin-orbit coupling. It is convenient to give the principal values of the **g**-tensor (g_x, g_y, g_z) as the deviation from g_e multiplied by a factor 1000 (in ppt), e.g. $\Delta g_i = (g_i - g_e) \times 1000$, i = x, y, z.

The Becke exchange functional [91, 163] was used in conjunction with the Perdew correlation functional [93, 164] (BP86). The BP86 functional has been shown to yield best magnetic resonance parameters of the pure GGA functionals [129]. The basis sets used were relativistic ZORA basis sets from the ADF1999 distribution. Basis set II refers to a double-ζ basis set for light atoms and triple-ζ for first row transition metals. Basis set IV denotes a triple-ζ basis set with one added polarization function for light atoms (C, N, S), basis V has a further polarization function on atoms C, N, S. Basis set V+1s (for Ni and S only) possesses an added tight 1s function in order to improve the description of the wave function near the atomic core. The basis set ”Big” denotes a large basis set. This basis set is triple-ζ in the core and quadruple-ζ in the valence with at least three polarization or diffuse functions added.

Calculations for the **g**-tensor were also performed using a traditional second-order perturbation theory (SPT) approach. The spin-orbit coupling constants were calculated from fully relativistic numerical (basis-free) atomic calculations: ξ(Ni) = 855.4 cm^{-1} and ξ(S) = 460.4 cm^{-1}. For comparison Gaussian94 [165] calculations were also performed using the B3LYP hybrid functional with an admixed exact Hartree-Fock (HF) exchange [95, 96]. The hyperfine coupling constants in this case are non-relativistic and of first-order only following refs. [122–124].

4.3 Results and Discussion

4.3.1 Ni(mnt)$_2^-$

In the Bis(malenonitriledithiolato)-nickelate(III) complex (**I**, Figure **4.1**) the central nickel atom is coordinated in a square-planar arrangement by four sulphur atoms (point group D_{2h}). From the magnetic resonance studies on single crystals, the orientation of the principal axes of the hyperfine tensor **A** and the **g**-tensor were obtained in a molecule-fixed coordinate system. Maki *et al.* determined the orientation of the **g**- and ^{61}Ni **A**-tensors in magnetically diluted single crystals of the diamagnetic host (n-Bu$_4$N)$_2$[Ni(mnt)$_2$] [149]. They found that **g**- and ^{61}Ni **A**-tensors are collinear (within experimental error of 2-3°) and that the magnetic axes systems in the crystal are coincident with the symmetry axes of the complex in the crystal. A (3d$_{yz}$)^1 electronic configuration was inferred with the z-axis perpendicular to the molecular plane and the y-axis bisecting each ligand (see Figure **4.1** top). This assignment was later confirmed by EPR experiments of the ^{33}S enriched complex in single crystals [150]. The ^{33}S hyperfine tensor has axial symmetry within experimental error and the unique axis was found to lie along the molecular z-axis. The measured hyperfine tensor is consistent with the **g**-tensor analysis and a 3d$_{yz}$ unpaired electron with significant delocalization into sulphur ligand p$_z$ orbitals [150]. Experimental **g**- and hyperfine tensors are given in Tables **4.2** and **4.3**.

4.3.1.1 Geometrical Parameters

Table **4.1** compares calculated structural parameters with averaged experimental data from the X-ray structure analysis [166]. With a small basis set (Basis II) the deviation in bond lengths is 0.07 Å for Ni–S bonds and 0.08 Å for S–C bonds, while bond angles are satisfactorily described. Carbon-carbon single and double bonds as well as C≡N bonds are well described (deviation 0.01 to 0.05 Å). A systematic improvement in bond lengths is obtained when the basis set is enlarged from double-ζ to triple-ζ (basis set II to IV) and when a further set of polarization functions is added (basis set V). The average deviation at the ZORA SR BP86/V geometry is 0.02 Å in bond lengths and 0.9° in bond angles and therefore agrees with the X-ray structure analysis to within experimental uncertainty.

The effect of (scalar)-relativistic effects on the structural parameters of Ni(mnt)$_2^-$ is shown by comparing scalar-relativistic (SR) ZORA and non-relativistic (NR) geometries. Both calculations used the same functional and basis set. The Ni–S bond lengths are reduced by 0.01 Å when SR effects are included in the ZORA Hamiltonian. The decrease in Ni–S bond lengths causes an increase in the S-Ni-S bond angle form 91.70° to 91.91° when SR effects are considered. All other bond lengths and bond angles remain nearly unaffected upon inclusion of such effects.

For comparison also calculations with the B3LYP hybrid-functional are included. A large Gaussian type orbital (GTO) valence-triple-ζ basis set with added polarization functions (VTZP) was used [167]. Hayes [127] very recently reported a UKS B3LYP/6-311+G* geometry optimization of the Ni(mnt)$_2^-$ complex. His findings for the structural parameters are essentially identical to our B3LYP/VTZP results and are therefore not given here. The B3LYP functional proves to be better in the description of bonding parameters of light elements, i.e. the C=C double bond, the C-CN single bond and the C≡N triple bond

Table 4.1: Comparison of experimental and calculated structural parameters of Ni(mnt)$_2^-$.
Bond lengths (r) in Å, bond angles (⟨) in degree.

	X-ray structure [166]	ZORA SR BP86/II	ZORA SR BP86/IV	ZORA SR BP86/V	NR BP86/V	NR B3LYP/VTZP
r(Ni-S)	2.15	2.216	2.163	2.156	2.165	2.190
r(S-C)	1.72	1.805	1.737	1.733	1.733	1.747
r(C=C)	1.37	1.381	1.390	1.388	1.389	1.372
r(C-C)	1.44	1.415	1.419	1.417	1.418	1.421
r(C≡N)	1.13	1.181	1.169	1.167	1.168	1.156
⟨ (S-Ni-S)	92.5	92.58	92.04	91.91	91.70	91.80
⟨ (Ni-S-C)	103.0	103.39	104.23	104.45	104.43	103.61
⟨ (S-C=C)	120.0	120.32	119.74	119.59	119.73	120.49
⟨ (C=C-C)	121.0	122.59	122.75	122.89	122.84	122.44
⟨ (C-C≡N)	179.0	179.02	178.71	178.77	178.70	178.57

are slightly more accurately reproduced (by $\approx$ 0.01 Å) compared to the ZORA SR/V case. Ni-S and S-C bond lengths are, however, too long with the B3LYP functional with respect to the data from X-ray analysis. The hybrid functional also gives slightly better results for bond angles as compared with the X-ray data but the differences between the pure GGA and the hybrid functional are very small (less than 0.8°).

4.3.1.2 Electronic Structure and g-Tensor Calculations

In the calculations the unpaired electron resides in the 5b$_{3g}$ orbital. A Mulliken population analysis of this singly occupied molecular orbital (SOMO) yields only a 21% contribution of the Ni 3d$_{yz}$ orbital, 60% S 3p$_z$ orbitals, 12% C=C 2p$_z$ orbitals and 6% N 2p$_z$ orbitals. The exact numbers will depend on the basis set used but the overall picture remains unchanged. The SOMO has a node on the C≡N carbon atom which contributes to less than 1%. The highest fully occupied molecular orbital (HOMO-1) is made up of 62% Ni 3d$_{xz}$, 19% S 3p$_z$, 11% C 2p$_z$ and 5% N 2p$_z$. The lowest unoccupied molecular orbital (LUMO) consists of 33% Ni 3d$_{xy}$, 32% S 3p$_x$ and 22% S 3p$_y$. Upon electrochemical two electron reduction, the SOMO would be doubly and the LUMO singly occupied to yield the paramagnetic complex Ni(mnt)$_2^{3-}$ [168].

The **g**-values determined by Maki *et al.* [149] and by Huyett *et al.* [151] differ in the g$_x$ and g$_z$ values

(See Table **4.2**). The deviation along g_x (0.02) and along g_z (0.01) is probably due to crystal packing effects or interaction with the host lattice in the single crystal experiments [149] or solvent effects in the case of the frozen solution measurements [151]. The g principal values from the most recent frozen solution experiments [151] are to be favoured because they provided the basis for the complex analysis and simulation of ENDOR and ESEEM spectra. Table **4.2** gives a comparison of experimental and calculated **g**-tensor components for $Ni(mnt)_2^-$. The calculations using the ZORA approach for relativistic effects with inclusion of spin-orbit coupling and a small basis set (basis II) yields g-values of 2.102, 2.032, 1.978 for g_x, g_y and g_z, respectively. The deviation of the calculation is largest for the g_x-component (38 ppt), smallest for g_y (8 ppt) and intermediate for g_z (12 ppt) as compared with the experimental values. The extension of the basis set from a double-ζ to a triple-ζ basis (basis IV) and to one with added polarization functions (basis V) does not improve results but slightly increases the deviation of the calculated **g**-tensor components from the experimental ones. Patchkovskii and Ziegler also observed such an independence of the DFT calculated **g**-tensors from the basis set [143]. Increase of the core region, obtained by adding a further tight 1s function to basis V, does also not improve the **g**-tensor results. This is due to the fact that the **g**-tensor is a property of the valence electrons [142]. All calculated **g**-tensor principal values are systematically smaller than the experimental ones. This is due to

Table 4.2: Comparison of calculated and experimental **g**-tensor of $Ni(mnt)_2^-$. $\Delta g_i = g_i - g_e$, i = x,y,z.

	g-value					
	g_x	g_y	g_z	Δg_i [ppt]		
exp. [149]	2.16	2.04	2.00	158	38	-2
exp. [151]	2.14	2.04	1.99	138	38	-12
ZORA SO BP86/II	2.102	2.032	1.978	100	30	-24
ZORA SO BP86/IV	2.092	2.031	1.976	90	29	-26
ZORA SO BP86/V	2.094	2.031	1.976	92	29	-26
ZORA SO BP86/V+1s	2.094	2.031	1.976	92	29	-26
ZORA SO BP86/Big	2.101	2.033	1.974	99	31	-28
SPT ROKS BP86/II	2.123	2.020	1.988	121	18	-14
SPT UKS BP86/II	2.105	2.020	1.984	103	18	-18
SPT UKS BP86/II (ξ(S)=0)	2.104	2.020	1.984	102	18	-18
SPT UKS BP86/II (ξ(Ni)=0)	2.0024	2.0023	2.0023	0.1	0	0

All calculations were performed at the ZORA SR UKS BP86/V optimized geometry.

The orientation of the **g**-tensor axes is along the symmetry axes of the complex. See Figure **4.1**.

the fact that the paramagnetic contribution to the **g**-tensor is too small which is also observed in **g**-tensor calculations of other transition-metal complexes (M. Kaupp, personal communication).

In order to validate whether the deviations of the calculated **g**-tensors were due to the ZORA approach, a traditional second-order perturbation approach was also used (SPT). A restricted open shell Kohn-Sham calculation in the SPT treatment gives a **g**-tensor with smaller deviation along g_x (17 ppt) and g_z (2 ppt) but larger deviation along g_y (20 ppt). The consideration of spin-polarization effects in the perturbation treatment leads to **g**-values of 2.105, 2.020 and 1.984 and, again, comes very close to the ZORA BP86/II results. The effect of spin-orbit coupling is incorporated in the second-order perturbation approach and the ZORA formalism. Both give a very similar value for the influence of spin-orbit coupling [131].

It is known that the deviation of the g-value from that of the free electron g_e is determined by spin-orbit coupling which gives the unpaired electron some small angular momentum and thus alters its effective magnetic moment. The SPT methodology offers the opportunity to selectively switch the spin-orbit coupling of different nuclei on or off. The contribution of spin-orbit coupling by the nickel nucleus alone to the **g**-tensor can be obtained by setting the spin-orbit coupling constant of the sulphur nucleus to zero. In the SPT UKS BP86/II(ξ(Ni)=0) calculation only spin-orbit coupling due to the sulphur nuclei is considered. As expected, for g_z and g_y isotropic values of the free electron **g**-factor are obtained. The spin-orbit coupling of the sulphur nuclei only contribute to g_x for which a marginal deviation from g_e (2.0024 vs. 2.0023) is obtained. From the comparison of the SPT UKS BP86/II(ξ(S)=0) calculation to the SPT UKS BP86/II calculations it is immediately clear that 100% of the g_z- and g_y-values originate from spin-orbit coupling of the nickel atom. The only slight reduction is obtained for g_x (2.105 vs. 2.104).

For $\mathrm{Ni(mnt)}_2^-$, ZORA calculations with a small basis set already give **g**-tensor magnitude and orientation in satisfying agreement with the experimental values. The agreement cannot be significantly improved by enlarging the basis set. The absolute deviation between calculation and experiment increases with the deviation from the free electron value while the relative error remains about constant. Patchkovskii and Ziegler also observed that the deviation between calculated and experimental **g**-tensors increased when going from 3d to 4d and 5d transition metal complexes [143]. This gives an indication of the accuracy of **g**-tensor calculations one could expect in related work on the active centre of [NiFe] hydrogenases. For the oxidized Ni(III) Ni-B EPR spectrum with $g_{x,y,z}$ = 2.33, 2.16, 2.01 one might get the largest deviation for g_x (if the error is strictly proportional to the deviation from g_e one would expect a deviation of up to 0.1) and better agreement for the g_y and g_z components. Furthermore, for the comparison of “gas phase” **g**-tensor calculations and experiments in single crystals an agreement of

10-15% would already be considered satisfying [126].

4.3.1.3 Spin Density Distribution and Hyperfine Interactions

Figure **4.2** shows contour plots of the unpaired spin density at 0.003 e/a_0^3. The spin density is not fully localized at the central nickel atom, but the four surrounding sulphur atoms carry significant spin density in p_π lobes oriented perpendicular to the horizontal mirror plane. The carbon atoms of the carbon-carbon double bond also bear unpaired spin density in their π-bonds. In contrast, the carbon atoms of the cyanide group carry no unpaired spin density while the terminal nitrogen atoms exhibit a small lobe of unpaired spin in a p-orbital perpendicular to the plane of the molecule.

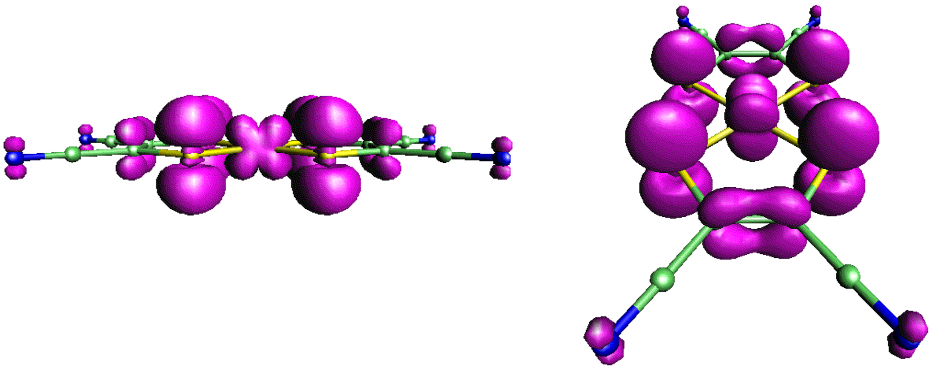

Figure 4.2: Views of the unpaired spin density distribution of $\mathrm{Ni(mnt)}_2^-$ at 0.003 e/a_0^3. The left view is along the yz-plane of the complex with the x-axis coming out of the paper plane. In the right view, the complex is rotated in the xy-plane by 90° and tilted by approx. 20° out of the plane .

Unrestricted ZORA SR BP86/V calculations yield total atomic spin populations of 0.26 at the nickel atom, 0.16 at each sulphur atom, 0.02 at each carbon in the double bond, -0.003 at each carbon of the cyanide group and 0.01 at each N. The Ni-S_4 core thus bears 90% of the unpaired spin. This value is slightly larger than the one from BLYP/LANLDZ results by Huyett *et al.* [151], who found 75%, and is close to Xα [152] calculations where 82% were found. In the non- and scalar relativistic calculations one may discuss atomic spin densities as the difference between α and β electron densities. In relativistic calculations, where spin-orbit coupling requires spin mixing, the resulting SO-coupled states will no longer be pure spin states. This will complicate the interpretation in atomic spin densities [132].

The high covalency of Ni–S bonds and the significant delocalization of spin density into ligand orbitals might have a significant influence on the interpretation of EPR and ENDOR spectra of a biological Ni–S centre, for instance in the case of [NiFe] hydrogenase for which large isotropic ^{1}H hyperfine coupling constants were measured for β-CH$_2$ protons of a cysteine amino acid adjacent to a nickel atom [169].

The single crystal experiments by Maki *et al.* [149] yielded the ^{61}Ni hyperfine tensor. It was found to be collinear with the **g**-tensor principal axes within experimental error. Unfortunately. the signs of the principal hyperfine tensor components (A$_{xx}$ = 45 ± 6 MHz, A$_{yy}$ = 9 ± 3 MHz, A$_{zz}$ = $<$ 6 MHz) are not known. From the measured hyperfine interaction in liquid solution is a$_{iso}$ = +12.6 ± 2.8 MHz. If one assumes that the A$_{zz}$ component is zero, one only arrives at two possibilities: Choice I, where all tensor components are positive: A$_{xx,yy,zz}$ = (+45, +9, 0) MHz yields a$_{iso}$ = +18 MHz and for the purely anisotropic components A'$_{xx,yy,zz}$ = (+27, -9, -18) MHz. Choice II: A$_{xx,yy,zz}$ = (+45, -9, 0) yields a$_{iso}$ = +12 MHz, A'$_{xx,yy,zz}$ = (+33, -21, -12). Estimates where A$_{zz}$ is small but not zero, do not fundamentally change the discussion of the results [1]. A discrimination between the two combinations can be done on the basis of calculations of the (anisotropic) ^{61}Ni hyperfine interaction (see Table **4.3**).

The analysis of naturally abundant ^{33}S satellites yielded an axial ^{33}S hyperfine tensor (A$_{zz}$ = A$_{||}$ = 42.8 MHz, A$_{xx}$ = A$_{yy}$ = A$_{\perp}$ = 13.6 MHz). Two choices of the signs of the hyperfine tensor were discussed in ref. [150]. I: All signs are positive, the isotropic value is 23.3 MHz and the anisotropic values A'$_{xx,yy,zz}$ (-9.7, -9.7, 19.5) MHz. II: A$_{\perp}$ = A$_{xx}$ = A$_{yy}$ is negative, then the isotropic coupling is 5.2 MHz and the anisotropic hyperfine tensor A'$_{xx,yy,zz}$ = (-18.8, -18.8, 37.6) MHz. The atomic spin population at the sulphur was estimated from the uniaxial hyperfine tensor and using the theoretical atomic values of Morton and Preston [159] to be between 0.13 (A$_{||}$ and A$_{\perp}$ same sign) and 0.26 (A$_{||}$ and A$_{\perp}$ opposite signs) [150]. This agrees with the picture in which a 3p$_z$ orbital occupation induces a polarization of the Ni–S σ orbitals. From this, one expects a small isotropic hyperfine interaction. The larger value of 23.3 MHz, however, appears unrealistic.

Table **4.3** shows a comparison of experimental and calculated hyperfine tensors of Ni(mnt)$_2^-$. For the experimental ^{61}Ni and ^{33}S hyperfine interactions a plausible choice of signs of the hyperfine tensor components was made (see above). In the case of ^{13}C and ^{14}N nuclei the choice of hyperfine tensor signs from ref. [151] is given (which proved to be in agreement with the calculations). All calculations

---

[1] Assuming that A$_{zz}$ takes the largest value (6 MHz) one has: I: All tensor components positive yields a$_{iso}$ = +20 MHz and A'$_{xx,yy,zz}$ = (+25, -11, -14) MHz II: A$_{xx,yy,zz}$ = (+45, +9, -6) MHz yields a$_{iso}$ = +16 MHz and anisotropic A'$_{xx,yy,zz}$ = (+29, -7, -22) MHz). III: A$_{xx,yy,zz}$ = (+45, -9, -6) MHz yields a$_{iso}$ = +10 MHz, A'$_{xx,yy,zz}$ = (+35, -19, -16) MHz. IV: A$_{xx,yy,zz}$ = (+45, -9, +6) yields a$_{iso}$ = +14 MHz and A'$_{xx,yy,zz}$ = (+31, -23, -8) MHz.

were done at the unrestricted SR ZORA geometry (see Table **4.1**). For means of comparison also spin-unrestricted B3LYP calculation with a valence-triple-ζ basis set with polarization functions given by Schäfer *et al.* [167] were performed.

SR ROKS calculations yield reliable anisotropic hyperfine tensors while the isotropic hyperfine interaction is not trustworthy since the effect of spin-polarization is not considered. For ^{61}Ni, the calculated anisotropic hyperfine tensor deviates by a factor of two for the anisotropic hyperfine tensor components A'$_{xx}$, A'$_{yy}$. The agreement for A'$_{zz}$ is much better. Spin-polarized ZORA SR calculations (SR UKS) yield an isotropic hyperfine interaction of +18.60 MHz for ^{61}Ni which nicely corresponds to an experimental value of +18 MHz (choice I). The effect of spin-polarization on the anisotropic hyperfine tensor components is less pronounced. A'$_{xx}$ and A'$_{zz}$ are increased by approx. 4 MHz in absolute numbers upon consideration of polarization effects, whereas the effect on A'$_{yy}$ is very small. Still, the agreement with experimental data is far from satisfying. Non-relativistic UKS B3LYP calculations with a VTZP basis set give similar numbers but the agreement with experimental data is even worse. This obvious discrepancy which was also observed by Hayes [127] led the author to the pessimistic conclusion that density functional calculations on Ni(mnt)$_2^-$ are unable to reliably assign the signs of the ^{61}Ni hyperfine tensor. The disagreement with experimental data, however, is not due to deficiencies of either the basis set or the functional but due to a systematic neglect of spin-orbit coupling as shown below.

The spin-orbit coupling manifests itself as a pseudocontact contribution to a$_{iso}$ and a second-order contribution to the anisotropic hyperfine tensor [77, 79, 80, 87, 128]. The effect of spin-orbit coupling is very large for nickel. The inclusion of spin-orbit coupling even inverts the sign of the a$_{iso}$ (Table **4.3**). It must be kept in mind that a considerable part of this difference is due to the neglect of spin-polarization in the spin-orbit coupled equations. A better estimate of the effect of spin-orbit coupling can be made if the spin-restricted SR results and those including spin-orbit coupling are compared. This gives an effect of spin-orbit coupling of approximately 15 MHz. When isotropic hyperfine interactions are to be calculated one still has to resort to spin-polarized (UKS) SR ZORA values until spin-polarized spin-orbit coupling can be treated in the ZORA Hamiltonian. This work is in progress.

The influence of SO coupling on the anisotropic hyperfine tensor (second order contribution) can, however, calculated very calculated in the ZORA approach. The absolute signs of the anisotropic hyperfine interaction are retained upon inclusion of spin-orbit coupling but their magnitude is decreased by 22 MHz, 16 MHz and 6 MHz for A'$_{xx}$, A'$_{yy}$ and A'$_{zz}$, respectively when comparing SR ROKS and SR+SO ROKS calculations. The lower hyperfine values agree to within a few MHz with the experimental ones of Choice I. If one assumes that the effect of spin-polarization on the spin-orbit coupled anisotropic hyperfine tensor is the same as for the scalar-relativistic anisotropic hyperfine tensor then the effect can be estimated to increase A'$_{xx}$ and A'$_{zz}$ by approx. 4 MHz and leave A'$_{yy}$ unchanged and thus give a perfect agreement with the Choice I of signs of the hyperfine tensor.

The other choice (Choice II) of the signs of the experimental ^{61}Ni hyperfine tensors can therefore be ruled out on the basis of our ZORA calculations. Neither isotropic (from the spin-polarized SR ZORA calculation) nor SO-coupled anisotropic hyperfine tensors support this possibility.

Our findings indicate that the inclusion of spin-orbit coupling is an absolute necessity when trying to calculate the hyperfine interaction of a transition metal ion. The influence of SO coupling on the anisotropic ^{61}Ni hyperfine interaction reduces it by a factor of two and brings it to within excellent agreement with experimental values.

For the ^{33}S hyperfine interaction in Ni(mnt)$_2^-$, the effect of spin-orbit coupling is less pronounced than for the ^{61}Ni nucleus but still noticeable. ZORA SR UKS calculations give an isotropic hyperfine interaction of +3.11 MHz which corresponds to the choice of experimental signs II (a_{iso} = +5.2 MHz). Choice I would lead to an unrealistic high value of +23.3 MHz which can also not be reproduced by the calculations. Furthermore, the calculated hyperfine interaction of (-15.79,-14.38,+30.16) MHz supports choice II whereas the anisotropic hyperfine tensor components of choice I appear too low. The effect of spin-polarization becomes obvious when comparing restricted (ROKS) and unrestricted (UKS) open shell SR ZORA calculations. Spin-polarization leads to an increase of A'$_{xx}$, A'$_{yy}$ and A'$_{zz}$ in absolute magnitude by 2.3, 1.2 and 3.5 MHz, respectively. The agreement with the experimental values is improved. ZORA calculations with spin-orbit coupling yield an a_{iso} value of only 0.19 MHz. The anisotropic hyperfine tensor does not change much upon inclusion of spin-orbit coupling (changes lie within 0.5 MHz). If the effect of spin-polarization is taken from the SR calculations, values to within 0.5 MHz of the SR UKS can be estimated. The isotropic hyperfine interaction of ^{33}S is due to spin polarization and yields a small but detectable isotropic hyperfine interaction.

For the ^{13}C hyperfine interaction in the C=C double bond, ZORA SR UKS calculations yield isotropic and anisotropic hyperfine interactions to within 0.5 MHz of the experimental ones. The importance of spin polarization again is illustrated by comparing restricted and unrestricted SR calculations. Spin polarization reduces the anisotropic hyperfine tensor components by 0.5-1 MHz and brings them closer to the experimental values. When the effect of spin-polarization is taken from SR calculations the results with SO coupling represent an improvement of 0.4 MHz. B3LYP calculations give good results for the ^{13}C isotropic hyperfine interaction but the anisotropic part is less well reproduced (see also [127]). The experimental ^{13}C hyperfine tensor was assumed to be collinear with the **g**-tensor principal axes system. Only in this coordinate system the tensor is of uniaxial symmetry. The deviation of the calculated anisotropic hyperfine tensor from uniaxiality is indeed small. The orientation, however, is not collinear with the **g**-tensor principal axes system but rotated by 6° from the x- and y-axes. A'$_{zz}$ is along the g$_z$-axis. This was also noticed by Hayes [127].

The case of the ^{13}C nucleus of the cyanide group is more difficult. The negative isotropic hyperfine interaction is well reproduced by unrestricted calculations (-2.47 MHz calculated vs. -2.9 MHz experimental). All theoretical calculations, however, agree that A'$_{xx}$ is negative and A'$_{yy}$ positive while the simulation of the experimental spectra yielded A'$_{xx}$ and A'$_{yy}$ both of positive sign. Theory and experiment agree that the component perpendicular to the molecular plane, A'$_{zz}$ is negative. One must bear in mind that the experimental values give the hyperfine tensor in the **g**-tensor's principal axes system, e.g. **g**- and **A** are assumed to be collinear. The calculations yield the diagonalized hyperfine tensor in its own principal axes system A'$_{xx}$, A'$_{yy}$, A'$_{zz}$ which is not necessarily collinear with the **g**-tensor. In fact, A'$_{xx}$ and A'$_{yy}$ are rotated by 30° from the respective **g**-tensor principal axes and A'$_{zz}$ is along g$_z$ (similar values were obtained by Hayes [127]).

For the ^{14}N hyperfine interactions of the CN group spin-polarized (UKS) ZORA SR calculations give excellent results. The deviation from the experimental values is less than 0.5 MHz for both isotropic and anisotropic contributions. B3LYP calculations give slightly better values for the anisotropic hyperfine interaction of the ^{14}N nucleus. The numbers given in [127] for the experiment from ref. [151] correspond to the experimental values for the ^{15}N nucleus and have to be corrected by the ratio of the ^{15}N and ^{14}N Larmor frequencies (1.403). For a cyanide group one expects a nearly axial quadrupole tensor with its largest component along the C≡N triple bond. The calculated ^{14}N (I = 1) quadrupole tensor agrees well with the experimental values. The deviation from experimental values might be due to environmental effects in frozen solution. The calculated quadrupole tensor has its smallest component perpendicular to the molecular plane (0.85 MHz) and its largest component (-2.09 MHz) along the C≡N triple bond. The third component (1.23 MHz) lies in the molecular plane and is perpendicular to the C≡N bond. This orientation was also found experimentally by Huyett *et al.* [151]. The thorough analysis of pulsed-ENDOR and ESEEM data by simulation of the experimental spectra and the assignment of absolute signs [151] of the hyperfine tensors is confirmed by our calculations.

For means of comparison, a calculation using the popular B3LYP functional and a valence-triple-ζ basis set with polarization functions (VTZP) of Schäfer *et al.* [167] was also performed. The geometry of the ZORA SR UKS BP86/V (Table **4.1**) calculation was used. The hyperfine interactions were calculated using a non-relativistic, first-order approach (see for example [122–124]). Strictly speaking, the comparison can only be made with spin-polarized scalar relativistic ZORA calculations where spin-orbit coupling is not considered. The isotropic ^{61}Ni hyperfine interaction is of positive sign and significantly larger than the ZORA SR value. This may be due to the different density functionals or basis sets used in the calculations. Gaussian basis functions do not correctly describe the cusp region near the core in contrast to the use of Slater basis functions in ADF, which means that one needs more GTOs than STOs in the basis set to obtain the same accuracy[2]. The signs of the anisotropic hyperfine tensor components are reproduced in the B3LYP calculations but the values are larger than the corresponding ZORA values. This deficiency is due to the neglect of spin-orbit coupling as shown above. For all other nuclei, the absolute signs of the tensor components agree with the ZORA results. The agreement is of the order of a few MHz or less but the B3LYP functional does not represent a systematic improvement over the pure GGA functional. This observation was also made by Munzarova and Kaupp who compared all usual GGA and hybrid functionals in the calculation of transition metal hyperfine interactions [126].

To summarize, ZORA calculations yield hyperfine parameters for all (light and heavy) atoms in Ni(mnt)$_2^-$ in good agreement with experimental values. The ambiguity of the signs of the ^{33}S and ^{61}Ni hyperfine tensors could be resolved on the basis of our ZORA calculations. The calculations support *one* specific choice of signs of the hyperfine tensor components. Spin-orbit coupling plays an important role in the calculation of heavy element anisotropic hyperfine interaction. The isotropic hyperfine interaction must still be taken from a spin-polarized SR ZORA calculation.

In the oxidized states of the [NiFe] hydrogenase, the EPR signal also originates from the Ni metal alone as was shown by ^{61}Ni enrichment [64]. The Fe metal in the active centre does not contribute to the EPR spectrum. The hyperfine interaction of the ^{61}Ni enriched hydrogenase from *Desulfovibrio gigas* in the oxidized Ni-B state shows a hyperfine splitting of 6 to 17, 6 to 17, and 76 MHz along the **g**-tensor components g$_{xx}$, g$_{yy}$ and g$_{zz}$, respectively [45]. The hyperfine interaction is thus of the same order of magnitude as in Ni(mnt)$_2^-$ and the spin population at the Ni nucleus in [NiFe] hydrogenase can be expected to be similar to that in this model complex Ni(mnt)$_2^-$.

---

[2] NR BP86/VTZP calculations with a GTO basis set yielded a$_{iso}$(^{61}Ni) = +69.85 MHz. The difference between spin-polarized SR ZORA and NR BP86 calculations still lies in the different basis sets (STOs vs. GTOs) and/or the consideration of scalar relativistic effects in the ZORA Hamiltonian.

Table 4.3: Experimental and calculated hyperfine and quadrupole parameters of Ni(mnt)$_2^-$ in MHz.

Nucleus		exp.	SR ROKS	SR UKS	SO+SR ROKS	UKS B3LYP
exp. ref.			BP86/V+1s	BP86/V+1s	BP86/V+1s	VTZP
^{61}Ni^a [149]	a$_{iso}$	+18	-0.12	**+18.60**	-15.03	+30.82
	A'$_{xx}$	+27	+47.15	+51.93	**+25.87**	+66.92
	A'$_{yy}$	-9	-23.53	-24.03	**-7.88**	-28.52
	A'$_{zz}$	-18	-23.85	-27.35	**-17.99**	-38.40
^{33}S^b [150]	a$_{iso}$	+5.2	+0.12	**+3.11**	+0.19	**+7.20**
	A'$_{xx}$	-18.8	-13.49	-15.79	-13.81	**-18.46**
	A'$_{yy}$	-18.8	-13.15	-14.38	-12.65	**-15.32**
	A'$_{zz}$	+37.6	+26.65	+30.16	+26.45	**+33.77**
^{13}C=C^c [151]	a$_{iso}$	-2.1	+0.003	-1.63	+0.11	**-2.32**
	A'$_{xx}$	-2.5	-3.49	**-2.95**	-3.09	-2.09
	A'$_{yy}$	-2.5	-3.15	**-2.63**	-3.26	-1.49
	A'$_{zz}$	+5.0	+6.65	**+5.59**	+6.37	+3.58
^{13}CN^c [151]	a$_{iso}$	-2.9	-0.001	**-2.47**	+0.01	-1.95
	A'$_{xx}$	+0.33	-0.31	**-0.25**	-0.51	-0.50
	A'$_{yy}$	+0.13	+0.81	**+0.80**	+0.83	+0.62
	A'$_{zz}$	-0.47	-0.50	**-0.54**	-0.31	-0.12
^{14}N^c [151]	a$_{iso}$	+0.39	+0.001	**+0.15**	+0.007	**+0.15**
	A'$_{xx}$	-0.26	-0.72	-0.59	-0.73	**-0.40**
	A'$_{yy}$	-0.29	-0.60	-0.47	-0.59	**-0.22**
	A'$_{zz}$	+0.55	+1.33	+1.05	+1.31	**+0.62**
	Q$_{xx}$	+0.85	+0.86	**+0.85**	+0.86	+0.41
	Q$_{yy}$	+1.10	+1.23	**+1.23**	+1.23	+1.80
	Q$_{zz}$	-1.95	-2.09	**-2.09**	-2.09	-2.21

a$_{iso}$ is the isotropic (Fermi contact) hyperfine interaction, A'$_{ii}$ i = x,y,z are the anisotropic hyperfine tensor components. a Only Choice I of the signs of the experimental hyperfine tensor components is given (see text for details).

b Only Choice II of the experimental hyperfine tensor components is given (see text for details).

c The absolute signs of the experimental tensors are fixed assuming a 2p$_z$ spin population [151].

The best agreements with experimental values are given in bold font.

4.3.2 Ni(CO)$_3$H

In Ni(CO)$_3$H (**II** Figure **4.1**) the central nickel atom is coordinated by three CO ligands in the equatorial plane and axially by a hydrogen atom (C$_{3v}$ symmetry). Formally, the complex may be described either as a Ni(I) with a H$^-$ bound ((CO)$_3$-Ni(I)-H$^-$) or as a Ni(0) with a hydrogen atom bound ((CO)$_3$-Ni(0)-H)). In the thorough analysis of the krypton matrix EPR spectrum Morton and Preston concluded that the structure of the complex is best described as (CO)$_3$-Ni(I)-H$^-$ [170]. While the oxidized states of the hydrogenase are usually referred to as Ni(III), the two electron more reduced form Ni-C might be a Ni(I) species. Since Ni-C is an intermediate in the catalytic process, either a H$_2$ molecule, or a H$^+$ or H$^-$ are supposed to be bound to the Ni. Ni(CO)$_3$H therefore represents a good model for the calculation of the magnetic resonance parameters for such a bonding situation.

For Ni(CO)$_3$H there is no X-ray structure available. The comparison of calculated structural parameters is therefore made with DFT calculations by Munzarova and Kaupp [126] who used the B3LYP functional with a relativistic pseudopotential for Ni. Table **4.4** compares the calculated structural parameters of Ni(CO)$_3$H in the ZORA approach at the scalar-relativistic (SR) level using a large basis set (basis V) with those using a relativistic effective core potential (RECP) [126] and non-relativistic all electron calculations. NR calculations agree well with the B3LYP/RECP(Ni) calculations in the Ni–H bond length (1.502 vs. 1.512 Å). The Ni–C bond length is shorter by 0.027 Å in the NR calculation and so is the C=O bond length by 0.015 Å. The difference in bond angles is only ≈ 1 degree. The influence of scalar relativistic effects can be observed by comparing non-relativistic ADF calculations with SR ZORA calculations. They are manifested in a reduction of the Ni–H bond length by 0.007 Å and of the Ni–C bond length by 0.017 Å. The effect on the C=O bond length is almost negligible. Due to the shorter Ni–H and Ni–C bonds the H–Ni-C and Ni–C=O bond angles widen by 0.4 degrees. The importance of

Table 4.4: Comparison of calculated structural parameters of Ni(CO)$_3$H. Bond lengths (r) in Å, bond angles (⟨) in degree.

	ZORA SR ROKS BP86/V	ZORA SR UKS BP86/V	NR UKS BP86/V	B3LYP/RECP(Ni) [126]
r(Ni-H)	1.485	1.495	1.502	1.512
r(Ni-C)	1.807	1.807	1.824	1.851
r(C=O)	1.150	1.149	1.150	1.135
⟨ (H-Ni-C)	90.87	90.93	89.90	90.87
⟨ (Ni-C=O)	173.19	173.79	172.38	171.29

spin-polarization for structural parameters is highlighted by comparing restricted open shell Kohn-Sham and unrestricted Kohn-Sham scalar-relativistic ZORA calculations (Table **4.4**). Spin-polarization leads to an increase in Ni–H bond length by 0.01 Å while all other structural parameters remain nearly unchanged. In general, SR UKS ZORA calculations agree well with those using the B3LYP functional and a relativistic core potential. Spin-polarization is important for the description of the Ni–H bond.

4.3.2.1 g-Tensor and Hyperfine Interaction

The EPR spectrum of $Ni(CO)_3H$ was measured in a krypton matrix by Morton and Preston [170]. They found an axial **g**-tensor with $g_{||} = g_{zz}$ = 2.0674 and $g_\perp = g_{xx} = g_{yy}$ = 2.0042. The orientation of the **g**-tensor is $g_{||}$ along the z-axis and $g_\perp$ in the xy-plane of the complex (see Figure **4.1**). Table **4.5** gives the results of ZORA calculations of the **g**-tensor of $Ni(CO)_3H$. All calculated values are smaller than the corresponding experimental values. For the small double-ζ basis (basis set II) the deviation of the $g_{||}$ component is 4 ppt from the experimental value and for $g_\perp$ it is 20 ppt. A better description of the valence electrons does not significantly improve the results. The increase is only 1 ppt in $g_\perp$. The addition of an extra tight 1s function also only marginally improves the results.

Table 4.5: Comparison of ZORA calculated and experimental **g**-Tensor of $Ni(CO)_3H$.
$\Delta g_i = g_i - g_e$, i = $\perp$, $||$.

	g-value		Δg_i [ppt]	
	$g_\perp$	$g_{\|\|}$		
exp. [170]	2.0674	2.0042	65	2
BP86/II	2.0468	2.0003	45	-2
BP86/IV	2.0478	2.0003	46	-2
BP86/V	2.0480	2.0003	46	-2
BP86/V+1s	2.0486	2.0003	46	-2

Figure **4.3** shows a contour plot of the unpaired spin density at a value of 0.003 e/a_0^3. The contour plot shows that the spin density distribution is of centroid symmetry. The form of the spin density at the Ni resembles that of a d_{z^2} orbital. A Mulliken analysis yields atomic spin populations of ρ(Ni) 0.48, ρ(H) 0.22, ρ(C) 0.06 and ρ(O) 0.04. The contribution of the atomic orbitals to the $13A_1$ SOMO are as follows (arranged by decreasing percentage): 24% $3d_{z^2}$(Ni), 21% $4p_z$(Ni), 19% $2p_z$(C), 17% 1s(H), 14% $2p_z$(O), and 4% 2s(C). This indicates that the $4p_z$ of the Ni contributes significantly.

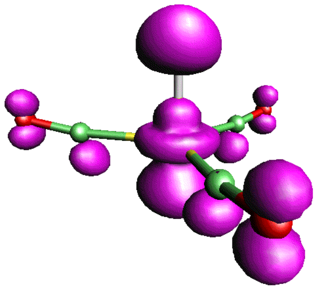

Figure 4.3: View of the Unpaired Spin Density Distribution of $Ni(CO)_3H$ at 0.003 e/a_0^3.

Due to the axial bonding of the hydride ion to the Ni atom, the H atom may acquire a significant amount of spin density which leads to a very large hyperfine coupling caused by the large magnetic moment of the nucleus. Consequently, the ^{1}H hyperfine structure could be resolved in the Kr matrix EPR spectra [170]. The hyperfine interaction is dominated by a very large isotropic hyperfine interaction a_{iso} of 293 MHz while the uniaxial anisotropic interaction is only 5.5 MHz.

Table **4.6** compares the ^{61}Ni and ^{1}H experimental hyperfine interactions with ZORA calculations at various levels of theory and non-relativistic B3LYP calculations by Munzarova and Kaupp [126]. The comparison is only made with the results using the B3LYP functional because it is the one most frequently used in DFT investigations of transition metals. The ZORA SR UKS BP86/V optimized geometry of Table **4.4** was used.

The ^{61}Ni isotropic hyperfine interaction is well reproduced by unrestricted (UKS) SR ZORA calculations whereas the B3LYP functional overestimates the isotropic coupling constant by a factor of three. The inclusion of spin-polarization reduces $A'_\perp$ and $A'_{||}$ by 2 and 4 MHz indicating only a moderate effect of polarization. SO coupling reduces the anisotropic coupling by 5 and 10 MHz for $A'_\perp$ and $A'_{||}$, respectively, when comparing SR ROKS and SO + SR ROKS calculations. The effect is weaker than in the case of $Ni(mnt)_2^-$ because the SOMO consists here of p_z and d_{z^2} orbitals at the Ni. If the assumption of similar spin-polarization for SR and SO-coupled calculations holds, the agreement with the experimental values is perfect. $A'_\perp$ would be brought down to 44 MHz and $A'_{||}$ to 88 MHz by spin-polarization. The resulting anisotropic tensor is in excellent agreement with the experimental value and superior to the results by Munzarova and Kaupp [126]. (The BP86 values by Munzarova and Kaupp [126] are in close agreement with our values. Still, the isotropic coupling constant is overestimated by a factor of two.) The isotropic hyperfine interaction of the Ni changes from +10.10 to -18.70 MHz upon inclusion of spin-orbit coupling and neglecting spin-polarization. This large effect of -28.8 MHz agrees very well with the

Table 4.6: Comparison of experimental and calculated hyperfine and quadrupole interactions in Ni(CO)$_3$H in MHz.

Nucleus		exp. [170]	SR ROKS BP86/V+1s	SR UKS BP86/V+1s	SR+SO ROKS BP86/V+1s	B3LYP/DZPD(Ni), IGLO-III [126]
^{61}Ni	a_{iso}	+9.0	-9.94	**+10.10**	-18.70	+33.3
	$A'_{\perp}$	+44.0	+50.88	+48.56	**+45.76**	+56.9
	$A'_{\|\|}$	-88.0	-101.75	-97.11	**-91.52**	-113.8
	$Q_{\perp}$	-4.1	-4.4	**-4.1**	-4.4	/
	$Q_{\|\|}$	+8.2	+8.8	**+8.2**	+8.8	/
^{1}H	a_{iso}	+292.8	**+276.54**	+335.58	+275.25	+208.0
	$A'_{\perp}$	-5.50	-4.05	-2.68	**-4.21**	-3.15
	$A'_{\|\|}$	+11.10	+8.11	+5.36	**+8.42**	+8.43
^{13}C	a_{iso}		+20.75	+7.61	+20.74	+5.10
	A'_{xx}		-5.46	-5.71	-5.59	-5.50
	A'_{yy}		-1.34	-2.60	-1.19	-3.20
	A'_{zz}		+6.80	+8.31	+6.79	+8.70
^{17}O	a_{iso}		-1.31	-3.72	-1.35	-3.70
	A'_{xx}		+7.92	+8.60	+8.00	-8.70
	A'_{yy}		+6.98	+6.99	+6.83	-5.30
	A'_{zz}		-14.90	-15.59	-14.83	+14.0

Calculations were performed at the ZORA SR UKS BP/V geometry (see Table **4.4**).

Best agreements with experimental values are given in bold font.

estimated value of spin-orbit coupling by Munzarova and Kaupp [126] who used an empirical formula by Abragam and Pryce (see ref. [79]) and obtained -26.8 MHz. This effect is overestimated, since in our calculated effect also spin-polarization is neglected. A comparison of the SR ROKS results with the SR UKS results shows that spin-polarization effects already explain for a large part the calculated difference.

Because of the cylindrical spin density distribution (see Figure **4.3**) one expects the largest quadrupole interaction of the ^{61}Ni nucleus (I = 3/2) to be along the Ni–H bond and smaller values perpendicular to it. This is found experimentally: $Q_{||}$ = 8.2 MHz and $Q_{\perp}$ = -4.1 MHz. These numbers are exactly obtained from a spin-polarized SR calculation while non-polarized calculations slightly overestimate the parallel value and underestimate the perpendicular value.

The ^{1}H isotropic hyperfine interaction is overestimated by SR UKS calculations by 43 MHz and also the anisotropic part is not very well described (deviation 3 and 6 MHz). It is in particular the isotropic component that is most sensitive to spin polarization. The calculated B3LYP ^{1}H value by Munzarova and Kaupp [126] deviates from the experimental value by 85 MHz but into the other direction (208 MHz calculated vs. 293 MHz measured). A comparison of the spin-restricted (ROKS) SR results and those including spin-orbit (SR + SO ROKS) coupling shows that the effect of spin-orbit coupling is small for the ^{1}H nucleus.

For the ^{13}C and ^{17}O nuclei there are no experimental values available. Here, a comparison is made with the calculated B3LYP values by Munzarova and Kaupp [126] which are also included in Table **4.6**. For the ^{13}C nucleus the agreement between SR UKS ZORA and non-relativistic B3LYP calculations is very good. The difference in the isotropic hyperfine interaction is 2.5 MHz at most. In the case of ^{17}O, in contrast, the SR UKS calculated signs of the anisotropic hyperfine interaction are inverted with respect to the values by Munzarova and Kaupp (see Table **4.6**). The calculation was repeated using the SR ZORA BP/V geometry, a VTZP basis set by Schäfer *et al.* [167] and the B3LYP hybrid functional in the Gaussian94 program. The obtained values are, in general, very similar to that of Munzarova and Kaupp and are therefore not given here. The only noteworthy difference is in the ^{17}O hyperfine interaction. The isotropic part in our calculation is a_{iso} = -4.35 MHz and the anisotropic part $A'_{xx,yy,zz}$ = (+9.64, +6.11, -15.75) MHz. Our findings of the absolute signs of the anisotropic hyperfine interaction are in agreement with our ZORA results and contradict the signs given by Munzarova and Kaupp. This may be due to a typing error in their manuscript. The effect of spin-orbit coupling is very small for ligands in the molecular xy-plane. The anisotropic part of the hyperfine tensor of the ^{13}C and ^{17}O nuclei remains nearly unchanged upon inclusion of SO coupling.

It should be mentioned as an aside that the popular B3LYP functional does not necessarily lead to an improvement in the calculation of hyperfine parameters compared to pure GGA functionals as was already stated by Munzarova and Kaupp [126] and by Hayes [127].

The Ni-C state of the [NiFe] hydrogenase is two electrons more reduced than the oxidized states, and might formally correspond to a Ni(I) species. The observation of the Ni-C EPR spectrum correlates with the catalytic activity of the enzyme [45] and is thus assigned to be an intermediate in the heterolytic cleavage of molecular hydrogen. For the Ni(I) in Ni-C a $3d_{z^2}$ ground state is sometimes discussed [65, 69, 70]. As shown here, a hydride axially bound to a Ni $3d_{z^2}$ orbital would lead to a much larger ^{1}H hyperfine coupling than the one observed in hydrogenase (16-20 MHz [69,70]). Such a bonding situation seems therefore to be unrealistic in the Ni-C state [12]. A hydride ion bound to nickel in the xy-plane can, however, not be excluded.

4.4 Conclusion

The calculation of magnetic resonance parameters from first principles offers a straight forward route to the comparison of experimental and theoretical values for transition metal complexes. The detour via atomic spin populations is no longer required.

The accuracy of the ZORA formalism to calculate the magnetic resonance parameters of nickel containing model complexes both in the Ni(III) and Ni(I) oxidation states was demonstrated. The hyperfine tensors can be computed relatively accurately, whereas the agreement in **g**-tensors is less good. Effects of spin-orbit coupling may be large for both the calculated isotropic and the calculated anisotropic metal hyperfine interactions. The effects on the ligand hyperfine interactions are in general much smaller.

In the case of $\mathrm{Ni(mnt)}_2^-$, the calculations helped to resolve ambiguities in the choice of signs of the ^{61}Ni and ^{33}S nuclei. The unpaired electron was found to reside in the $5b_{3g}$ orbital consisting mainly of the Ni $3d_{yz}$ orbital and S $3p_z$ orbitals. The covalent bonding leads to a delocalization of 64% of the spin population into sulphur ligand orbitals. This large Ni–S bond covalency is an important result and has to be taken into consideration in the interpretation and analysis of ENDOR data from the [NiFe] hydrogenases.

In $\mathrm{Ni(CO)_3H}$, a hydride ion is bound axially to a hybrid Ni $3d_{z^2}$, $4p_z$ orbital. The large hyperfine interaction of the hydrogen rules out such a bonding situation for the Ni-C state of the [NiFe] hydrogenase. An in-plane bound hydride can, however, not be ruled out.

The ZORA formalism's accuracy and computational efficiency holds great promise for the elucidation and interpretation of EPR and ENDOR data of Ni complexes in biological systems and other active centres in metalloenzymes.

Chapter 5

The Electronic Structure of the Paramagnetic States of [NiFe] Hydrogenase

5.1 Introduction

The active centre of the [NiFe] hydrogenase consists of a heterobimetallic Ni-Fe cluster. The Ni and Fe atoms are bridged by sulphur atoms of two cysteine amino acids. In addition, there are two further cysteines as terminal ligands to the Ni atom (see Fig. **5.1**). *D. gigas* and *D. vulgaris* Miyazaki F [NiFe] hydrogenases display identical EPR spectra [39]. The details of their active centres [27, 28, 171] with regard to the nature of the bridging ligand X and the identification of the three non-protein ligands to the Fe atom are controversely discussed. The electron density peak in the oxidized states between Ni and Fe was tentatively assigned to an oxygen species in *D. gigas* [27] and to a sulphur species *D. vulgaris* [28]. Recently, liberation of H_2S upon reduction of *D. vulgaris* was reported [172] indicating the presence of a sulphur ligand in this species. Furthermore, there are three diatomic, non-protein ligands terminally bound to the Fe. In the case of the [NiFe] hydrogenase from *Allochromatium vinosum* they have been identified to be 1 CO and 2 CN ligands by FTIR spectroscopy [51] and chemical analysis [173]; and by FTIR spectroscopy for *D. gigas* [27]. In *D. vulgaris* Miyazaki F two CO, and one SO ligand were postulated from X-ray crystallography [28].

Recently, a high resolution X-ray structure (1.4 Å resolution) of the reduced enzyme from *D. vulgaris* Miyazaki F was published [174] in which removal of the bridging ligand in the reduced state was reported. There were no significant changes in the bonding parameters associated with this reduction.

Density Functional Theory (DFT) calculations have already been applied to [NiFe] hydrogenases by Pavlov *et al.* [71] who have proposed a reaction mechanism for the dissociation of molecular hydrogen by [NiFe] hydrogenases. The emphasis in this work was on the activation of H_2 by the enzyme. The Fe was proposed to be the site of H_2 binding. In their work, the electronic ground state was not correctly calculated, making a comparison with experimental data difficult. In a subsequent publication [72], the initial reaction mechanism was slightly revised. The first attempt to describe the redox states of the enzyme was recently addressed by De Gioia *et al.* [74]. These authors obtained the correct (S=1/2) ground state but the reported spin populations were not in good agreement with experimental data (see below). Later, Niu *et al.* [75] characterized the intermediate states of the [NiFe] hydrogenase by their CO stretching frequencies but no atomic spin populations were reported. Amara *et al.* suggested atomic compositions for the Ni-A and Ni-C paramagnetic states based on QM/MM calculations [76]. The obtained spin populations, however, seem questionable due to large contributions from higher spin states (see below).

In this chapter DFT investigations performed on the different paramagnetic states of the active centre (Ni-A, Ni-B, Ni-C) are reported. Several candidates for the bridging ligand are suggested and the different paramagnetic states are traced back mainly to modifications of this bridging ligand. Some aspects of the non-protein ligands at the Fe atom are also discussed. The proposed atomic structures of the active centre in the different paramagnetic states are in agreement with experimental results derived from EPR and ENDOR spectroscopy. This yields an understanding at the atomistic level of the Ni-A, Ni-B and Ni-C states. The obtained data for these states form the basis for establishing a reaction mechanism for the activation of hydrogen by [NiFe] hydrogenases.

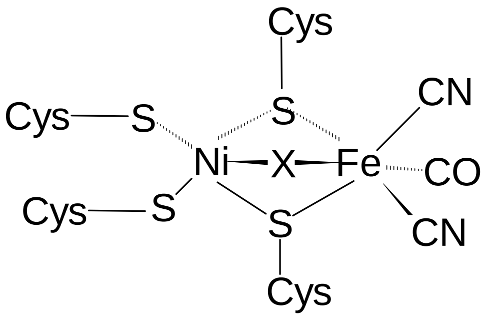

Figure 5.1: Schematic picture of the active centre of [NiFe] hydrogenase from *D. gigas*. The diatomic ligands are 1 CO and 2 CN as shown [27], in *D. vulgaris* 1 CO, 1 CN, and 1 SO are postulated [28]. The bridging ligand X is either an oxygen (*D. gigas* [27]) or a sulphur species (*D. vulgaris* [28]).

5.2 Computational Details

The efficiently parallelized density functional code DGauss4.0 [175] was used and run on a Cray T3E computer using up to 128 processors. Large cluster models (42 atoms for Ni-B, 41 atoms for Ni-A/Ni-C) of the active site of [NiFe] hydrogenase were completely geometry optimized imposing no constraints on the structure. Due to the absence of point group symmetry and the open-shell nature of the species considered here, typical CPU usage times for a geometry optimization were 50 - 100 h . Cysteine amino acids were represented by a S–CH_2–CH_3 moiety leading to a realistic description of the active site of the enzyme (see below). Smaller cluster models lead to erroneous results and are insufficient to describe the spin density distribution correctly. Two CN and one CO ligands were chosen as prosthetic groups to the Fe atom but also 1 SO, 1 CN, and 1 CO ligand were alternatively considered.

The DFT-optimized DZVP basis set of Godbout *et al.* [176] was applied. The atomic basis set was of the following contraction scheme: H 41, C 621/41/1, N 621/41/1, O 621/41/1, S 6321/521/1, Ni 63321/531/41, Fe 63321/531/41. The auxiliary basis set for the exchange-correlation and coulomb part was of the following type: H 4, C 6/3/3, N 7/3/3, O 7/3/3, S 9/4/4, Ni 10/5/5, Fe 10/5/5. This basis set was successfully used in the description of the electronic structure of blue-copper proteins [177]. The Becke exchange functional and the Lee-Yang-Parr gradient-corrected correlation functionals were used (BLYP) [91, 92]. The BLYP functional was shown to yield structural parameters (bond lengths and vibrational harmonic frequencies) virtually identical to the hybrid B3LYP functional and to sophisticated post-HF techniques in case of neutral and positively charged transition metal hydrides [178]. All structures reported here converged to doublet (S = 1/2) states as experimentally observed. The deviation of the expectation value of $< \mathrm{S}^2 >$ from the theoretical value of 0.75 were $\leq$ 0.008.

5.3 Results and Discussion

5.3.1 Structural Parameters for The Oxidized States

One of the aims of the calculations was to elucidate the nature of the bridging ligand X between the Ni and Fe atoms in the oxidized states that was postulated to be an oxygen [27] or a sulphur species [28]. O^{2-}, OH^-, S^{2-} and SH^- were tested as plausible candidates for this bridging ligand X. A protonation of an oxygen or sulphur bridge would not be detectable by X-ray crystallography.

In Table **5.1** data from the two X-ray structures of the oxidized enzyme are collected. In the *D. gigas* X-ray structure refined to 2.5 Å an electron density peak between the Ni and Fe atoms was discovered [27] and assigned to an oxygenic species. The crystals consist of enzyme that is predominantly in the “unready“ Ni-A state (85% Ni-A, 15% Ni-B) [171]. The structure of the homologous [NiFe] hydrogenase from *D. vulgaris* Miyazaki F [28] (1.8 Å resolution) differs from that of *D. gigas*. The Ni $\cdots$ Fe distance is significantly shorter (2.55 Å) and so are nearly all Ni–S and Fe–S bond lengths. A sulphur species is postulated to occupy the bridging position. In *D. vulgaris* [28] the diatomic ligands to the Fe atom are given as 2 CO and 1 SO ligand. The assignment of S as bridging ligand and SO as terminal Fe ligand is based on higher temperature factors and electron density peaks of these atoms. It was shown by EPR that the enzyme of *D. vulgaris* Miyazaki F was crystallized in the “ready” form Ni-B (70% Ni-B, 30% Ni-A) [179].

Table 5.1: Comparison of selected structural parameters from X-ray and BLYP/DZVP optimized structures of the oxidized active centre of [NiFe] hydrogenase. In the calculations 2 CN and 1 CO ligands were chosen as diatomic ligands to the Fe. Bond lengths in Å, bond angles (∠) in degrees.

	Exp.		Calc.			
	D. gigas	*D. vulgaris*	Bridging Ligand			
distances/angles	[27]	[28]	X= O^{2-}	X= OH^-	X= S^{2-}	X= SH^-
Ni $\cdots$ Fe	2.90	2.55	2.96	3.05	3.22	3.19
Ni $\cdots$ SCys533	2.62	2.37	2.49	2.51	2.50	2.48
Ni $\cdots$ SCys68	2.58	2.38	2.41	2.36	2.40	2.38
Ni $\cdots$ SCys530	2.27	2.33	2.40	2.31	2.39	2.32
Ni $\cdots$ SCys65	2.16	2.22	2.44	2.29	2.46	2.31
Ni $\cdots$ X	1.74	2.16	1.84	1.98	2.26	2.36
Fe $\cdots$ SCys533	2.20	2.37	2.61	2.47	2.56	2.48
Fe $\cdots$ SCys68	2.23	2.14	2.50	2.46	2.52	2.46
Fe $\cdots$ X	2.14	2.22	1.97	2.09	2.40	2.44
∠ Ni-X-Fe	96.5	71.0	102.1	96.8	87.3	83.5
∠ Ni-SCys533-Fe	73.6	64.1	71.0	75.5	79.1	82.5
∠ Ni-SCys68-Fe	73.9	66.2	74.1	78.3	81.8	80.1

The error in the X-ray coordinates is estimated to be 0.27 Å at 2.5 Å [27] and 0.2 Å at 1.8Å [28] resolution.

Table **5.1** compares selected features of the BLYP/DZVP optimized structures with the X-ray data. [1]

---

[1] The offset in enumeration of amino acid residues between [NiFe] hydrogenases from *D. gigas* and *D. vulgaris* is +16 residues but in the following only the *D. gigas* enumeration of amino acid residues will be used for reasons of consistency.

In the calculations the Ni $\cdots$ Fe distance is larger when a sulphuric species occupies the bridging position (3.22 Å for S^{2-} and 2.96 for O^{2-}). The same holds for a protonated bridging ligand (3.19 Å for SH^- and 3.05 Å for OH^-). The angle between Ni, the bridging cysteines Cys533 and Cys68 and the Fe is about 7-8° larger with a sulphur atom. The Ni $\cdots$ X and Fe $\cdots$ X distances react most drastically upon sulphur substitution. The distances increase by as much as 0.4 Å when a sulphur is in the bridging position. The increase in bond length between the metal and the bridging atom is partly compensated by a decrease of the Ni–X–Fe bond angle from 102.1° (96.8°) for O^{2-} (OH^-) to 87.3° (83.5°) for S^{2-} (SH^-). The overall increase of the Ni $\cdots$ Fe distance is modest with 0.26 Å (O^{2-} vs. S^{2-}). The metal-cysteine bond lengths are almost independent of the nature of the bridging ligand (see Table **5.1**). Slightly larger values are obtained for a doubly negatively charged bridge (e.g. O^{2-} and S^{2-}) than for singly negatively charged bridges (OH^- and SH^-). The excess negative charge of the bridging ligand X leads to a weakening of the Ni–S and Fe–S bonds, i.e. an elongation of the metal–S bonds. This indicates a charge transfer from the Ni–X (X = sulphur or oxygen species) towards all coordinating four sulphur atoms of the cysteine residues.

The optimized geometries for the four different bridging ligands are compared with the experimental geometrical data obtained from the X-ray structure analysis in Table **5.1**. The best agreement between the calculated structures and those from X-ray crystallography is obtained for the structure of *D. gigas* [27] and an oxygenic species, O^{2-} or OH^-, occupying the position of the bridging ligand. The differences between calculated bond lengths and those from X-ray coordinates are at most 0.1-0.2 Å and thus within the range of error of the X-ray structure coordinates. Bond angles agree within 2-4° (see Table **5.1**). In particular the Ni$\cdots$X, Fe$\cdots$X, Ni$\cdots$Fe bond lengths and Ni–SCys(bridging)–Fe bond angles agree favourably with the data from *D. gigas*. A discrimination between either an OH^- or an O^{2-} bridge can, however, not be made on the basis of structural parameters alone. This can be derived from features of the electronic structure (see below).

According to the calculations a sulphur bridging ligand would lead to Ni$\cdots$Fe distances of 3.22 Å (S^{2-}) and 3.19 Å (SH^-) which does not agree with the heavy atom distance of 2.55 Å in the crystal structure from *D. vulgaris* [28] (see Table **5.1**). Considering a bond length error of 0.2 Å for the X-ray structure at 1.8 Å resolution, the deviation is clearly outside the range of error. The discrepancy between calculated structural parameters and those from the X-ray analysis is most striking for parameters associated with the sulphur bridging ligand (Ni$\cdots$X, Fe$\cdots$X bond lengths, $\angle$ Ni-X-Fe bond angle, see Table **5.1**). Ni–SCys and Fe–SCys bond lengths are well reproduced, but these are nearly independent of the nature of the bridging ligand. The deviation between calculated and measured Ni–Cys–Fe bond angles is about 15°.

To conclude, BLYP/DZVP calculations are able to describe the structural parameters of the active centre of [NiFe] hydrogenase from *D. gigas* quite accurately. The cluster model chosen in the calculation can therefore be used for elucidation of the electronic structure of the active centre and a comparison with experimental data.

5.3.2 Electronic Structure of the Oxidized States

The spin density distribution of a molecule embedded in a protein environment is obtained from the measured and assigned hyperfine coupling constants which are available from EPR and ENDOR spectroscopy [66]. In particular, the isotropic hyperfine coupling constants are directly proportional to the spin density at the nucleus whereas the anisotropic part is related to the spin density in non-spherically symmetric orbitals.

The observation of large hyperfine splittings in EPR spectra from ^{61}Ni (I=3/2) labelled hydrogenases [45,59] the Ni atom has been recognized to bear the largest part of the unpaired spin density. Furthermore, EPR of ^{33}S substituted hydrogenase showed that *one* sulphur atom has a large hyperfine splitting [62]. This indicates that spin delocalization occurs predominantly onto one sulphur, probably from a cysteine residue ligated to the Ni atom. Experiments on ^{57}Fe enriched hydrogenase showed virtually no line broadening in the EPR spectra. ^{57}Fe-ENDOR experiments revealed a small hyperfine interaction of $\approx$ 1 MHz in Ni-A, whereas for Ni-B and Ni-C no coupling was detectable [61]. This indicates that the Fe remains in a S = 0 (Fe(II) low spin) state in all paramagnetic intermediates of the enzyme. The low spin state of the iron was also confirmed by Mössbauer spectroscopy [180].

When Ni-C is reoxidized with $^{17}O_2$, a line broadening is observed in samples of Ni-B (increase in line width of 0.0, 0.4, 0.7 mT for the g_x, g_y and g_z components, respectively) and of Ni-A (increase by 0.5, 0.5, 0.55 mT at g_x, g_y, g_z, respectively) [63]. This implies that an oxygen species binds in the vicinity of the Ni atom and that a small amount of unpaired spin density is transfered to this oxygen. It has been discussed that this oxygen occupies the bridging position between the Ni and Fe [171]. This cannot explicitly exclude the possibility of a sulphur atom as a bridging ligand in a different organism and/or spin state.

The existence of a sulphur bridging ligand was supported by the reported release of H_2S [172] upon reduction of the *D. vulgaris* Miyazaki F enzyme and the simultaneous removal of the bridging ligand. There are, at present, no further magnetic resonance data which might support or contradict this hypothesis.

A reliable model of the active site of oxidized [NiFe] hydrogenase must be able to reproduce all of the above mentioned experimental findings. This strict condition could not be fulfilled by any of the theoretical studies so far [71, 72, 74–76]. Clearly, Ni and S must bear the largest part of the unpaired spin density because they are the only nuclei leading to large hyperfine splittings in EPR and ENDOR spectra. The spin density at the Fe atom can only be estimated to be very small. [2]

Table **5.2** gives calculated atomic spin populations for the four different bridging ligands investigated. The spin population at the nickel atom is nearly independent of the bridging ligand (0.52 for O^{2-}, OH^- and SH^- , 0.56 in the case of S^{2-}) and is in agreement with the experimental finding of ^{61}Ni hyperfine splitting. The insensitivity of the Ni spin density to the type of bridging ligand (OH^- or O^{2-}) is in agreement with the experimental finding that the electron density at the Ni remains unchanged between Ni-A and Ni-B [181].

The spin population at the Fe atom is small and negative. The negative sign may be due to spin polarization effects of spin density from the nickel via the bridge to the Fe site. When a singly negatively charged bridge (OH^-, SH^-) is present the spin population is only -0.002; it is about a factor of ten larger (-0.02) when a doubly negatively charge bridge (O^{2-}, S^{2-}) is present. This small spin population is in good agreement with the results from ^{57}Fe-ENDOR studies [61]. In Ni-B no ^{57}Fe-ENDOR effect is observed, whereas Ni-A gives a small but detectable hyperfine interaction of $\approx$ 1 MHz. Thus, it is proposed that Ni-B is associated with either OH^- or SH^- leading to a vanishing spin density at the Fe site. Ni-A might possess either an O^{2-} or S^{2-} as bridging ligand which might give rise to a small hyperfine interaction.

When going from a singly to a doubly negatively charged bridging ligand, the spin population at the Cys533 sulphur atom is reduced (from 0.34 for OH^- to 0.24 for O^{2-} and from 0.33 for SH^- to 0.28 for S^{2-}, see Table **5.2**). Since no complete hyperfine tensors for ^{33}S are available for the two forms Ni-A and Ni-B, neighbouring β-CH_2 protons of the cysteine amino acid can be used to probe the magnitude of the spin density at the sulphur atom itself. The reduction of atomic spin density at the sulphur of Cys533 is in agreement with the decrease of isotropic hyperfine couplings by about 2-3 MHz of the β-CH_2 protons of that cysteine residue [182]. In addition, the spin density at the terminal cysteine Cys530 is reduced by a factor of two (from 0.06 in Ni-B to 0.03 in Ni-A, see Table **5.2**).

The atomic spin populations presented here were used in the analysis of the deviation of the anisotropic hyperfine tensors from axiality of the two β-CH_2 from Cys533 in the Ni-B state [169]. The

---

[2] The atomic spin populations are usually derived from experimentally determined hyperfine couplings by relating them to the values expected for a free ion from Morton and Preston [159]. The situation is complicated due to the fact that the sign of the hyperfine splittings is not known. One thus has to make a plausible choice of signs of the hyperfine splitting and *a priori* assume an atomic ground state and a specific orbital occupancy. The situation is hopeless for heavy atoms where spin-orbit coupling significantly contributes to the hyperfine interaction, i.e. Ni, Fe and S.

experimentally obtained anisotropic hyperfine tensors could be explained by a coupling of the protons to the adjacent sulphur atom with an atomic spin population of ≈ 0.3 and to the central nickel atom with ≈ 0.5.

Table 5.2: BLYP/DZVP calculated atomic spin populations for oxidized [NiFe] hydrogenase

Nucleus					De Gioia *et al.* Ni-B [74]	Amara *et al.* Ni-A [76]
X =	O^{2-}	OH^-	S^{2-}	SH^-	empty	O^{2-}
(Ni)	0.52	0.52	0.56	0.52	0.43	1.17
(Fe)	-0.02	-0.002	-0.02	-0.002	0.19	-0.12
(S_{Cys533})	0.24	0.34	0.28	0.33	0.006/-0.003[a]	0.19
(S_{Cys530})	0.03	0.06	0.03	0.06	0.172/0.217[a]	0.07
(X)	0.18	0.003	0.08	0.02	/	-0.48

[a] No assignment to a specific cysteine is made. They are only classified as bridging or terminal cysteines.

The recent theoretical work by Pavlov *et al.* [71, 72] has focused on the activation process of [NiFe] hydrogenase. However, in their work the enzyme's paramagnetic states were not accurately described, i.e. structural parameters and atomic spin populations for Ni-A or Ni-B were not given. Thus, these data cannot be compared with the results in this chapter. De Gioia *et al.* [74] were the first to attempt a description of the paramagnetic states of oxidized [NiFe] hydrogenase. Ni-A was not considered but atomic spin populations for Ni-B were given. Their values are included in Table **5.2**. De Gioia *et al.* do not place a bridging ligand between the Ni and Fe atoms. The spin population at the Ni (0.43) is only slightly smaller than the result here (0.52). The spin population at the Fe is, however, too large and in clear disagreement with the ^{57}Fe-ENDOR results.

Calculations on a cluster model with an *empty* bridging position yield a spin density distribution which is not in agreement with the measured g-tensor orientation and ^{1}H-ENDOR results (see below). In this bonding situation, the sulphur atoms of the terminally bound cysteine amino acids (Cys65 and 530) would bear a significant amount of unpaired spin population (0.23 and 0.20, respectively). These results also do not agree with the finding that the spin is localized along the Ni–SCys533 bond. Furthermore, the calculated Ni $\cdots$ Fe distance of 3.10 Å is not in good agreement with the one from the X-ray crystallographic analysis (see above). Such a model can therefore be ruled out for the oxidized states of [NiFe] hydrogenases. [3]

---

[3] BLYP calculations also rule out a water molecule as bridging ligand. The calculated Ni$\cdots$Fe distance is 3.25 Å and the

Figure **5.2** summarizes the findings for the Ni-B state. The figure (top) displays the calculated atomic spin populations which are in good agreement with the data derived from EPR and ENDOR spectroscopy. The lower figure shows a contour plot of the spatial spin density distribution in Ni-B. The spin density is oriented along the Ni–S(Cys533) bond, as was also found in single crystal EPR studies [179, 183]. This also explains the large isotropic hyperfine interactions of β-CH_2 protons of the cysteine Cys533 observed in pulsed-ENDOR investigations of protein single crystals [184] and orientation-selected cw-ENDOR of frozen solution of *A. vinosum* [169] in the Ni-B state. The calculated isotropic hyperfine coupling constant for the two protons β-$CH_{1,2}$ from the bridging cysteine Cys533 are 10.1 and 10.5 MHz, respectively, and compare well the experimental ones of 12.5 MHz for these protons [169].

Figure **5.3** shows the unpaired spin density distribution at a contour value of 0.005 e/a_0^3 when there is a μ-oxo bridge between the Ni and Fe atoms. This is a model for the Ni-A state. Amara *et al.* recently also suggested a Ni-A state with a μ-oxo bridging ligand based on the X-ray structure of the [NiFe] hydrogenase from *D. gigas* [76] (see Table **5.2**). Their B3LYP/ECP QM/MM calculation for the Ni-A form suffered from a major spin-contamination ($< S^2 >$ = 1.37 vs. a theoretical value of 0.75 for a S= 1/2 state). The given high spin population at the Ni of 1.17 (see Table **5.2**) therefore seems unrealistic. The BLYP/DZVP calculations presented in this chapter do not exhibit such a high spin-contamination (see Computational Details). The results by Amara *et al.* agree with the data presented here that the unpaired spin density in the Ni-A form is primarily on the Ni and SCys533 atoms. Furthermore, Amara *et al.* also found that the bridging ligand O^{2-} in the Ni-A state may acquire a significant amount of spin density. They report a spin population of -0.48 for the μ-oxo bridge for their S = 1/2 solution with high spin contamination. This large value seems questionable. The μ-oxo bridge in the BLYP/DZVP calculations exhibits a smaller spin population of 0.18 which appears more realistic when experimental findings are considered [63]. In the work by Amara *et al.*, the magnitude of spin population at the Fe is also large (see Table **5.2**).

5.3.3 Structural Parameters for the Reduced Enzyme (Ni-C)

The recent X-ray structure analysis of [NiFe] hydrogenase crystallized under H_2 atmosphere [174] indicated a vacant bridging position between the Ni and Fe atoms. In the case of the Ni-C state the place of the bridging ligand may be taken by a hydride species and not be detectable by X-ray crystallography [34]. This assumption was here investigated by further DFT BLYP/DZVP calculations.

---

water molecule is only loosely coordinated to the Ni (at a distance of 3.23 Å) and the Fe (at a distance of 2.27 Å). The spin populations are (Ni) = 0.45, (Fe) = 0.02 and nearly equal on the terminal cysteines (SCys65) = 0.22 and (SCys530) = 0.20. This is not in agreement with experimental findings.

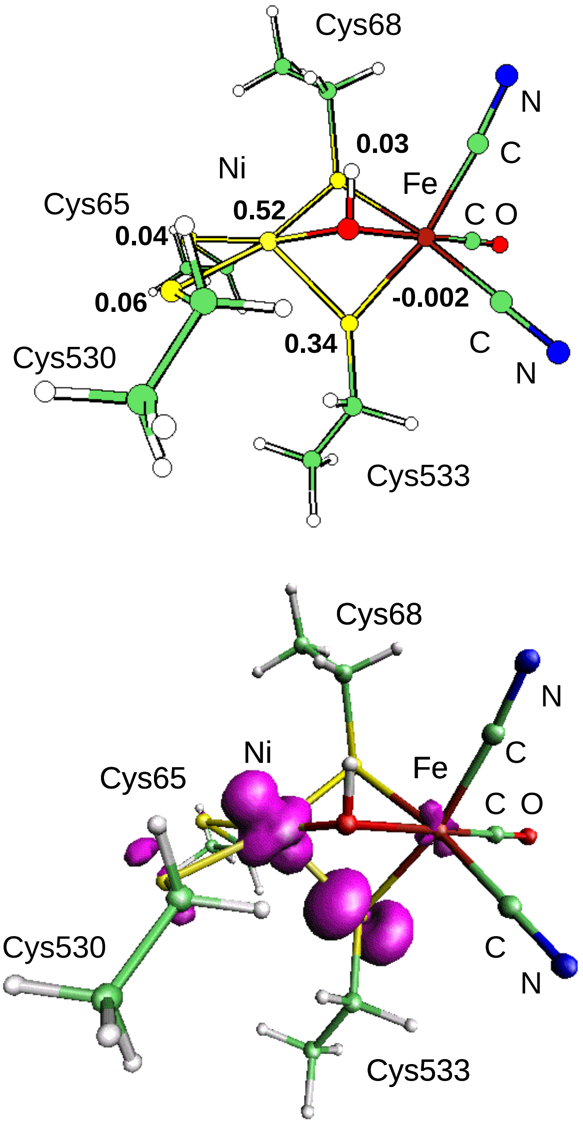

Figure 5.2: Top: BLYP/DZVP calculated Mulliken spin populations for the active centre of [NiFe] hydrogenase in the Ni-B state. Bottom: BLYP/DZVP contour plot at 0.005 e/a$_0^3$ of the unpaired spin density distribution

Table **5.3** compares selected structural parameters of the reduced enzyme from the X-ray structure [174] with those obtained from DFT BLYP/DZVP calculations where a hydride ion bridges Ni and Fe and the position of the bridging ligand is vacant. The results from X-ray analysis of the reduced [NiFeSe] hydrogenase from *Desulfomicrobium baculatum* [185] are also included in Table **5.3**. The [NiFeSe] hydrogenase contains a selenocysteine in the position of the Cys530 in *D. gigas* and the bond distance to

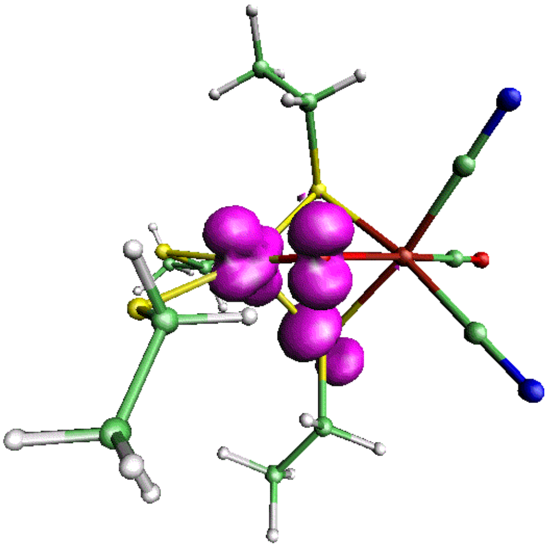

Figure 5.3: BLYP/DZVP calculated spin density distribution in the Ni-A state at a contour value of 0.005e/a_0^3

this residue is elongated because of the larger van der Waals radius of selenium compared to sulphur. A vacant position of the bridging ligand can be ruled out since the Ni$\cdots$Fe distance is too large by 0.5 Å in the calculations.

The calculated structural parameters agree very well with those from the high-resolution (1.4 Å) X-ray structure of *D. vulgaris* [174] and *D. baculatum* [185] when a hydride ion occupies the bridging position. The agreement in bond lengths and angles is better for the reduced state than for the oxidized states which is probably due to the higher resolution of the X-ray analysis in the reduced enzyme. There is less heterogeneity in the reduced state. The oxidation state of the active Ni-Fe cluster in the reduced crystals, however, could not be determined yet. It thus remains not clear whether the paramagnetic state Ni-C or the completely reduced state Ni-R is present in the crystal. When a further electron is added to the model for the Ni-C state, and a diamagnetic, closed-shell cluster is obtained, the structural parameters do not change significantly (less than 0.01 Å in bond distances). This may be a model for the Ni-R state which structurally would be very similar to the Ni-C form.

The Ni $\cdots$ Fe distance is 2.60 Å in the crystal structure of the reduced [NiFe] hydrogenase from *D. vulgaris* and hardly differs from that in the oxidized form (2.55 Å). In contrast, the calculations suggest that the heavy atom distance shortens by approximately 0.4-0.5 Å upon replacement of the bridging ligand (O or S) by a hydride ion (cf. Tables **5.1** and **5.3**). One reason for this discrepancy between experiment and calculation may be that the oxidation state for which the X-ray structure of the oxidized

Table 5.3: Comparison of selected structural parameters from X-ray and BLYP/DZVP optimized structures of the reduced active centre of [NiFe] hydrogenase. Bond lengths (r) in Å, bond angles (∠) in degrees.

	Exp.		Calc.	
	D. vulgaris	*D. baculatum*[a]		
distances/angles	[174]	[185]	X=H$^-$	empty
Ni · · · Fe	2.60	2.53	2.67	3.10
Ni–SCys533	2.45	2.62	2.43	2.23
Ni–SCys68	2.37	2.33	2.35	2.28
Ni–SCys530	2.21	2.46[a]	2.27	2.22
Ni–SCys65	2.30	2.25	2.31	2.24
Ni · · · X	/	/	1.69	/
Fe–SCys533	2.34	2.37	2.44	2.33
Fe–SCys68	2.29	2.29	2.39	2.36
Fe · · · X	/	/	1.73	/
∠ Ni-X-Fe	/	/	106.3	/
∠ Ni-SCys533-Fe	65.7	60.7	66.5	85.4
∠ Ni-SCys68-Fe	67.8	66.5	68.7	83.6

[a] Note that the [NiFeSe] hydrogenase from *Desulfomicrobium baculatum* contains a selenocysteine at the position 530. This explains the large bond length to this residue.

form was solved predominantly corresponds to a different, e.g. Ni-Si, species.

5.3.4 Electronic Structure of the Reduced Enzyme (Ni-C)

The calculated spin populations for the situation where either a hydride ion occupies the position of the bridging ligand or it is empty are given in Table **5.4**. For the reduced Ni-C state, less experimental data are available than for the oxidized states. The hyperfine tensors of ^{61}Ni or ^{33}S were not fully obtained; the absence of a ^{57}Fe ENDOR effect [61], shows that the Fe is kept in its Fe(II) low spin state. The calculations show that only 1% of the unpaired spin resides on the Fe atom when the two metal are μ-hydrido bridged and 3% when the bridge is absent. Furthermore, the calculations show that the spin density distribution does not drastically change in Ni-C when a hydride occupies the bridging position (compare Tables **5.2** and **5.4**). The situation where the bridging position is empty appears unrealistic.

Table 5.4: BLYP/DZVP calculated atomic spin populations for reduced [NiFe] Hydrogenase

Nucleus			De Gioia *et al.*	Pavlov[b] *et al.*	Amara *et al.*
	X=H$^-$	empty	Ni-C [74]	Ni-C [72]	Ni-C [76]
(Ni)	0.51	0.41	0.53	1.39	0.90
(Fe)	0.01	0.03	0.08	0.14	0.03
(S$_{Cys533}$)	0.29	0.05	0.14/0.14 [a]	0.00	0.00
(S$_{Cys530}$)	0.10	0.20	0.001/0.19 [a]	0.69	0.02

[a] No assignment to a specific cysteine is made. They are only classified as bridging or terminal cysteines.

[b] The calculations by Pavlov *et al.* were done on a S = 3/2 state.

It would be associated with a redistribution of spin density from the bridging cysteine Cys533 in the oxidized states to the terminal cysteine Cys530 in the reduced state (compare Tables **5.2** and **5.4**). In addition, such a bonding situation could not explain the large, D_2O-exchangeable ^{1}H-ENDOR coupling in the Ni-C state [69, 70].

When a hydride ion bridges the Ni and Fe atoms, the largest part of the unpaired spin density still resides along the Ni–SCys533 bond as also found in the oxidized states. Figure **5.4** shows a plot of the unpaired spin density at a contour value of 0.005 e/a_0^3. The spin population at the sulphur atom of the bridging cysteine Cys533 is slightly reduced from 0.34 in Ni-B (X=OH$^-$) to 0.29 in Ni-C (X=H$^-$). The sulphur atom of the terminal cysteine Cys530 acquires 10% of the spin which may lead to small additional hyperfine splittings of the β-CH_2 protons in ENDOR.

In X-ray absorption spectroscopy (XAS) experiments it was found that the electron density at the Ni atom does only slightly change between Ni-A/Ni-B/Ni-C [186]. In this work, it was concluded that the Ni atom would not the redox active metal. This is in agreement with the finding that the atomic spin population at the Ni remains nearly constant (Ni-A/B 0.52, Ni-C 0.51). The conclusion [186] that Ni is not the redox active metal, however, is not quite correct.

Results for the proposed Ni-C were also obtained from earlier calculations [72, 74, 76] (Table **5.4**). In the work by De Gioia *et al.* [74], the presence of a μ-hydrido ligand leads to a decrease of atomic spin population at the Fe from 0.19 (no bridge in Ni-B) to 0.08 (Ni-C). Pavlov *et al.* also reported an atomic spin population at the Fe of 0.08 in Ni-C (bearing in mind their S= 3/2 ground state this comes close to the experimental value) [72]. Amara *et al.* suggested a μ-hydrido bridge and a protonated

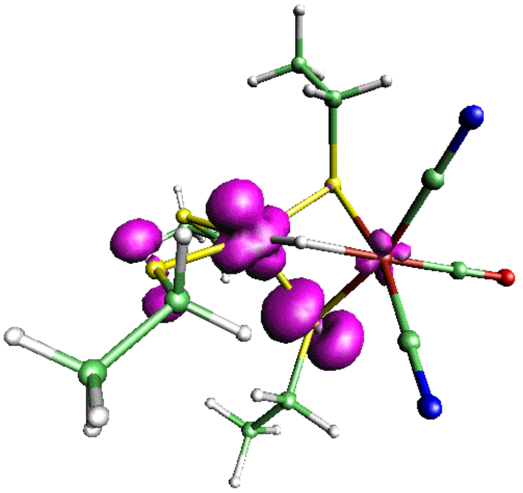

Figure 5.4: BLYP/DZVP calculated spin density distribution in Ni-C at a contour value of 0.005 e/a_0^3.

cysteine Cys530 [76]. This explains the vanishing spin population on the sulphur nucleus of that cysteine amino acid in their calculations (see Table **5.4**). Their results also agree with the findings here that the spin population at the Fe atom is small. In their work, however, the spin density is almost exclusively localized at the Ni nucleus. This cannot explain the large hyperfine couplings of β-CH_2 protons in the Ni-C state [69, 70] and the similar ^{61}Ni hyperfine couplings in the Ni-B and Ni-C states [45].

The BLYP/DZVP calculated isotropic ^{1}H hyperfine splittings of the β-CH_2 protons from Cys533 are 8.0 and 8.3 MHZ, respectively, which agree well with the experimental values [69, 70]. The calculated ^{1}H isotropic hyperfine interaction for a Ni–μ-hydrido–Fe bridge is -8.5 MHz and in good agreement with the experimental value of -11 MHz for the solvent-exchangeable proton in the Ni-C state [69]. It was argued that the sign is negative due to a hydride directly bound to the Ni atom in the nodal plane of a d_{z^2} orbital. The isotropic hyperfine coupling may arise from a $3d_{z^2} \rightarrow 3d_{x^2-y^2}$ spin polarization [69].

In the model suggested for the Ni-C form, Ni is still in its formal Ni(III) oxidation state. Possibly, a reduction takes place in the ligand sphere for which the bridging ligand is a potential candidate.

5.3.5 Influence of the Small Ligands at the Iron on the Electronic Structure

In *D. vulgaris* Miyazaki F the diatomic ligands to the Fe were initially assigned to two CO and one SO molecule in the X-ray structure [28]. These ligands, however, cannot explain the IR vibrations detected above 2000 cm^{-1} which are characteristic for CN stretching vibrations. They were also observed for

D. vulgaris so at least one CN must be present (Y. Higuchi, K. Bagley, personal communication). The model of the oxidized *D. vulgaris* Miyazaki F enzyme chosen here incorporates one CO, one CN and one SO ligand as prosthetic group to the Fe. Although a sulphur species was postulated in this enzyme [28] to constitute the bridging ligand a OH^- instead of SH^-/S2$-$ was chosen. The spin density distribution is rather independent of the nature of the bridge.

The calculated spin density distribution (Figure **5.5**) is remarkably different from the *D. gigas* model. The terminal SO withdraws spin density from SCys533 and leads to a spin population at the Fe of -0.08. In this case, atomic spin populations are (Ni) = 0.44, (Fe) = -0.08, (SCys533) = 0.24, (SCys530) = 0.01, ($\underline{\mathrm{S}}$O) = 0.16, (S$\underline{\mathrm{O}}$) = 0.11. The calculations cannot positively rule out a terminal SO ligand. Its influence on the spin density distribution, however, makes it an unlikely candidate for a non-protein ligand in [NiFe] hydrogenase. The issue should easily be clarified by FTIR experiments.

D. gigas and *D. vulgaris* have very similar hyperfine interactions and g-factors. If *D. vulgaris* would have SO instead of CN one would expect, according to the calculations, $\geq$ 25 % of the spin population at the SO ligand, and a reduction of the same amount at the other positions (Ni, S). Furthermore, a deviation of the g-tensor principal values would be expected. Since this is not observed in the experiments, a SO ligand seems to be unlikely – although it cannot be completely ruled out because no direct hyperfine coupling for ^{33}SO or S^{17}O have been measured (^{32}S^{16}O contains no magnetic isotope and shows no hyperfine splittings).

5.4 Summary and Conclusion

DFT calculations of the heterobimetallic centre of [NiFe] hydrogenases yielded structural parameters, atomic spin populations and spin density distributions that are in good agreement with the existing related experimental data for the paramagnetic states Ni-A/Ni-B/Ni-C. The differences between the paramagnetic states can be primarily attributed to a modification of the bridging ligand.

With regard to the so far unassigned bridging ligand X, a OH^- ligand in the case of Ni-B and a O^{2-} in the case of Ni-A seem to be plausible. Ni-B would be described as a Ni(III)-μOH-Fe(II) and Ni-A as a Ni(III)-μO-Fe(II) system. A bulkier sulphur SH or S^{2-} species are unlikely since they would lead to a significant elongation of the Ni $\cdots$ Fe distances. The calculated spin density distribution is in agreement with the experimentally determined g-tensor orientation in the Ni-A and Ni-B forms. A vacant bridging position would lead to a spin density distribution which is not in agreement with experimental findings. When the bridge is occupied by an OH^- ligand, the calculated isotropic hyperfine couplings of the β-CH_2 protons of cysteine Cys533 agree well with available experimental data.

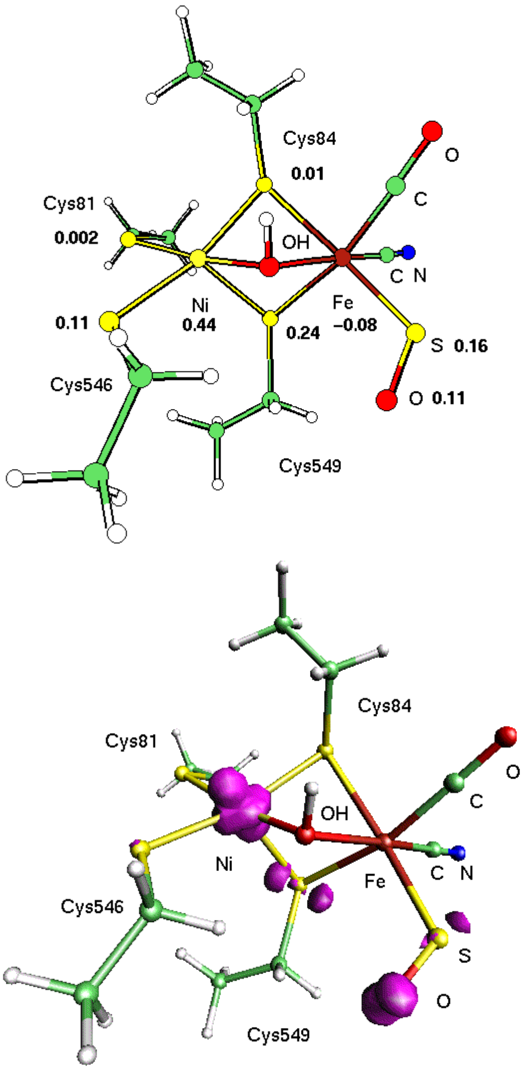

Figure 5.5: Top: BLYP/DZVP calculated Mulliken spin populations for the active centre of [NiFe] hydrogenase from *D. vulgaris* (1 CO, 1 CN, 1 SO ligand) in the Ni-B state (OH^- bridging ligand).
Bottom: BLYP/DZVP contour plot at 0.005 e/a_0^3 of the unpaired spin density distribution in the Ni-B state.

The replacement of the bridging ligand in the oxidized states (O^{2-} and OH^-) by a hydride ion in the reduced Ni-C state leads to a decrease of the Ni· · ·Fe distance by 0.4 Å. The Fe(II) is kept in its low spin state in all intermediates. The calculated isotropic hyperfine interaction for the hydride ion is in good agreement with the respective experimental value.

As to the nature of the non-protein diatomic ligands of the Fe atom, the proposed 2 CN and 1 CO ligands appear most realistic. A terminal SO ligand would act as a sink of spin density and lead to *g*-

values and spin density distribution which is not in agreement with experimental findings. The detection of H_2S upon reduction of the hydrogenase from *D. vulgaris* Miyazaki F [172] may still originate from a degradation product of the cysteine amino acids which coordinate the active centre or one of the Fe-S clusters.

When a possible mechanism is discussed, experimental findings must be taken into account. It is known that bridging ligand is liberated upon reduction and might possibly take up the proton from the heterolytic dissociation of H_2. The difference between Ni-A and Ni-B (O^{2-} vs. OH^- bridging ligand) might reflect their different kinetics upon reductive activation. An OH^- would be easier to activate and liberate than an O^{2-} ligand.

Now that an understanding of the atomic composition of the active centre in the Ni-A, Ni-B and Ni-C states evolves, the *first principles* calculation of magnetic resonance parameters from a Kohn-Sham wavefunction and the comparison with experimental data is required.

Chapter 6

ENDOR Crystallography of the Oxidized States

6.1 Introduction

The ‘as-isolated’, oxidized [NiFe] hydrogenase is a mixture of two paramagnetic states Ni-A and Ni-B. From the similarities of the g-values of Ni-A (2.32, 2.24, 2.01) and Ni-B (2.33, 2.16. 2.01) a drastic change in the electronic structure in the Ni-A state compared to Ni-B can be ruled out. The two, however, differ in their rates of activation. Ni-B (or ‘ready’) is reduced within minutes under an H_2 atmosphere while Ni-A (or ‘unready’) requires incubation for several hours.

Details of the structure of the active centre of [NiFe] hydrogenase have been revealed by X-ray structure analysis of protein single crystals [28,32,36]. Figure **6.1** displays the active centre of the [NiFe] hydrogenase from *Desulfovibrio vulgaris* Miyazaki F. The Ni atom is coordinated by four cysteinyl sulphur atoms (Cys80, 84, 546, and 549), two of which (Cys84 and Cys549) form a bridge to the Fe atom. In addition, three electron density peaks in the vicinity of the Fe were observed. They were identified by FTIR measurements to be 2 CN^- and one CO ligand in *D. gigas* and *A. vinosum* [27,51]. An unidentified electron density peak ‘X’ between the Ni and Fe atoms of the active centre was tentatively assigned to an oxygenic species in *D. gigas* and to a sulphur atom in *D. vulgaris.* In the hydrogenase from *D. vulgaris*, the diatomic ligands of the Fe have been modeled as 1 CO, 1 CN^- or CO and one SO ligands (due to a larger electron density) [28]. The symmetry of the ligand sphere of the Ni is close to square-pyramidal and that of the Fe is close to octahedral.

The coordination of the active centre in the two oxidized states is similar (the crystallized [NiFe] hydrogenase from *D. gigas* is predominantly in the Ni-A state [27], that of *D. vulgaris* Miyazaki F in

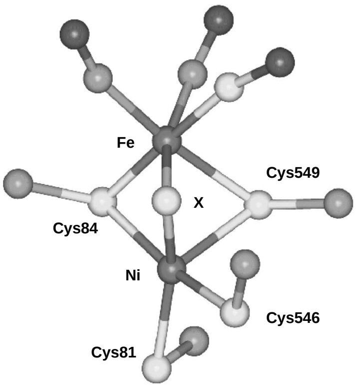

Figure 6.1: Details of the active centre of the [NiFe] hydrogenase from *D. vulgaris* Miyazaki F [28].

the Ni-B state [28]). One difference between the two forms may lie in their proton environment - a modification of which would not be detectable by X-ray crystallography.

In hydrogenases and other transition-metal containing enzymes, the large EPR linewidth prevents the detection of proton hyperfine splittings. Thus Electron Nuclear Double Resonance (ENDOR) spectroscopy must be used to obtain further information about the interaction of the unpaired electron with nuclear spins, In frozen solution, the determination of complete hyperfine coupling tensors **A** is possible by stepping the magnetic field over the range of EPR absorption, i.e. taking advantage of the orientational dependence of the molecules with respect to the magnetic field [187–189]. The analysis of orientation-selected ENDOR spectra in frozen solution is difficult and sometimes it is not possible to follow hyperfine interactions over the complete EPR envelope. Recently, an orientation-selected ENDOR study of the Ni-B state of the [NiFe] hydrogenase from *A. vinosum* has been published and three hyperfine tensors were reported [169]. Earlier ENDOR investigations of the active site of [NiFe] hydrogenases have been limited to one or a few field positions only and were primarily concerned with the Ni-C state [69, 70]. No hyperfine tensors were given and no spatial assignment to protons in the active centre was done since no information about the ligand environment was available at that time.

A challenging alternative to the investigation of proteins in frozen solution (powder) is the EPR and ENDOR study of protein single crystal if these are available. The g- and hyperfine tensor magnitudes *and* orientations can independently be obtained. EPR investigations of single crystals of *D. vulgaris* Miyazaki F hydrogenase [179, 190] have recently revealed the orientation of the principal g-tensor axes in the crystal for Ni-A and Ni-B. It was shown that the structure of the active site remained unaffected by freezing the protein single crystal and the orientation of the g-tensor persisted [190]. The ENDOR investigation of protein single crystals of the [NiFe] hydrogenase will reveal isotropic, anisotropic hyperfine contributions and *spatial* information about the unpaired spin density distribution in the ligand environment of the active centre. Both continuous wave (cw) and pulsed-ENDOR can, in principle, be used.

Pulsed-ENDOR has the advantage of being essentially free from the restrictions of balancing relaxation and induced transition rates [83, 191]. To the best knowledge, there is only one application of pulsed-ENDOR spectroscopy to protein single crystals in the literature so far [192].

Of the two common pulse sequences of pulsed-ENDOR (Mims- [193] and Davies-ENDOR [194]), Davies-ENDOR provides a ”blind-spot”-free determination of nuclear spin-electron spin interactions. Doan *et al.* [195] showed that Mims-ENDOR is most useful for observing nuclei with hyperfine interactions smaller than 5 MHz while Davies-ENDOR is more sensitive to larger couplings. In the catalytic cycle changes in the proton environment of [NiFe] hydrogenases are expected to be associated with large hyperfine interactions since the Ni atom is believed to be the catalytically active transition metal and either bind the substrate (H_2) or one of its dissociation products. A large hyperfine interaction with a hydrogen species is detected in the Ni-C state (approx. 20 MHz [70]). Thus Davies-ENDOR is the method of choice to investigate [NiFe] hydrogenases. Here, results of pulsed-ENDOR spectroscopy of single crystals of the oxidized enzyme in the ‘ready’ Ni-B and ‘unready’ Ni-A states are presented. The enzyme is characterized prior to catalytic activity and subsequent comparative investigations on the reduced form may reveal changes in the proton environment and contribute to the understanding of the reaction mechanism of the enzyme. Since protons are usually not detectable in the X-ray structures of proteins, the detection of the position of protons in the active centre gives information which are not accessible by X-ray crystallography.

First principles, in particular Density Functional Theory (DFT), calculations can provide additional insight into the electronic structure of transition metal complexes [90, 101]. Evidence is here presented that the ground state of the unpaired spin distribution in the active centre of [NiFe] hydrogenase in the oxidized states can be described as a Ni $3d_{z^2}$ orbital overlapping with a sulphur p_π orbital to yield a delocalized $S = \frac{1}{2}$ state. A natural bond orbital (NBO) analysis yields mutually orthogonal atomic orbitals which are familiar to a chemist’s point of view. The resulting natural atomic orbitals (NAOs) recover the picture of a Lewis (valence bond) structure concept. The isotropic and anisotropic hyperfine tensors can be obtained directly from a DFT (Kohn-Sham) wavefunction. The isotropic hyperfine interaction is related to the value of the wavefunction at the nucleus, the anisotropic hyperfine interaction is obtained by integrating over the spatial distribution of the spin density. This is the first application to systems as complex as the active centre of a transition metal enzyme and supports the assignment of experimental proton hyperfine tensors in the Ni-A and Ni-B oxidation states.

6.2 Materials and Methods

6.2.1 Protein Purification and Crystal Mounting

The membrane-bound hydrogenase from *D. vulgaris* Miyazaki F was isolated and purified according to the published procedure [37]. By means of vapour diffusion, orthorhombic single crystals belonging to space group $P2_12_12_1$ with four sites in the unit cell could be obtained which diffracted to more than 2.5 Å. Recently, an X-ray structure at 1.8 Å resolution was published and revealed details of the active site and its protein environment [28]. Protein single crystals of the approximate dimensions 1 mm × 0.5 mm × 0.5 mm were transfered to a Wilmad $\leq$ 4 mm o.d. quartz EPR tube in a sealed quartz container [196]. Care was taken to avoid an orientation along one of the crystal axes.

6.2.2 Computational Details

Geometry optimizations were performed with DGauss4.0 [175] on a Cray T3E supercomputer using up to 128 processors. The DFT-optimized DZVP basis set of Godbout *et al.* [176] was applied. This basis set was already successfully applied to the description of the electronic structure of blue-copper proteins [177]. The Becke exchange functional and the Lee-Yang-Parr gradient-corrected correlation functionals were used (BLYP) [92]. The recently developed HCTH functional [94] (also a 'pure', non-hybrid functional) was shown to yield improved energetics for reaction barriers and significantly improved geometries for transition metal compounds compared to the BLYP functional. The HCTH functional was also used to validate the sensitivity of the results with respect to the optimized structures. Starting from the X-ray structure, 42 and 41 atom cluster models (Ni-B and Ni-A, respectively) were completely geometry optimized imposing no constraints on the structure. Cysteinyl amino acids were represented by ethanethiolate ($-S-CH_2-CH_3$) groups. At the BLYP/DZVP and HCTH/DZVP geometry, property analyses were done with Becke's three parameter hybrid functional (B3LYP [95, 96]) in the GAUSSIAN94 [165] suite of programs. A sufficiently large Pople-type basis set with added diffuse and two sets of polarization functions (6-311*G(2d,2p)) was used. Essentially, it is a Wachters-Hay all-electron basis set for first row transition metals [197, 198] using the scaling factors of Raghavachari and Trucks [199] and a McLean-Chandler [200, 201] basis set for second row atoms. The polarization functions are from [202]. This basis set was shown to yield accurate hyperfine parameters. Reviews of the calculation of hyperfine coupling parameters from DFT are given in [122–124]. The isotropic Fermi contact hyperfine interaction is related to the unpaired spin density at the corresponding nucleus by [78]

$$a_{iso}(N) = \frac{4\pi}{3} g_e \beta_e g_N \beta_N \langle S_z \rangle^{-1} \rho^s(r_N) \tag{6.1}$$

in which β_e is the Bohr magneton, β_N the nuclear magneton, g_e the free electron g-value and g_N the nuclear g-value and $\langle S_z \rangle$ is the expectation value of the z-component of the total electron spin. The spin density at the nucleus $\rho^s(r_N)$ can be expressed as

$$\rho^s(r_N) = \sum_{\mu,\nu} P^{\alpha-\beta}_{\mu,\nu} \langle \phi_\mu | \delta(r_N) | \phi_\nu \rangle \tag{6.2}$$

where r_N is the position of the nucleus, $P^{\alpha-\beta}_{\mu,\nu}$ is the spin density matrix. The formula for the anisotropic (dipolar) component is derived from the classical expression of two interacting dipoles [123]

$$A_{ij}(N) = \frac{1}{2} g_e \beta_e g_N \beta_N \langle S_z \rangle^{-1} \sum_{\mu,\nu} P^{\alpha-\beta}_{\mu,\nu} \langle \phi_\mu | r_{kN}^{-5} (r_{kN}^2 \delta_{i,j} - 3 r_{N,i} r_{N,j}) | \phi_\nu \rangle \tag{6.3}$$

where $r_{kN} = r - r_N$. The integration was performed following [122, 123]. The thus obtained hyperfine parameters are non-relativistic and of first-order only and may only be applied to ligand hyperfine interactions where second-order effects are expected to be small. A natural bond orbital (NBO) analysis [203, 204] was performed to derive atomic spin populations which are less sensitive to the choice of the basis set than Mulliken atomic spin populations. The transformation from the molecular basis set to the *minimal* atomic basis is done by a occupancy-weighted symmetric orthogonalization. The resulting natural atomic orbitals (NAOs) recover the picture of a familiar Lewis (valence bond) structure concept. The occupation numbers of core orbitals is close to two, that of non-participating orbitals close to zero while bonding orbitals have an occupation number close to unity. The electronic ground state was also derived from a NAO analysis.

6.2.3 EPR and ENDOR Setup

All experiments were performed on a Bruker ESP 380 E FT-EPR spectrometer [205] equipped with a dielectric ring cavity (ESP 380-1052 DLQ-H) and an Oxford cryostat (helium gas flow system).

One of the advantages of pulsed-ENDOR compared with cw-ENDOR is the fact that the length of the pulse sequence can be shorter than relaxation effects in the sample. Also, the ENDOR effect of pulsed experiments is much higher than that of continuous wave studies. In Davies-ENDOR the first soft π pulse (preparation) burns a hole with a width of $\omega_1 = \gamma_e B_1$ in the inhomogeneously broadened EPR

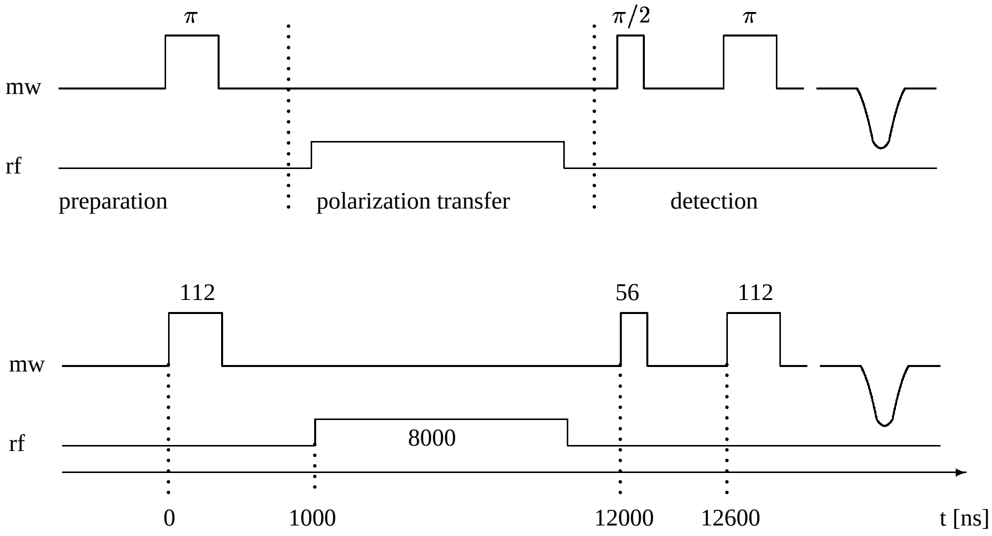

Figure 6.2: Davies-ENDOR.

line. The population of electronic sublevels is inverted with respect to an initial equilibrium state. When the (mixing) radio frequency (RF) pulse is in resonance with one of the NMR transitions, the population change of the electronic levels is detected as an increase of the echo amplitude. Davies-ENDOR signals in the frequency range ω_1 around the free nuclear Larmor frequency are suppressed. Mims-ENDOR provides higher sensitivity for small hyperfine interactions which are centred around the free nuclear frequency but suffers from the drawback of containing "blind-spots" for certain pulse distances τ. Mims thus can be considered as complementary to Davies type ENDOR. In the Davies-ENDOR experiment the separation between first and second microwave pulses was 12 μs, the width of the first π-pulse was 112 ns (see Figure **6.2**). The mixing radio frequency pulse was applied for 8 μs covering a range from 0.5-25.5 MHz. The echo was detected after a traditional Hahn-echo sequence ($\pi/2$—π pulses).

6.2.4 EPR Data Analysis

The analysis of EPR spectra of single crystals of the [NiFe] hydrogenase of *D. vulgaris* Miyazaki F has already been described elsewhere [179, 183, 196].

The transformation matrices between the three axes systems

L the laboratory axes system $(1, 2, 3)$

C the crystal axes system (a, b, c) with crystallographic axes a, b, c

I the intrinsic coordinate system (x, y, z) in which g and g^2 tensors are diagonalized to yield their principal values

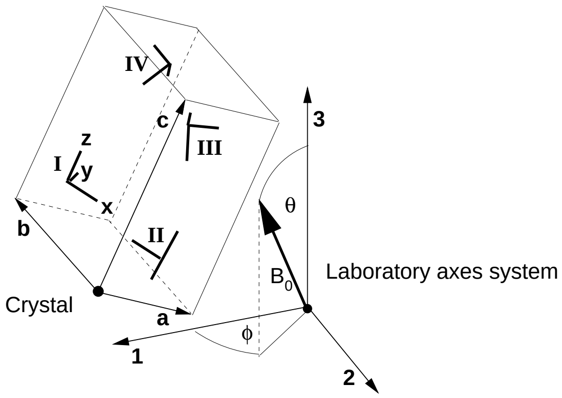

Figure 6.3: Definition of the laboratory axes system **L**, the crystal axes system **C** and the intrinsic coordinate system **I**.

have to be determined (see Figure **6.3**). $\mathbf{X}$ is the rotation matrix between the intrinsic coordinate axes system **I** and the crystal axes system $\mathbf{C}$. The columns of $\mathbf{X}$ then are the direction cosines of the g-tensor axes x, y, z with respect to the crystal axes a, b, c. The four sites in the unit cell of space group symmetry $P2_12_12_1$ are related by symmetry operations $\mathbf{R_i}$ (corresponding to 180° rotations around the crystal axes).

The relation between the diagonal g^2-tensor of one site ${}^{\mathbf{1}}\mathbf{G^2}$ and those of the four sites per unit cell is then

$$ {}^{\mathbf{C}}\mathbf{G^2} = \mathbf{R_i} \cdot \mathbf{X} \cdot {}^{\mathbf{1}}\mathbf{G^2} \cdot \mathbf{X^{-1}} \cdot \mathbf{R_i^{-1}}, \qquad i = 0, 1, 2, 3 \tag{6.4} $$

With $\mathbf{M}$ being the transformation matrix between crystal and laboratory axes systems and $\mathbf{b}(\theta, \phi)$ the unit vector along the magnetic field $\mathbf{B_0}$ the g-values of the four sites can be calculated according to

$$ g_i(\theta, \phi) = (\mathbf{b} \cdot \mathbf{M} \cdot {}^{\mathbf{C}}\mathbf{G_i^2} \cdot \mathbf{M^{-1}} \cdot \mathbf{b})^{\frac{1}{2}} \tag{6.5} $$

or, explicitly,

$$ g_i(\theta, \phi) = (\mathbf{b} \cdot \mathbf{M} \cdot \mathbf{R_i} \cdot \mathbf{X} \cdot {}^{\mathbf{1}}\mathbf{G_i^2} \cdot \mathbf{X^{-1}} \mathbf{R_i^{-1}} \cdot \mathbf{M^{-1}} \cdot \mathbf{b})^{\frac{1}{2}} \tag{6.6} $$

6.2.5 ENDOR Data Analysis

The total hyperfine tensor is accessible from ENDOR single crystal studies. If the g-tensor is assumed to be isotropic, the spin Hamiltonian can be written as

$$ H = g\beta\mathbf{B} \cdot \mathbf{S} - \sum_i g_{ni}\beta_{ni}\mathbf{B} \cdot \mathbf{I_i} + h \sum_i \mathbf{S} \cdot \mathbf{A_i} \cdot \mathbf{I_i} \tag{6.7} $$

where A_i is the hyperfine coupling tensor for the ith nucleus. In the high field approximation (electron Zeeman (H_{EZ}) $\gg$ nuclear Zeeman (H_{NZ}), hyperfine interaction (H_{HF})) the orientation-dependent hyperfine splitting is observed in the principal axis system x, y, z of the hyperfine tensor $\mathbf{A}$

$$|A_{obs}| = (A_{xx}^2 l_x^2 + A_{yy}^2 l_y^2 + A_{zz}^2 l_z^2)^{1/2}. \tag{6.8}$$

Here, A_{ii} are the principal values of the hyperfine tensor and the l_i are the direction cosines of the orientation of the hyperfine tensor axes with respect to the crystallographic axes. The energy expression for ENDOR transitions with selection rules $\Delta M_S = 0$ and $\Delta M_I = 1$ reads [206]

$$\Delta E = \{M_S^2(\mathbf{I}\cdot\mathbf{A}\cdot\mathbf{A}\cdot\mathbf{I}) + \gamma^2 B_0^2 - 2M_S\gamma B_0(\mathbf{I}\cdot\mathbf{A}\cdot\mathbf{I})\}^{1/2} \tag{6.9}$$

Since ENDOR transitions are usually given in frequency units one obtains

$$\nu^2 = \nu_N^2 + \frac{M_S^2}{h^2}(\mathbf{I}\cdot\mathbf{A}\cdot\mathbf{A}\cdot\mathbf{I}) - \frac{2M_S\nu_N}{h}(\mathbf{I}\cdot\mathbf{A}\cdot\mathbf{I}) \tag{6.10}$$

where

$$h\nu_N = \gamma B_0. \tag{6.11}$$

When restricting to the $S = \frac{1}{2}$ case, the two ENDOR frequencies are

$$\nu_\pm^2 = \nu_N^2 + \frac{1}{4h^2}(\mathbf{I}\cdot\mathbf{A}\cdot\mathbf{A}\cdot\mathbf{I}) \mp \frac{\nu_N}{h}(\mathbf{I}\cdot\mathbf{A}\cdot\mathbf{I}) \tag{6.12}$$

with the upper sign referring to $M_S = +\frac{1}{2}$ and lower signs to the $M_S = -\frac{1}{2}$ transitions. The spectrum is no longer symmetric with respect to the free nuclear frequency ν_N since the vector of the applied magnetic field $\mathbf{B}_0$ and the hyperfine field $\mathbf{A}$ are not collinear. The expression reduces to a symmetric splitting only if the hyperfine coupling $\mathbf{A}$ is purely isotropic, or if the magnetic field lies along a principal direction of $\mathbf{A}$. The elements of $\mathbf{A}$ can be directly determined from a fit of both transitions ν_- and ν_+ (here shown for a special orientation in the xy plane with an angle θ to the magnetic field axis) [206]

$$\frac{h}{2\nu_N}(\nu_-^2 - \nu_+^2) = A_{xx}\cos^2\theta + A_{yy}\sin^2\theta + 2A_{xy}\sin\theta\cos\theta. \tag{6.13}$$

This approach still implies an isotropic g-tensor but was already successfully applied to fit the ENDOR transitions in γ-irradiated artificial Fe-S clusters [207]. In [NiFe] hydrogenases, the anisotropy of the g-tensor in Ni-B ($g_{x,y,z}$ = 2.31, 2.16, 2.01) is still modest with ± 7% around g_{av}, i.e. $(g_x - g_z)/g_{av}$. In analogy to Equation **6.5** the following approach was applied to fit the ENDOR spectra of all four sites simultaneously

$$A_i(\theta,\phi)^{1/2} = (\mathbf{b}\cdot\mathbf{M}\cdot\mathbf{R_i}\cdot\mathbf{X}\cdot{}^{\mathbf{1}}\mathbf{A_i}\cdot\mathbf{X^{-1}}\mathbf{R_i^{-1}}\cdot\mathbf{M^{-1}}\cdot\mathbf{b}), \qquad i = 0, 1, 2, 3 \tag{6.14}$$

The tensor is then diagonalized, and the principal values of $\mathbf{A_i}$ are determined in its principal axes system. The experiments only give the square of the elements of the hyperfine coupling tensor, the absolute signs of the hyperfine coupling constants therefore can not be deduced.

The total hyperfine coupling tensor $\mathbf{A}$ is composed of isotropic and anisotropic (dipolar) components

$$\mathbf{A}_i = a_{\mathrm{iso}}\mathbb{1} + \mathbf{A}_i^{\mathrm{aniso}} \tag{6.15}$$

where $\mathbb{1}$ is the unity matrix. The isotropic part is given by

$$a_{\mathrm{iso}} = \frac{1}{3}\mathrm{Tr}\mathbf{A}_{ii} = \frac{1}{3}(A_{xx} + A_{yy} + A_{zz}) \qquad . \tag{6.16}$$

The anisotropic contributions are obtained from

$$\mathbf{A}_{ii}^{\mathrm{aniso}} = \mathbf{A}_{ii} - a_{\mathrm{iso}}\mathbb{1}, \qquad i = x, y, z \tag{6.17}$$

6.3 Results

6.3.1 cw-EPR

Initially, rotation angle-dependent cw-EPR spectra (in steps of 5 deg) were recorded at T = 80 K in order to determine the quality of the single crystal and its orientation in the laboratory axes system. The orientation of the g-tensor in the crystal axes system was already determined before and checked again [179, 183]. Below T = 77 K the Ni EPR signal is superimposed by an intense signal at g = 2.02 from a [3Fe-4S] cluster [39, 208]. This prevented ENDOR measurements of some EPR signals below $g \approx 2.03$. Figure **6.4** shows the angular dependence of the EPR signals with an arbitrary rotation angle θ in steps of 5 degrees.

The ratio of Ni-B to Ni-A is approximately 70 % to 30 % as determined from dissolved single crystals [179, 196]. For the space group $P2_12_12_1$ there are four sites of the protein molecule in the unit cell. Depending on the orientation of the crystal with respect to the magnetic field $\mathbf{B_0}$ one expects a varying number of EPR transitions. In an arbitrary orientation, four EPR signals corresponding to the four sites per unit cell are to be seen. If the magnetic field is along one crystal plane, two EPR signals are expected (the two are pairwise degenerate). In the special case when the magnetic field is exactly along one of the crystal axes, only one EPR transition can be observed (all four sites are degenerate).

In the angular-dependent EPR spectra (Figure **6.4**) between three and seven lines are observed which correspond to the presence of two paramagnetic species (Ni-A and Ni-B) in the crystal. The EPR spectra of both forms show the periodicity of 180° which is expected from the space group symmetry of the

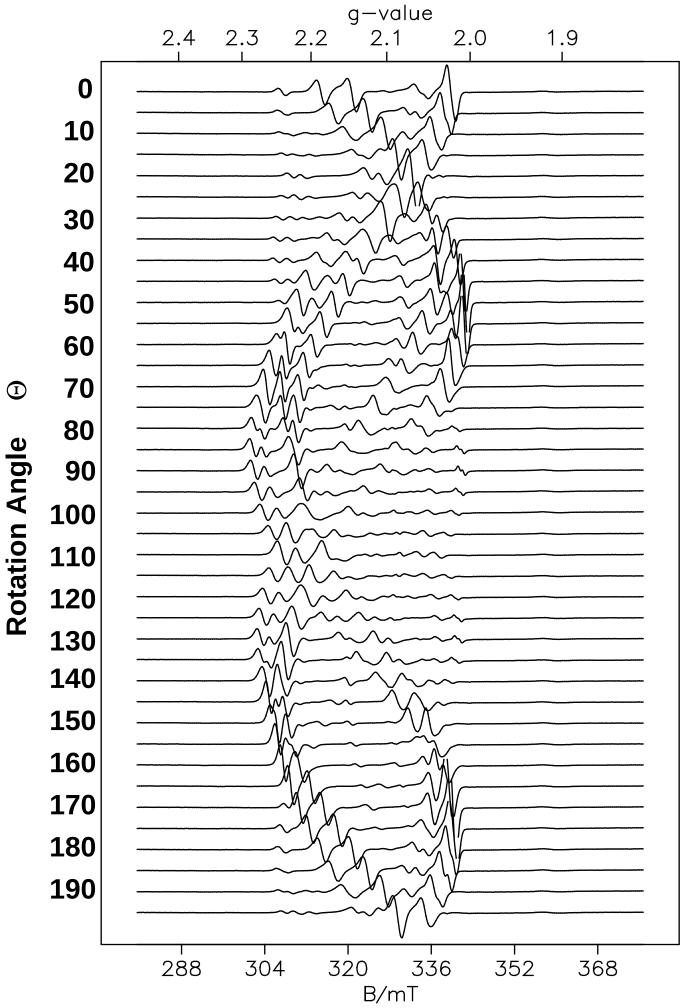

Figure 6.4: Angular-Dependence of the EPR line positions of protein single crystals of the [NiFe] hydrogenase from *D. vulgaris* Miyazaki F. Parameters: T = 80K, microwave frequency 9.728 GHz, field modulation 100 kHz, modulation amplitude 0.5 mT, microwave power 0.4 mW.

crystal. Initially, the more intense EPR signals were fitted. They were shown to originate from the Ni-B form. Next, the weaker EPR signals (from Ni-A) were analyzed. For each form, all four sites were fitted simultaneously, taking into account the symmetry operations between each site. EPR is used here to distinguish between the Ni-A and Ni-B forms in the single crystal and assign sites I-IV to each form. Details of the assignment of specific sites and the discussion of the g-tensor orientation can be found in [190, 209] and are not repeated here. The most plausible assignment of the g-tensor principal axes system to the molecular structure is such that the g_z-axis in both forms Ni-A and Ni-B is oriented along the Ni–S(Cys549) bond (deviation 6° in Ni-A and 11° in Ni-B) and that g_x- and g_y-axes are rotated by

3°. The ground state for both forms was determined to be d_{z^2} based on a ligand field analysis [66, 196] with an orientation of the special z-axis along the Ni–SCys549 bond.

6.3.2 Pulsed-EPR

Pulsed-EPR spectroscopy (T = 10 K) with the same pulse lengths later used in the ENDOR experiments (56 ns and 112 ns for $\pi/2$- and π-pulses, respectively) was applied (see Figure **6.5**, top). The orientation of the crystal in the EPR tube was reconfirmed and it was ensured that site separation and Ni-A/Ni-B separation was still achieved under the chosen conditions. It was possible to show that the excitation bandwidth (8.9 MHz) is small enough to ensure site separation. Inhomogeneous line broadening did not affect the site separation and separation of Ni-A/Ni-B species. Angular-dependent pulsed-EPR (field swept echo) of the paramagnetic species in the crystal were recorded at T = 10 K in steps of 10 degrees

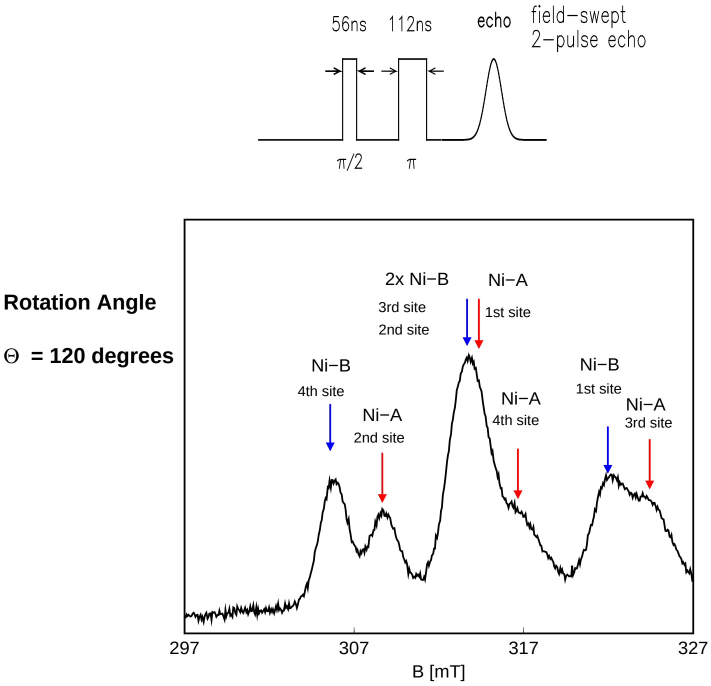

Figure 6.5: Pulsed-EPR of the single crystal of the [NiFe] hydrogenase from *D. vulgaris* Miyazaki F. Top: pulse sequence and pulse lengths; bottom: pulsed-EPR spectrum at the rotation angle of Θ = 120 °. (centre field at 312 mT, sweep-width 30 mT, T = 10 K) Arrows indicate the contribution of each paramagnetic species (Ni-A and Ni-B) to the EPR signal. The enumeration of each site in the unit cell (1-4) is arbitrary and used only in order to differentiate their individual contributions to the pulsed-EPR and subsequent pulsed-ENDOR spectra at the chosen field value.

prior to ENDOR experiments (complete data set not shown). The field position of each EPR resonance transition was measured and chosen for a subsequent Davies pulsed-ENDOR experiment. Only one typical example is shown here.

Figure **6.5** (bottom) shows the pulsed-EPR spectrum that was recorded at an rotation angle of 120° (see Figure **6.4**). The assignment of the Ni-A and Ni-B forms and the four sites in the unit cell for each species to the pulsed-EPR signals was done on the basis of the single crystal cw-EPR spectra. The analysis of the g-tensor magnitudes and orientations allowed a distinction between the different species and sites. The EPR signal at 310 mT corresponds to one site (labelled 4th site) of Ni-B only (see Figure **6.5**). Thus, an ENDOR spectrum recorded at this rotation angle and this field value is expected to exhibit features of one site of Ni-B only. The pulsed-EPR spectrum at 314 mT is a superposition of two sites from the Ni-B species (site 2 and 3) and one site from the Ni-A form (site 1). In an ENDOR experiment, one would thus expect contributions according to this composition. In addition, contributions from the neighbouring 1st site of Ni-A (peak at 316 mT) are also expected. At this rotation angle, pulsed-ENDOR spectra at five different field values were subsequently collected (see trace at 120° in Figure **6.6**).

6.3.3 Pulsed-ENDOR

Figure **6.6** shows the field positions selected for pulsed-ENDOR measurements. Since the crystal contained predominantly Ni-B, the ENDOR effect was more pronounced for this form and the spectra displayed a better signal to noise ratio. Figure **6.7** shows the rotational angular-dependent pulsed-ENDOR spectra of the four separate sites of Ni-B. The numeration is only used to label the four magnetically distinguishable sites in the unit cell. Angular-dependent ENDOR spectra (Figure **6.7**) could be followed over a complete range of 180°. The spectra were adjusted to the free nuclear frequency which is also field-dependent, and plotted centred around ν_H. No spectra are shown (straight line is given) for a few field values below g = 2.03 since the ENDOR spectra contained contribution of the paramagnetic [3Fe-4S] cluster. At some field positions, a superposition of different Ni-B sites is obtained, furthermore overlap with spectra from Ni-A could not always be avoided. Via the cw- and pulsed-EPR experiments and the subsequent fit of the EPR spectra, the composition of each ENDOR spectrum at each field position could, however, be accurately determined.

Starting from the field positions where only Ni-B and only one specific site was selected (‘single-site ENDOR’), the ENDOR lines could be followed over the complete range of rotation angle. In Figure **6.7** clearly two hyperfine split line pairs at ± 5-6 MHz around the free proton frequency can be detected. They vary only slightly with the rotation angle and thus indicate a large isotropic hyperfine coupling with a small anisotropic contribution. There is a further hyperfine interaction which appears outside the

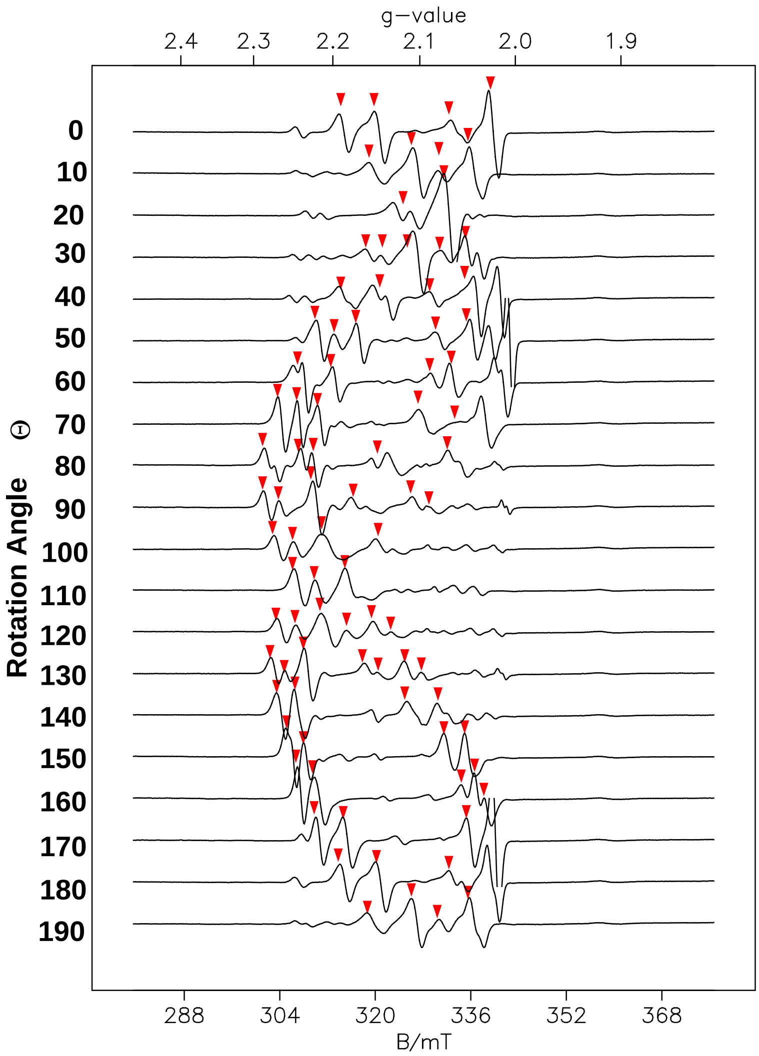

Figure 6.6: Selection of field positions for ENDOR in the angular dependent EPR spectra of single crystals of [NiFe] hydrogenase. The positions of subsequent pulsed-ENDOR measurements are marked by arrows.

matrix and shows a significant angular dependence (ranging from a hyperfine coupling of ≈ 1-2 MHz at θ = 0° to 8-9 MHz near 100° for site 1 of Ni-B). Here, isotropic and anisotropic hyperfine interactions are of similar magnitude. The proton matrix range is very broad and a number of peaks can still be detected in the ± 1-2 MHz range around ν_H. The large number of hyperfine interactions, however, makes it impossible to follow them over the complete rotation angle. The analysis and interpretation of the angular-dependent pulsed-ENDOR spectra which correspond to the Ni-A form (see Figure **6.8**) is more complicated. The spectral resolution is not as good as for Ni-B since the ENDOR resonances are broader. The two largely isotropic hyperfine interactions at ± 5-6 MHz around the free proton frequency are also present but not completely be resolved and appear as one broad signal. The angular dependence of the ENDOR transitions could, however, not be fitted with the approach given above. This might be due to the following reasons:

- Ni-A is only the minority species in crystal of *D. vulgaris* Miyazaki F which complicates the analysis.
- Relaxation characteristics might be different for Ni-A and the pulse experiments were not specifically optimized for this species.
- Ni-A could also possess a more heterogeneous environment; this is indeed indicated by higher temperature factors of some cofactors in the Ni-A containing single crystals of *D. gigas* [27, 32].

Despite these difficulties several statements about the Ni-A form can be made. The large couplings of the Ni-B form are also present in Ni-A. The third hyperfine coupling of Ni-B with significant angular dependence is *absent* in the Ni-A spectra. Where peaks of such a coupling can be seen in Figure **6.8** they stem from a contribution of the Ni-B form to the Ni-A spectra (superposition of Ni-A and Ni-B sites).

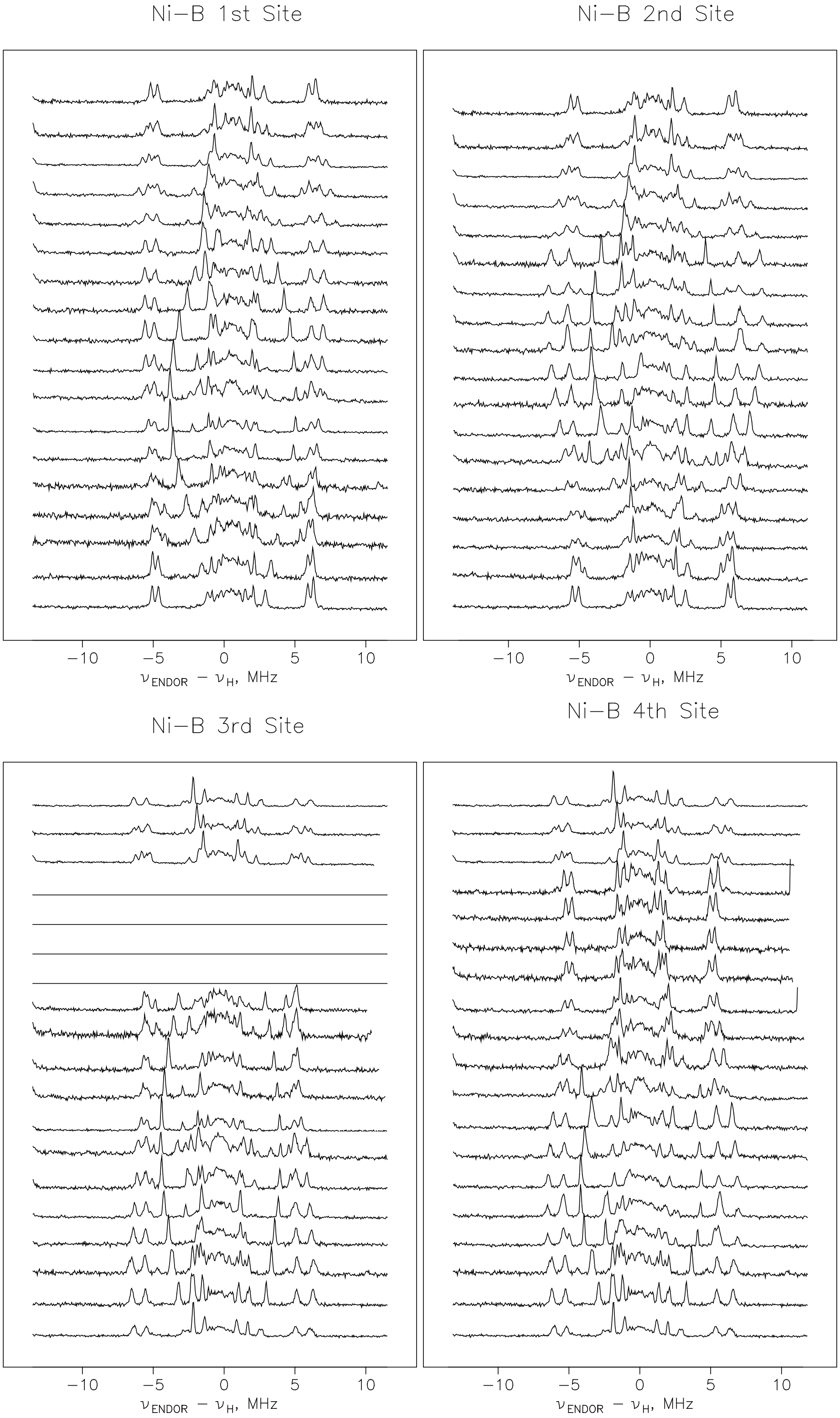

Figure 6.7: Pulsed-ENDOR spectra of Ni-B in protein single crystals from *D. vulgaris* Miyazaki F.

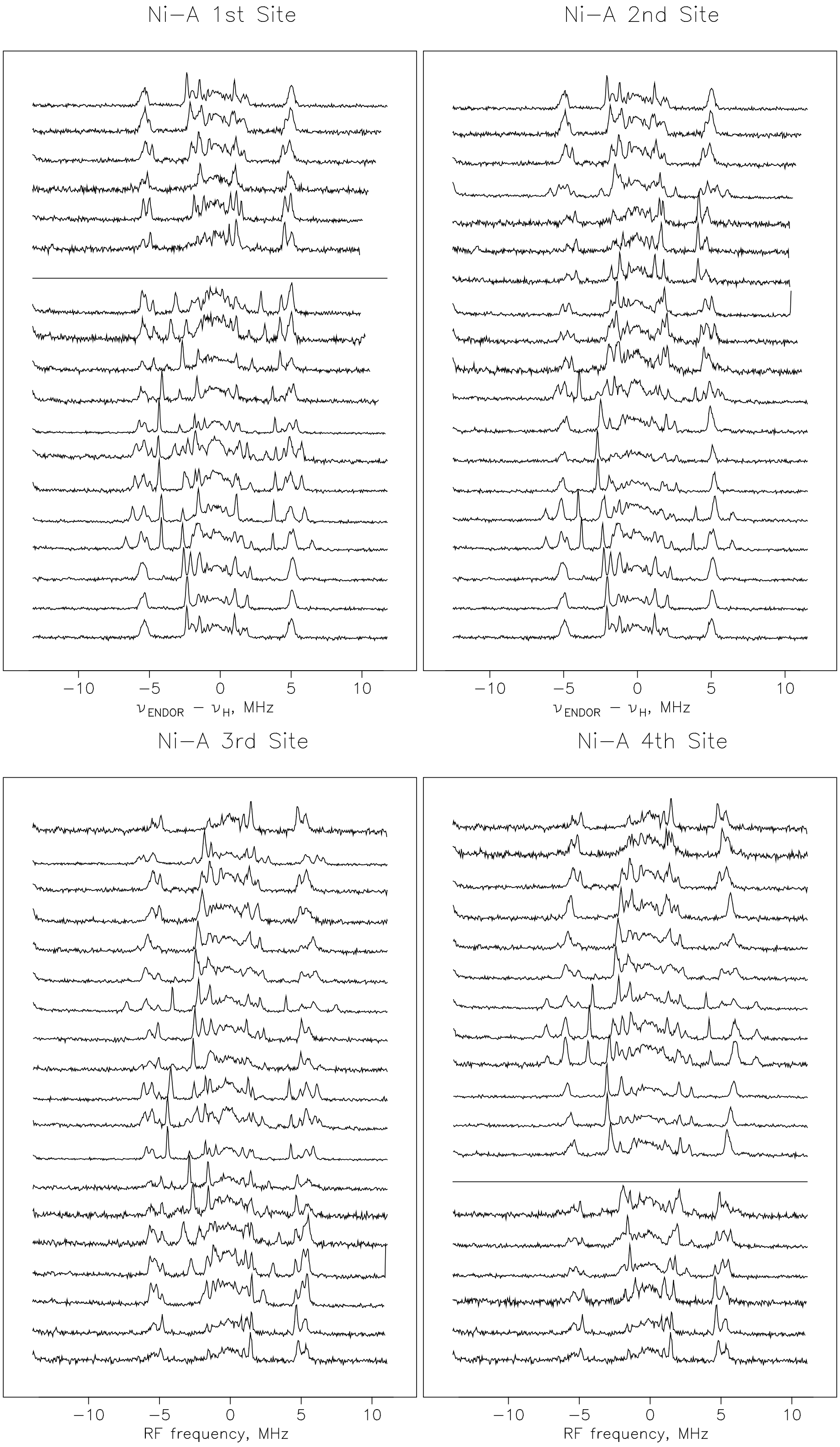

Figure 6.8: Pulsed-ENDOR spectra of Ni-A in protein single crystals from *D. vulgaris* Miyazaki F.

6.3.4 Analysis of ENDOR Spectra

Initially, the matrix $\mathbf{M}$ relating laboratory and crystal axes systems, was held fixed in the fits of the ENDOR spectra since it was already determined in the analysis of the cw-EPR spectra. The crystal orientation was not changed between the cw-EPR and pulsed-ENDOR experiments and thus $\mathbf{M}$ had to remain constant within error. In this way, the number of fitting parameters was reduced from 9 to 6 and facilitated the analysis. After satisfying fits were achieved, also the values of $\mathbf{M}$ were allowed to vary but did not change drastically (at most a deviation of 3° was observed).

Figure **6.9** shows the results of the obtained fits for the three hyperfine interactions in Ni-B. All three hyperfine tensors were simultaneously fitted for all four sites of Ni-B. The colour code distinguishes the four magnetically inequivalent sites in the unit cell. The agreement between measured ENDOR transitions (points) and fitted curves (solid lines) is very good. The deviation of fitted curves from experimental data was less than 100 kHz, i.e. smaller than the linewidth. The largest coupling $\mathbf{A}_1$ ranges from 11-13 MHz (top of Figure **6.9**) , the second coupling $\mathbf{A}_2$ covers a range from 10-11 MHz (middle of Figure **6.9**) and the third coupling $\mathbf{A}_3$ ranges from 2-8 MHz (bottom of Figure **6.9**) . The results of the fitted hyperfine tensors are given in Table **6.1**. $\mathbf{A_{ii}}$ are the obtained principal values of the total hyperfine tensor and the direction cosines $l_{ai,bi,ci}, i = x, y, z$ describe the orientation of the hyperfine tensor principal axes x, y, z in the crystal axes system a, b, c.

$\mathbf{A}_1$ and $\mathbf{A}_2$ both exhibit a large isotropic hyperfine interaction of 12.85 MHz and 10.67 MHz, respectively. This indicates that the protons associated with these hyperfine tensors must be connected to an atom which bears unpaired spin density. The values correspond to the range of ENDOR couplings ($\mathbf{A}_1$ 11-13.5 MHz, $\mathbf{A}_2$ 10.1-11.1 MHz). This provides evidence that the signs of the hyperfine principal values of these coupling must all be positive or negative yielding the maximum isotropic hyperfine contribution. The possibility that all principal values of the hyperfine tensor have negative signs (this would yield isotropic hyperfine interaction with opposite, negative signs) can be ruled out (see Discussion, below). The anisotropic traceless contribution labelled $\mathrm{A}^{`}_{ii}$ in Table **6.1**, in some cases deviates from axiality ($\mathrm{A}^{`}_{ii}$(axial) = (-A$_{dip}$, -A$_{dip}$, 2 A$_{dip}$). Very often, the interpretation of ENDOR hyperfine couplings is done under the assumption of axial hyperfine tensors in which the ‘dipolar’ axis is the special axis. For $\mathbf{A}_1$ $\mathrm{A}^{`}_{ii}$ = (4.19, -1.71, -2.47) axiality is not fulfilled, indicating a more complex hyperfine interaction than that of classic expansionless spins. In the case of $\mathbf{A}_2$, axiality is nearly fulfilled $\mathrm{A}^{`}_{ii}$ = (1.09, -0.54, -0.55) which might be explained by a larger distance between the coupled nuclear and electron spins. This is also reflected in the lower values of the elements of the anisotropic hyperfine tensor since that indicates a larger distance between electron spin and nuclear spin.

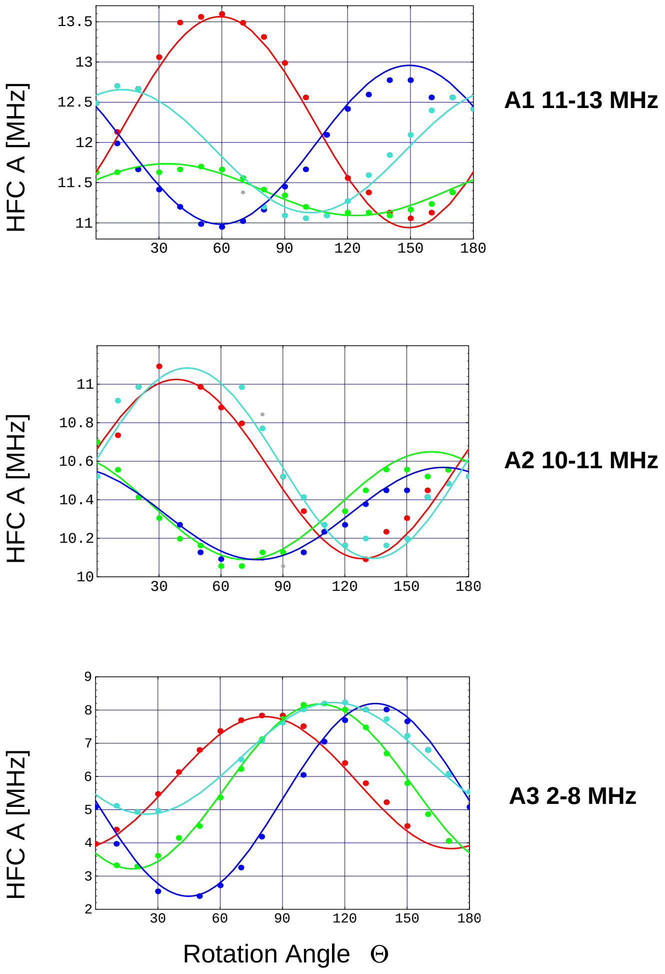

Figure 6.9: Fit of three hyperfine tensors of angular dependent pulsed-ENDOR spectra of Ni-B in protein single crystal of *D. vulgaris* Miyazaki F. The colour code refers to the four magnetically distinguishable sites in the unit cell.

$\mathbf{A}_3$ exhibits a smaller isotropic hyperfine contribution which is only half of that of $\mathbf{A}_1$ and $\mathbf{A}_2$ (a_{iso} = 5.20 MHz). Again, this value is the isotropic part estimated from the angular dependence of the complete hyperfine tensor from 2.5-8.1 MHz. The signs of the complete hyperfine tensor $\mathbf{A}_3$ must again be chosen to be all positive or negative to yield this isotropic value. The resulting anisotropic hyperfine tensor A'_{ii} = (3.07, 2.14, -5.20) also significantly deviates from axiality.

Table 6.1: Hyperfine tensor principal values and direction cosines of hfccs for Ni-B (‘ready‘-state) in [NiFe] hydrogenase from *D. vulgaris* Miyazaki F (T = 10 K)

		x	y	z
$\mathbf{A}_1$	A$_{ii}$	17.04	11.14	10.38
	l$_{ai}$	0.511	-0.410	0.755
	l$_{bi}$	-0.308	-0.908	-0.285
	l$_{ci}$	0.803	-0.087	-0.590
	a$_{iso}$		12.85	
	A$^{‘}_{ii}$	4.19	-1.71	-2.47
$\mathbf{A}_2$	A$_{ii}$	11.76	10.13	10.12
	l$_{ai}$	0.605	0.723	-0.335
	l$_{bi}$	0.023	0.404	0.915
	l$_{ci}$	0.796	-0.561	0.227
	a$_{iso}$		10.67	
	A$^{‘}_{ii}$	1.09	-0.54	-0.55
$\mathbf{A}_3$	A$_{ii}$	8.27	7.34	0.00
	l$_{ai}$	0.110	0.738	-0.666
	l$_{bi}$	-0.977	-0.041	0.208
	l$_{ci}$	-0.181	0.674	0.716
	a$_{iso}$		5.20	
	A$^{‘}_{ii}$	3.07	2.14	-5.20

A$_{ii}$: HFC-tensor principal values (i = x,y,z);

l$_{ki}$: Direction cosines of HFC-tensor principal axes (i = x,y,z) in the crystal axes system (k = a,b,c) for one of the four magnetically inequivalent sites.

6.3.4.1 Assignment of $\mathbf{A}_1$ and $\mathbf{A}_2$

In the rotation-dependent pulsed-ENDOR pattern (Figure **6.7**) of the Ni-B state, signals which were later labeled $\mathbf{A}_1$ and $\mathbf{A}_2$ appear pairwise and exhibit a similar angular dependence. Consequently, it can be assumed that the signals stem from a pair of protons of the same residue in close proximity to each other. The large isotropic contributions of 12.85 MHz and 10.67 MHz, respectively, indicate that they are either bound directly to a spin-bearing atom or they are bound in the vicinity of the spin-bearing atom and aquire isotropic hyperfine interaction via hyperconjugation. The anisotropic contribution of the hyperfine tensor $A_{ii}^{\text{`}}$ was used in order to assign $\mathbf{A}_1$ and $\mathbf{A}_2$. Protons were added to the X-ray structure of the *D. vulgaris* hydrogenase [28] by means of the INSIGHTII software [210] and an algorithm based on standard bond lengths, bond angles and dihedral angles. From the anisotropic hyperfine interaction the component with the largest value was considered to be along the dipolar axis. The deviations between the corresponding direction cosines and Ni–H vectors of possible candidates were calculated. The results are given in Table **6.2**.

Table 6.2: Deviation [degree] Between Dipolar Axes and Ni–Proton Vectors for Ni-B in [NiFe] Hydrogenase of *D. vulgaris* Miyazaki F

	Hyperfine Tensor		
Proton	$\mathbf{A}_1$	$\mathbf{A}_2$	$\mathbf{A}_3$
Cys81_H1	56	69	19
Cys81_H2	89	83	17
Cys84_H1	51	54	63
Cys84_H2	47	59	80
Cys546_H1	29	41	43
Cys546_H2	52	68	27
Cys549_H1	38	**18**	89
Cys549_H2	**16**	**6**	82
X553_H	80	85	**14**

Minimum deviations are given in bold and correspond to most probable assignments (see text for details).

For $\mathbf{A}_1$ β-CH_2 protons of cysteines Cys81, Cys84, Cys546 can be excluded since the deviations are 56, 89, 51, 47, 29, and 52 degrees, respectively. Also, a protonated bridging ligand X533 can be ruled out since the angle between dipolar axis and Ni–X553_H vector is 80 degrees. The minimum deviation for $\mathbf{A}_1$ is obtained for one of the β-CH_2 protons of cysteine Cys549 (Cys549_H2 with angle of 16°).

The same also holds for $\mathbf{A}_2$ for which deviations of less than 20° were only obtained for the two β-CH_2 protons of cysteine Cys549 (18 and 6 degree, respectively). Since Cys549_H2 was already assigned to $\mathbf{A}_1$, the hyperfine tensor $\mathbf{A}_2$ must be assigned to the second proton Cys549_H1. This is in agreement with the cw-ENDOR orientation-selected study of the Ni-B form in *Allochromatium vinosum* [169]. The two large hyperfine interactions exhibited isotropic contributions of 12.5 and 12.6 MHz. From comparison of the dipolar axes with Ni–proton vectors in the molecular structure they were shown to originate from β-CH_2 protons of the bridging cysteine Cys533 (Cys549 in *D. vulgaris* enumeration of amino acids).

The assignment of $\mathbf{A}_1$ and $\mathbf{A}_2$ to β-CH$_2$ protons of cysteine Cys549 has to be considered to be on firm grounds. The g-tensor of Ni-B was shown to have its g_z-axis along the Ni–S(Cys549) bond [183]. In the oxidized states, the Ni atom is assumed to be in a formal Ni(III) oxidation state with the unpaired electron in a 3d$_z^2$ orbital. The five-fold coordination of the Ni is square-pyramidal in the oxidized forms (four cysteinyl sulphur atoms and the bridging ligand bind to the Ni atom). The open coordination site is opposite the Ni–S(Cys549) bond which makes that Ni–S bond a special axis. The spin bearing orbital was assumed to be along the Ni–S(Cys549) bond. The isotropic hyperfine contributions of $\mathbf{A}_1$ and $\mathbf{A}_2$ indicate a significant spin delocalization into the sulphur p$_z$ orbitals of Cys549. The β-CH$_2$ protons thus couple directly to the fraction of spin on the sulphur atom of Cys549 and also to that at the Ni atom (see Figure **6.10**).

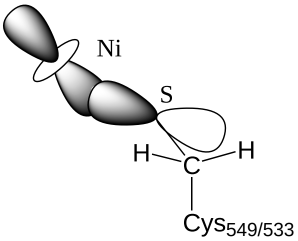

Figure 6.10: Bonding situation for the β-CH$_2$ protons from cysteine Cys549. They may couple to both the fraction of unpaired spin at the cysteinyl sulphur atom and that at the Ni central atom.

This complicated coupling scheme may explain the rather large deviations of 16 and 18 degrees between the dipolar axes and the corresponding Ni–H vectors for the cysteine Cys549. The deviation from axiality and the large deviation of the direction cosines from the Ni–H vectors in Ni-B of the [NiFe] hydrogenase from *Allochromatium vinosum* were analyzed [169]. The anisotropic hyperfine tensor was simulated for the situation where the β-CH$_2$ protons couple simultaneously to a nickel atom and a sulphur atom or to one of them alone. The spin populations at the Ni was varied from 1 to 0.5 and that on the sulphur atoms was increased from 0 to 0.5. Both the X-ray coordinates from the *D. gigas* structure and the DFT optimized cluster model were used. Best agreement with the experimentally determined hyperfine tensors was found for the case where the spin density ρ at the Ni is 0.5 and at the sulphur is 0.3. The remaining 0.2 were delocalized over the complete cluster. This is also in good agreement with the calculated atomic spin populations (see Chapter 5).

The isotropic hyperfine interactions of 12.9 and 10.7 MHz indicate dihedral angles between the β-CH$_2$ protons and the sulphur p$_\pi$ orbital of equal magnitude (see Figure **6.11**).

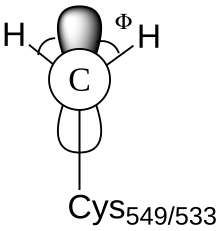

Figure 6.11: Newman projection and definition of the dihedral angle Φ of β-CH_2 protons with respect to the $3p_z$ orbital of the cysteinyl sulphur atom

In general, the angular dependence is of the form $a_{iso} = B\rho_S[C/B + \cos^2(\Phi + \Theta)]$ with Φ the dihedral angle and $\Theta = \pi/2$ [177]. C and B are system-specific constants and not known for hydrogenase. The largest coupling arises when one C-H bond is collinear with the sulphur p_π orbital and minimum coupling is achieved when the C-H bond is perpendicular to the lobes of the p-orbital. The positive sign of the isotropic hyperfine interaction of the β-CH_2 protons can be explained by an analogy to organic radicals where the sign of the spin density at the proton nucleus next to a C_β carbon atom is determined by hyperconjugation.

6.3.4.2 Assignment of $\mathbf{A_3}$

The third proton with the hyperfine tensor $\mathbf{A}_3$ is only present in Ni-B (see Figure **6.7**) and absent in Ni-A (Figure **6.8**). The hyperfine interaction $\mathbf{A}_3$ in Ni-B exhibits an isotropic contribution of 5 MHz (Table **6.1**) which is only half of that of $\mathbf{A}_1$ and $\mathbf{A}_2$. A proton directly bound to a nucleus with a significant amount of unpaired spin density in the active centre of [NiFe] hydrogenase can thus be excluded. One therefore has to find the proton that is associated with an isotropic coupling of that magnitude in the Ni-B form but absent in Ni-A.

The anisotropic hyperfine tensor $A^{`}_{ii}$ = (3.07, 2.14, -5.20) has its large component along the A_z axis but also deviates from axiality. From a comparison of the dipolar axis of the hyperfine tensor $\mathbf{A}_3$ with that from Ni–H vectors in the X-ray structure of *D. vulgaris*, two possibilities remain (see Table **6.2**). The angle between the dipolar axis and Ni–H vectors is small for β-CH_2 protons of the terminal cysteine Cys81 (19 and 17 degrees), large for all other β-CH_2 cysteinyl protons in question and minimum for a possibly protonated bridging ligand X (deviation between dipolar axis and X553_H 14°) spanning Ni and Fe in the active centre. It was investigated whether DFT calculations could contribute to the resolution of this ambiguity in the assignment of $\mathbf{A_3}$.

6.3.5 DFT Calculations of the Electronic Ground State

DFT calculations can accurately reproduce the structural parameters of [NiFe] hydrogenase (see Chapter 5). Good agreement between experimental and BLYP/DZVP calculated bond lengths and angles was found for the X-ray structure of *D. gigas* when the bridging ligand was an oxygen species, e.g. a OH^- for Ni-B and a O^{2-} for Ni-A. The consideration of a sulphur bridging ligand led to bond distances, especially Ni $\cdots$ Fe distances, that were significantly larger than those obtained from X-ray analysis (see Chapter 5). 2 CN and 1 CO ligand were chosen as non-protein ligands to the iron atom since a SO ligand did not lead to a reasonable spin density distribution (see Chapter 5).

Table **6.3** gives structural data for the cluster models of the Ni-A and Ni-B state which were used here in the calculation of the ^{1}H hyperfine couplings. The structures were re-optimized from those in Chapter 5 using a finer integration grid and tight convergence criteria ($5{\cdot}10^{-4}$ in gradient, $1{\cdot}10^{-7}$ in energy). The obtained BLYP/DZVP and HCTH/DZVP optimized geometries are very similar (see Table **6.3**). Usually, the HCTH functional leads to bond lengths that are shorter than those of the BLYP functional. This was also found in [94]. The difference in bond lengths can be as much as 0.05 Å for the Fe–S distances and 0.04 Å for the Ni $\cdots$ Fe distance. Bond angles agree to within 0.5 degrees between the two functionals. The calculated structural parameters which were obtained with the HCTH functional, especially the Ni $\cdots$ Fe and Ni $\cdots$ X bond distances and the Ni–X–Fe bond angle, agree slightly better with those from X-ray analysis for *D. gigas* [27] than those calculated with the BLYP functional. One has to bear in mind the experimental uncertainties in structural parameters from X-ray structures (ca. 0.2 Å at 2.0 Å resolution). The calculated structural parameters do not agree with those from the X-ray structure of the [NiFe] hydrogenase from *D. vulgaris* Miyazaki F [28] (for a Discussion see Chapter 5).

Single point calculations at the optimized geometries and subsequent analyses of the Kohn-Sham wavefunction provide insight into the electronic structure of the active site. It was shown by crystal field analysis that the ground state of the oxidized enzyme may correspond to a Ni(III) with a $3d_{z^2}$ ground state [66]. This assumption was the basis for the assignment of the g-tensor orientation in the oxidized states [179, 183]. In the calculations, the Ni is in its formal Ni(III) oxidation state, coordinated by four cysteine amino acid residues. The iron atom is in its formal Fe(II) oxidation state and ligated by one CO and two CN^-. The position of the bridging ligand is occupied by either an OH^- (Ni-B) or an O^{2-} (Ni-A) ligand leaving the Ni in a five-fold, square-pyramidal coordination sphere. A natural atomic orbital (NAO) analysis was performed in order to determine the orbital occupancy of the Ni atom and gain insight into the electronic structure of the active site.

Table **6.5** gives the total atomic spin densities as obtained from the NAO analysis, the orbital occu-

Table 6.3: Comparison of selected structural parameters from X-ray and DFT optimized models of the oxidized active centres of [NiFe] hydrogenase.

	exp.		BLYP/DZVP		HCTH/DZVP	
	D. gigas [27]	*D. vulgaris* [28]	X= O^{2-}	X= OH^{-}	X= O^{2-}	X= OH^{-}
Ni · · · Fe	2.90	2.55	2.94	3.04	2.90	3.00
Ni–SCys549(533)	2.62	2.37	2.48	2.53	2.48	2.50
Ni–SCys84(68)	2.58	2.38	2.40	2.36	2.35	2.33
Ni–SCys546(530)	2.27	2.33	2.40	2.31	2.39	2.28
Ni–SCys81(65)	2.16	2.22	2.46	2.29	2.46	2.27
Ni · · · X	1.74	2.16	1.85	1.98	1.81	1.96
Fe–SCys549(533)	2.20	2.37	2.62	2.46	2.57	2.40
Fe–SCys84(68)	2.23	2.14	2.52	2.46	2.47	2.41
Fe · · · X	2.14	2.22	1.94	2.08	1.93	2.07
∠ Ni-X-Fe	96.5	71.0	101.7	96.8	101.5	96.1
∠ Ni-SCys549(533)-Fe	73.6	64.1	70.2	75.0	69.9	75.4
∠ Ni-SCys84(68)-Fe	73.9	66.2	73.4	78.0	73.8	78.5

The enumeration of amino acid residues corresponds to that of *D. vulgaris* Miyazaki F. The related sequence number of *D. gigas* is given in parentheses.

pation of the unpaired spin and the natural orbital configuration for the Ni-B form.

63% of the unpaired spin rest on the Ni atom, this is qualitative agreement with the ^{61}Ni hyperfine splitting of isotope-enriched hydrogenases [59]. The difference to the results of the spin population presented in Chapter 5 (0.52) may originate from the use of different functionals, basis set, integration schemes etc.. The Fe atom only possesses 1% of the spin density which agrees with the absence of any ^{57}Fe-ENDOR effect in isotope-enriched samples of Ni-B [61]. *One* of the sulphur atoms bears significant spin density (23%, the sulphur atom of the bridging cysteine 533). This agrees well with the observed hyperfine splitting in EPR due to *one* ^{33}S nucleus [62]. The spin density at the remaining other three cysteinyl sulphur atoms is 0.02, 0.03, 0.07, respectively (data not included in Table **6.5**) and is thus significantly smaller than that of the cysteine 533. 86% of the unpaired spin density resides alone in the bond Ni–S_{Cys549}. A closer inspection of the orbital occupancies of the unpaired spin at the two nuclei gives the following picture: The largest fraction of the unpaired spin density is in the Ni $3d_{z^2}$ orbital, but

Table 6.4: B3LYP/6-311G NAO analysis of the Ni-B state.

Atom	Total Atomic Spin Population	Natural Orbital Spin Occupancy		Natural Electron Configuration
Ni	0.63	$3d_{xy}$	0.027	[core] $4s^{0.4}$ $3d^{8.4}$ $4p^{0.01}$ $5s^{0.01}$
		$3d_{xz}$	0.204	
		$3d_{yz}$	0.055	
		$3d_{x^2-y^2}$	0.003	
		$3d_{z^2}$	0.341	
Fe	0.01	$3d_{xy}$	0.001	[core] $4s^{0.4}$ $3d^{6.8}$ $5s^{0.01}$ $4d^{0.01}$
		$3d_{xz}$	0.001	
		$3d_{yz}$	0.001	
		$3d_{x^2-y^2}$	0.005	
		$3d_{z^2}$	0.007	
SCys549	0.23	$3p_x$	0.076	[core] $3s^{1.8}$ $3p^{4.5}$ $4s^{0.01}$ $4d^{0.01}$
		$3p_y$	0.000	
		$3p_z$	0.149	

also a significant amount in the $3d_{xz}$ orbital. The $3d_{yz}$, $3d_{xy}$ $3d_{x^2-y^2}$ orbital occupancies are smaller. At the sulphur atom of cysteine 533, the largest fraction of unpaired spin density resides in the $3p_z$ orbital, about half as much in the $3p_x$ and zero in the $3p_y$ orbital. This shows that the ground state of the nickel atom in the Ni-B state is indeed composed of mainly a $3d_{z^2}$ orbital with a slightly smaller contribution from the $3d_{xz}$ orbital.

If the Ni orbital occupation were purely $3d^1_{z^2}$ (m_l = 0) then one could not explain the deviation of the g_x- and g_y-values from g_e by 0.33 and 0.16, respectively. For a pure $3d^1_{z^2}$ ground state, g-values much closer to g_e are expected (for an example see Chapter 4, $Ni(CO)_3H$). The admixture of $3d_{xz}$ character ($m_l \neq 0$) can contribute to the g-tensor via spin-orbit coupling and induce g-values larger than g_e.

The bonding situation of the Ni atom is characterized by a NBO analysis as follows: The sulphur nuclei of Cys81 and Cys530 form two single bonds with the Ni atom. The bonds are S $\rightarrow$ Ni donor bonds with a contribution of 76% from the sulphur (of which 5% are from s- and 95% from p-orbitals) and 24% from the Ni (of which are 44% from s-, 0.6% from p- and 55% from d-orbitals). Furthermore, there are two anti-bonding orbitals with reversed contributions (24% from S and 76% from Ni atoms). For the α-spin, there is an *additional* single bond between the sulphur from Cys549 (71% S, 29% Ni) and the corresponding anti-bonding (25% S and 75% Ni) interaction. This bond is *not present* for β-spin orbitals and thus shows that the unpaired spin resides in that bond. This is an *a posteriori* justification of the assumptions made in the analyses of experimental g-tensor orientations [179, 190].

A Ni(0) has the electron configuration [core] $4s^2$ $3d^8$, Ni(I) [core] $4s^1$ $3d^9$, Ni(II) [core] $4s^0$ $3d^8$ and Ni(III) [core] $4s^0$ $3d^7$. From the natural atomic configuration (Ni [core] $4s^{0.4}$ $3d^{8.4}$) it becomes obvious that the oxidation state, however, is not a formal Ni(III) but due to sulphur–Nickel donation its charge is reduced. The nickel atom can be described as a Ni(+1.2). The relation between the formal oxidation state and the actual charge on an atom is not straight forward. Nevertheless, the discussion of formal oxidation states is frequently done in the field of bioinorganic chemistry. The stabilization of high Ni oxidation states by sulphur ligands can be explained by a favourable energetic proximity of S 3p- and Ni 3d-orbitals. The covalency of S–Ni bonds then leads to a compensation of the charge on the central metal atom.

The same argumentation also holds for the Ni-A state (see Table **6.5**).

Table 6.5: B3LYP/6-311G NAO analysis of the Ni-A state.

Atom	Total Atomic Spin Population	Natural Orbital Spin Occupancy		Natural Electron Configuration
Ni	0.88	$3d_{xy}$	0.235	[core] $4s^{0.4}$ $3d^{8.4}$ $4p^{0.01}$ $5s^{0.01}$
		$3d_{xz}$	-0.167	
		$3d_{yz}$	0.042	
		$3d_{x^2-y^2}$	0.175	
		$3d_{z^2}$	0.591	
Fe	-0.05	$3d_{xy}$	-0.008	[core] $4s^{0.4}$ $3d^{6.7}$ $5s^{0.4}$ $4d^{0.01}$
		$3d_{xz}$	-0.009	
		$3d_{yz}$	-0.009	
		$3d_{x^2-y^2}$	-0.012	
		$3d_{z^2}$	-0.012	
SCys549	0.12	$3p_x$	0.018	[core] $3s^{1.8}$ $3p^{4.6}$ $4s^{0.01}$ $4p^{0.02}$
		$3p_y$	0.003	
		$3p_z$	0.084	

The atomic spin population at the Ni is increased to +0.88, that of the bridging sulphur of the cysteine 533 decreased to 0.12. The Fe still bears only a small amount of spin density (5%) possibly due to spin polarization from the Ni atom via the O^{2-} bridge. The bridging ligand O^{2-} would acquire itself unpaired spin density (0.3) and transfer it from the Ni to the Fe atom. This might explain the small but detectable ^{57}Fe-ENDOR signal in Ni-A [61] and an increased hyperfine splitting in $^{17}O_2$ treated samples in Ni-A compared to Ni-B [63] . The numbers given here must be critically discussed. The atomic spin populations significantly differ from those given in Chapter 5. The B3LYP functional has a bias towards higher spin contaminations compared to the pure GGA functionals since more 'ionic' contributions are considered from the Hartree-Fock exchange. As a result, the expectation value of the S^2 operator differs from that expected for a S = 1/2 state (S(S+1) = 0.75), for the B3LYP/6-311G calculation the $\langle S^2 \rangle$ value was 1.0001. This indicates contributions from spin states different from S = 1/2 to the Kohn-Sham wavefunction.

The natural orbital configurations do not change on the Ni and Fe atoms (cf. Tables **6.4** and **6.5**). The Ni atom remains in its Ni(+1.2) state in agreement with results from EXAFS experiments [55, 186] which do not point to a change of electron density at the Ni.

6.3.6 DFT Calculated Hyperfine Tensors

Table **6.6** gives the calculated isotropic and anisotropic hyperfine coupling constants for the Ni-B case in which the bridging ligand is OH^- and 2 CN and 1 CO are the non-protein ligands to the Fe atom. The 6-311+(2d,2p) basis set was used with a diffuse function on all heavy atoms and two sets of d-functions for S,C,O,N (respectively f-functions for Ni and Fe) and two sets of p-functions for hydrogen atoms (1231 basis functions for a Ni-B, 1220 basis functions for a Ni-A cluster model). A single point calculation at the BLYP/DZVP optimized geometry was carried out. The B3LYP functional is known to yield good agreement between experimental and theoretical hyperfine coupling constants for organic radicals (for a review, see [124, 125]). Calculations with the Becke exchange and Perdew correlation functional (BP86) were also performed using the same geometry and basis set.

Despite recent arguments against the classification of 'spin contamination' in DFT methods [211], the term will be used here in the same context as in HF theory (see for example [212]). The effect of spin-contamination on the calculated hyperfine coupling parameters is pronounced since the expectation value of the S_z operator enters the formulae for the isotropic (Eq. 6.1) and anisotropic (Eq. 6.3) hyperfine interactions. The spin contamination for the B3LYP calculation is significantly larger (0.8153) than in the BP86 case (0.7589). For a doublet, the exact expectation value $\langle S^2 \rangle$ is 0.75. The deviation originates from the contribution of spin states of higher multiplicity. The isotropic (Fermi contact) hyperfine interaction is most sensitive to the choice of basis set and functional. The largest value is obtained for the two β-CH_2 protons of cysteine Cys549 (Cys533 in *D. gigas* nomenclature) 12.65 and 13.69 MHz

Table 6.6: DFT Calculated Isotropic and Anisotropic ^{1}H-Hyperfine Coupling Parameters [MHz] in Ni-B

Functional/Basis	B3LYP/6-311+G(2d,2p)		BP86/6-311+G(2d,2p)		B3LYP/6-311+G(2d,2p)	
Geometry	BLYP/DZVP		BLYP/DZVP		HCTH /DZVP	
$\langle S^2 \rangle$	0.8153		0.7589		0.7988	
	a_{iso}	A_{aniso}	a_{iso}	A_{aniso}	a_{iso}	A_{aniso}
Proton						
Cys81(65)_H1 terminal	-0.40	-1.85,-1.17,3.02	1.02	-1.39,-0.96,2.34	-0.48	-1.79,-1.18,2.97
Cys81_H2	0.80	-1.83,-1.74,3.57	2.98	-1.74,-1.06,2.80	1.32	-1.73,-1.68,3.41
Cys84(68)_H1 bridge	1.09	-1.00,-0.93,1.93	3.80	-0.87,-0.74,1.61	1.70	-1.00,-0.92,1.92
Cys84_H2	1.57	-2.59,-2.29,4.89	3.94	-1.99,-1.56,3.55	2.09	-2.50,-2.16,4.66
Cys546(530)_H1 terminal	-2.19	-2.45,-1.82,4.26	1.57	-1.61,-1.45,3.06	-1.21	-2.25,-1.8 0,4.05
Cys546_H2	3.77	-1.32,-1.06,2.38	5.99	-1.08,-0.93,2.01	4.59	-1.30,-1.10,2.40
Cys549(533)_H1 bridge	13.69	-1.80,-1.06,2.85	17.53	-1.86,-0.97,2.83	16.40	-1.88,-1.10,2.89
Cys549_H2	12.65	-2.82,-1.60,4.42	16.72	-2.44,-1.02,3.46	13.97	-2.69,-1.46,4.15
X=OH	1.31	-4.42,-4.11,8.53	0.31	-3.24,-2.49,5.72	1.45	-4.35,-4.09,8.44

The enumeration of amino acid residues corresponds to that of *D. vulgaris* Miyazaki F. The related sequence number of *D. gigas* is given in parentheses.

with the B3LYP and 16.72 and 17.53 MHz with the BP86 functional. The calculated isotropic hyperfine couplings of the β-CH$_2$ protons of the terminal cysteine Cys546 (Cys530) are about a factor of three smaller. The hyperfine interactions for β-CH$_2$ protons of the cysteines Cys81 and Cys84 (Cys65 and Cys68 in *D. gigas* nomenclature) are also given in Table **6.6**. The isotropic ^{1}H hyperfine interaction of the μ-hydroxo ligand is calculated to be 1.31 MHz with the B3LYP functional and 0.31 MHz with the BP86 functional. In general, the hybrid functional B3LYP gives smaller isotropic and larger anisotropic hyperfine interactions compared to the ‘pure’ BP86 functional. This may originate from the admixture of ‘exact’ Hartree-Fock exchange in the B3LYP calculations. Hartree-Fock is biased towards ionic solutions of the wavefunctions. This may lead to an increase of spin density at the nuclei (thus larger isotropic values) and therefore also to a larger anisotropic hyperfine interaction. Pure functionals, on the other hand, tend to favour a more covalent, delocalized spin density distribution (the isotropic and anisotropic values therefore decrease). The overall picture, however, given by the two calculations is similar.

For means of comparison and in order to test the sensitivity of the results with respect to the chosen geometry, geometry optimization using the recently developed HCTH functional [94] were also performed. HCTH is a ‘pure’ functional without admixture of Hartree-Fock contributions and was shown to yield structural parameters, vibrational frequencies and energetics of superior quality to those of other pure functionals, the results are sometimes comparable in quality to those of the hybrid B3LYP functional. In addition, also transition metal complexes were part of the training set from which the HCTH functional was derived [94]. A B3LYP/6-311+G(2d,2p) single point calculation at the HCTH/DZVP optimized geometry was performed. The $\langle S^2 \rangle$ value of 0.799 is intermediate between that of the BP86 and the B3LYP functionals. The influence of the geometry becomes obvious when comparing B3LYP calculations which were performed at the BLYP and HCTH optimized geometries (see Table **6.6**). The isotropic hyperfine interactions are generally large for the HCTH functional. This may originate from the fact that the bond lengths with the HCTH functional are shorter than those with the BLYP functional (see Table **6.3**) or that the HCTH functional shows the same trend towards delocalization as the BLYP functional (see above).

Table 6.7: DFT Calculated Isotropic and Anisotropic ^{1}H-Hyperfine Coupling Parameters [MHz] in Ni-A

Functional/Basis	B3LYP/6-311+G(2d,2p)		BP86/6-311+G(2d,2p)		B3LYP/6-311+G(2d,2p)	
Geometry	BLYP/DZVP		BLYP/DZVP		HCTH /DZVP	
$\langle S^2 \rangle$	0.9204		0.7625		0.8645	
	a_{iso}	A_{aniso}	a_{iso}	A_{aniso}	a_{iso}	A_{aniso}
Proton						
Cys81(65)_H1 terminal	0.21	-1.90,-1.67,3.57	0.14	-1.31,-1.16,2.47	0.17	-3.84,-1.13,4.97
Cys81_H2	-0.10	-2.22,-1.82,4.04	-0.17	-1.61,-1.22,2.83	-0.17	-1.25,-1.14,2.29
Cys84(68)_H1 bridge	1.71	-3.52,-2.19,5.71	4.08	-2.35,-1.95,4.30	3.28	-3.05,-2.20,5.25
Cys84_H2	4.90	-1.27,-0.72,1.99	5.43	-1.07,-0.73,1.80	4.96	-1.21,-0.84,2.04
Cys546(530)_H1 terminal	-2.37	-5.60,-0.44,6.05	0.63	-2.41,-2.15,4.56	-1.78	-1.86,-1.61,3.48
Cys546_H2	2.76	-1.26,-1.12,2.39	4.68	-1.06,-0.94,1.99	3.03	-1.93,-1.57,3.50
Cys549(533)_H1 bridge	9.78	-1.79,-0.62,2.41	12.27	-1.77,-0.66,2.43	8.48	-1.64,-0.79,2 .43
Cys549_H2	5.07	-3.34,-1.45,4.81	8.74	-2.43,-1.46,3.89	7.76	-3.06,-1.72,4.78
X=O^{2-}	-16.44	80.71,-31.89,-48.83	-3.89	32.74,17.05,-49.78	-16.22	70.24,-20.07,-50.18

The enumeration of amino acid residues corresponds to that of *D. vulgaris* Miyazaki F. The related sequence number of *D. gigas* is given in parentheses.

Table **6.7** gives the DFT calculated hyperfine coupling constants for a model of Ni-A where an O^{2-} ligand is assumed to occupy the bridging position. Again, the spin contamination (deviation from the theoretical $\langle S^2 \rangle$ value 0.75) increases in the range BP86//DZVP (0.76) $>$ B3LYP//HCTH (0.86) $>$ B3LYP//BLYP (0.92). The isotropic hyperfine interactions of the β-CH_2 protons of cysteine Cys549 are again the largest. Their magnitudes are reduced compared to the Ni-B form by 3-8 MHz.

The hyperfine tensor of the bridging μ-oxo atom reacts most sensitively to the choice of functional.

While B3LYP//BLYP and B3LYP//HCTH yield very similar isotropic and anisotropic hyperfine interactions, the BP86//BLYP calculations yield an isotropic hyperfine interaction reduced by 12 MHz and a strongly changed anisotropic contribution (see Table **6.7**).

6.4 Discussion

In [NiFe] hydrogenases, it has been shown that the EPR signal arises from the nickel atom (^{61}Ni substitution and subsequent hyperfine splitting in EPR [59]) and one sulphur atom (^{33}S substitution and subsequent hyperfine splitting in EPR [62]). There are, however, at least four sulphur atoms ligating the nickel ion (two terminal cysteines Cys81 and Cys546, and two bridging cysteines Cys549 and Cys84, see Figure **6.1**). [1]

$\mathbf{A_1}, \mathbf{A_2}$: Frozen solution Q-Band cw-ENDOR experiments were performed on samples of *D.gigas* hydrogenase by Fan *et al.* [69]. Ni-A and Ni-B were taken as a reference for Ni-C and no assignment of hyperfine couplings in the oxidized states was made. The largest hyperfine interactions were A^H = 12.8 MHz (Ni-A) and A^H = 15 MHz (Ni-B). No estimate of isotropic and anisotropic contributions was given but this range is also obtained in the pulsed-ENDOR experiments presented here.

DFT calculations are in agreement with the experimental assignment of the hyperfine tensors $\mathbf{A}_1$ and $\mathbf{A}_2$ to the β-CH$_2$ of Cys549 in the Ni-B form. The calculated isotropic hyperfine coupling constants for the β-CH$_2$ protons are in in good agreement with experiment (compare Table **6.1** and Table **6.6**). Best agreement for the β-CH$_2$ protons of Cys549(Cys533 in *D. gigas*) is obtained with the calculations using the B3LYP functional at the BLYP optimized structure (B3LYP//BLYP). The calculated isotropic hyperfine interactions are larger than the experimental (by ca. 5 MHz at BP86//BLYP, ca. 4 MHz at B3LYP//HCTH and ca. 1 MHz at B3LYP//BLYP). The agreement between the calculated and experimental anisotropic hyperfine interaction is very good (deviations less than 0.5 MHz) for the slightly more remote proton Cys549_H2. For Cys549_H1 the deviation is up to 1.8 MHz for the largest anisotropic hyperfine tensor component. This may originate from the complete neglect of relativistic effects (scalar-relativistic and spin-orbit coupling) in the calculations. They may be important for the description of the electronic structure of the Ni atom and likewise influence ligands in the surrounding of the Ni. At this point, it cannot be decided whether the agreement of the B3LYP results is only a fortuitous cancellation of errors and the BP86 results could be systematically improved by consideration of second-order effects (i.e. spin-orbit coupling, see Chapter 4). The reduced spin-contamination of the BP86 results suggests

---

[1] A possible fifth sulphur atom was assigned to an electron density peak in *D. vulgaris* Miyazaki F [28] but considered to be an oxygen species in *D. gigas* [27].

that work along that line is promising.

In the Ni-A state, the two large couplings seem to be also present although no complete analysis is done for the single-crystal spectra. The assignment of the two large coupling to the β-CH_2 protons of cysteine Cys549 for Ni-A is supported by the following arguments:

- the g_z-axis is along that Ni-SCys549 bond in both Ni-B and Ni-A [190]
- the oxidation state of the Ni is unchanged compared to Ni-B
- there is no drastic spin reorientation in the active centre and the spin density resides mainly on Ni and the sulphur of Cys549
- the isotropic hyperfine interaction is reduced by approximately 2 MHz in the Ni-A case compared to Ni-B (compare Figures **6.7** and **6.8**) and the two couplings exhibit very similar isotropic hyperfine interaction and cannot be separated.

DFT calculations yield isotropic hyperfine interactions for the two β-CH_2 of 9.8/5.1 MHz (B3LYP//BLYP), 12.3/8.7 MHz (BP86//BLYP) and 8.5/7.8 MHz (B3LYP//HCTH) (see Table **6.7**). The calculation at the HCTH geometry seems to give best results since the difference between the two protons is only marginal (0.7 MHz) while it is approximately 4 MHz at the BLYP optimized geometry. Experimentally, the protons appear so similar that they cannot be separated.

$\mathbf{A_3}$: Fan *et al.* [69] reported a hyperfine interaction in Ni-B of A = 4.4 MHz which was obtained after solvent-exchange to D_2O in the reduced Ni-C state and subsequent re-oxidation. The hyperfine interaction was tentatively assigned to either a H_2O or OH^- molecule bound to the nickel site. Chipman *et al.*, by means of 2-pulse ESEEM spectroscopy, showed that there is no D_2O exchangeable proton in the vicinity of the Ni atom in the Ni-A state [119]. Consequently, the difference between the Ni-A and Ni-B states can either lie in a different protein conformation which allows solvent accessibility in the Ni-B but not in the Ni-A state or an additional, solvent-exchangeable proton in the active centre in the Ni-B state. Deprotonation of the bridging ligand OH^- in Ni-B to give a O^{2-} ligand in Ni-A is a plausible model. According to the calculations, a protonated bridging ligand (i.e. OH^-) in the Ni-B state would lead to an isotropic hyperfine interaction of $\approx$ 0.31 - 1.45 MHz (see Table **6.6**) and can be ruled out as a candidate for $\mathbf{A}_3$. It may, however, correspond to the solvent-exchangeable proton observed by Fan *et al.* [69].

The second possible assignment is that to a β-CH_2 of the terminal cysteine Cys81. In the Ni-B model, the calculated isotropic hyperfine interaction for the two β-CH_2 protons are -0.40/0.80 MHz (B3LYP//BLYP), 1.02/2.98 MHz (BP86//BLYP) and -0.48/1.32 MHz (B3LYP//HCTH) for H1 and H2, respectively, and smaller than the experimental value. As stated above, the BP86 values appear reliable due to its lower spin-contamination. In the model for the Ni-A state, the isotropic hyperfine interaction is reduced for these two β-CH_2 protons and close to zero in all calculations. Thus a deprotonation of the bridging ligand also leads to a vanishing unpaired spin density at the terminal cysteine Cys81 (from 3 MHz isotropic coupling in Ni-B to 0.2 MHz in Ni-A). According to the calculations, the μ-oxo bridge in the Ni-A form might acquire significant spin density and withdraw it from the sulphur ligands i.e. the bridging cysteine Cys549 and the terminal cysteine Cys81. There is, still, ample room for improvement of the calculation of the isotropic hyperfine interactions, e.g. the inclusion of second-order effects or the use of Slater-type orbitals (STOs) which give a better description of the core region of the electron distribution. This is done in Chapter 7. [2]

Experimentally, the anisotropic hyperfine tensor component seems to be overestimated. The fitted ENDOR transitions range from 2-8 MHz (see Figure **6.9 bottom**). With an isotropic value of 5 MHz, the anisotropy can be estimated to be 3 MHz at most. Thus, a dipolar tensor of the order of magnitude (-1.5, -1.5, 3.0) MHz appears plausible. Due to numerical instabilities of the fit routines, it was not possible to fit the hyperfine tensors $\mathbf{A}_3$ with these values.

The cw-ENDOR orientation-selected study by Geßner *et al.* [169] also revealed a third hyperfine interaction. The measured isotropic part was, however, significantly smaller than the one reported here (0.5 MHz) and assigned to either one β-CH_2 proton from Cys81 or a directly protonated cysteine Cys84. The first possibility is in agreement with the finding in this work since a protonated Cys84 seems very unlikely. A fourth hyperfine interaction was also reported but could not be analyzed because of its maximum near the g_z component [169]. It was labelled 'M' and only tentatively assigned to either a protonated bridging ligand or a β-CH_2 proton of the terminal cysteine Cys546 [169].

6.5 Conclusion and Outlook

The complete hyperfine tensors $\mathbf{A}_1$, $\mathbf{A}_2$, $\mathbf{A}_3$ of three protons in Ni-B in the active centre of the [NiFe] hydrogenase from *D. vulgaris* Miyazaki F have been determined from Davies pulsed-ENDOR experiments on protein single crystals. Figure **6.12** depicts the assigned proton hyperfine tensors.

$\mathbf{A}_1$ and $\mathbf{A}_2$ showed the same angular dependence and both exhibited a large isotropic contribution (13 and 11 MHz, respectively). From the direction of the anisotropic contribution, the protons were

---

[2] Calculations using a STO basis set in the ADF99 program support the results obtained here. The BP86 calculated isotropic hyperfine coupling constants are +13 and +12 MHz for the two β-CH_2 protons of the bridging cysteine Cys549 in Ni-B and +9.5 and +6 MHz in Ni-A. One of the β-CH_2 protons of the terminal cysteine Cys81 exhibits an isotropic coupling of +3 MHz in the Ni-B cluster model but it is absent in the Ni-A cluster model (reduced to +0.2 MHz).

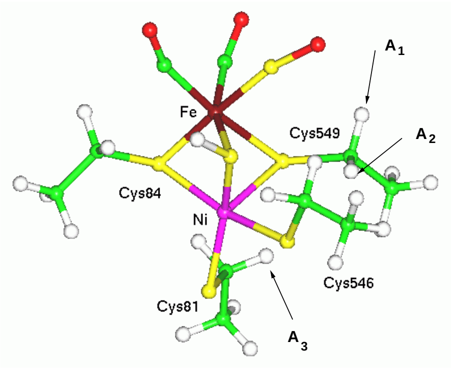

Figure 6.12: Assigned Hyperfine Tensors in the Ni-B State

shown to be β-CH_2 protons of the bridging cysteine Cys549. This assignment is in agreement with previous work of orientation-selected cw-ENDOR measurements [169], the interpretation of the g-tensor in single crystals with its g_z-axis along the Ni–S(Cys549) bond [179, 190] and DFT calculations. In the Ni-A form, the environment of the active site is more microheterogeneous and the ENDOR transitions could not be completely analyzed. The hyperfine tensors $\mathbf{A}_1$ and $\mathbf{A}_2$ are also present in Ni-A but show a reduced isotropic hyperfine interaction (8-9 MHz). This was also confirmed by DFT calculations. The sensitivity of the DFT calculated hyperfine tensors with respect to the optimized geometry and functional was investigated.

The third hyperfine interaction $\mathbf{A}_3$ is only present when the enzyme is in the Ni-B form and absent in Ni-A. It can originate from a either protonated bridging ligand, i.e. X = OH^- or SH^-, or from a β-CH_2 proton of the terminal cysteine Cys81 . The isotropic hyperfine interaction of 5 MHz makes it unlikely to come from an OH^- bridging ligand. The DFT calculations support an assignment according to the second possibility that of a β-CH_2 of Cys81.

For the first time, the difference between the Ni-A and Ni-B forms of the [NiFe] hydrogenase is given, i.e. a O^{2-} bridge in Ni-A and an OH^- in Ni-B. The accumulation of spin density on the μ-oxo bridge in the Ni-A form leads to a withdrawal of spin population from the sulphur ligands to the bridging atom. This modification of the bridging ligand might reflect the different activation kinetics of Ni-A and Ni-B. The OH^- ligand in the Ni-B state may be more easily liberated upon activation than the μ-oxo bridge in Ni-A.

Pulsed-ENDOR investigations on the reduced crystal will reveal changes in the proton environment of the active site during the catalytic cycle and thus help to elucidate the reaction mechanism of this enzyme. Neither the electronic structure nor the hyperfine interaction with protons is accessible from

X-ray crystallographic studies. ENDOR crystallography in conjunction with DFT calculations therefore are indispensable for the investigation of the intermediate states in hydrogenase catalysis.

Chapter 7

Relativistic DFT Calculations of the Paramagnetic Intermediates of [NiFe] Hydrogenase

7.1 Introduction

The paramagnetic states of the enzyme are experimentally well-characterized and are subject of intense research [12, 65]. Their electronic or geometrical structures have, however, not been understood on an atomic level. In the ‘as-isolated‘ oxidized states the [NiFe] hydrogenase is a mixture of two paramagnetic forms (Ni-A and Ni-B). The two only slightly differ in their g-values (Ni-A $g_{x,y,z}$ = 2.32, 2.24, 2.02; Ni-B $g_{x,y,z}$ = 2.32, 2.16, 2.01, see Table **7.1**). In these states, the enzyme is catalytically inactive. It can be activated by reductive incubation under an H_2 atmosphere. Ni-B (or ‘ready’) is reduced within minutes while Ni-A (or ‘unready’) requires incubation for several hours. During reduction, an EPR-silent state Ni-Si is passed before a third paramagnetic state of the active centre (Ni-C) is reached. Ni-C is believed to be a catalytic intermediate in the H_2 dissociation and may bind either H_2, H^- or H^+. Upon illumination, the Ni-C state is converted into a fourth paramagnetic state Ni-L. CO is an inhibitor of the enzyme yielding a paramagnetic CO-bound state Ni-CO. The completely reduced state Ni-R is EPR-silent and believed to be in equilibrium with H_2 [57]. The sequence of redox states reads

$$\mathrm{Ni-A/Ni-B} \rightleftharpoons \mathrm{Ni-Si} \rightleftharpoons \mathrm{Ni-C} \rightleftharpoons \mathrm{Ni-R} \qquad . \tag{7.1}$$

Table **7.1** collects the g-values for the paramagnetic states of the [NiFe] hydrogenase from *Allochromatium vinosum* for which the most complete set of data is available.

Table 7.1: g-Values of the paramagnetic states of the [NiFe] hydrogenase from *Allochromatium vinosum*.

State	g_x	g_y	g_z	Ref.
Ni-A	2.32	2.24	2.02	[63]
Ni-B	2.33	2.16	2.01	
Ni-C	2.19	2.15	2.01	[67]
Ni-L	2.29	2.13	2.05	
Ni-CO	2.12	2.07	2.02	[40, 213]

Previous quantum mechanical studies [71–74] have addressed the question of H_2 activation by [NiFe] hydrogenases but were not aimed at a description of intermediate states based on experimental observables. Niu *et al.* [75] and Amara *et al.* [76] obtained good agreement between calculated and experimental IR CO and CN stretching frequency bands of the non-protein ligands but no attempt was made to correctly describe the electronic structures of the paramagnetic states. In order to characterize the paramagnetic states, it is necessary to calculate observables of magnetic resonance experiments directly from relativistic DFT wavefunctions.

Here, the first relativistic description and calculation of magnetic resonance parameters (g- and A-tensors) of a transition metal containing enzyme is presented. By correlating the g-values to structural parameters and observing their changes between the different paramagnetic states, a possible reaction mechanism may be suggested later.

7.2 Computational Details

We use the ‘zero-order regular approximation‘ for relativistic effects [112, 113, 214, 215], the efficient implementation of the four-component wavefunction in a two-component picture. Recently, the calculation of g-tensors [146], hyperfine tensors [131] and quadrupole tensors [216] including scalar relativistic effects and spin-orbit coupling have become available. The Amsterdam Density Functional (ADF) package was employed [160] which has the advantage of an efficient numerical integration scheme developed by te Velde and Baerends [161]. Slater-typer orbitals (STOs) are used throughout. The calculations are single-point calculations at non-relativistic BP86 [91, 93, 163, 164] geometry-optimized structures. The BP86 functional has been shown to yield good structural and magnetic resonance parameters for transition metal complexes (see Chapter **4**). A double-zeta Slater-type basis set with polarization functions (basis II in ADF nomenclature) was used. A triple-zeta basis set is used for the 3d shells of the first transition metals. The following orbitals were frozen during geometry optimizations : C 1s, N 1s, O 1s, S up to 2p, Ni up to 2p, Fe up to 2p. The calculations of magnetic resonance parameters were performed in an all-electron basis. For g-tensor calculations, a double-zeta Slater-type basis set with polarization functions (basis II in ADF nomenclature) was used. A triple-zeta basis set is used for the 3d shells of the first transition metals. This basis set produced reliable results for Ni model complexes (see Chapter 4) and an increase of basis set did not lead to an improvement of the results. For the calculation of **A**-tensors, a larger basis set is needed. In particular the isotropic hyperfine interaction $\mathrm{a}_{\mathrm{iso}}$ is most sensitive to the quality of basis set. Basis IV in ADF nomenclature was shown to produce rather accurate results. Hyperfine tensors using the smaller basis set (basis II in ADF nomenclature) were also obtained but are not presented here. The difference between the two basis sets was $\approx$ 1 MHz or less for light nuclei but up to 5 MHz for heavy elements.

For reasons of comparison, the ‘quasi-relativistic’ (QR) Pauli-Hamiltonian of Schreckenbach and Ziegler [142] was also used. It is a modification of the ADF program and employs the same BP86 exchange-correlation functional, the same integration routines and the same basis set. Differences in the results may therefore only originate from a different treatment of relativistic effects (i.e. spin-orbit coupling). Scalar relativistic effects are treated self-consistently and spin-orbit coupling and thus the g-tensor are treated as a first order perturbation. Although, the Pauli-Hamiltonian is not bounded from below, the use of an all-electron basis set was not a problem in these cases. The QR g-tensor calculations allow the use of a spin-unrestricted DFT wavefunction which is important for the description of the Ni-A state (see below).

7.3 Results

7.3.1 Ni-B

7.3.1.1 g-Tensor

In preparations of the [NiFe] hydrogenase from *Desulfovibrio vulgaris* Miyazaki F, Ni-B is the largest constituent in solution and single crystals [179, 190]. Its g-tensor orientation in the active centre was determined from angular-dependent EPR spectra of protein single crystals [179, 190]. From the fact that the smallest g-value is close to the free electron value g_e (see Table **7.1**) a $3d_{z^2}$ ground state was deduced.

In the X-ray structure of the [NiFe] hydrogenase from *D. vulgaris* Miyazaki F, a sulphur species was found to occupy the position of the bridging ligand [28] which could either be a S^{2-}, SH^{-} or H_2S ligand. These possibilities were first tested in the calculations. After complete geometry optimizations the Ni–Fe distances are 3.15 Å for H_2S, 3.11 Å for SH^- and 3.19Å for S^{2-}. The experimental Ni–Fe distances from the X-ray structures are 2.55 Å (*D. vulgaris* Miyazaki F [28]) and 2.90 Å (*D. gigas* [27]). Clearly. the calculated values are outside the error margin of the X-ray structure analyses.

Table 7.2: Comparison of experimental and calculated g-tensor principal values using the ZORA Hamiltonian for the oxidized states of [NiFe] hydrogenase.

	State/ Bridging ligand	g_x	g_y	g_z	Ref.
exp.	Ni-A	2.32	2.24	2.01	[63]
	Ni-B	2.33	2.16	2.01	
calc.	H_2S	2.19	2.06	2.01	
	SH^-	2.19	2.15	1.99	
	S^{2-}	2.31	2.07	1.92	
	H_2O	2.22	2.09	2.01	
	OH^-	2.21	2.17	1.98	
	O^{2-}	2.36	1.95	1.84	

The calculated g-values also do not agree with the experimental values for either oxidized state Ni-A or Ni-B (see Table **7.2**). A H_2S ligand gives calculated g-values $g_{x,y,z}$ = 2.19, 2.06, 2.01; a SH^- ligand yields $g_{x,y,z}$ = 2.19, 2.15, 1.99 and a S^{2-} ligand yields $g_{x,y,z}$ = 2.31, 2.07, 1.91. Together with the deviation in structural parameters, these discrepancies make a sulphur species an unlikely candidate for the bridging ligand in the paramagnetic oxidized states of [NiFe] hydrogenase.

A sulphur species (i.e. S^{2-} or SH^-) in the position of the bridging ligand can also not explain the ^{17}O hyperfine coupling in the Ni-A and Ni-B states observed by van der Zwaan *et al.* [63]. In the X-ray structure, Volbeda *et al.* [27, 32] also suggested an oxygenic species as a candidate for the bridging ligand. This was investigated next. When an OH^- ligand occupies the position of the bridging ligand, the calculated Ni–Fe distance is 3.00 Å which agrees with the experimental value of 2.90 Å for the hydrogenase from *D. gigas* [27].[1] The calculated g-tensor principal values $g_{x,y,z}$ = 2.21, 2.17, 1.98 for an OH^- bridging ligand agree with the experimental values $g_{x,y,z}$ = 2.33, 2.16, 2.01 for the g_y- and g_z-components. The deviation of the calculated g_x-value from the experiment value is not unusual for

---

[1] The experimental value of the hydrogenase from *D. vulgaris* Miyazaki F could not be reproduced (see above). One reason might be that the X-ray structures collected for the two hydrogenases refer to different oxidation states, e.g. the data collected from *D. vulgaris* Miyazaki F could belong to an EPR-silent Ni-Si species.

the ZORA approach (see Chapter 4 on model complexes).

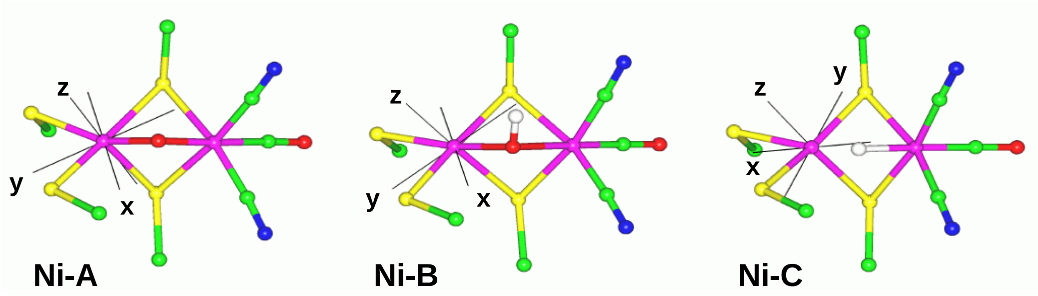

Figure 7.1: ZORA calculated g-tensor orientations of the Ni-A, Ni-B and Ni-C paramagnetic states in [NiFe] hydrogenase.

Also, the experimental g-tensor orientation was reproduced when a OH^- ligand occupies the position of the bridging ligand (see Figure **7.1**). Experimentally, the g_z-axis was shown to be approximately oriented along the Ni–SCys533 bond (deviation 16°). The g_y axis pointed towards the bridging ligand X and g_x was oriented along the Ni–SCys65 bond. When the experimental g-tensor orientation in the active centre is superimposed onto the geometry-optimized cluster with a OH^- bridging ligand such that the heavy atoms show minimal deviations, the difference in the axes orientations is 10° for g_x, 12° for g_y and 14° for g_z. Due to the absence of any symmetry elements in the active center of this metalloenzyme, the agreement can be considered satisfactory. The orientation of the g_z-axis is in agreement with structural information from orientation-selected ^{1}H cw-ENDOR of frozen solution of *A. vinosum* [169] and the pulsed-ENDOR spectroscopy of protein single crystals from *D. vulgaris* Miyazaki F [184] (see Chapter 6). In these experiments, large isotropic ^{1}H hyperfine couplings were measured and assigned to β-CH_2 protons of the bridging cysteine Cys533. This shows that the unpaired spin density is localized along that Ni–S bond.

For means of comparison, also spin-unrestricted QR calculations of the g-tensor were performed (see Table **7.2**). Identical geometry, basis set and exchange-correlation functional (BP86) compared to the ZORA calculation were used. The QR values for the g_x and g_y components are smaller than the corresponding ZORA results. This may be due to the different treatment of spin-orbit coupling in the two approaches. In the QR calculations the spin-orbit coupling is treated as a perturbation while in the ZORA case it is treated variationally. The g_z value of the QR calculation is larger than the corresponding ZORA value and closer to experiment. This may be due to an effect of spin-polarization along the g_z axis which is taken into account in the QR calculation. The QR calculated g-tensor orientation is very similar to the ZORA results. The g_x- and g_y-axes are rotated by 14° while the g_z-axis remains nearly unchanged (3° difference).

Table 7.3: Comparison of spin-restricted ZORA and spin-unrestricted QR results for the Ni-B state.

	ROKS ZORA			UKS QR		
	x	y	z	x	y	z
g-value	2.209	2.173	1.984	2.187	2.148	2.028
l_{xi}	0.65786	0.16489	-0.73487	0.69707	0.02767	-0.71647
l_{yi}	-0.40064	0.90284	-0.15609	-0.16520	-0.96617	-0.19804
l_{zi}	0.63773	0.39711	0.66000	0.69771	-0.25640	0.66892

g_x, g_y, g_z are the g-tensor principal values; l_{xi}, l_{yi}, l_{zi} i = x, y, z are the g-tensor eigenvectors. The eigenvectors of the ZORA Hamiltonian represent an orthonormal, right-handed coordinate axes system (the triple product of the eigenvetors is +1); the eigenvectors of the QR calculation represent a left-handed coordinate axes system (the triple product of the eigenvetors is -1).

7.3.1.2 Hyperfine Interaction

Table **7.4** gives the ZORA calculated hyperfine parameters for the Ni-B state when a hydroxo group bridges the Ni and Fe atoms. The effect of spin-polarization on the hyperfine tensors can be rationalized when comparing the results from scalar-relativistic spin-restricted (SR ROKS) calculations with those from spin-unrestricted (SR UKS) calculations (cf. columns 1 and 2 in Table **7.4**). The influence of spin-orbit coupling becomes clear when one compares scalar-relativistic spin-restricted (SR ROKS) with spin-orbit-coupled spin-restricted (SR+SO ROKS) results (cf. columns 1 and 3 in Table **7.4**). The isotropic hyperfine interaction a_{iso} is to be taken from spin-unrestricted scalar-relativistic (SR UKS) calculations, except for hydrogen atoms for which also SO+SR ROKS results are reliable (see Chapter 4).

^{61}**Ni**: The isotropic ^{61}Ni hyperfine interaction is calculated to be small and positive (+5 MHz). in the SR UKS calculation. The influence of spin-polarization is not large when going from SR ROKS to SR UKS values. However, there is a striking effect of spin-orbit coupling when comparing SR ROKS and SO+SR ROKS results. The anisotropic hyperfine interaction is reduced by a factor of two when SO coupling is considered. Although there is no experimental data for the ^{61}Ni hyperfine tensor in the Ni-B state (see Table **2.5**), the SO coupled values seem unrealistically low. Ni-A and Ni-C display a total ^{61}Ni hyperfine interaction along A_z of 76 MHz (see Table **2.4**) and Ni-B would be expected to exhibit a hyperfine interaction of the same order of magnitude. Such a value was recently obtained from hyperfine splitting of ^{61}Ni enriched protein of the [NiFe] hydrogenase from *D. vulgaris* Miyazaki F (S.

Foerster, personal communication). The SR UKS values, in particular for the A_z component, appear more realistic.

^{57}**Fe**: The ^{57}Fe hyperfine interaction is calculated to be small at all levels of the calculations due to the strong CN and CO ligands which keep the iron in its formal Fe(II) low spin (S = 0) state. A weak spin polarization via the bridging hydroxo bridge leads only to a small ^{57}Fe hyperfine interaction. The effect of spin-polarization (cf. SR ROKS and SR UKS values) reduces the hyperfine coupling by about 1 MHz for A_x and A_z. Spin-orbit coupling (cf. SR ROKS and SR+SO ROKS values) further reduces A_x and A_z components by 0.3 and 0.9 MHz, respectively. The A_y components is also reduced in magnitude and even inverts the sign. An extrapolated spin-polarized, spin-unrestricted ^{57}Fe hyperfine coupling then is very small indeed. Despite a reported absence of ^{57}Fe-ENDOR couplings [61] in the Ni-B state, there is new evidence that this result has to be revised. A value of 0.8 MHz was reported (J. Moura, B. M. Hoffman, personal communication). The calculated small ^{57}Fe hyperfine interaction is thus in agreement with most recent experimental findings.

^{33}**S**: In the Ni-B cluster model, only the sulphur atom of the bridging cysteine Cys533 exhibits a significant hyperfine interaction (15 MHz isotropic hyperfine interaction). The isotropic hyperfine interactions from the sulphur atoms of cysteine Cys530, Cys65 and Cys68 are 2.4 MHz, 0.3 MHz and 3.0 MHz and thus much smaller. Therefore these sulphur atoms are not included in Table **7.4**. The calculated ^{33}S coupling of the bridging cysteine Cys533 agrees with the experimental findings that there is hyperfine splitting due to *one* sulphur nucleus only [62] in Ni-B, that the g_z-axis (associated with a $3d_{z^2}$ orbital) is along the Ni–SCys533 bond [190] and there is large hyperfine interaction of the β-CH$_2$ protons of cysteine Cys533 [169, 184]. Neither spin-polarization. nor spin-orbit coupling largely influence the calculated anisotropic ^{33}S coupling. The isotropic hyperfine interaction is about +15 MHz and the anisotropic part very close to uniaxiality with A_{dip} = -27 MHz. Albracht *et al.* report a ^{33}S hyperfine splitting of 27 MHz and 39 MHz along the g_x and g_y components [62]. A splitting along g_z was not reported. Reasons for the differences between experimental and calculated hyperfine splitting may come from the number of simulation parameters that enter the analysis of the experimental splitting (e.g. number of sulphur nuclei, degree of enrichment, g- and A-tensor relative orientation). The excellent agreement between measured and calculated ^1H hyperfine splitting of the β-CH$_2$ protons of that SCys533 nucleus gives confidence that the spin density at the sulphur atom and thus the hyperfine interaction are well described by the calculations (see below).

^{17}**O**: The ^{17}O coupling of the hydroxo oxygen exhibits an isotropic coupling of -7 MHz (SR UKS results) and a small anisotropic contribution at all levels of the calculations. The total hyperfine tensor of [-6 , -6, -10] MHz is in approximate agreement with the reported experimental ^{17}O hyperfine broadening of EPR linewidth of 11 and 20 MHz for g_y and g_z [63]. The experimental data must be critically regarded, i.e. the use of an EPR modulation amplitude of 1 mT and the detection of line-width broadenings of the order of 0.4-0.7 mT seem not reliable.

^{1}**H**: In the Ni-B cluster model, the β-CH$_2$ protons from the bridging cysteine Cys533 exhibit a large hyperfine interaction. The agreement between calculated and experimental data from cw-ENDOR of frozen solution (isotropic couplings +12.5 MHz) [169] and pulsed-ENDOR experiments of protein single crystals (+13 and +11 MHz) (Chapter 6) is very good. The isotropic hyperfine interaction of the two β-CH$_2$ of cysteine Cys533 is overestimated by 3 and 7 MHz in the spin-polarized SR ZORA calculations, but reproduced to within 1 MHz when spin-orbit coupling (SR+SO ROKS) is considered. The effect of spin-orbit coupling on the anisotropic hyperfine tensor is small (comparing SR ROKS with SO+SR ROKS data). One of the β-CH$_2$ protons of the terminal cysteine Cys65 displays a hyperfine coupling of +2.2 MHz (SR UKS value), respectively +2.6 MHz at the SO+SR ROKS level of calculation. This would correspond to the third hyperfine coupling $\mathbf{A_3}$ assigned in Chapter 6. The calculations also give an isotropic hyperfine interaction of +5 MHz for one β-CH$_2$ proton from the terminal cysteine Cys530. This can either originate from the coupling A_3 in single crystals or the one labelled 'M' in frozen solution [169]. The hyperfine interaction of the hydroxo bridge is rather small. The proton exhibits a very small isotropic hyperfine interaction of about 1 MHz and a larger anisotropic coupling. This may correspond to the solvent-exchangeable coupling of +4.4 MHz at g_x resported by Fan *et al.* for the Ni-B state [69]. It was tentatively assigned by the authors to originate from a OH$^-$ or H$_2$O bound in the vicinity of the Ni atom.

Table 7.4: ZORA calculated hyperfine interaction in Ni-B in MHz.

Nucleus	hf component	SR ROKS	SR UKS	SO+SR ROKS
^{61}Ni	a_{iso}	-17.28	+5.46	-55.19
	A'_x	+56.15	+55.67	+24.26
	A'_y	+21.10	+21.20	+9.58
	A'_z	-77.26	-76.86	-33.85
^{57}Fe	a_{iso}	+0.08	-1.00	+0.78
	A'_x	-3.07	-1.95	-2.72
	A'_y	-0.32	-0.44	+0.13
	A'_z	+3.41	+2.41	+2.58
$^{33}S_{Cys533}$	a_{iso}	+13.13	+15.30	+12.52
	A'_x	-25.88	-27.54	-26.24
	A'_y	-25.79	-26.64	-26.08
	A'_z	+51.68	+54.18	+52.33
$^{17}O_{OH-}$	a_{iso}	-4.85	-7.26	-4.68
	A'_x	+1.77	+1.63	+2.38
	A'_y	+1.41	+1.38	+1.48
	A'_z	-3.19	-3.00	-3.81
$^{1}H_{Cys533-H1}$	a_{iso}	12.60	15.06	12.54
	A'_x	-2.39	-2.41	-2.54
	A'_y	-0.40	-1.12	-0.43
	A'_z	+2.78	+3.52	+2.92
$^{1}H_{Cys533-H2}$	a_{iso}	12.42	13.92	12.34
	A'_x	-1.84	-1.68	-1.89
	A'_y	-0.80	-1.07	-1.89
	A'_z	+2.62	+2.76	+2.67
$^{1}H_{Cys530-H1}$	a_{iso}	+2.16	+1.26	+2.23
	A'_x	-1.56	-1.59	-1.71
	A'_y	-0.87	-1.58	-1.02
	A'_z	+2.42	+3.15	+2.73
$^{1}H_{Cys530-H2}$	a_{iso}	+4.70	+4.89	+4.69
	A'_x	-0.95	-1.10	-1.02
	A'_y	-0.90	-0.91	-0.96
	A'_z	+1.85	+2.02	+1.99
$^{1}H_{Cys65-H2}$	a_{iso}	+2.60	+2.22	+2.60
	A'_x	-1.84	-1.89	-1.99
	A'_y	-0.64	-1.15	-0.65
	A'_z	+2.48	+3.04	+2.64
$^{1}H_{OH-}$	a_{iso}	+1.21	+0.30	+1.33
	A'_x	-2.70	-3.37	-3.25
	A'_y	-1.51	-2.34	-1.06
	A'_z	+4.20	+5.71	+4.84

7.3.2 Ni-A

7.3.2.1 g-Tensor

The g-tensor orientation of the Ni-A form was determined from angular-dependent EPR of single crystals [179, 190] in which Ni-A was the minor compound in the protein. From the similarity of the g-values a drastic change in the electronic structure of the active site could be ruled out. Indeed, the g-tensor orientation was experimentally found to be very similar to that of Ni-B [190]. Only a slight reorientation of about 3-4° was detected. A modification of the bridging ligand or one of the terminal cysteines was discussed which would cause a shift in the g_y-value [190]. These hypotheses were tested with the following results (see also Table **7.2**).

1. A protonation of the terminal cysteine Cys530 leads to a g-tensor of $g_{x,y,z}$ = 2.29, 2.14, 1.92 which appears implausible because of its low g_z-value. Such a modification also could not explain the different activation kinetic of Ni-A and Ni-B and their similarities in the g-tensor orientations (data not shown).

2. Also, a doubly protonated bridging ligand H_2O can be ruled out (the calculated g-tensor principal values are 2.22, 2.09, 2.01).

3. ZORA calculations with a deprotonated bridging ligand, e.g. leaving a O^{2-} bridge, gave g-values of $g_{x,y,z}$ = 2.36, 1.95, 1.84 which appear unrealistic.

In a next step, it was investigated whether the unrealistic values below g_e derive from the spin-restricted nature of the wavefunction. Spin-unrestricted quasi-relativistic (QR) calculations using the Pauli-Hamiltonian [142] but otherwise the same basis set, exchange-correlation functional and integration scheme yielded values of $g_{x,y,z}$ = 2.187, 2.148, 2.028 when X = OH^- and $g_{x,y,z}$ = 2.183, 2.159, 2.046 for X = O^{2-}. The QR-values are generally smaller than the corresponding ZORA results but the trends are reproduced: the g_x component of Ni-B (OH^-) is slightly larger than for Ni-A (O^{2-}), the g_y value for Ni-A is larger than for Ni-B. The QR g_z values are larger than the ZORA results perhaps due to the perturbative treatment of spin-orbit coupling. In any case, the consideration of spin-polarisation drastically improves the description of the Ni-A state. If one assumes that the trends can be extrapolated to the ZORA values for Ni-B, (i.e. Ni-A - Ni-B shifts Δg_x = -0.004, Δg_y = 0.011, Δg_y = 0.018) one arrives at reasonable g-values of 2.20, 2.19, 2.02. The ZORA calculated g-tensor orientation is given in Figure **7.1**. The tensor orientation is very similar to that of Ni-B as was also found experimentally [190]. The g_z axis is along the Ni–SCys533 bond and the g_y-axis roughly points to the bridging ligand.

Table 7.5: Comparison of spin-restricted ZORA and spin-unrestricted QR results for the Ni-A state.

	ROKS ZORA			UKS QR		
	x	y	z	x	y	z
g-value	2.357	1.948	1.846	2.183	2.159	2.046
l_{xi}	0.49499	-0.18690	-0.84856	-0.01959	0.41151	-0.91120
l_{yi}	-0.85012	-0.30610	-0.42848	-0.77154	-0.58585	-0.24799
l_{zi}	-0.17966	0.93347	-0.31040	0.63588	-0.69817	-0.32897

g_x, g_y, g_z are the g-tensor principal values; l_{xi}, l_{yi}, l_{zi} i = x, y, z are the g-tensor eigenvectors. The eigenvectors of the ZORA Hamiltonian represent an orthonormal, right-handed coordinate axes system (the triple product of the eigenvetors is +1); the eigenvectors of the QR calculation represent a left-handed coordinate axes system (the triple product of the eigenvetors is -1).

The difference between the spin-restricted ZORA and the spin-unrestricted QR g-tensor orientations is also quite large. The g_z-axes agree to within 11° while g_y- and g_x-axes differ by 57° and 58°, respectively. From a comparison of the signs of the eigenvectors it becomes clear that the x- and y-axes interchange when going from the spin-restricted ZORA to the spin-unrestricted QR calculations. The z-axis is retained. It is found that the axes orientation of the ZORA calculation is in better agreement with the experimental assignment of the Ni-A form. It is the g_y axis that points to the bridging ligand

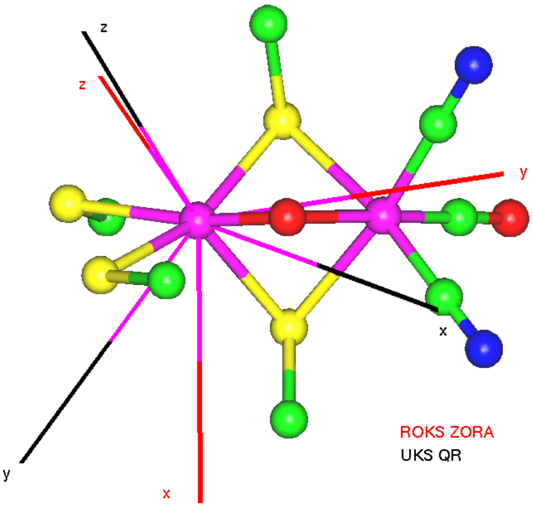

Figure 7.2: Comparison of ROKS ZORA and UKS QR g-tensor orientations for the Ni-A state.

in the ZORA calculation but the g_x axis in the QR calculation and vice versa for the other axes. Experimentally, the exact orientation of the g-tensor axes with respect to the crystal axes was determined from X-ray scattering experiments [179, 196]. The Ni-B species is the major constituent of protein single crystals from *D. vulgaris* Miyazaki F. Strictly speaking, the confirmed orientation of g- and crystal axes orientation only holds for the Ni-B form. The orientation of a and b crystal axes with respect to the corresponding g-tensor axes may be different for Ni-A but it was assumed to be similar to that of Ni-B. Unless a protein single crystal from *D. vulgaris* Miyazaki F which is predominantely in the Ni-A form is investigated first by room temperature EPR and then by X-ray scattering, a definite answer about the experimental g-tensor orientation in Ni-A cannot be made.

The potential assignment of an O^{2-} bridging ligand in the Ni-A form is supported by the following experimental facts.

- $^{17}O_2$ line broadening was observed for Ni-A and Ni-B EPR signals which suggests that an oxygen species binds in the vicinity of the Ni [63].
- In the active centre, no D_2O exchangeable proton could be detected in the Ni-A state [68, 70].
- Ni-A requires prolonged exposure to H_2 to be activated compared to Ni-B. An OH^- ligand would be more easily removable upon protonation than the proposed O^{2-} ligand.

7.3.2.2 Hyperfine Interaction

Table **7.6** gives the results of ZORA calculations of the hyperfine interaction in the model for the Ni-A state.

^{61}**Ni**: The scalar-relativistic (SR UKS) calculated isotropic ^{61}Ni hyperfine interaction is positive (+13 MHz). The value of the SR UKS anisotropic A'_z component agrees rather well with the experimental values by Albracht *et al.* [59] and Moura *et al.* [45] (see Table **2.5**) of 76 MHz. The sign of the experimental hyperfine coupling could not be determined. According to the calculations, it is negative. Experimentally, however, a smaller A_x hyperfine interaction (21 MHz) was detected [59]. When comparing SR ROKS and SR UKS calculations, the effect of spin-polarization can be seen: upon consideration of spin-polarization A'_x increases by 2 MHz, A'_y is reduced by 4 MHz and A'_z increases by 2 MHz. The effect of spin-orbit coupling (cf. columns 1 and 3 in Table **7.6**) reduces A'_x by 14 MHz, A'_z by 4 MHz but A'_y increases by 9 MHz.

^{57}**Fe**: The isotropic ^{57}Fe hyperfine coupling is calculated to be very small (-0.5 MHz) from the SR UKS calculation. The anisotropic hyperfine interaction is also very small (less than 1 MHz) at all levels of the calculations and neither spin-polarization nor spin-orbit coupling are of drastical influence. This is in agreement with a small experimental ^{57}Fe-ENDOR hyperfine splitting of $\approx$ 1 MHZ in the Ni-A state [61].

^{33}**S**: The calculated ^{33}S coupling of the sulphur of Cys533 shows a larger isotropic (+29 MHz in the SR UKS calculation) and smaller anisotropic hyperfine coupling compared to the Ni-B state. The total hyperfine tensor, however, remains about constant. All other cysteinyl sulphur nuclei exhibit smaller isotropic hyperfine interactions of the order of 1/3 or less than that of the bridging cysteine Cys533; they are not included in Table **7.6**. The large hyperfine interaction of the sulphur atom of that bridging cysteine supports the consistency between the Ni-B and Ni-A g-tensor orientations and the hyperfine interaction of the β-CH_2 protons of the residue (see below and Chapter 6).

^{17}**O**: The calculated isotropic ^{17}O coupling (-8.8 MHz) is very similar to that in the Ni-B state (-7.3 MHZ) while there is a drastic increase in the anisotropic hyperfine interaction compared to Ni-B. The experimental ^{17}O hyperfine coupling that increases the EPR linewidth in Ni-A (14, 11, 13 MHz for A_x, A_y, A_z) does not show this large anisotropy [63] (see Table **2.5**). One reason for that might be an unfavourable orientation of g- and A-tensors which would make the determination of the ^{17}O tensor principal values more difficult. The experimental study by van der Zwaan *et al.* [63] only aimed at a characterization of the environment of the nickel nucleus but not at an accurate determination of the ^{17}O hyperfine tensor principal values. Under the experimental conditions chosen by these authors (see above), the reported increase in line-width can only serve as proof of an oxygenic species in the vicinity of the nickel atom in the Ni-A state. ^{17}O-ENDOR experiments are in progress (J. Moura, B. M. Hoffman, personal communication) and will provide a more sensitive tool to address the question of oxygen binding in the oxidized states of [NiFe] hydrogenase.

^{1}**H**: The calculated isotropic hyperfine splittings of the β-CH_2 protons from the bridging cysteine Cys533 (SR UKS values of +11 and +7 MHZ) are in agreement with experimental findings by Fan *et al.* of a total hyperfine splitting of 12.8 MHz at g_y in the Ni-A form (see Table **2.6**) and pulsed-ENDOR of protein single crystals (see Chapter **6**). Neither spin-polarization nor spin-orbit coupling have a large influence on the ^{1}H hyperfine tensor components (at most 1 MHz). Experimentally, the two β-CH_2 protons appear closer to equivalence than in the calculation. The reason for this might be a slight torsional change with respect to the sulphur 3p_z orbital. The deprotonation of the hydroxo bridge in the Ni-B form leads to a μ-oxo bridge in Ni-A. The ENDOR spectra of Ni-A in H_2O and D_2O are identical while a small D_2O-exchangeable coupling was detected in Ni-B [69] which supports this model (see above). One of the β-CH_2 protons of the terminal cysteine Cys65 displayed an isotropic hyperfine interaction of 2-3 MHz in the Ni-B model cluster (see above). This hyperfine interaction is in the Ni-A model cluster reduced to almost zero (-0.15 MHz at the SR UKS level of calculation) and would no longer be easily detectable by ENDOR. This is in angreement with the postulated difference between the Ni-A and Ni-B forms in Chapter 6.

Table 7.6: ZORA calculated hyperfine interaction in Ni-A in MHz.

Nucleus	hf component	SR ROKS	SR UKS	SO+SR ROKS
^{61}Ni	a_{iso}	-17.05	+12.98	-85.10
	A'_x	+75.75	+77.44	+62.18
	A'_y	+0.95	-3.06	+10.06
	A'_z	-76.71	-74.38	-72.24
^{57}Fe	a_{iso}	0.08	-0.47	0.80
	A'_x	-0.78	-0.52	-0.79
	A'_y	+0.23	+0.13	-0.23
	A'_z	+0.55	+0.39	+1.02
$^{33}S_{Cys533}$	a_{iso}	+29.83	+28.72	+30.17
	A'_x	-19.54	-19.48	-14.30
	A'_y	-19.51	-19.43	-19.75
	A'_z	+39.06	+38.90	+34.06
^{17}O	a_{iso}	-0.05	-8.83	-0.33
	A'_x	+21.89	+29.94	+28.27
	A'_y	+20.19	+14.08	+18.33
	A'_z	-42.19	-44.03	-46.61
$^{1}H_{Cys533-H1}$	a_{iso}	+9.56	+10.61	+9.47
	A'_x	-1.79	-1.75	-1.70
	A'_y	-0.58	-0.61	-0.76
	A'_z	+2.38	+2.37	+2.46
$^{1}H_{Cys533-H2}$	a_{iso}	+6.10	+7.41	+6.22
	A'_x	-2.43	-2.47	-2.53
	A'_y	-0.90	-1.57	-1.10
	A'_z	+3.33	+4.06	+3.64
$^{1}H_{Cys530-H1}$	a_{iso}	+1.88	+0.31	+1.56
	A'_x	-2.61	-2.44	-2.81
	A'_y	-1.69	-2.25	-2.30
	A'_z	+4.30	+4.70	+5.12
$^{1}H_{Cys530-H2}$	a_{iso}	+4.39	+4.20	+4.13
	A'_x	-0.98	-1.09	1.14
	A'_y	-0.90	-0.94	-1.08
	A'_z	+1.88	+2.03	+2.22
$^{1}H_{Cys65-H2}$	a_{iso}	+0.24	-0.15	+0.17
	A'_x	-1.52	-1.71	-1.20
	A'_y	-0.98	-1.30	-1.13
	A'_z	+2.50	+3.01	+2.33

7.3.3 Ni-C

7.3.3.1 g-Tensor

In the X-ray structure analysis of the reduced enzyme, the position of the bridging ligand is vacant [172, 185]. This indicates that the bridging ligand X must be liberated upon activation when going from the oxidized Ni-A/Ni-B states to the reduced Ni-C (or Ni-R) state. However, either the substrate H_2 or the dissociation products H^+ and H^- may still be bound to the active centre in the Ni-C state and not be detectable by X-ray analysis.

Table 7.7: Comparison of experimental and calculated g-tensor principal values using the ZORA Hamiltonian for the reduced Ni-C state of [NiFe] hydrogenase.

	Bonding Sit.	g_x	g_y	g_z	Ref.
exp.		2.19	2.15	2.01	[67]
		2.20	2.15	2.01	[209]
calc.	Ni(III) empty bridge	2.28	2.03	1.99	
	Ni(III) H^- axial	2.13	2.06	2.02	
	Ni(III) H^+ axial, H^- bridge	2.13	2.02	1.96	
	Ni(III) H^- bridge	2.20	2.10	2.00	
	Ni(I) H^- bridge	2.09	2.03	2.03	

First, calculations with a formal Ni(III) oxidation state were performed. Calculations with an empty bridging position yield g-values $g_{x,y,z}$ = 2.28, 2.03, 1.99 which are in poor agreement with experiment (see Table **7.7**). When one assumes that the hydride occupies the position opposite to Cys533 at the vacant coordination site in the active centre (axially coordinated to the Ni $3d_{z^2}$ orbital, see Figure **7.3**), the calculated g-values are $g_{x,y,z}$ = 2.13, 2.06, 2.02 which are not in agreement with experimental values (see Table **7.7**). Likewise, under the assumption that both products of the heterolytic cleavage of H_2 (H^+ and H^-) remain in the active site (one in the position of the bridging ligand and one at the open coordination site) the calculated g-values are $g_{x,y,z}$ = 2.13, 2.02, 1.96. They also do not support this bonding situation (Table **7.7**). When a hydride ion occupies the position of the bridging ligand and the Ni is in a formal Ni(III) oxidation state, the calculated g-tensor principal values ($g_{x,y,z}$ = 2.20, 2.10, 2.00) agree well with those from frozen solution $g_{x,y,z}$ = 2.20, 2.15, 2.01 (see Table **7.7**). The calculated g-tensor orientation is depicted in Figure **7.1**. The orientation of the g_z-axis remains unchanged as compared with the oxidized states (along Ni–SCys533) whereas the axes in the x,y-plane change quite remarkedly. In Ni-C it is the

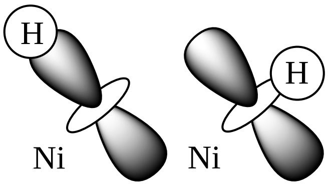

Figure 7.3: Modes of Hydride Binding to a Ni 3d$_{z^2}$ Orbital.

g$_x$-axis that points approximately to the position of the bridging ligand H$^-$ while it is the g_y-axis in the oxidized states. In Ni-C the g$_y$ axis roughly points to the terminal cysteine Cys65. For means of an independent check of the results, a spin-unrestricted QR calculation was performed (see Table **7.8**). The spin-unrestricted QR values are again very similar to the spin-restricted ZORA results. This indicates that spin-polarization does not play a major role for the electronic structure of the Ni-C state. Compared to the ZORA results, the g_x- and g_y-values are smaller in the QR calculation and the g_z-value is slightly larger (for a discussion see above). The QR g-tensor orientation is also very comparable to the ZORA calculated one. The g_x-axes differ by 3°, the g_y-axes by 2° and the g_z-axes by 2° (see Table **7.8**).

Table 7.8: Comparison of spin-restricted ZORA and spin-unrestricted QR results for the Ni-C state.

	ROKS ZORA			UKS QR		
	x	y	z	x	y	z
g-value	2.200	2.097	2.001	2.163	2.104	2.026
l_{xi}	-0.34837	0.63152	0.69269	0.40226	0.61099	0.68182
l_{yi}	0.93735	0.23761	0.25479	-0.91548	0.27569	0.29307
l_{zi}	-0.00368	0.73805	-0.67473	0.00891	0.74208	-0.67025

g_x, g_y, g_z are the g-tensor principal values; l_{xi}, l_{yi}, l_{zi} i = x, y, z are the g-tensor eigenvectors. The eigenvectors of the ZORA Hamiltonian represent an orthonormal, right-handed coordinate axes system (the triple product of the eigenvetors is +1); the eigenvectors of the QR calculation represent a left-handed coordinate axes system (the triple product of the eigenvetors is -1).

The DFT calculations suggested a g-tensor orientation before experimental studies on protein single crystals in the Ni-C state were performed. Recent experimental findings indicate that there is indeed the possibility for an agreement with the theoretical result. Here, the theoretically proposed g-tensor orientation helped to resolve an ambiguity with respect to the orientation of the x- and y-axes with respect to the crystal axes a and b ([209] and S. Foerster, personal communication).

The assumption of a hydride bridge in-plane bound to the Ni 3d$_{z^2}$ orbital (see Figure **7.3**) is in agreement with the observation of a rather large, D_2O-exchangeable ^{1}H hyperfine coupling in the Ni-C state [69, 70] (see below).

Formally, Ni-C is two electrons more reduced than the oxidized Ni-A/Ni-B states. Recent EXAFS results, however, do not report a large shift in electron density at the Ni atom [186]. This is in agreement with our model that Ni-C formally contains Ni(III) which implies that an oxidation in the ligand sphere or one of its cofactors or Fe-S clusters must take place upon Ni-A/B $\rightarrow$ Ni-C conversion. A formal Ni(I) oxidation state with a hydride bridge yields calculated g-values $g_{x,y,z}$ = 2.09, 2.03, 2.03 and does not agree with experimental data.

7.3.3.2 Hyperfine Interaction

The bonding situation when a hydride is bound axially to the Ni(III) 3d$_{z^2}$ orbital (see Figure **7.3**) does not lead to satisfying g-values (see above). The proton hyperfine tensors are also not in agreement with experimental findings, i.e. the β-CH_2 protons from Cys533 show isotropic hyperfine interactions of -0.7 and 1.7 MHz and the axial hydride displays a hyperfine tensor of [-16, -11, 14] MHz. Such a situation seems unrealistic for the Ni-C state in particular because of the small calculated couplings of the β-CH_2 protons from the bridging cysteine (see below).

Table **7.9** gives the ZORA calculated hyperfine parameter for the Ni-C state when a hydride occupies the position of the bridging ligand and is in-plane bound to the Ni 3d$_{z^2}$ orbital.

^{61}**Ni**: The isotropic ^{61}Ni hyperfine interaction from the SR UKS calculation is small and of negative sign (-2 MHz). The effect of spin-polarization (obtained when one compares SR ROKS and SR UKS calculations) on the anisotropic hyperfine tensor is small and increases A'_x by 3 MHz, A'_y is reduced by the same amount and A'_z remains nearly unchanged. The anisotropic hyperfine tensor exhibits a large effect upon consideration of spin-orbit coupling. SO coupling reduces the anisotropic components by a factor of two compared to the SR ROKS case. This drastic reduction seems unrealistic since the spin-polarized tensor is in good agreement with the experimental value for the hyperfine splitting along g_z by Moura *et al.* (76 MHz) [45]. Values for the splitting along the g_x and g_y components were not given.

^{57}**Fe**: The isotropic ^{57}Fe hyperfine splitting is very small (-0.9 MHz in the SR UKS calculation). The anisotropic hyperfine tensor shows only a small effect upon consideration of spin-polarization (A'_x increases while A'_y and A'_z slightly decrease; cf. columns 1 and 2). Spin-orbit coupling slightly decreases A'_x by 0.5 MHz and increases A'_y by 1 MHz (compare columns 1 and 3). This small value of the ^{57}Fe hyperfine coupling is in agreement with the experimental finding by Huyett *et al.* [61] who reported an absence of any ^{57}Fe-ENDOR signal in the Ni-C state.

^{33}**S**: Of the four cysteinyl sulphur atoms only that of the bridging cysteine Cys533 shows a significant hyperfine interaction (isotropic hyperfine interaction +14 MHz). The isotropic hyperfine couplings of the remaining three sulphur nuclei are smaller (+0.9 MHz for Cys65, +6 MHz for Cys68 and +1.9 MHz for Cys530). The ^{33}S coupling of Cys533 is very similar to the Ni-B case and is in agreement with the g-tensor orientation which has its g_z axis along the Ni–SCys533 bond.

^{1}**H**: The β-CH$_2$ protons of the Cys533 display isotropic and anisotropic hyperfine couplings of the same order of magnitude as in the Ni-B state. The isotropic part is slightly reduced by 1-2 MHz which was also found experimentally [70]. Whitehead *et al.* assigned this reduction to a slightly different torsional angles of the β-CH$_2$ protons with respect to the sulphur 3p$_z$ orbital [70]. According to the calculations, it is a shift of unpaired spin density away from the bridging cysteine to the terminal cysteine Cys530 that is responsible for this reduction. The two β-CH$_2$ protons from Cys530 exhibit nearly identical hyperfine interactions with a_{iso} = +7 MHz and +6 MHz. These may correspond to the unassigned ^{1}H hyperfine splitting $\leq$ 5 MHz in the Ni-C state which were shown not to be solvent-exchangeable [70].

The bridging hydride exhibits a rather unusual hyperfine interaction. The isotropic contribution is positive in both SR ROKS and SO+SR ROKS calculations but negative when spin-polarization is considered. The hydride is bound to the unpaired spin density in a Ni 3d$_{z^2}$ orbital (see Figure **7.3**). In case of an axial binding (see Figure **7.3**, left) a large isotropic hyperfine interaction is expected. If the analogy to an α proton bound to an unpaired spin in a carbon 2p$_z$ orbital holds, the sign of the isotropic hyperfine interaction may be negative in case of a hydride bound in the nodal plane of a Ni 3d$_{z^2}$ orbital (see right hand side of Figure **7.3**). Spin-polarization also increases the anisotropic hyperfine interaction by 3 MHz. The effect of SO coupling on the anisotropic hyperfine interaction, however, is small. The calculated hyperfine tensor is in good agreement with experiments where a total hyperfine tensor of [+15, -22, -25] MHz was reported [69] which gives an isotropic hyperfine interaction of -11 MHz. The value for the A_z component given by Fan *et al.* [69] cannot be rationalized since no spectra near the z-component were measured. From the spin-polarized calculation one arrives at [-20, -16, +10] MHz with a_{iso} = -9 MHz which is in good agreement with experiment. This large hyperfine coupling was shown to be D$_2$O exchangeable and the corresponding ^{2}H coupling was detected [69, 70, 196]. A nickel hydride species would be easily solvent-exchangeable due to the acidity of the hydrogen. Furthermore, the large coupling was also lost upon photoillumination and conversion to the Ni-L form for which photodissociation of a proton ligand was discussed [70]. When such a removal of either the hydride bridge or a proton from the bridging position is investigated in the conversion to the Ni-L species, one also has an *a posteriori* confirmation or falsification of the electronic structure of the precursor Ni-C form.

Table 7.9: ZORA calculated hyperfine interaction in Ni-C in MHz.

Nucleus	hf component	SR ROKS	SR UKS	SR+SO ROKS
^{61}Ni	a_{iso}	-20-20	-2.16	-55.11
	$A_x^{'}$	+62.14	+65.43	+31.72
	$A_y^{'}$	+16.63	+13.89	+7.83
	$A_z^{'}$	-78.78	-79.33	-39.55
^{57}Fe	a_{iso}	+0.04	-0.93	+0.23
	$A_x^{'}$	-2.81	-1.88	-3.38
	$A_y^{'}$	+0.51	+0.24	+1.15
	$A_z^{'}$	+2.29	+1.65	+2.23
$^{33}S_{Cys533}$	a_{iso}	+11.35	+14.45	+10.70
	$A_x^{'}$	-24.70	-25.21	-24.94
	$A_y^{'}$	-24.58	-24.20	-25.22
	$A_z^{'}$	+49.28	+49.43	+50.16
$^{1}H_{Cys533-H1}$	a_{iso}	+10.56	+11.85	+10.48
	$A_x^{'}$	-1.74	-1.66	-1.75
	$A_y^{'}$	-0.89	-1.03	-0.88
	$A_z^{'}$	+2.63	+2.69	+2.65
$^{1}H_{Cys533-H2}$	a_{iso}	10.55	12.90	10.50
	$A_x^{'}$	-2.60	-2.49	-2.76
	$A_y^{'}$	-0.09	-0.96	-0.05
	$A_z^{'}$	+2.70	+3.44	+2.80
$^{1}H_{Cys530-H1}$	a_{iso}	+7.01	+7.25	+6.98
	$A_x^{'}$	-1.68	-1.63	-1.79
	$A_y^{'}$	-0.47	-1.00	-0.51
	$A_z^{'}$	+2.13	+2.62	+2.30
$^{1}H_{Cys530-H2}$	a_{iso}	+5.68	+5.62	+5.66
	$A_x^{'}$	-1.18	-1.26	-1.18
	$A_y^{'}$	-0.85	-0.97	-0.97
	$A_z^{'}$	+2.02	+2.22	+2.14
$^{1}H^{-}$ bridge	a_{iso}	+10.04	-8.65	+10.89
	$A_x^{'}$	-8.00	-11.12	-9.77
	$A_y^{'}$	-4.19	-7.46	-4.88
	$A_z^{'}$	+12.15	+18.57	+14.65

7.3.4 Ni-L

7.3.4.1 g-Tensor

The reduced Ni-C state is light-sensitive [67, 217]. Upon illumination at low temperatures

$$\mathrm{Ni-C} \xrightarrow{h\nu} \mathrm{Ni-L} \tag{7.2}$$

a new rhombic signal evolves with $g_{x,y,z}$ = 2.29, 2.13, 2.05 (see Table **7.1**). In the oxidized Ni-A and Ni-B states and the reduced Ni-C state g_z was always close to the free electron value from which a 3d_{z^2} ground state was deduced. In Ni-L, the g_z-value argues for a d_{xy} or $d_{x^2-y^2}$ ground state [66]. The photoreaction is reversible and tempering at 180 K fully recovers the Ni-C signal [67, 218]. After photolysis, the large ^{1}H-ENDOR coupling is lost and photodissociation of a ligand was discussed [70]. When the hydride would be lost upon illumination, the Ni remains in its formal Ni(III) oxidation state.

$$\mathrm{Ni(III)-C} \xrightarrow{-H^-} \mathrm{Ni(III)-L} \tag{7.3}$$

The calculated g-values for this situation are $g_{x,y,z}$ = 2.28, 2.03, 1.99. They cannot explain the shift of the g_z value in the Ni-L state compared to the Ni-C state. Therefore, this configuration for the Ni-L state appears implausible.

Upon removal of a proton from the bridging position, the Ni atom is left in its formal Ni(I) state

$$\mathrm{Ni(III)-C} \xrightarrow{-H^+} \mathrm{Ni(I)-L} \quad . \tag{7.4}$$

In the protein, the dissociated proton might be taken up by a nearby amino acid, i.e. the arginine Arg463 residue which resides like a lid on top of the active site and might be protonated at the -NH_2 group. The calculated ZORA values ($g_{x,y,z}$ = 2.26, 2.10, 2.05) for Ni-L are in excellent agreement with the frozen solution values (Table **7.1**). The difference between spin-restricted ZORA and spin-unrestricted QR calculations is small and follows the trends discussed above (see Table **7.10**).

The QR calculated g-tensor orientation is rotated by 18° in the yz-plane compared to the ZORA orientation. (The g_x-axes differ by 1°, the g_y-axes by 18° and the g_z-axes by 18°.) The orientation of the g-tensor in the Ni-L state is similar to that of the Ni-C state with the g_x-axis pointing to the position of the empty bridge (see Figure **7.4**).

7.3.4.2 Hyperfine Interactions

The calculated hyperfine parameters for the Ni-L state are collected in Table **7.11**.

Table 7.10: Comparison of spin-restricted ZORA and spin-unrestricted QR results for the Ni-L state.

	ROKS ZORA			UKS QR		
	x	y	z	x	y	z
g-value	2.257	2.097	2.049	2.211	2.138	2.090
l_{xi}	-0.32790	-0.86757	-0.37391	0.34651	-0.70001	-0.62443
l_{yi}	0.94351	-0.28079	-0.17589	-0.93742	-0.23415	-0.25771
l_{zi}	0.04761	-0.41046	0.91063	-0.03419	-0.67466	0.73734

g_x, g_y, g_z are the g-tensor principal values; l_{xi}, l_{yi}, l_{zi} i = x, y, z are the g-tensor eigenvectors. The eigenvectors of the ZORA Hamiltonian represent an orthonormal, right-handed coordinate axes system (the triple product of the eigenvetors is +1); the eigenvectors of the QR calculation represent a left-handed coordinate axes system (the triple product of the eigenvetors is -1).

^{61}**Ni**: The isotropic ^{61}Ni hyperfine interaction obtained from a SR UKS calculation is of positive sign and small (+12 MHz). The influence of spin-polarization on the anisotropic hyperfine tensor (obtained from a comparison of columns 1 and 2) lies in a reduction of the A'_x component by 8 MHz, the A'_y component is reduced in absolute values by 6 MHz and A'_z by 2 MHz. Spin-orbit coupling further reduces A'_x by 45 MHz, A'_y by 25 MHz and A'_z by 20 MHz in absolute values (comparing SR UKS and SR+SO ROKS calculations). The effect of spin-polarization is certainly overestimated and further work on spin-orbit-coupled spin-polarized relativistic calculations is needed. Compared to the other states, the A'_z component is reduced by $\approx$ 25 MHz. A'_x component increases by the same amount. Here, maximum coupling is no longer obtained along the z- but along the x-direction. This indicates a redistribution of the spin density from axiality with preference of the z-direction to a more evenly distributed unpaired spin in the xy-plane. This is in agreement with experimental findings for the soluble hydrogenase from *Ralstonia eutropha* (SH) in the Ni-L state [60], in which hyperfine splittings of 56 MHz, 28 MHz and 14 MHz were obtained at the g_x-, g_y- and g_z-components, respectively, and recent results for the hydrogenase from *D. vulgaris* Miyazaki F (S. Foerster, personal communication).

^{57}**Fe**: The isotropic hyperfine interaction (-0.8 MHz in the SR UKS calculation) is small and of the same order as in the Ni-C, Ni-A and Ni-B states. In the case of a vacant bridging position, the anisotropic ^{57}Fe hyperfine interaction is larger than in the other paramagnetic states investigated so far. The consideration of spin-polarization leads to an increase of the anisotropic hyperfine tensor components by 5 MHz in magnitude along A'_x, 2.5 MHz along A'_y and 3.5 MHz along A'_z. The inclusion of spin-orbit coupling, on the other hand, does not show this large effect. The SR+SO ROKS values are very similar to

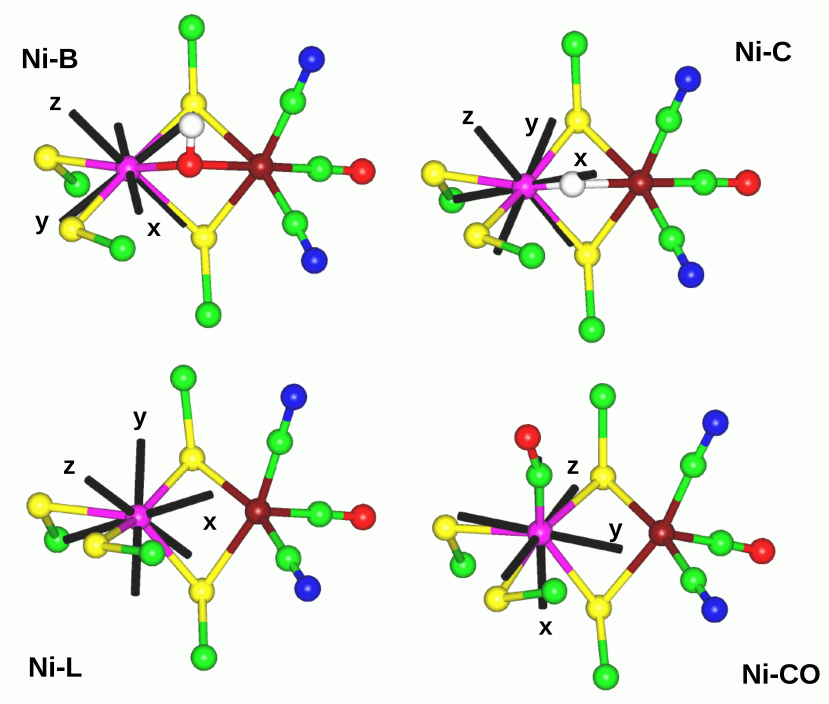

Figure 7.4: Comparison of the ZORA calculated g-tensor orientations for the Ni-B, Ni-C, Ni-L and Ni-CO paramagnetic states of [NiFe] hydrogenase.

those obtained at the SR ROKS level of theory (compare columns 3 and 1). This shows that the hyperfine interaction is now mostly through space with the electron spin at the Ni and that the direct transfer of unpaired spin density in the Ni-A, Ni-B and Ni-C states is mediated by the bridging ligands. There are no experimental ^{57}Fe-ENDOR data to compare with.

^{33}**S**: The sulphur nuclei also sense the more evenly distributed spin density. The sulphur nucleus of Cys533 shows a reduced anisotropic hyperfine interaction, while the isotropic term (+16 MHz) remains constant compared with the Ni-C form. The sulphur nuclei of the other three cysteines also exhibit ^{33}S hyperfine splittings which are not drastically smaller than that of Cys533 (SCys530 +7 MHz, SCys68 +15 MHz, SCys65 +10 MHz). The isotropic component of Cys68 is comparable to that of Cys533 and only differs in the smaller anisotropic part. The hyperfine interactions of the sulphur nuclei of Cys530 and Cys65 are slightly smaller. Neither spin-polarization nor the consideration of spin-orbit coupling show large effects on the anisotropic hyperfine tensors. The maximum effect of spin-polarization is obtained for the sulphur nuclei of Cys533 and Cys530 in which spin-polarization reduces the A_z' component by 3 MHz.

^{1}**H**: The largest hyperfine coupling of the hydride bridge in Ni-C is no longer present in the Ni-L form. The decrease of the anisotropic hyperfine interaction of the sulphur nucleus of Cys533 is also shown by the β-CH$_2$ protons of that residue. The isotropic parts are reduced by 3.5 and 3 MHz compared to the Ni-C form. This was also observed experimentally by Whitehead *et al.* [70]. The couplings of 12.8 MHz in the Ni-C form reduce to $\approx$ 10 MHz in the Ni-L state. The latter protons were neither photolabile nor D$_2$O-exchangeable. As a consequence of the sulphur nuclei being closer to equivalence, the β-CH$_2$ protons of the respective cysteines also show hyperfine interactions of the order of 3-7 MHz isotropic hyperfine interaction and may thus be detectable by ^{1}H-ENDOR of the Ni-L state.

Table 7.11: ZORA calculated hyperfine interaction in Ni-L in MHz.

Nucleus	hf component	SR ROKS	SR UKS	SR+SO ROKS
^{61}Ni	a_{iso}	-23.76	+12.22	-76.04
	A'_x	+97.27	+89.32	+45.63
	A'_y	-42.11	-36.30	-11.93
	A'_z	-55.16	-53.01	-33.69
^{57}Fe	a_{iso}	+0.05	-0.83	+0.10
	A'_x	-2.22	-7.16	-2.39
	A'_y	+0.33	+2.93	+0.64
	A'_z	+1.90	+4.24	+1.73
$^{33}S_{Cys533}$	a_{iso}	+12.16	+15.98	+11.41
	A'_x	-14.26	-13.21	-14.33
	A'_y	-14.12	-10.98	-15.08
	A'_z	+28.39	+24.19	+29.40
$^{33}S_{Cys530}$	a_{iso}	+2.70	+7.22	+1.42
	A'_x	-8.51	-7.77	-10.74
	A'_y	-7.83	-6.69	-7.76
	A'_z	+10.23	+7.16	+10.75
$^{33}S_{Cys68}$	a_{iso}	+15.72	+15.49	+15.30
	A'_x	-5.17	-4.76	-5.09
	A'_y	-5.06	-2.40	-5.67
	A'_z	+10.23	+7.16	+10.75
$^{33}S_{Cys65}$	a_{iso}	+5.32	+10.27	+5.22
	A'_x	-2.67	-3.75	-2.96
	A'_y	-2.65	-1.42	-2.26
	A'_z	+5.02	+5.17	+5.22

continued on next page

Nucleus	hf component	SR ROKS	SR UKS	SR+SO ROKS
^{1}H$_{Cys533-H1}$	a$_{iso}$	+5.50	+6.53	+5.44
	A$'_x$	-1.35	-1.59	-1.38
	A$'_y$	-0.75	-0.49	-0.76
	A$'_z$	+2.09	+2.07	+2.15
^{1}H$_{Cys533-H2}$	a$_{iso}$	+6.04	+7.05	+5.95
	A$'_x$	-2.37	-2.77	-2.59
	A$'_y$	-0.75	-0.49	-0.76
	A$'_z$	+2.88	+4.25	+3.12
^{1}H$_{Cys530-H1}$	a$_{iso}$	+6.21	+6.05	+6.15
	A$'_x$	-1.74	-1.95	-1.86
	A$'_y$	-0.65	-1.46	-0.77
	A$'_z$	+2.39	+3.40	+2.62
^{1}H$_{Cys530-H2}$	a$_{iso}$	+4.61	+4.65	+4.56
	A$'_x$	-1.18	-1.41	-1.20
	A$'_y$	-0.85	-1.21	-0.96
	A$'_z$	+2.04	+2.62	+2.17
^{1}H$_{Cys68-H1}$	a$_{iso}$	+3.45	+3.40	+3.44
	A$'_x$	-2.13	-2.92	-2.34
	A$'_y$	-0.91	-1.48	-1.02
	A$'_z$	+3.02	+4.40	+3.95
^{1}H$_{Cys68-H2}$	a$_{iso}$	+6.32	+6.56	+6.27
	A$'_x$	-1.20	-1.20	-1.24
	A$'_y$	-0.60	-0.66	-0.61
	A$'_z$	+1.78	+1.86	+1.85

The calculated hyperfine interactions, in conjunction with the good results obtained for the g-tensor principal values, lead to a model picture of the Ni-L state and, *a posteriori*, support the proposed Ni-C binding situation.

7.3.5 Ni-CO

The [NiFe] hydrogenase is irreversibly inhibited by binding of exogenous CO. This is accompanied by a dramatic change in EPR g-values (g$_{x,y,z}$ = 2.12, 2.07, 2.02) (see Table **7.1**) and a large almost isotropic ^{13}C hyperfine coupling of 85 MHz [63] at the g-components. Initially, it was discussed that the Ni-C state binds CO [40, 213].

A number of possible CO binding possibilities to a Ni(III) species were investigated by relativistic DFT calculations, the results of which (g-tensor principal values and ^{13}C isotropic hyperfine coupling constant) are given in Table **7.12**. With respect to the g-tensor principal values alone, the bonding situation where CO binds at the Fe atom and points to the position of the bridging ligand shows best agreement with the experimental values. The isotropic hyperfine interaction, in contrast, is far too small. When the CO axially binds to the Ni(III), a bonding situation proposed by van der Zwaan *et al.* [63] due to the largely isotropic hyperfine interaction, the calculated ^{13}C isotropic hyperfine interaction is by a factor of two larger than the experimental value irrespective of the presence or absence of a bridging hydride (184 MHz and 155 MHz, respectively).

Table 7.13: Results of investigated CO-binding to a Ni(III) species

Binding situation	g-values	^{13}C a_{iso} [MHz]
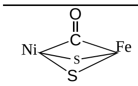 CO bridging	2.10, 2.04, 2.01	11.6
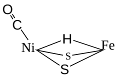 CO axial @Ni; H$^-$ bridge	2.07, 2.05, 2.01	183.9
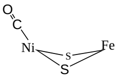 CO axial @Ni; no bridge	2.20, 2.03, 2.00	154.6
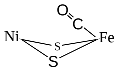 CO@Fe	2.11, 2.06, 2.01	9.9
experiment	2.12, 2.07, 2.02	85

Only recently, Happe *et al.* [58] brought forward the hypothesis, that it could actually be the Ni-L state that binds CO. This hypothesis was investigated by probing different CO bonding situations to a Ni-L species (see Table **7.13**). A possible binding place of exogenous CO is the position of the bridging ligand. CO and H$^-$ would then be in competition for binding to the Ni and the stronger Ni-CO bond would inhibit the enzyme. In order to achieve this bonding situation, photodissociation of the bridging hydride or a proton is also required. The calculated g-values for a Ni(I) with a CO molecule bridging Ni and Fe are $g_{x,y,z}$ = 2.09, 2.05, 1.99 which are somewhat too small. The calculated isotropic ^{13}C hyperfine interaction is also too small (26 MHz) compared with experimental data and such a bonding situation for Ni-CO may therefore be ruled out. For the same reasons, a Ni(I) with CO binding on the Fe atom and the CO pointing towards the Ni atom, may be excluded, too.

If one assumes that the Ni(I)-L cluster model binds CO in an axial position at the Ni, the calculated g-tensor principal values are $g_{x,y,z}$ = 2.11, 2.06, 2.00 and agree very well with the experimental data

Table 7.14: Results of investigated CO-binding to a Ni(I) species

Binding situation	g-values	^{13}C a$_{iso}$ [MHz]
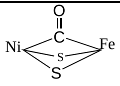 CO bridging	2.09, 2.05, 1.99	25.9
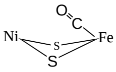 CO@Fe	2.09, 2.05, 1.99	26.5
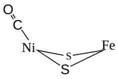 CO axial @Ni	2.11, 2.06, 2.00	72.3
experiment	2.12, 2.07, 2.02	85

(g$_{x,y,z}$ = 2.12, 2.07, 2.02). The spin-unrestricted QR results (see Table **7.14**) are very similar both in magnitude and orientation which indicates that spin-polarization is not of major importance for the Ni-CO state. Also the isotropic ^{13}CO hyperfine interaction is well reproduced by spin-unrestricted SR ZORA calculations (72 MHz calculated vs. 85 MHz experimental, see Table **7.13**). The proposed g-tensor orientation from the ZORA calculation is shown in Figure **7.4**. It quite drastically differs from that of the other investigated paramagnetic states of the [NiFe] hydrogenase. In the CO-inhibited form, the g_x-axis points to the axially coordinated CO molecule and g_y points approximately to the vacant bridging position. Compared to the formal Ni(III) Ni-B state the orientation in the Ni(I)-CO form corresponds to an interchange of $x-$ and z-axes.

Table 7.15: Comparison of spin-restricted ZORA and spin-unrestricted QR results for the Ni-CO state.

	ROKS ZORA			UKS QR		
	x	y	z	x	y	z
g-value	2.112	2.056	2.000	2.108	2.070	2.016
l_{xi}	-0.87738	0.01010	0.47969	0.89049	0.04804	0.45247
l_{yi}	-0.30734	0.75591	-0.57805	0.23208	0.80738	-0.54247
l_{zi}	-0.36844	-0.65460	-0.66011	0.39137	-0.58808	-0.70781

g_x, g_y, g_z are the g-tensor principal values; l_{xi}, l_{yi}, l_{zi} i = x, y, z are the g-tensor eigenvectors. The eigenvectors of the ZORA Hamiltonian represent an orthonormal, right-handed coordinate axes system (the triple product of the eigenvetors is +1); the eigenvectors of the QR calculation represent a left-handed coordinate axes system (the triple product of the eigenvetors is -1).

The calculation was repeated using the large triple-ζ basis set (basis IV in ADF nomenclature). The isotropic ^{13}CO hyperfine interaction was slightly reduced to +67.61 MHz and A_{aniso} = [-6.04, -1.61, 7.64] MHz. The agreement with the experimental values a_{iso} = 85 MHz and A_{aniso} = [-4, 0, 5] MHz [63] is more than satisfying. The assignment of the CO-treated enzyme to a Ni(I) species without a hydride bridge is in agreement with the absence of any line broadening in EPR spectra upon H_2O/ D_2O solvent exchange of the Ni-CO EPR signal [213]. In Ni-C, there is such an effect [67] which can be assigned, according to the calculations, to originate from the ^{1}H hyperfine coupling of the bridging hydride. Furthermore, the carbon monoxide-treated hydrogenase is light-sensitive and upon illumination the Ni-L EPR spectrum is fully recovered [213].

The proposed coordination of CO axially bound to the Ni is in agreement with most recent experimental findings. The X-ray structure analysis of the CO-inhibited [Fe]-only hydrogenase from *Clostridium pasteurianum* CpI also showed axial binding of CO to one of the Fe atoms in the active site [219]. The recently obtained X-ray structure of the reduced, carbon monoxide treated [NiFe] hydrogenase from *D. vulgaris* Miyazaki F contains two conformations of the bound CO (Y. Higuchi, personal communication). One shows a CO bound to the Ni atom opposite to Cys533 in an unusual bent mode, the other one shows a CO molecule linearly bound to the Ni atom. At the moment, a statement about the oxidation state of the Ni atom in the crystallized CO-treated enzyme cannot be made. It may be a product of the active centre either in the Ni-Si, Ni-L or Ni-R form. Preliminary structural data for the bent CO coordination are for the Ni–CO distance 1.76 Å, the C=O bond length is 1.22 Å with a Ni–C–O angle of 118 ° (Y. Higuchi, personal communication). This bonding situation is discussed in Chapter 9.

Recent EXAFS investigations of the Ni-Si CO-treated enzyme gave a Ni–CO distance of 1.78 Å, a Ni–O distance of 2.90 Å which led to a C–O bond length of 1.12 Å [55]. The structural parameters from the calculations are 1.74 Å for the Ni–CO distance, 2.93 Å for the Ni–O distance and 1.21 Å for the C=O bond length. The agreement is satisfying but the authors suggested a slightly different bonding situation in which the CO would be bound to the Ni atom but would point towards the Fe atom [55].

The inhibition of the enzymatic cycle by CO binding in an axial position to the Ni atom suggests a participation of this coordination site in the mechanism.

7.4 Discussion of Hyperfine Interactions

7.4.1 ^{61}Ni Hyperfine Interaction

Figure **7.5** shows the relative orientations of the SO-coupled ZORA calculated g-tensors and the ^{61}Ni hyperfine tensor. For Ni-A the angle between g_x and A_x is 10°, between g_y and A_y 10°, between g_z

and A_z 9°. For Ni-B, the angles are only 2°, 15° and 15°, respectively. For Ni-C, the hyperfine tensor principal axes system is rotated by 42° away from g_x and g_y and by 18° from g_z. For the Ni-L form, the angle between g- and A-tensor principal axes system is 18° for the x-direction, 21° for the y-direction and 18° for the z-direction. Experimentally, only the ^{61}Ni hyperfine splitting along the g-tensor components is known. The information gained from the theoretically postulated relative orientations of g- and A-tensor principal axes systems may help to improve the analysis and simulation of experimental spectra in frozen solution. Independently, the relative orientation of the g-tensor and ^{61}Ni A-tensor coordinate axes systems could be determined from angular-dependent EPR spectra of ^{61}Ni enriched protein single crystals.

Figure 7.5: Relative orientations of g- and ^{61}Ni A-tensors from SR+SO ZORA BP86/IV calculations

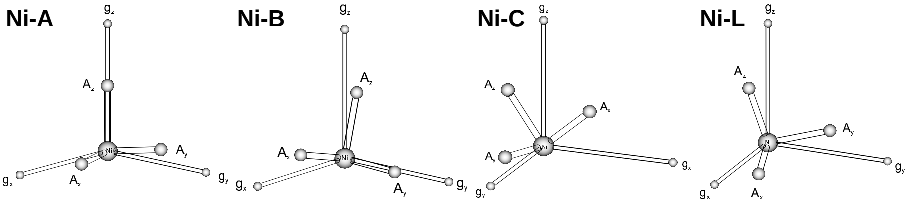

For Ni-A, Ni-B, and Ni-C the magnitude of the A_z hyperfine interaction is almost unchanged (-61 MHz for Ni-A, -70 MHz for Ni-B, -81 MHz for Ni-C). This is in agreement with findings by Moura *et al.* [45] for the Ni-A and Ni-C forms and Albracht *et al.* [59] for the Ni-A form. The authors obtained hyperfine splitting of 76 MHz along the g_z component and implicitly assumed A_z to be parallel to g_z. According to the calculations, in the Ni-L state A_z reduces to -41 MHz. Ni-L is believed to be a formal Ni(I) oxidation state with the unpaired spin in a 3d$_{x^2-y^2}$ orbital. As a consequence, the hyperfine interaction is no longer largest along the z-axis associated with a 3d$_{z^2}$ SOMO but along A_x. This is supported by a recent analysis of ^{61}Ni enriched samples from the [NiFe] hydrogenase from *D. vulgaris* Miyazaki F (S. Foerster, personal communication).

Spin-polarization effects seem to be very important for the description of hyperfine interaction along the z-direction. Spin-orbit-coupled spin-restricted calculations underestimate the A_z hyperfine interaction by a factor of two. Spin-orbit coupling reduces the hyperfine interactions A_x and A_y quite drastically and brings them into the range of experimental values. In the Ni-A, Ni-B and Ni-C forms, the unpaired spin density distribution is of spherical symmetry along the Ni–SCys533 bond. Therefore, one might expect spin-polarization to be important for this direction. The hyperfine interactions perpendicular to z, are obviously very sensitive to the effect of spin-orbit coupling. For the time being, one may not accurately differentiate between the effects of spin-polarization and spin-orbit coupling. Once spin-polarized, SO-coupled hyperfine tensors become available further insight is expected.

It is very difficult to comment on the signs and magnitudes of the isotropic ^{61}Ni hyperfine interactions. They are calculated to be +13 MHz for Ni-A, +5 MHz for Ni-B, -2 MHz for Ni-C, and +12 MHz for Ni-L. They are small and of the same order of magnitude for all four paramagnetic states. Due to the absence of reliable experimental data, a definitive conclusion may not be drawn.

7.4.2 ^{57}Fe Hyperfine Interaction

The calculated ^{57}Fe interaction is very small in all paramagnetic states. This indicates that the Fe is in its formal Fe(II) oxidation state in a low spin configuration due to the strong ligand field caused by the CO and CN ligands. Experimentally, there is only one value for the Ni-A state of $\approx$ 1 MHz from ^{57}Fe-ENDOR measurements [61]. In the Ni-B and Ni-C states no ^{57}Fe-ENDOR signal could be detected but a ^{57}Fe hyperfine coupling of 0.8 MHz for the Ni-B state was recently reported (J. Moura, B. M. Hoffman personal communication). The signs of the ^{57}Fe hyperfine couplings are not known from experiment. The calculated isotropic hyperfine interaction from spin-unrestricted ZORA calculations is smaller than or equal to -1 MHz and makes a comparison with experimental data very difficult. The anisotropic part of the ^{57}Fe hyperfine tensor is also generally very small. The anisotropic contribution in the Ni-L form is a factor of 3-5 larger than that of the corresponding Ni-A, Ni-B and Ni-C states. In our model, the Ni-L form exhibits a vacant bridging position while an O^{2-}, OH^-, or a H^- bridge is present in the other forms, respectively. This may indicate that the presence of a bridging ligand significantly reduces the anisotropic hyperfine interaction of the Fe atom. Unfortunately, there is no experimental ^{57}Fe coupling for the Ni-L state which is predicted to be larger than in the other paramagnetic forms.

7.4.3 ^{33}S Hyperfine Interaction

Experimentally, Albracht *et al.* concluded that there was hyperfine interaction due to *one* ^{33}S nucleus only in the oxidized states [62]. This interpretation is supported by the ZORA calculations. The sulphur nucleus of the cysteine Cys533 exhibits significant isotropic and anisotropic hyperfine interaction. The isotropic hyperfine interaction is largest in the Ni-A form ($\approx$ 30 MHz), and about half of that in the Ni-B, Ni-C, and Ni-L forms. The anisotropic part is almost of uniaxial symmetry. The decrease in isotropic hyperfine interaction in the Ni-B, Ni-C and Ni-L forms with respect to Ni-A is compensated by an increase in the anisotropic contribution. The total hyperfine tensor thus remains nearly unchanged in the four paramagnetic states. Experimentally, there are only data available for the oxidized Ni-B form in the hydrogenase from *Wollinella succinogenes* which is only remotely related to the 'standard hydrogenases'. The ^{33}S hyperfine tensor of [27, 39,–] MHz given by Albracht *et al.* [62] appears to be too large for the x- and y- components. No value for the A_z component could be obtained.

In the Ni-L form, the spin density is not only delocalized onto the bridging cysteine Cys533 but all four Ni-coordinating cysteines may exhibit an appreciable ^{33}S coupling according to the calculations. This is due to the formal Ni(I) oxidation state in Ni-L. The isotropic hyperfine interaction is largest for the bridging Cys533 and Cys68 (both exhibit an isotropic coupling of +15 MHz). The terminal cysteines Cys530 and Cys68 display +7 and +10 MHz isotropic couplings, respectively. This is in agreement with the finding that the ^{61}Ni hyperfine interaction in Ni-L is no longer largest along the z-direction but in the x,y-plane (see above). This leads to a more evenly distributed spin density onto all four sulphur atoms. The sulphur nuclei are brought closer to equivalence and the coordination sphere of the Ni therefore closer to being symmetric.

7.4.4 ^{17}O Hyperfine Interaction

In order to explain the experimental ^{17}O hyperfine splitting in EPR spectra of the oxidized states, there are potentially three candidates as ligands bridging the Ni and Fe atoms in the active centre: a water molecule H_2O, a hydroxo OH^- or an oxo O^{2-} ligand. A water molecule leads to an isotropic ^{17}O coupling of -23.50 MHz and an anisotropic coupling of [+1.94, +0.84, -2.79] MHz. Such a large isotropic coupling is not observed experimentally and a water bridging ligand can be ruled out on the basis of g-tensor calculations (see above) and the calculated hyperfine interaction. A μ-oxo bridge and a hydroxo bridge would both give very similar isotropic couplings of -9 and -7 MHz, respectively. The anisotropy, however, would allow a discrimination between the two candidates. The anisotropy of a hydroxo ligand [+2, +1, -3] MHz is very moderate compared to [+30, +14, -44] MHz for an oxo bridge. A definite comparison with experimental data is very difficult. The experimental data by van der Zwaan *et al.* [63] come from estimates of the increase of EPR line widths upon re-oxidation with $^{17}O_2$. The values are all below the intrinsic EPR linewidth of typical [NiFe] hydrogenase samples and must be treated with care. Here, orientation-selected ^{17}O-ENDOR would be of importance and contribute to a more profound characterization of the bridging ligand in the oxidized states. Furthermore, from pulsed-ENDOR or ESEEM spectroscopies the ^{17}O quadrupole tensor would also be accessible. These experiments are in progress (J. Moura, B. M. Hoffman personal communication). Unfortunately, the calculated quadrupole tensors of $^{17}O^{2-}$[+0.29, +0.03, -0.32] MHz and $^{17}OH^-$ [+0.31, +0.05, -0.36] MHz are very similar and would make a definite assignment difficult.

7.4.5 ^{1}H Hyperfine Interaction

In all four paramagnetic states Ni-A, Ni-B, Ni-C and Ni-L the β-CH$_2$ protons of the bridging cysteine amino acid Cys533 exhibit a large hyperfine interaction. For these two couplings, the difference between the Ni-A, Ni-B and Ni-C forms is small. This indicates that a major part of the spin density is oriented along the Ni–SCys533 bond in all three states. There is no major spin density reorientation between the three states.

The difference between the Ni-A and Ni-B forms lies in a protonation of the bridging oxo ligand for Ni-B. This not only causes a massive ^{17}O coupling for Ni-A (see above) but also leads to an elongation of all Ni–S bonds. This is responsible for the absence of a third β-CH$_2$ proton hyperfine interaction in the Ni-A state. In the Ni-C form, the spin density slightly shifts to the terminal cysteine Cys530 and an isotropic coupling of 5-6 MHz is predicted for the β-CH$_2$ of this amino acid residue. Furthermore, a bridging hydride in the Ni-C state exhibits a large hyperfine interaction. In Ni-L, the largest hyperfine interaction is lost upon illumination. The oxidation to a Ni(I) species results in a more evenly spread spin density distribution in the xy-plane (see above) away from the preferred axiality in the Ni-A, Ni-B and Ni-C states. As a consequence, a larger number of hyperfine interactions from β-CH$_2$ protons is predicted and the coupling of those from Cys533 are reduced by a factor of two compared to the other states.

7.5 ^{14}N Hyperfine and Quadrupole Interaction

Experimentally, hyperfine and quadrupole interactions due to *one* nitrogen nucleus were observed by ESEEM spectroscopy. Chapman *et al.* measured ESEEM spectra of a frozen protein solution of the [NiFe] hydrogenase from *D. gigas* in the Ni-A and Ni-C states [68]. A relatively small quadrupole coupling (e^2qQ/h = 1.9 MHz) was obtained for both forms and tentatively assigned to a directly coordinated nitrogen of a weakly coupled imidazole [68].

Protein single crystals of the [NiFe] hydrogenase from *D. vulgaris* Miyazaki F were investigated by 3-pulse ESEEM spectroscopy. A set of quadrupole parameters for Ni-A (e^2qQ/h = 1.98 MHz and η = 0.37) and for Ni-B (e^2qQ/h = 1.90 and η = 0.37) were determined [184]. These values are almost identical with those of Dikanov *et al.* who obtained e^2qQ/h = 1.87 and η = 0.39 for both Ni-A and Ni-B states of frozen protein solution of the [NiFe] hydrogenase from *D. gigas* [220]. The isotropic hyperfine interaction is about 2 MHz. Based on the magnitudes of the quadrupole parameters, both studies assign the coupling to the N$^\epsilon$ nitrogen of a histidine, possibly that of His88 (His72 in *D. gigas*) which might be hydrogen bonded to the bridging cysteine Cys533.

This assignment was verified by ZORA calculations by adding a histidine protonated at the N$^{\epsilon}$ to the bare active site cluster models. This hydrogen bond would allow the transfer of unpaired spin density from the bridging cysteine Cys533 to the nearby histidine His72.

Complete geometry optimizations were carried out on the cluster models consisting of approx. 50 atoms. Hyperfine and quadrupole parameters were then calculated from a spin-polarized scalar-relativistic BP86 DFT calculation using a double-ζ basis set (basis II in ADF nomenclature). The geometry-optimized structures are given in Figure **7.6**.

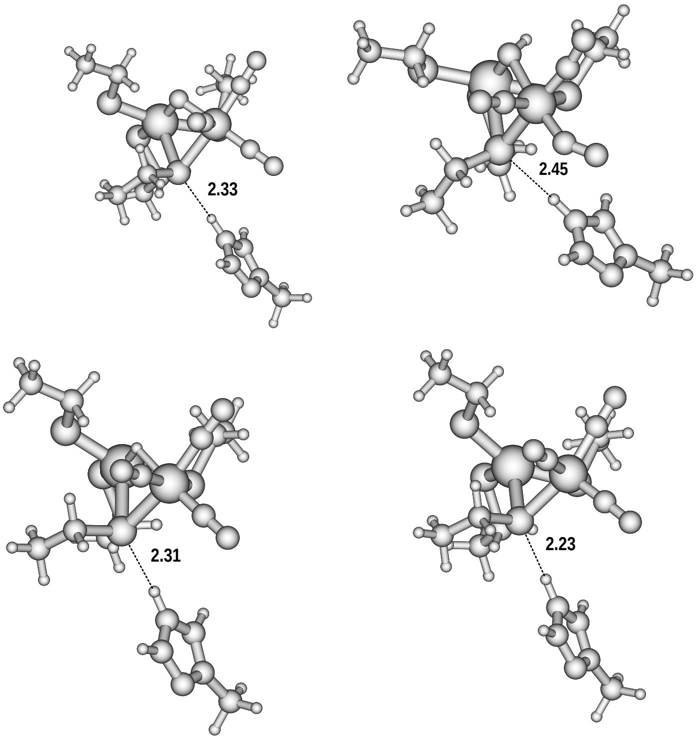

Figure 7.6: Histidine coordination of the active centre of [NiFe] hydrogenase: BP86/DZP geometry optimized structures Ni-A (top, left), Ni-B (top, right), Ni-C (bottom, left), Ni-L (bottom, right). Hydrogen bond lengths in Å.

The calculated parameters for the ^{14}N$^{\epsilon}$ for Ni-B are A$_{tot}$ = [1.72, 1.74, 2.32] MHz with a_{iso} = 1.93 MHz. The calculated quadrupole tensor Q = [-1.02, +0.34, +0.68] leads to quadrupole parameters e^2qQ/h = 2.04 MHz and η = 0.33 which agree nicely with the experimental values. The N$^{\delta}$ nucleus of the histidine reveals a quadrupole tensor Q = [-1.86, 0.82, 1.04] which does not agree with experimental findings. For Ni-A, a quadrupole tensor Q = [-0.96, +0.74, +0.22] was obtained which yielded e^2qQ/h = 1.92 and η = 0.54. The calculated Ni-C ^{14}N$^{\epsilon}$ quadrupole tensor Q = [-1.09, +0.38, +0.71] leads to

e^2qQ/h = 2.18 MHz and η = 0.30. For Ni-L the ^{14}N$^{\epsilon}$ quadrupole tensor is Q = [-0.92, 0.21, 0.71] which gives e^2qQ/h = 1.84 MHz and η = 0.54. The calculated quadrupole parameters agree well with experimental data where those are available. They are rather untypical for a N$^{\epsilon}$ coordinated histidine. The increase of both quadrupole parameters in the Ni-A and Ni-L forms may originate from the reduced hydrogen bond distances in these models (2.33 Å in Ni-A, 2.23 Å in Ni-L).

To conclude, based on the DFT calculations the experimentally observed quadrupole interaction can be assigned to the N$^{\epsilon}$ nucleus of histidine His72. The ^{14}N quadrupole parameters are of the same order of magnitude in all paramagnetic states since the hyperfine interaction along the Ni–SCys533–His72 direction does not change drastically. In the geometry-optimized cluster models, the hydrogen bond lengths (Ni-A 2.33 Å, Ni-B 2.45Å, Ni-C 2.31 Å, Ni-L 2.23 Å) slightly varies with the oxidation state. One reason might be the different total charges of the cluster models in the different states. In *vivo* the histidine ligand may be held in place by the protein environment.

7.6 The Influence of the Protein Matrix

One point of criticism with respect to the *ab initio* or DFT calculation of the active centres of proteins is the complete neglect of the protein environment. One tries to compare *in vacuo* model cluster calculations with experimental data obtained in liquid or frozen solution or single crystals of the complete protein. The aim of this section is to investigate whether the satisfying agreement between experimental and calculated g-tensor magnitudes and orientations were a mere artefact of the model and due a fortuitous cancellation of errors.

All covalently bound cofactors of the active site (namely the four cysteine amino acids) were already considered. Further interaction of the protein might be mediated by hydrogen bonds. The arguments for a potential hydrogen bond are

- the proximity of a potential hydrogen bond donor (-OH,-NH, -CH) and acceptor (CN,CO,O),
- a heavy atom distance smaller than 3.5 Å,
- an approximate linear arrangement of hydrogen bond donor and acceptor.

There are, potentially, three hydrogen bond interactions of nearby amino acids with the active centre (see Figure **7.7**). Possibly, there are more van der Waals, neither covalent nor hydrogen bonding interactions but they were not considered here. The histidine His72 can form a hydrogen bond to the bridging cysteine Cys533 (see above) and transfer unpaired spin density from the cysteinyl sulphur to the N$^{\epsilon}$

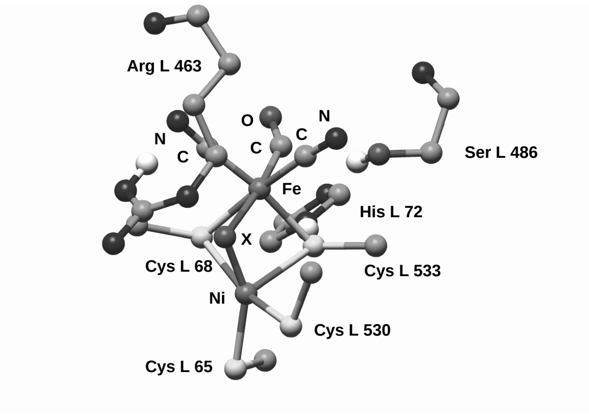

Figure 7.7: Protein-cofactor interactions in the active centre of the [NiFe] hydrogenase from *D. gigas* [27].

nitrogen of that residue and account for the ^{14}N quadrupole interaction measured in [NiFe] hydrogenases [68, 184, 220]. Furthermore, the inorganic ligands at the Fe site can also form hydrogen bonds. The assignment of the three non-protein ligands in the X-ray structure of *D. gigas* was done by their ability to form hydrogen bonds [27]. From FTIR measurements and chemical analysis one knows that there were 2 CN and 1 CO ligand coordinating the Fe atom [51, 54, 173]. Two of the inorganic ligands point towards polar neighbouring amino acids and the third is directed towards an unpolar protein pocket. It was concluded that the two cyanides would be more efficient hydrogen bond acceptors than CO while the carbon monoxide would sit in the unpolar pocket (see Figure **7.7**) [27, 54]. The arginine Arg 463 sits like a lid on top of the active site and may enter into one or more hydrogen bonds to one of the CN ligands. Serine Ser486 could form a hydrogen bond to the other CN ligand (see Figure **7.7**).

It was investigated whether the consideration of these hydrogen bonding partners would significantly change the calculated g-values. Successively, the cluster was enlarged by first considering the histidine residue and then also the arginine and serine amino acids. Each cluster was again completely geometry-optimized using frozen core orbitals (see Computational Details) and the g-tensors were calculated in an all-electron basis. The number of atoms increased from 40 for the bare active site to 50 when the histidine was added to 90 when all three amino acids were taken into account. This posed a significant challenge on the computational side. For a picture of the clusters optimized with coordinating His 72, please refer to Figure **7.6**. The geometry-optimized structures of Ni-A, Ni-B and Ni-C with all potential hydrogen bonding partners are given in Figure **7.8**.

In the Ni-A state where a O^{2-} occupies the position of the bridging ligand, there are in total five hydrogen bonds formed. The amino acids surrounding the active site are hydrogen bond donors and

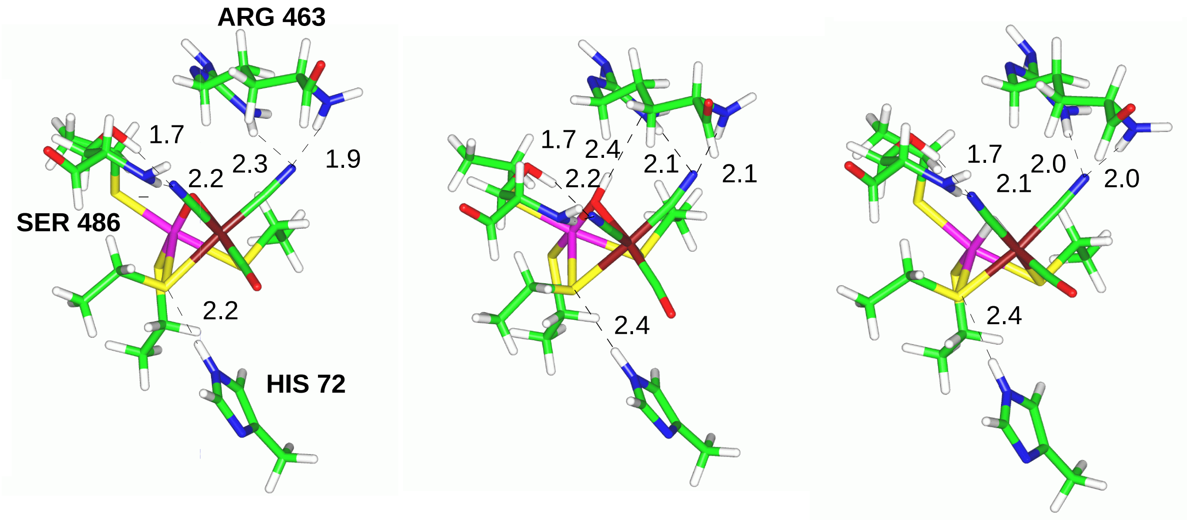

Figure 7.8: BP86 geometry-optimized clusters considering protein-cofactor interactions in the Ni-A(left), Ni-B(middle) and Ni-C (right) states. Hydrogen bond lengths in Å.

the sulphur of Cys533 and the CN groups act as hydrogen bond acceptors. Histidine His72 is hydrogen bonded to the bridging cysteine Cys533 in all three states. The hydrogen bond length is slightly shorter in the Ni-A form, possibly due to the increased negative charge in that cluster model compared to the Ni-B and Ni-C clusters. Serine Ser486 forms two hydrogen bonds to one of the cyanide groups. A strong one from the -OH group (1.7 Å) and a weaker one from the -NH group (2.2 Å). Arginine Arg486 coordinates the second cyanide group via two hydrogen bonds, one of 1.9 Å length, the other of 2.3 Å length. This picture is retained in all three states. The hydrogen bonds from the serine residue are unchanged in length and those by the arginine residue shorten and become equivalent in length (2.0 Å) in the Ni-C state. This may imply a participation of the latter residue in the reaction cycle of the [NiFe] hydrogenase, i.e. in the transfer of a proton from the active site to the protein surface.

In addition to the five hydrogen bonds described above, there is an additional sixth hydrogen bond in the Ni-B state. Arginine 463 resides on top of the active site like a lid. The proton of the bridging hydroxo group may form a donator bond to the arginine Arg463 residue. The hydrogen bond length is rather long with 2.4 Å but it may assist the release of that ligand upon activation of the enzyme. This may explain the different activation kinetics for ‘ready’ Ni-B and ‘unready’ Ni-A.

The structural parameters do not change significantly when the hydrogen bonds are considered. The Ni–Fe distances remain constant to within 0.01 Å and the C≡N triple bonds are only marginally expanded by 0.002 Å upon hydrogen bond formation.

Table 7.16: ZORA calculated g-tensor principal values upon successive consideration of protein-cofactor interactions

Cluster		Oxidation State Ni-A	 Ni-B	 Ni-C
Active Site	No. of Atoms	41	42	41
	g-values	2.36,1.95,1.85	2.20,2.17,1.98	2.20,2.10,2.00
+His72	No. of Atoms	53	54	53
	g-values	2.69,0.58,0.41	2.19,2.12,2.00	2.23,2.10,1.99
+Arg463	No. of Atoms	91	92	91
+Ser486	g-values	2.35,1.99,1.90	2.20,2.18,1.98	2.19,2.10,1.99
experiment		2.32,2.24,2.02	2.33,2.16,2.01	2.19,2.15,2.01

The protein environment considered so far does not significantly influence the calculated magnetic resonance parameters (see Table **7.16**). The calculated g-values do not drastically change when hydrogen bonding is considered. A caveat, however, must be issued that a balanced description of the protein environment is important. The largest changes in the calculated g-tensor principal values are found, when only His72 is considered (along the g_z direction of the g-tensor). In particular, the g_y component is affected when only this residue is taken into account, e.g. for Ni-B the g_y value changes from 2.17 in the bare active site to 2.12 when the histidine is added and back to 2.18 when all three amino acids are considered. The same effect is observed for Ni-C where the g_x value is mostly affected (bearing in mind the suggested interchange the x- and y-axes orientations in the Ni-C form compared to Ni-B, the effect is comparable).

7.7 Conclusion

With the ability to correlate a shift of g-values with structural changes, one has a powerful tool at hand to discriminate different paramagnetic states and intermediates in the reaction mechanism of the hydrogenase enzyme. There is, however, some systematic deviation between calculated and experimental g-values. The results obtained from DFT calculations for g- and hyperfine tensors therefor always need a critical inspection and evaluation. The ZORA approach seems to give reliable results with the exception of the Ni-A state for which spin-polarization effects have to be considered in order to achieve a reasonable description of the electronic structure.

For Ni-B a μ-hydroxo ligand gives best agreement with experimental values. For Ni-A, a μ-oxo bridge appears most plausible while for Ni-C a μ-hydrido bridging ligand is suggested. In these forms, the Ni is in its formal Ni(III) oxidation state. The model of the Ni-C form is supported by results for the Ni-L form in which the bridging ligand would be lost upon illumination as a proton and leaves the Ni in a formal Ni(I) oxidation state. For Ni-CO, best agreement with experimental data is obtained when it axially binds to a Ni(I) originating from the Ni-L state. Since CO is an inhibitor of the enzyme, this may suggest a participation of the open coordination site opposite to Cys533 in the reaction mechanism.

The size of the calculated cluster model was successively enlarged by considering some of the surrounding amino acids, i.e. those which form hydrogen bonds with the active site. It was found that the protein environment does not impose energetically unfavourable conformations on the active centre since the structural parameters were nearly unchanged compared to the gas phase cluster models alone. Neither did the three amino acids considered so far strongly influence the electronic structure. The calculated g-values were similar for all cluster sizes. A participation of the protein in the catalytic mechanism, however, is still possible.

Further work will suggest a connection of the intermediate paramagnetic states via EPR-silent diamagnetic states and thus contribute to the unravelling of the enzymatic mechanism.

Chapter 8

Orientation-Selected ENDOR of the Ni-C State

8.1 Introduction

The investigation of the reduced Ni-C state of the [NiFe] hydrogenase from *Desulfovibrio vulgaris* Miyazaki F is complicated by the spin-spin interaction of the Ni centre with that of the S = 1/2 reduced form of the proximal $[4Fe\text{-}4S]_p$ cluster [209]. The shortest distance (edge to edge) between the two cofactors is 13Å. The result of which is a complicated splitting of the Ni-C EPR signal at low temperatures [209]. At temperatures above 70 K, due to the the fast relaxation of the $[4Fe\text{-}4S]_p$ spin, the interaction averages out and the Ni-C EPR signal appears ‘unsplit’ Below 70 K, the spin-spin interaction is detectable and some structural information can be gained about the relative orientations of the g-tensors of the Ni centre and the proximal iron-sulphur cluster [46, 47]. This interaction, however, leads to a fast relaxation of the Ni spin and prevents the detection of any cw-ENDOR or Davies pulsed-ENDOR signal from the Ni-C form (data not shown).

The regulatory hydrogenase (RH) from *Ralstonia eutropha* (formerly *Alcaligenes eutrophus*) does not exhibit this spin-spin interaction between the Ni-Fe and $[4Fe\text{-}4S]_p$ cluster spins. The RH is a hydrogenase consisting of two subunits (HoxB, HoxC). HoxA and HoxJ are two additional proteins [221] (see Figure **8.1**). HoxB and HoxC share significant similarity [222] with the small and large subunits, respectively, of the standard [NiFe] hydrogenases from *Desulfovibrio gigas* and *Desulfovibrio vulgaris* Miyazaki F for which crystal structures are available [28, 32]. The cysteine and histidine residues that coordinate the three Fe-S clusters in the small subunit are well conserved in HoxB. However, the lack of an N-terminal signal sequence indicates a cytoplasmic location of the RH. HoxC contains signal motifs

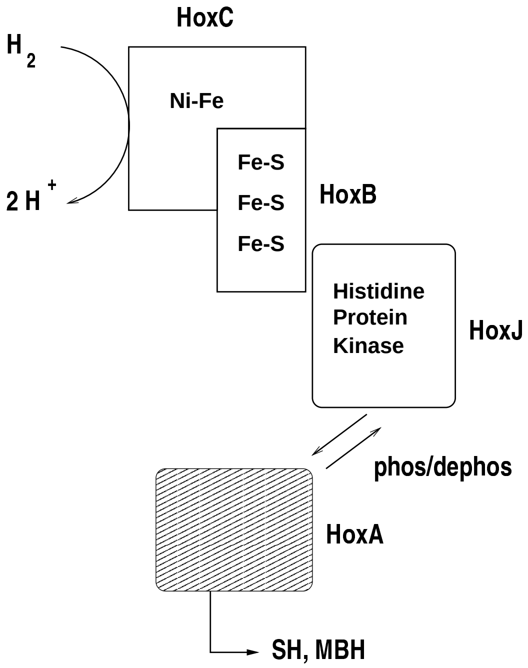

Figure 8.1: Schematic drawing of the role of the regulatory hydrogenase (RH) from *Ralstonia eutropha*. Upon hydrogen sensing in the large subunit (HoxC) and electron transfer to the small subunit (HoxB), connection to the histidine protein kinase (HoxJ) is established via phosphorylation/dephosphorylation. The transcriptional activator HoxA then induces the expression of the genes coding for the soluble hydrogenase (SH) and the membrane-bound hydrogenase (MBH).

of the large subunit which harbours the active site. The two pairs of cysteines that coordinate both Ni and Fe are also present in the RH. HoxC displays the conserved amino acid motifs which are considered essential elements for the coordination of the NiFe cofactor. It is noteworthy, however, that the RH contains slight modifications in the histidine motifs of the large subunit. HoxB has potentially three Fe-S clusters similar to the small subunit of *D. gigas*. Four cysteines coordinate a proximal [4Fe-4S] cluster, three cysteines and a histidine coordinate the distal [4Fe-4S] cluster. The intermediate cluster may also be a [4Fe-4S] cluster since there are four instead of three conserved cysteine residues [222]. *hoxJ* shows homologies to sensor kinases of bacterial two-component systems [221]. Lenz and Friedrich also showed that HoxJ mediates RH regulation [221]. HoxJ inactivates the transcriptional activator HoxA by phosphorylation. This negative effect is released upon H_2-sensing by the RH. The communication between the RH and HoxJ is not clear yet. In its non-phosphorylated form HoxA activates the transcription of genes coding for the other two, more efficient hydrogenases from *R. eutropha*, the soluble hydrogenase (SH) and the membrane-bound hydrogenase (MBH) (see Figure **8.1**).

The active site of the hydrogen sensor was characterized by EPR and FT-IR spectroscopies [223]. The RH has an active site much like that of standard [NiFe] hydrogenases [32, 51], i.e. a Ni-Fe site (Ni was shown to be a requirement for hydrogen sensing by Kleihues *et al.* [222]) and two CN and 1 CO as prosthetic ligands of the Fe atom. Pierik *et al.* showed that the uptake activity of H_2 is two orders of magnitude lower than that of standard hydrogenases [223] but insensitive to the presence of oxygen and carbon monoxide.

The EPR properties of the RH somewhat differ from that of standard hydrogenases, i.e. there is only *one* paramagnetic state. The as-isolated RH only exhibits a faint signal with two components $g_{x,y}$ = 2.29, 2.17 which resembles that of Ni-B. The g_z edge was not observed [223]. After incubation with H_2 a new EPR signal evolved with $g_{x,y,z}$ = 2.191, 2.133, 2.010 which resembles that of Ni-C. It is also light-sensitive and converts into a Ni-L signal with $g_{x,y,z}$ = 2.24, 2.09, 2.04. It is noteworthy that the g_x value of Ni-L is lower than that of other hydrogenases (2.29). The FT-IR spectra of the RH also show typical bands for the as-isolated (Ni-SI) and reduced (Ni-C) forms (see Table **8.1**).

Table 8.1: Comparison of the high-frequency bands from RH with standard [NiFe] hydrogenases. The frequencies of the two CN and one CO stretching modes are given in cm^{-1}.

	RH [223]			*A. vinosum* [50]			*D. gigas* [54]		
State	ν_{CN}		ν_{CO}	ν_{CN}		ν_{CO}	ν_{CN}		ν_{CO}
Ni-SI	2081	2073	1943	2086	2074	1932	2085	2075	1934
Ni-C	2084	2072	1962	2087	2074	1950	2086	2073	1952

Although the binding motifs for three Fe-S clusters in the small subunit are present in the RH, there is no report of an Fe-S EPR signal [223]. Furthermore, there is no evidence for a spin-spin interaction between the Ni-C spin and that of the proximal [4Fe-4S] cluster. The absence of that interaction and the similarity of the RH Ni-C EPR signal with that of standard [NiFe] hydrogenases make it an ideal candidate for ENDOR investigations of the Ni-C state. Since there are no protein single crystals available for the RH yet, one has to resort to orientation-selected ENDOR in frozen solution.

Orientation-selected ENDOR, in principle, allows the complete determination of hyperfine coupling tensors [224, 225]. This method has been successfully applied to biological systems to study hemoglobin [188], copper-enzymes [177] and to elucidate the reaction mechanism of enzymes, e.g. aconitase [189]. The method of orientation-selected ENDOR has been reviewed in [226, 227]. Recently, an orientation-selected cw-ENDOR study of the Ni-B state was reported and three hyperfine tensors were structurally assigned [169]. Here, an orientation-selected ^{1}H-ENDOR study which allows the full determination and assignment of the hyperfine tensors for several protons in the active center of [NiFe] hydrogenase in the reduced Ni-C state is presented. For this method, the knowledge of the g-tensor orientation in the molecular structure is a prerequisite. Since it was not reliably determined in [NiFe] protein single crystals yet, the *theoretically calculated* g-tensor of the Ni-C state will be used. Based on this assignment, the orientation of ^{1}H hyperfine coupling tensors with respect to the g-tensor axes will be used to characterize the proton environment of the active NiFe center during catalytic activity and help to further elucidate the reaction mechanism of [NiFe] hydrogenases.

8.2 Materials and Methods

8.2.1 Sample Preparation

The regulatory hydrogenase was overexpressed in the native host *R. eutropha*, grown, purified and assayed as described previously [222]. The final protein concentration was 0.5 mM. The solution was transferred to a Wilmad 707SQ, 4mm o.d. EPR tube. The enzyme was activated for 30 mins at room temperature with 100% H_2 under frequent stirring and then rapidly frozen in liquid nitrogen.

8.2.2 EPR and ENDOR Setup

Pulsed-EPR and pulsed-ENDOR experiments were performed with a Bruker ESP 380 E FT-EPR spectrometer. A sapphire ring resonator (1052 DLQ-H, Bruker) was used. Resonator and sample were cooled with a helium flow-cryostat (Oxford CF 935). The optimum ENDOR effect was found at T = 10 K. The pulse lengths were 96 and 48 ns for π and $\pi/2$ pulses, respectively. The spectra taken at field values of 3229 G, 3260 G, 3366 G, and 3430 G are from Davies-ENDOR experiments with selective π-$\pi/2$-π microwave pulse sequence and a radiofrequency pulse of 8 μs. The spectra that were recorded at field values of 3165 G, 3208 G, 3235 G, 3245 G, 3255 G, 3288 G, 3310 G, 3337 G, 3385 G, 3390 G, and 3410 G are Davies-ENDOR experiments with an ‘optimized polarization transfer’ which exhibit an increased ENDOR effect (for details see [84]) and thus decreased the accumulation time. The preparation phase is also a π-microwave pulse of 96 ns length, the mixing period consists of a non-selective microwave (16 ns) π-pulse sandwiched between two π-radiofrequency pulses of 8 μs each. The detection is done after a traditional π/2-π microwave pulse Hahn-echo sequence. Pulsed-ENDOR spectroscopy has been extensively reviewed in [83, 84, 189, 191].

8.2.3 Orientation-Selected ENDOR

The spin Hamiltonian used here for a system of one electron and several magnetic nuclei

$$H = \beta \mathbf{B_0} \mathbf{g} \hat{\mathbf{S}} + \sum_k \left(\hat{\mathbf{S}} \mathbf{A}_k \hat{\mathbf{I}}_k + \beta_N \mathbf{B_0} g_{n_k} \hat{\mathbf{I}}_k \right) \tag{8.1}$$

includes electron Zeeman, electron-nuclear hyperfine interaction and nuclear Zeeman terms. Diagonalization of the Hamiltonian yields the energy levels of the system. These levels can be labelled with the magnetic quantum numbers of the electron m_S and of the different nuclei $(m_I)_k$. Since nuclear-nuclear interactions are much smaller than electron-nuclear interactions, it is sufficient to discuss the interactions of the unpaired electron with one nucleus at a time.

In the ENDOR experiment, an EPR transition ($\Delta m_S = 1$) is monitored, while transitions between the nuclear sublevels within one m_S-manifold ($\Delta m_S = 0, \Delta m_I = 1$) are induced using an additional radio frequency field with appropriate resonance frequency ν_{NMR}. The detected EPR amplitude changes whenever ν_{NMR} matches a nuclear sublevel transition. The ENDOR transition frequency reflects the interaction of the nuclear spin with the electron spin acting on the nucleus (second term in the Hamiltonian). The observed lines are centred around the free nuclear frequency ν_N.

In the case of an isotropic g-tensor and isotropic hyperfine interaction $A = a_{\mathrm{iso}}$, the interactions in the Hamiltonian do not depend on the orientation of the molecular axis system in the external magnetic field. The ENDOR transition energies are then simply the sum of the nuclear Zeeman frequency and the additional contribution from hyperfine interaction, the sign of the latter being dependent on the electron spin m_S. In a system with electron spin $S = 1/2$ and nuclear spin $I = 1/2$ this leads to a pair of ENDOR transitions spaced symmetrically about the free nuclear Zeeman frequency, ν_N.

$$\nu^{\pm}_{\mathrm{ENDOR}} = |\nu_N \pm \frac{A}{2}|. \tag{8.2}$$

In the more general case of anisotropic g- and hyperfine tensors, the EPR and ENDOR transition energies depend on the orientation of the magnetic field relative to the molecular axes. Assuming that the hyperfine interactions are small compared with the electron Zeeman term, the EPR resonance condition is expressed as

$$h\nu = g(\theta, \phi) \beta B_0 \ , \tag{8.3}$$

with the effective g-value defined as

$$g(\theta, \phi) = \sqrt{\sum_j (g_j b_j)^2} \ , \tag{8.4}$$

where g_j $(j = 1,2,3)$ are the g-tensor principal values. b_j $(j = 1,2,3)$ are the direction cosines of the external field in the g-tensor principal axis system,

$$b_1 = \cos\phi\sin\theta,\ b_2 = \sin\phi\sin\theta,\ b_3 = \cos\theta\ . \tag{8.5}$$

Now at a given field value only the subset of molecules with appropriate orientations contributes to the EPR intensity and thus to the ENDOR spectrum recorded at that field value. Also, the hyperfine field is no longer parallel to the external field, it now depends on direction and magnitude on the electron spin quantum number m_S. This leads to a more complicated expression for the ENDOR frequencies, derived from diagonalization of the Hamiltonian in Eq.(**8.1**) for an ($S = 1/2,\ I = 1/2$)-system [224]:

$$\nu^{\pm}_{\mathrm{ENDOR}}(\theta,\phi) = \sqrt{\sum_{i=1}^{3}\left[b_i\nu_N \pm \sum_{j=1}^{3}\frac{g_j b_j}{2g(\theta,\phi)}A_{ij}\right]^2} \tag{8.6}$$

Due to the effect of the hyperfine field on the ENDOR signal intensities [85], signals at ν^{+}_{ENDOR} usually appear more intense in the ENDOR spectrum than the corresponding lines at ν^{-}_{ENDOR}. The determination of the complete hyperfine tensor $\mathbf{A}$ can, in principle, be obtained from ENDOR single crystal measurements but in the case of protein molecules single crystals are often not available. When applied to frozen-solution samples, angle-selected ENDOR spectra of samples with anisotropic magnetic interaction (non-axial g-anisotropy) in the EPR also allows the full determination of electron-nuclear interaction tensors in favorable cases. The EPR spectrum of a polycrystalline sample is a superposition of signals from a large number of molecules randomly oriented with respect to $\mathbf{B_0}$.

Over the complete EPR envelope (Figure **8.2**) ENDOR spectra are recorded at selected field positions B_0 from g_x to g_z. Only the fraction of molecules that are oriented according to Eq.(8.3) are contributing to the ENDOR spectrum at each field position. A subset of molecules is selected by stepping through the EPR spectrum. At the EPR edges g_x and g_z the selected subset is very small and single crystal-like ENDOR spectra are observed. At intermediate field values the selection is less restrictive and the resulting ENDOR spectra are superpositions of a larger number of molecular orientations.

8.2.4 Simulation of ENDOR Spectra

In the first step, the full EPR spectrum was simulated according to Eq.(**8.3**) (Figure **8.2** bottom). ENDOR frequencies were then calculated for specific field values and orientations for a given number of hyperfine tensors (A_{ij}) using Eq.(**8.6**), the intensity of the ENDOR transition was assumed to be proportional to that of the EPR transition. The ENDOR simulation program [196] allows the angle-dependent simulation of ENDOR spectra using an arbitrary number of fully anisotropic hyperfine tensors with arbitrary orientations relative to the g-tensor axes. Based on an algorithm by Mombourquette and Weil [228], a uniformly distributed set of orientations was created by stepping on a spiral path, typically using 5160 different orientations. A more detailed description of the algorithm can be found in [196]. ENDOR spectra with 1024 points each were simulated for each of the 15 field positions selected in the experiments.

The specific contribution of each orientation (θ, ϕ) to the EPR spectrum is calculated, including g-anisotropy and the hyperfine interactions. Contributions of this orientation to an ENDOR spectrum taken at a given field value are then calculated according to Eq. (**8.6**), weighted with the EPR amplitude at this field position and stored. In this way, a series of orientation-selected ENDOR spectra was simulated.

8.3 Results and Discussion

8.3.1 Characterization by EPR

The X-band (9.699 GHz) pulsed-EPR spectrum of the regulatory hydrogenase from *R. eutropha* at 10 K displays a Ni-C-like spectrum (Fig. **8.1**, top). The g-tensor principal values were determined from a simulation of the pulsed-EPR spectrum to be g_x = 2.192, g_y = 2.135, g_z = 2.011 and are identical to those obtained by Pierik *et al.* $g_{x,y,z}$ = 2.191, 2.133, 2.010 [223] within error. Furthermore, they are very similar to those reported for the Ni-C signal of the ‘standard hydrogenase’ from *D. gigas* which exhibited $g_{x,y,z}$ = 2.19, 2.14, 2.02 [66, 229]. This striking similarity indicates that the two active centres of the two functionally different hydrogenases must be very closely related, if not identical.

8.3.2 Analysis of Orientation-Selected Pulsed-ENDOR Spectra

Figure **8.3** shows the collected field-dependent pulsed-ENDOR spectra. The spectra were normalized to the free nuclear frequency ν_H. From top to bottom the magnetic field increases going from 3165 G (g = 2.189) to 3430 G (g = 2.020). Especially at the high-frequency side of the spectra ($\nu^+_{\mathrm{ENDOR}} > \nu_H$) several lines can clearly be distinguished. The splitting in the ENDOR spectra is nearly symmetric with respect to the free proton frequency with a maximum deviation of 0.2 MHz. In general lines at the ν^+_{ENDOR} side are more intense than those at ν^-_{ENDOR}. Three large hyperfine coupling can be directly deduced. At g = 2.189 there are large couplings of ν^+ = 8 MHz, 6 MHz and 3 MHz. The signals are rather broad and may contain contributions from more than one proton. When stepping through the EPR spectrum and going to larger field values, the intermediate signal splits and then becomes broader. Near g_y (g = 2.136), one large broad ENDOR signal is detectable at $\nu_\pm \approx 9$ MHz and a number of unresolved smaller hyperfine couplings appear between $\nu_\pm$ = 2 and 7 MHz. Here, the analysis is especially compli-

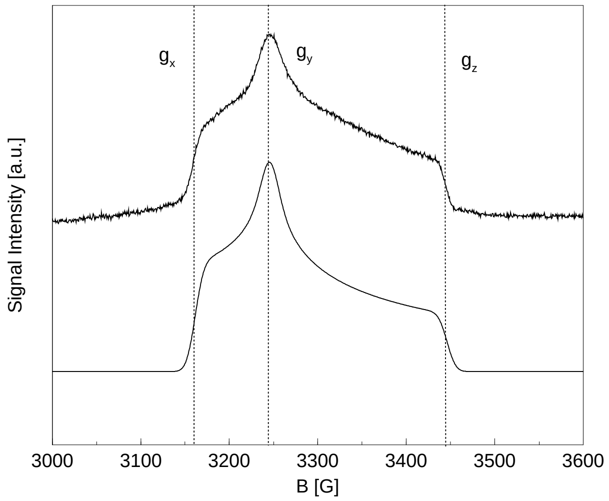

Figure 8.2: Pulsed-EPR spectrum of the RH. Comparison of experimental pulsed-EPR spectrum of the RH (top) and simulation (bottom), both in absorption mode. Experimental Details: T = 10 K, mw-frequency 9.699 GHz, (π/2-, π-pulses of 56 ns and 112 ns, respectively. Details of the simulation: centre field 3300 G, field sweep 600 G, EPR linewidth 18 G, $g_{x,y,z}$ = 2.192, 2.135, 2.011.

cated because a large number of orientations contribute to the ENDOR effect at g_y. At field values larger than g_y, the unresolved signals coalesce into two pairs of doubly split ENDOR resonances. The large and broad resonance signal moves to smaller hyperfine coupling values and a new very broad and flat signal evolves at the high frequency side (see for example spectrum at g = 2.077). Near g_z (g = 2.020), one sharp signal at $\nu_\pm$ = 3 MHz and two broad signals at $\nu_\pm$ = 6 MHz and $\nu_\pm$ = 9 MHz are observed.

Figure **8.4** shows a field-dependent plot of the ENDOR resonances. The hyperfine splitting with respect to ν_H is plotted versus the variation of the magnetic field. The situation is so complicated that one cannot trace a hyperfine coupling continuously over the whole field range. There may be multiple crossings of hyperfine interactions which complicate this procedure.

8.3.3 Simulations

For the analysis of the orientation-selected ENDOR spectra, the orientation of the g-tensor principal axes in the molecular coordinate axes system is a prerequisite. For Ni-C, the experimental g-tensor orientation is not yet unambiguously determined (S. Foerster, personal communication). The ZORA calculated g-tensor orientations were shown to be in good agreement with experimental findings for the Ni-A and Ni-B states [179, 190].

When one assumes that the composition and structural parameters of the Ni-C form of the regulatory

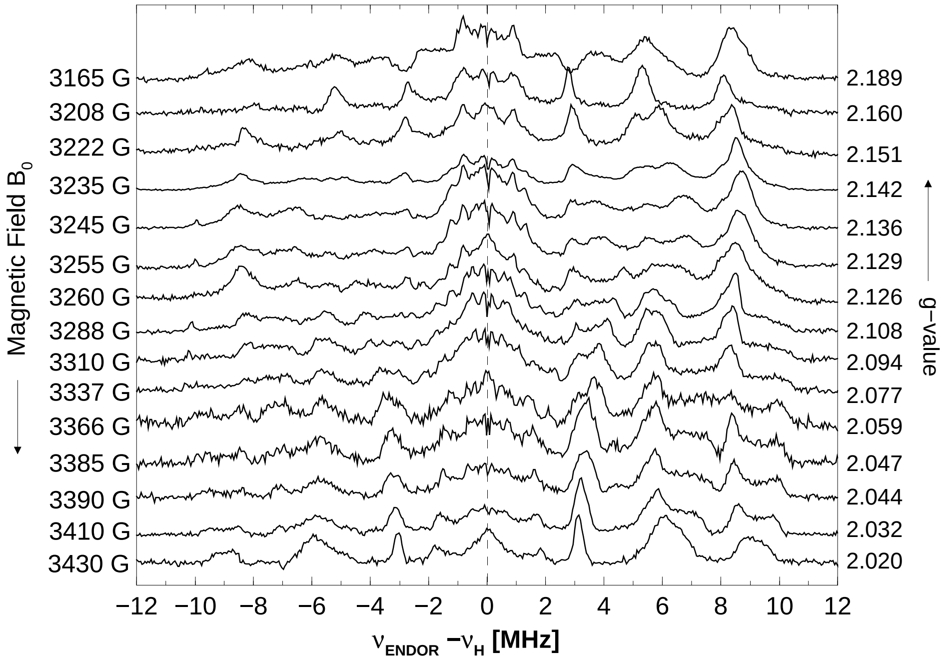

Figure 8.3: Orientation-selected pulsed-ENDOR spectra of the RH. The spectra are centred around the free nuclear frequency ν_H for each field position. T = 10 K, sweep width 1-26 MHz.

hydrogenase are similar if not identical to those suggested for the Ni-C state of standard hydrogenases (e.g. *D. gigas*, *D. vulgaris* Miyazaki F), the dilemma can be resolved by resorting to magnitudes and orientations of magnetic resonance parameters obtained from relativistic DFT calculations. The underlying assumption of the analysis presented in this chapter is therefore that a Ni(III)-μ hydrido-Fe(II) bridged active centre exists with four coordinating cysteine ligands and two CN and one CO inorganic ligands at the Fe atom.

The theoretically predicted g-tensor from the spin-orbit-coupled ZORA calculations in Chapter 7 may be a first starting point for the analysis of the orientation-selected ENDOR spectra. For protons, the spin-restricted SO-coupled ZORA hyperfine tensors were shown to be in good agreement (within $\approx$ 1 MHz for both isotropic and isotropic contributions) with experiments (see Chapter 7). Thus knowing the g-tensor orientation and the hyperfine tensors‘ magnitudes and orientations, one has a good starting point for the analysis of the ENDOR spectra.

Tables **8.2** and **8.3** give the calculated magnetic resonance parameters for the Ni-C form. The values come from spin-restricted spin-orbit-coupled ZORA calculations using a large basis set (basis IV in ADF nomenclature [160]). The principal values of the g- and A-tensors are given in their corresponding

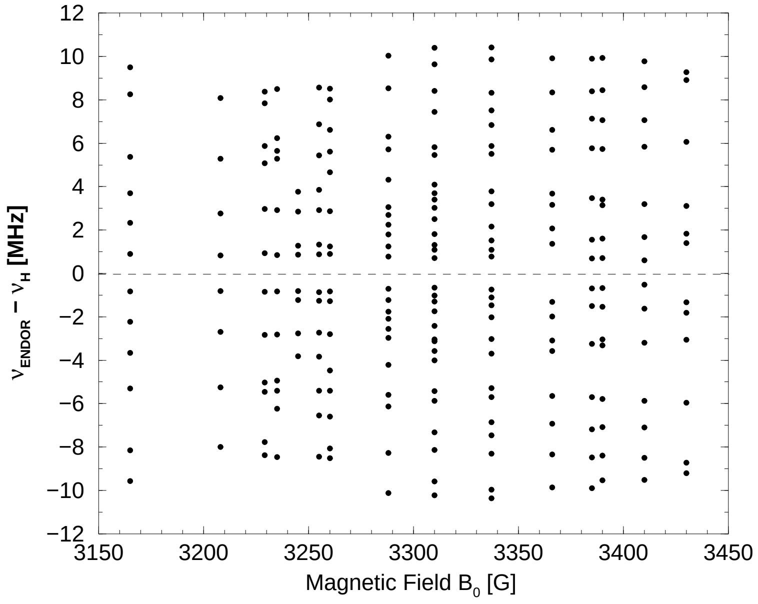

Figure 8.4: Field plot of ENDOR resonance positions

eigenvector systems.

For the simulations of the ENDOR spectra, the g-tensor orientation from ZORA calculations was used but the g-tensor principal values from the simulation of the pulsed-EPR spectrum of the RH were taken since the g-tensor principal values from DFT calculations are not accurate enough to allow a simulation with these. Deviations of up to 0.1 in g-magnitude are sometimes found for the largest components which is not tolerable for such a sensitive probe like orientation-selected ENDOR.

The total A-tensors in Tables **8.2** and **8.3** are given in their individual principal axes systems. The hyperfine tensors are then rotated to a common axes system, here the g-tensor principal axes system, according to

$$\mathbf{A_g} = \mathbf{S_g}^{-1} \cdot \mathbf{S_A} \cdot \mathbf{A_{diag}} \cdot \mathbf{S_A}^{-1} \cdot \mathbf{S_g} \tag{8.7}$$

where $\mathbf{A_{diag}}$ is the diagonal hyperfine tensor in its own eigenvector system, $\mathbf{S_A}$ and $\mathbf{S_g}$ are the eigenvectors of the g-tensor (the g-tensor principal axes system). $\mathbf{A_g}$ is the resulting, non-diagonal hyperfine tensor in the g-tensor principal axes system.

8.3.3.1 ENDOR Signals from β-CH$_2$ Protons

Figure **8.5** shows the simulated ENDOR transitions which are expected for the four β-CH$_2$ protons from the bridging cysteine Cys533 (left) and the terminal cysteine Cys530 (right). The ZORA calculated g-

Table 8.2: Prinicpal values and orientations of the g-tensor and β-CH$_2$ hyperfine tensors in the Ni-C state. Hyperfine couplings are given in MHz.

		x	y	z
g-Tensor	g_i	2.178	2.090	2.002
	l_{xi}	-0.37047	-0.60913	-0.70122
	l_{yi}	0.92801	-0.27462	-0.25174
	l_{zi}	-0.03923	-0.74401	0.66702
A-Tensor	A_i	+8.73	+9.60	+13.13
^{1}H Cys533-H1	l_{xi}	0.20484	-0.01154	-0.97873
	l_{yi}	0.87856	-0.43863	0.18905
	l_{zi}	-0.43148	-0.89859	-0.07971
A-Tensor	A_i	+7.74	+10.45	+13.30
^{1}H Cys533-H2	l_{xi}	-0.09268	-0.41085	-0.90698
	l_{yi}	0.99358	-0.09746	-0.05738
	l_{zi}	0.06482	0.90648	-0.41725
A-Tensor	A_i	+9.28	+5.19	+6.47
^{1}H Cys530-H1	l_{xi}	-0.68409	-0.58703	-0.43292
	l_{yi}	0.53783	-0.80689	0.24426
	l_{zi}	-0.49271	-0.06574	0.86771
A-Tensor	A_i	+7.80	+4.69	+4.48
^{1}H Cys530-H2	l_{xi}	-0.25378	-0.43947	-0.86166
	l_{yi}	0.71822	-0.68230	0.13646
	l_{zi}	-0.64788	-0.58423	0.48880

The labelling of amino acid residues according to the standard [NiFe] hydrogenase from *D. gigas* was used for which an X-ray structure is available [27]. The values are from relativistic SO ZORA BP86/IV calculations at the BP86/II optimized geometry using very tight convergence criteria. x, y, z are the g-tensor and $\mathbf{A}$-tensor principal values, respectively. l_{xi}, l_{yi}, l_{zi}, $i = x, y, z$, are the eigenvectors that diagonalize the $\mathbf{G^2}$ and $\mathbf{A}$ matrices, respectively.

tensor orientation and the hyperfine tensors of the four β-CH$_2$ protons was used. The β-CH$_2$ protons of cysteine Cys533 both exhibit an isotropic coupling of 10.5 MHz each (see Table **8.2**). Near g_x the spectra fall together to a splitting of A = 10-12 MHz, with increasing field value split into two components due to slightly different orientations with respect to the magnetic field and coalesce to a single signal at g_z at

A = 10 MHz (see Figure **8.5, left**). The anisotropy is rather small.

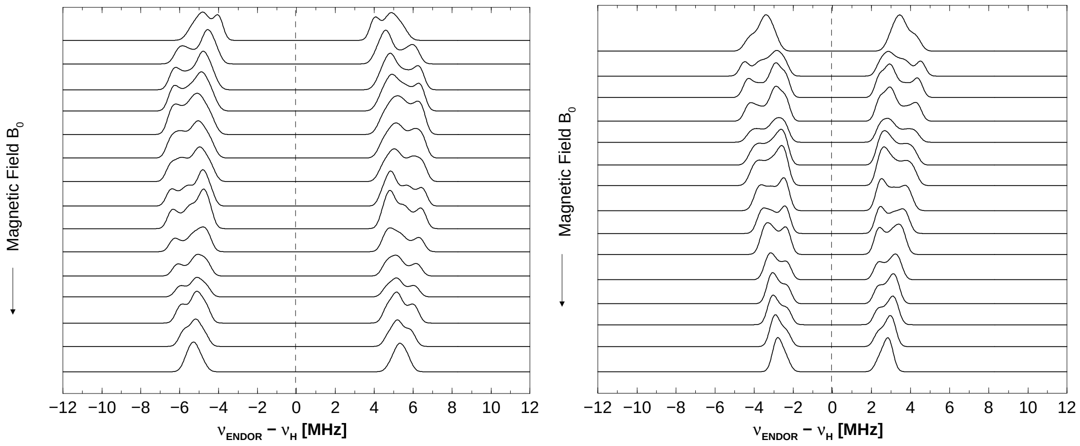

Figure 8.5: Simulation of Ni-C orientation-selected ENDOR spectra using the theoretically calculated g-tensor orientation and hyperfine tensors of β-CH_2 protons from cysteine residues Cys533 and Cys530.
Left: Simulations of the two β-CH_2 protons from the bridging cysteine Cys533
Right: Simulations of the two β-CH_2 protons from the terminal cysteine Cys530.

The β-CH_2 protons of the terminal cysteine Cys533 display a significantly reduced isotropic hyperfine interaction of 7 and 6 MHz, respectively (see Table **8.2**). At g_x they show a single hyperfine splitting of around 7 MHz. With increasing magnetic field, the two protons slightly split into a pair of 5 MHz and 8 MHz hyperfine splitting and at g_z again fall together to a single resonance at $\nu_\pm \approx 3$ MHz (see Figure **8.5, right**).

This set of four protons can, in general, satisfactorily explain a number of features of the experimental ENDOR spectra (Figure **8.3**). At g_x the ENDOR resonances at $\nu_\pm$ = 6 MHz can be assigned to the β-CH_2 protons of cysteine Cys533 and those at $\nu_\pm$ = 3 MHz to β-CH_2 protons of cysteine Cys530. The same holds for g_z. At intermediate field values the sets of pairs of protons split into individual splittings and the experimental ENDOR resonances are broader (see Figure **8.3**). The simulated spectra exhibit an additional slight splitting of the pairs of protons at g_x which is not observed experimentally. It may be not resolved in the broad ENDOR signals at g_x. Or alternatively, the splitting might be caused by a slight deviation of the calculated g-tensor orientation from the experimental one along the x-axis. Since the splitting is small, the difference between the g-tensor orientation can be assumed to be only a few degrees.

8.3.3.2 ENDOR Signals from the Bridging Hydride Ion

The experimental ENDOR spectra (Figure **8.3**) display an additional large hyperfine splitting of about 16 MHz at g_x, broad features of about 16-20 MHz near g_y and 17 MHz at g_z. This large hyperfine splitting cannot be explained by a coupling resulting from β-CH$_2$ protons. A candidate for this nucleus is the bridging μ-hydrido that may occupy the vacant bridging position in the Ni-C form [34]. Table **8.3** shows the calculated hyperfine parameters for such a bonding situation. Scalar-relativistic, restricted open-shell calculations (SR ROKS) yield all hyperfine tensor elements of positive sign. When spin-orbit coupling (SO) is additionally considered (SR + SO ROKS), the sign of the hyperfine tensor principal values is retained but A$_x$ increases by 3 MHz, A$_y$ decreases by about 1 MHz and A$_z$ remains nearly unchanged. When spin-polarization is considered at the scalar-relativistic level (SR UKS), a completely different picture is obtained: Compared to the SR ROKS results, A$_x$ is reduced by 55% upon consideration of spin-polarization, A$_y$ and A$_z$ show inverse signs and significantly larger values.

Table 8.3: A-tensor principal values in MHz and orientations for the bridging hydride in Ni-C

		A$_x$	A$_y$	A$_z$
SR ROKS				
A-Tensor		+22.19	+2.07	+5.85
Eigenvectors	l_{xi}	+0.45327	-0.79855	-0.39607
	l_{yi}	-0.89137	-0.40508	-0.20340
	l_{zi}	-0.00199	-0.44524	+0.89541
SR + SO ROKS				
A-Tensor		+25.54	+1.12	+6.01
Eigenvectors	l_{xi}	-0.46165	-0.77852	-0.42518
	l_{yi}	+0.88705	-0.40742	-0.21714
	l_{zi}	-0.00418	-0.47740	+0.87868
SR UKS				
A-Tensor		+9.92	-19.77	-16.12
Eigenvectors	l_{xi}	+0.46001	-0.71084	-0.53206
	l_{yi}	-0.88786	-0.37474	-0.26697
	l_{zi}	+0.00961	-0.59521	+0.80351

The values are from ZORA BP86/IV calculations at the BP86/II optimized geometry using very tight convergence criteria. l_{xi}, l_{yi}, l_{zi}, $i = x, y, z$ are the eigenvectors that diagonalize the **A** matrix.

A detailed discussion of the influence of spin-polarization and spin-orbit coupling can be done on the basis of the decomposition into isotropic and anisotropic hyperfine tensor components done in Table **8.4**. One must bear in mind, that the discussion presented here deals with the influence of relativistic effects (scalar relativistic effects and spin-orbit coupling) of the transition metals Ni and Fe on a μ-hydrido bridging ligand. For the bridging atom itself, the intrinsic effects are expected to be vanishingly small. Changes in the electronic structure and the hyperfine parameters originate from the adjacent transition metals.

Table 8.4: Influence of spin-polarization and spin-orbit coupling on the ^{1}H hyperfine tensor of a Ni–μ-hydrido-Fe bridge. All values are in MHz.

SR ROKS	A_{tot}	+22.19	+2.07	+5.85
	a_{iso}		+10.04	
	A_{aniso}	+12.15	-7.97	-4.19
SR + SO ROKS	A_{tot}	+25.54	+1.12	+6.01
	a_{iso}		+10.89	
	A_{aniso}	14.65	-9.77	-4.88
SR UKS	A_{tot}	+9.92	-19.77	-16.12
	a_{iso}		-8.66	
	A_{aniso}	+18.58	-11.11	-7.46
SR + SO UKS (extrapolated)	A_{tot}	+11.6	-22.4	-17.7
	a_{iso}		-9.5	
	A_{aniso}	+21.1	-12.9	-8.2

Spin-restricted calculations yield a positive isotropic hyperfine interaction for a hydride bridge. The influence of spin-orbit coupling is small (9%) when comparing SR ROKS and SR + SO ROKS calculations. Spin-unrestricted calculations give a negative isotropic hyperfine interaction of about the same magnitude. [1] Since the hydride is bound to the Ni $3d_{z^2}$ orbital in the nodal plane (see Figure **7.3**), the isotropic hyperfine interaction may be of *negative* sign if the analogy to an α-proton bound to a spin-carrying carbon $2p_z$ orbital holds (for discussion see for example [69]). The influence of spin-orbit coupling on the anisotropic hyperfine tensor becomes clear when one compares SR ROKS and SR +

---

[1] For comparison a non-relativistic unrestricted B3LYP/6-311+G(2d,2p) calculation at the same geometry was performed. The obtained values (a_{iso} = -41.74 MHz, A_{aniso} = (-15.76, -12.23, 28.04) MHz) are unrealistically large.

SO ROKS calculations. Spin-orbit coupling increases the $A_{\mathrm{aniso,x}}$ component by 2.5 MHz, the $A_{\mathrm{aniso,y}}$ component by 2 MHz and the $A_{\mathrm{aniso,z}}$ component by 0.6 MHz. One reason for this effect might be the relativistic contraction of the Ni p- and d-orbitals which would then lead to an increase of unpaired spin density near the core of the Ni nucleus and likewise increase the anisotropic hyperfine interaction of the neighbouring hydride.

It is difficult to calculate spin-polarization effects in spin-orbit coupled equations (see ref. [132]). One therefore has to assume that the effect of spin-orbit coupling can be taken from the SR ROKS $\rightarrow$ SR + SO ROKS calculation and may be added to the spin-polarized scalar-relativistic (SR UKS) data. The extrapolated values are also given in Table **8.4**.

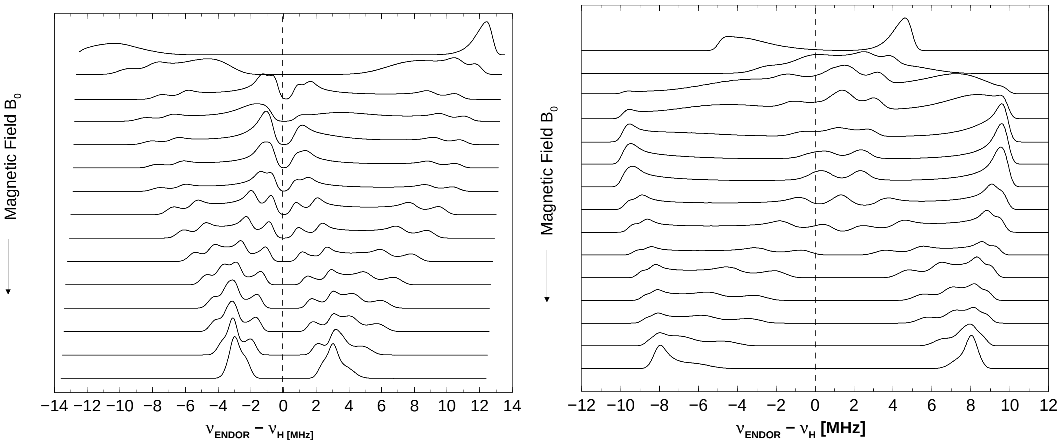

Figure 8.6: Simulation of Ni-C orientation-selected ENDOR spectra for the bridging hydride using theoretical data. Left: Simulations using the SO + SR ROKS ZORA hyperfine tensor (spin restricted).
Right: Simulations using the SR UKS ZORA hyperfine tensor (spin unrestricted).

Figure **8.6, left** shows the field-dependent simulations for a bridging hydride using the calculated spin-restricted spin-orbit-coupled ZORA hyperfine tensor. At g_x a very large hyperfine splitting of 25 MHz is obtained which then quickly splits into a pair of two weak ENDOR signals. At g_z the signals fall together to a single resonance signal at 6 MHz. This dependence is not in agreement with the experimental ENDOR spectra for the following reasons:

i) experimentally, there is no such large splitting of 25 MHz at g_x,

ii) the simulations cannot explain the large hyperfine splitting larger than 16 MHz for all field values.

Table **8.4** shows that there is a drastic influence of spin-polarization on the hyperfine tensor magnitude and orientation for the bonding situation of a hydride bound to a Ni $3d_{z^2}$ orbital. Also, the A-tensor orientation changes slightly. The eigenvectors of the A_x component in the SO ZORA calculation show an inversion of sign in the SR spin-unrestricted calculation. The eigenvectors of the A_y component in the SO ZORA calculation are rotated by 8° in the SR spin-unrestricted calculation. Those of the A_z component in the SO ZORA calculation are transformed to those in the spin-unrestricted calculation by likewise rotation by 8°. The result of a simulation using the spin-unrestricted data is given in Figure **8.6 right**. The hyperfine splitting at g_x of A = 10 MHz is too small. Over the complete range of field values, the general features of the spectra are well reproduced, i.e. an accumulation of an intense ENDOR signal at about A = 20 MHz at g_y to about A = 16 MHz at g_z. This indicates the importance of spin-polarization for the description of the hyperfine interaction of a μ-hydrido bridge as was suggested here.

The discrepancy between the simulated ENDOR spectrum (Figure **8.6**, right) with the experimental spectrum (Figure **8.3**) for field values near g_x may result from the neglect of spin-orbit coupling. From the experimental spectra at g_x (Figure **8.3**, top trace) one expects a hyperfine interaction of the large coupling of about 16 MHz at this field value. Fan *et al.* measured a hyperfine coupling of A = 16.8 MHz at the g_x-component of the Ni-C EPR spectrum of the [NiFe] hydrogenase from *D. gigas* [69] and showed that the nucleus associated with this signal was D_2O exchangeable and also belonged to the same nucleus that exhibited a coupling of A = 20 MHz at g_y [70]. Upon illumination, this signal is lost [70].

The effect of spin-orbit coupling is most pronounced for the $A_{\mathrm{aniso,x}}$ component, smaller for $A_{\mathrm{aniso,y}}$, and almost negligible for $A_{\mathrm{aniso,z}}$ (see Table **8.4**). If spin-orbit coupling were considered along these lines, an improvement of the simulations would be possible. Extrapolated values (SR + SO UKS) are given in Table **8.4** and suggest this trend. The simultaneous treatment of spin-polarization and spin-orbit-coupling might improve the agreement for the hyperfine interaction along the g_x-component but such a theoretical approach is currently out of reach.

There is such a large number of adjustable parameters in the simulations of orientation-selected ENDOR spectra (e.g. the g-tensor orientation, the hyperfine tensor principal values and the hyperfine tensor orientations) that a systematic improvement of the simulations is difficult.

8.4 Discussion and Conclusion

The orientation-selected pulsed-ENDOR spectra of the regulatory hydrogenase (RH) from *R. eutropha* were recorded for a number of field positions between g_x and g_z. Supported by the theoretically calculated g-tensor orientation and the hyperfine tensor magnitudes and orientations from relativistic DFT calculations in the ZORA approach, hyperfine tensors of five protons could be assigned to experimental ENDOR signals.

Given the number of approximations and parameters that enter the analysis of orientation-selected

ENDOR spectra, the impact and accuracy of theoretical calculations must be considered satisfying. Further work on spin-polarized spin-orbit-coupled DFT wavefunctions might improve the theoretically predicted g-tensor orientation and/or the calculated hyperfine tensors. Figure **8.8** displays the assigned hyperfine tensors at the ν_+ side of the spectra.

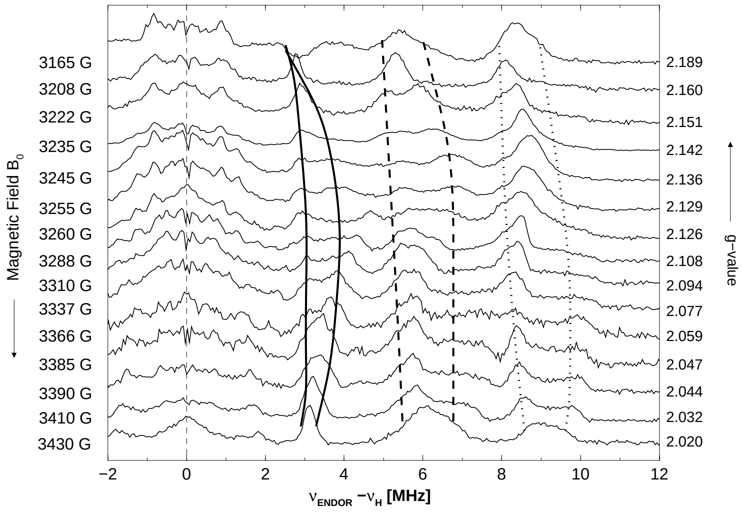

Figure 8.7: Assigned hyperfine couplings in the Ni-C form of the RH from *Ralstonia eutropha*. At the high frequency side, the ENDOR signals originating from the bridging hydride (dotted line), the β-CH$_2$ protons of Cys533 (dashed line), and the β-CH$_2$ protons of Cys530 (solid line) are marked.

The assignment of two β-CH$_2$ protons of the bridging cysteine Cys533 with isotropic values of 10.5 MHz each agrees well with orientation-selected cw-ENDOR measurements of the Ni-B form from *Allochromatium vinosum* [169]. In the Ni-B form 12.6 and 12.5 MHz were found. This indicates that the g_z-axis should be close to the Ni–SCys533 bond in both redox states. A complete reorientation of the g-tensor axes seems implausible and a reduction to a formal Ni(I) can therefore also be ruled out. This results was also obtained in the ZORA calculations of the g-tensor orientation (see Chapter 7). The decrease of the isotropic coupling might be explained by a slight reduction of spin density at the cysteine sulphur atom. The values obtained for the β-CH$_2$ protons of Cys533 also agree with values reported by Fan *et al.* [69] who measured a coupling of around 12 MHz at g_y for the [NiFe] hydrogenase from *D. gigas* in the Ni-C state. The coupling was found to be rather isotropic and not solvent-exchangeable. A tentative assignment was made to cysteinyl β-protons but a specific structural assignment was not possible due to the lack of an X-ray structure at that time.

The signals assigned to β-CH$_2$ protons from the terminal cysteine Cys530 in this work may correspond to those reported by Whitehead *et al.* [70] who observed a number of hyperfine coupling with $\leq$

5 MHz in the Ni-C state of *Thiocapsa roseopersicina.* An assignment, however, was not done. In the oxidized states Ni-A and Ni-B these couplings were not observed (see Chapter 6 and references [70,169]. The redistribution of spin density towards the terminal cysteine in the Ni-C state may explain the ^{77}Se hyperfine interaction of the hydrogenase from *Methanococcus voltae.* This [NiFeSe] hydrogenase possesses a selenocysteine in the position of Cys530. In the oxidized state, there is no ^{77}Se hyperfine interaction detectable in EPR while the Ni-C state exhibits a large ^{77}Se hyperfine splitting [230]. This indicates that in the Ni-C form, unpaired spin density is transfered to the position of Cys530. Given the ratio of the nuclear g-factors of ^{77}Se and of ^{33}S (1.0693/0.42911 = 2.49), a Se atom in place of the S atom of Cys530 may display such an effect. ^{77}Se hyperfine interactions that are 2.5 times larger than the corresponding ^{33}S are then expected.

The assignment of the large hyperfine coupling to a hydride ion in the position of the bridging ligand is supported by a number of experimental findings. The value reported by Whitehead *et al.* of 16-20 MHz agrees well with that found for the RH [70]. The coupling was shown to be solvent-exchangeable in D_2O and the corresponding deuterium-ENDOR signal was observed. Furthermore, upon photoillumination this coupling was completely lost. Fan *et al.* reported a solvent-exchangeable coupling of 17 MHz at g_x for the Ni-C form [69]. The authors also suggested a complete hyperfine tensor A^H = (+15, -22, -25) MHz and argued in favour of a negative sign of the isotropic hyperfine interaction (-11 MHz) for an in-plane bound hydride. From their work, it is not clear which g-tensor principal axes system and which hyperfine tensor orientation was used by the authors. Furthermore, since no ENDOR spectrum near g_z was reported, their estimate of the A_z hyperfine interaction is not comprehensible. The spin-unrestricted scalar-relativistic ZORA calculations yielded a complete tensor of (+10, -20, -16) MHz (a_{iso} = -9 MHz) in its own principal axes system which agrees reasonably well with that postulated by Fan *et al.*.

The regulatory hydrogenase from *R. eutropha* seems to possess an active centre that is very similar to that of the ‘standard hydrogenases’. The composition of the Ni-Fe cluster with its three diatomic ligands (2 CN and 1 CO) and four cysteines coordinating the Ni and Fe atoms appears to be very similar to that of other ‘standard [NiFe] hydrogenases’. The role of the RH, however, is distinct from that of the ‘standard hydrogenases’, i.e. its low activity, its resistivity towards oxygenation and the absence of S = 1/2 EPR signals from Fe-S clusters cannot be explained by a modification of the active site. The modulation of the function may result from a different protein environment or folding pattern. This issue cannot be decided yet.

Further experimental investigations are necessary in order to characterize the active centre of the RH. The determination of the g-tensor orientation from angular dependent EPR of protein-single crystals in the Ni-C form (either in one of the standard hydrogenases or in the RH) may support or contradict the orientation obtained from relativistic DFT calculations. In frozen solution, D_2O solvent exchange, observation of the disappearance of certain ENDOR signals and subsequent ^{2}H-ENDOR or ESEEM detection will shed more light on the hydrogen/deuteron binding site.

Chapter 9

Proposal of a Reaction Mechanism

Based on the findings in this thesis, the difference between the paramagnetic states of the [NiFe] hydrogenase can be explained. Ni-A can be described as a Ni–μ-oxo–Fe, Ni-B as a Ni–μ-hydroxo–Fe and Ni-C as a Ni–μ-hydrido–Fe bridged cluster.

For the first time, a model of the oxidation states and ligand environment can be proposed: Ni remains in its Ni(III) oxidation state in the Ni-A, Ni-B, and Ni-C forms. Ni-L originates from the Ni-C state by photodissociation of the bridging hydride which leaves its two electrons at the Ni atom (then a formal Ni(I) oxidation state). The CO-inhibited form Ni-CO is derived from the Ni(I)-L form; the agreement with a CO bound to Ni-C were not satisfying.

By characterization of the paramagnetic states, one only has an incomplete picture of the complete reaction cycle of the enzyme. The connection of the paramagnetic states is accomplished via diamagnetic and thus EPR-silent states Ni-Si$_{r,u}$ and Ni-R. According to the above findings, a sequence of redox states for the active site can be deduced (see Figure **9.1**).

However, a number of open questions remain to be answered.

- What is the role and function of the Ni and Fe metals, i.e. which of them is catalytically active?
- Where does the substrate hydrogen bind?
- What is the role of the Fe atom in the strong ligand field caused by the CO and CN ligands?
- Does the bridging ligand facilitate or participate in the splitting of H_2?
- Are the cysteine amino acids likewise involved in the reaction mechanism?
- Do the protein-cofactor interactions fine-tune the heterolytic splitting of hydrogen?

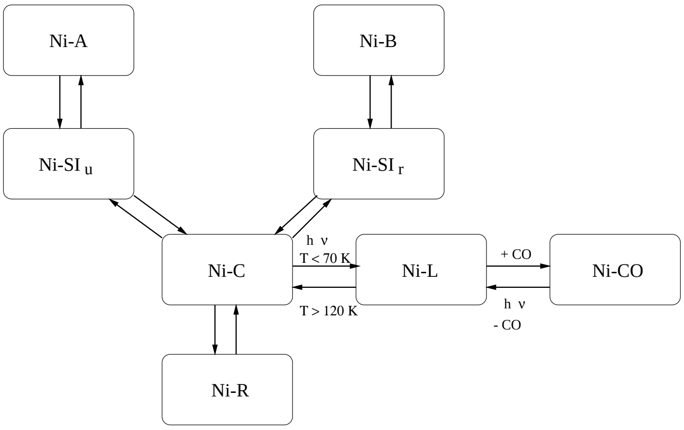

Figure 9.1: Sequence of redox states in [NiFe] hydrogenase

The number of electrons that flow into the active centre and the number of protons associated with each redox step were derived from redox titrations in the presence of dyes [40] (see Figure **9.2**). These results must be considered when a reaction mechanism is suggested. In the absence of artificial dyes, the redox potential of the protein is controlled by the H_2 partial pressure in solution [12]. Then, the exact number of redox equivalences (electrons and protons) that enter or leave the *active site* in each redox step cannot be determined. Only the overall conversions of H_2 by all metallic cofactors can be monitored.

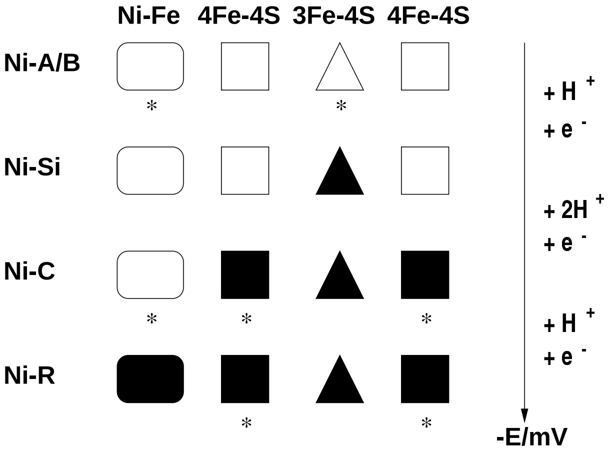

Figure 9.2: The redox equivalences that enter the active centre of [NiFe] hydrogenase. Symbols are explained in the caption of Figure **2.6**.

In a model for the heterolytic splitting of H_2, Ni-L and Ni-CO are not considered since they do not participate in the catalytic cycle. The investigation of those states, however, provides evidence for the light-sensitivity and inhibition of this enzyme.

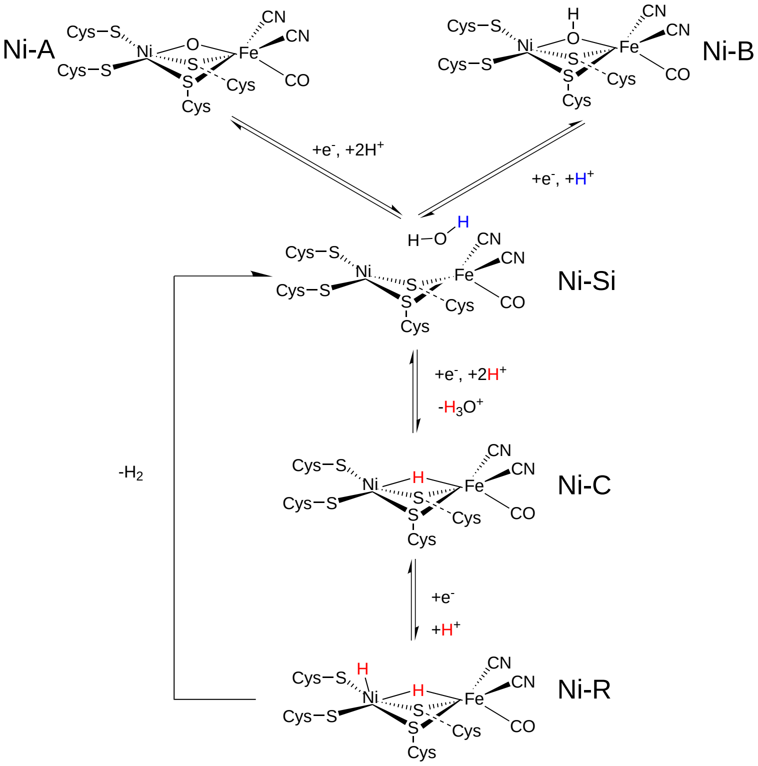

Figure 9.3: Reaction Pathway Proposed

Taking into account the results of the composition of the active centre in its paramagnetic states [Ni-A (X = O^{2-}), Ni-B (X = OH^-), Ni-C (X = H^-)] and the redox equivalents that enter the active site in each step (from Figure **9.2**), the following picture is obtained (Figure **9.3**): Upon activation of the enzyme, first the bridging ligand may be protonated. The resulting H_2O bridge would only be loosely bound and open the coordination site at the Ni atom. H_2 could then be heterolytically split. The hydride remains in the active centre as a Ni–Fe bridging ligand while the water molecule may take up the proton and leave the active site as a H_3O^+. Alternatively, the proton may be released via an amino acid assisted proton transfer chain. Formally, the completely reduced Ni-R state is one electron more reduced than Ni-C. The axial coordination site is a possible candidate for binding of an additional proton.

This is a plausible connection of the alternating paramagnetic and diamagnetic redox states of the active centre but there is no ultimate proof for the suggested mechanism.

All proposed intermediates [1] were characterized by DFT calculations using the ADF99 [160] program and the BP86 exchange correlation functional (for computational details see Chapter **7**). A detailed

---

[1] The Ni-A, Ni-B, Ni-C and Ni-L cluster models were identified as minima on the potential energy surface by analytical

comparison of the structural parameters of the calculated paramagnetic intermediates was already done in Chapters **5** and **7** and is not repeated here. Formally, the paramagnetic states correspond to Ni(III) and the diamagnetic states to Ni(II) oxidation states. Figure **9.4** shows the obtained structures for the intermediates. Only relevant structural parameters are given.

---

calculations of second derivatives. At the B3LYP/6-311+G level all harmonic frequencies were positive. Transition states could not be obtained so far.

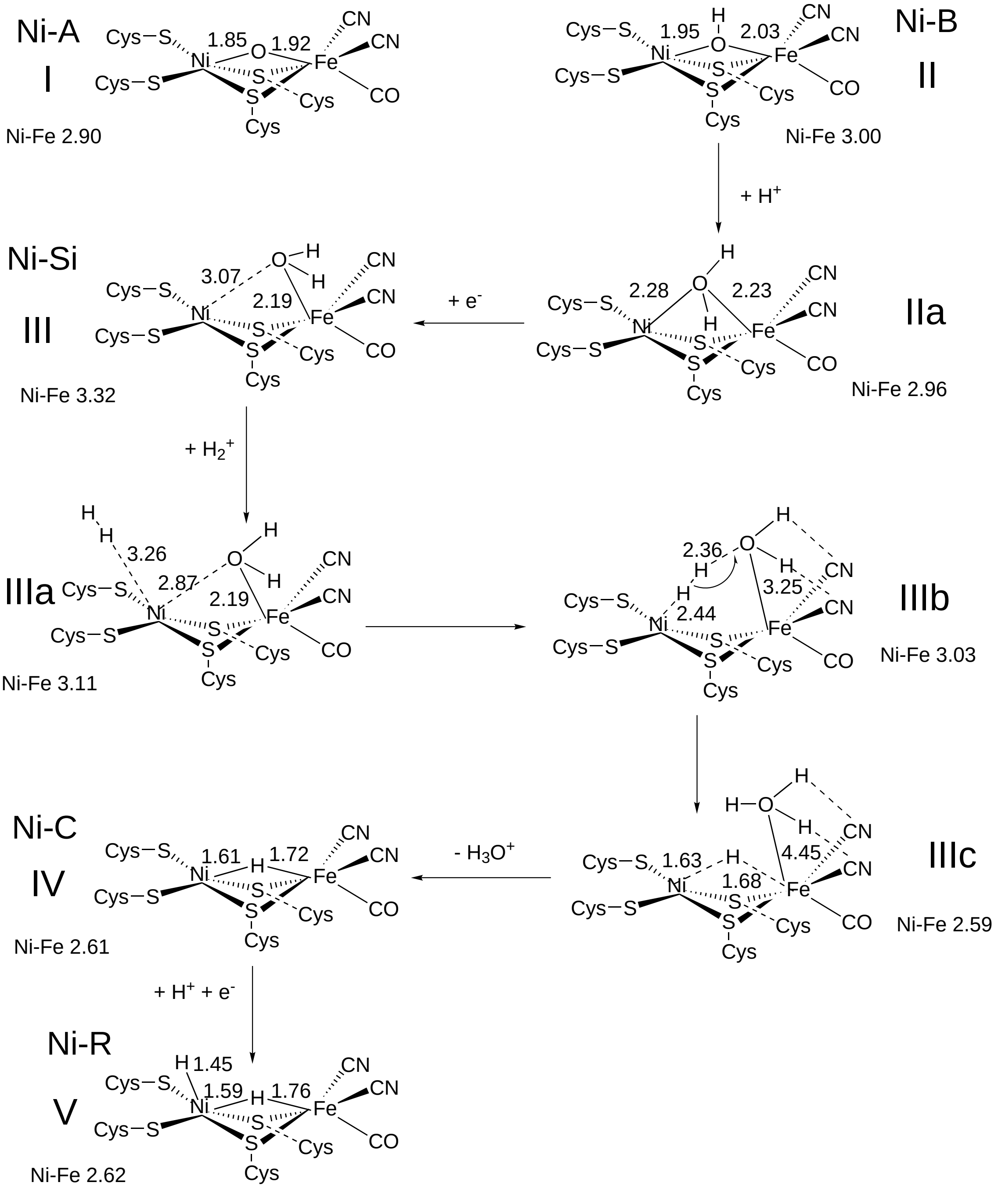

Figure 9.4: Calculated intermediates in the heterolytic splitting of H_2 by [NiFe] hydrogenase in the absence of the protein environment. Selected bond distances in Å.

Starting from the model for the Ni-B (**II**) form, a proton is added to the bridging OH^- ligand yielding a S = 1/2 state with a water molecule bridging Ni and Fe (**IIa**). The bond distances to the water molecule increase by 0.3 Å and 0.2 Å. The EPR-silent (S = 0) state Ni-Si is reached upon further adding an electron to the cluster (**III**) in which the Ni–OH_2 bond is already broken (3.07 Å). Next, molecular hydrogen may enter the active site. It is believed to diffuse through a hydrophobic channel towards the Ni atom [231]. An axial coordination (**IIIa**), however, is very weak (at a distance of 3.26 Å) but induces a decrease of the Ni–Fe distance from 3.32 Å to 3.11 Å. When the substrate is located between the Ni and water molecule (**IIIb**), a (local) minimum is reached. In an end-on coordination of the H_2 moiety, the Ni–H distance is 2.44 Å and the shortest distance to the water molecule 2.36 Å. This is accompanied by a decrease of the Ni–Fe distance to 3.03 Å. A proton transfer is only achieved when it is manually transfered to the water molecule yielding a formal H_3O^+ molecule (**IIIc**). The remaining hydride then occupies the position of the bridging ligand. The H_3O^+ is still hydrogen bound to the CN ligands. It may donate a proton to one of the ligands and remain coordinated in the vicinity of the active site or diffuse as a whole H_3O^+ away from the active centre. Thereby, the Ni-C state (**IV**) is obtained. The Ni-R (**V**) state is diamagnetic and contains one electron and one more proton than the Ni-C state (see [40] and references therein). An axial coordination of a formal hydrogen atom seems most plausible.

Experimental support for the suggested structure of the Ni-R form comes from the carbon monoxide-inhibited hydrogenase for which an axial coordination of the CO to the Ni was suggested (Y. Higuchi, personal communication). The crystallized reduced CO-inhibited hydrogenase from *D. vulgaris* Miyazaki F shows an unusual bent form of a CO axially coordinated to the Ni atom. This is reproduced in the calculations when the suggested Ni-R cluster model binds CO, the carbon monoxide molecule would insert into the Ni–H bond and give the experimentally found bent coordination (see Figure **9.5**).

Figure **9.6** displays the structures of the geometry-optimized intermediates.

In Chapter **7** it was shown that protein environment did not have a large influence on the calculated magnetic resonance parameters of the active centre of the [NiFe] hydrogenase. Next, it remained to be investigated whether the protein surrounding would then participate in or assist the heterolytic cleavage of H_2. Furthermore, it was investigated whether the local minimum of H_2 coordination to the Ni atom was an artefact of the cluster model approach. The suggested reaction path was then re-investigated using a larger cluster model in which the coordinating amino acids histidine His72, serine Ser486 and arginine Arg463 were explicitly considered. His72 forms a hydrogen bond to the bridging cysteine Cys533, Ser486 coordinates to one of the CN ligands, and Arg486 coordinates the second CN ligand and, in the Ni-B state, also the bridging ligand OH^- (see Chapter **7**).

Schematically, the obtained intermediates are given in Figure **9.7**.

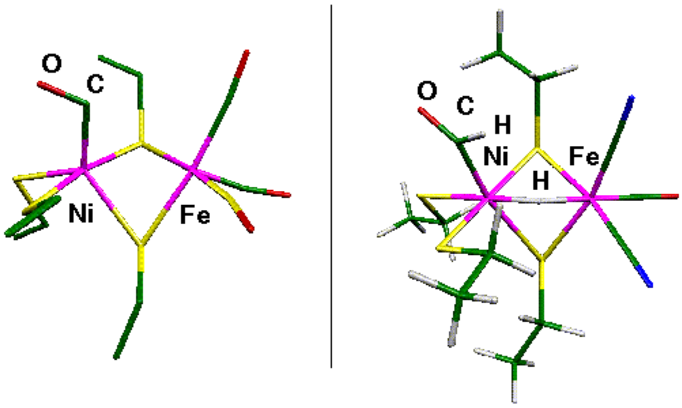

r (Ni-Fe)	2.64	2.68
r (Ni-CO)	1.76	1.95
r (C=O)	1.22	1.24
<(Ni-C-O)	118	127

Figure 9.5: Comparison of Ni-R_{CO} structures. Left: X-ray structure of the CO-inhibited [NiFe] hydrogenase from *D. vulgaris* Miyazaki F (Y. Higuchi, personal communication). Proton positions could not be determined. Right: BP86 calculated model cluster for Ni-R with CO inserted into the Ni–H_{axial} bond. Bond lengths (r) in Å, bond angle (⟨) in degree.

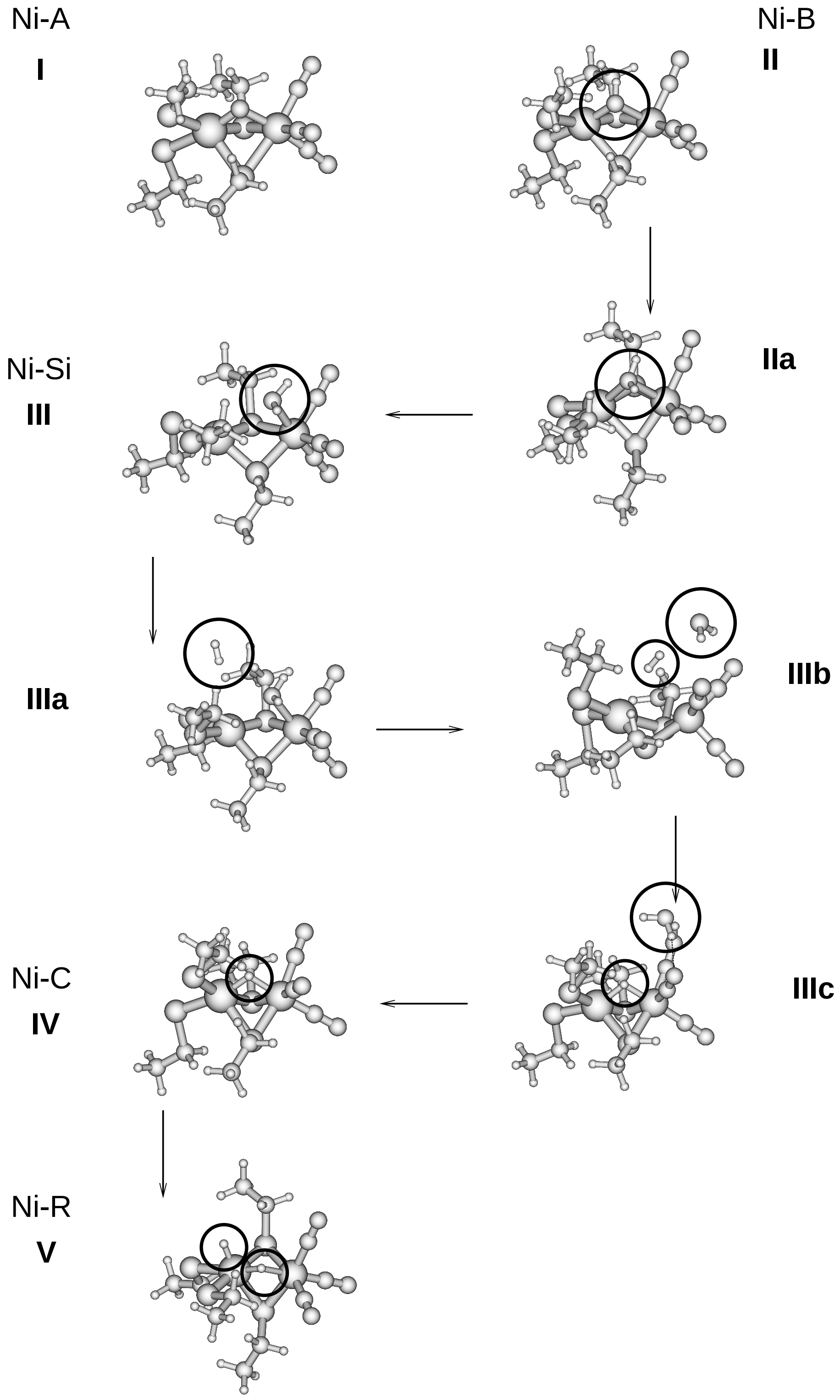

Figure 9.6: Geometry-optimized structures of the intermediates in the reaction cycle of [NiFe] hydrogenase in the absence of the protein environment (for a schematic drawing see Figure **9.4**).

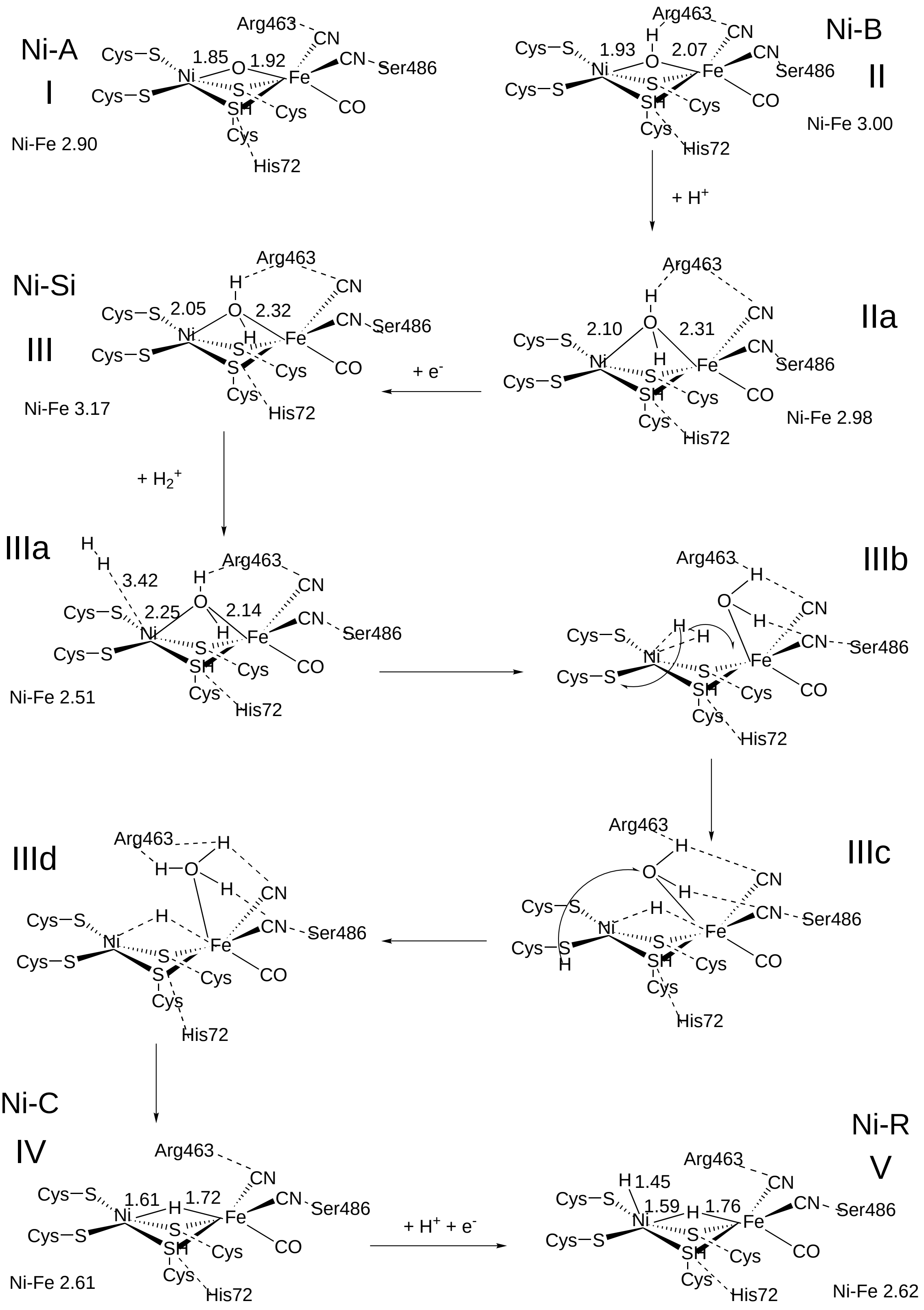

Figure 9.7: Calculated intermediates in the heterolytic splitting of H_2 by [NiFe] hydrogenase in the presence of the protein environment. Selected bond distances in Å.

When the bridging μ-hydroxo ligand in the Ni-B form (**II**) is protonated, a paramagnetic state with a bridging water molecule is generated (**IIa**). The hydrogen bond to the arginine Arg463 leads to a shorter Ni–OH_2 bond distance (2.10 Å) than in the absence of the arginine residue. Upon one-electron reduction, the Ni-Si state (**III**) is reached. In the absence of protein interaction (Figure **9.4**) the Ni–OH_2 bond was already mostly broken and the water was only loosely coordinated to the Fe atom. Here, the picture is different. The water is still firmly bound to the Ni atom (distance 2.05 Å) and slightly more remote from the Fe atom (distance 2.32 Å). As in the previously suggested reaction cycle in the absence of the protein environment, H_2 may approach the active centre through a hydrophobic protein channel and only loosely coordinate the Ni atom at a distance of 3.4 Å (**IIIa**). Still, the water molecule is held in place by a hydrogen bond to the arginine Arg463 residue.

When the substrate comes into the vicinity of the bridging water molecule, the Ni–OH_2 bond breaks and space is provided for the H_2 substrate (**IIIb**). Whereas an end-on coordination was found in the absence of any protein environment (see Figure **9.4 IIIb**), only a temporary side-on coordination of the substrate to the Ni atom is found here. During the course of a very long geometry optimization (more than 200 optimization steps for the 95 atom cluster model), without any bias or manual interference, the H_2 substrate is split.

One hydrogen atom (the later hydride) quickly forms a bond to the neighbouring Fe atom and occupies the position of the bridging ligand while the other hydrogen (considered to be a proton) is temporarily taken up by the sulphur atom of the terminal cysteine Cys530 (**IIIc**). Finally, the cysteine donates the proton to the approaching water molecule (**IIId**) and H_3O^+ is formed. The H_3O^+ moiety is still hydrogen-bound to both the arginine residue and the terminal cyanides and may donate a proton to either of these or diffuse away from the active site. Then the Ni-C state is obtained (**IV**) and finally the completely reduced Ni-R state (**V**).

The optimized geometries of the cluster models with relevance to the splitting of H_2 (from **IIIb** to **IIId**) are given in Figure **9.8**

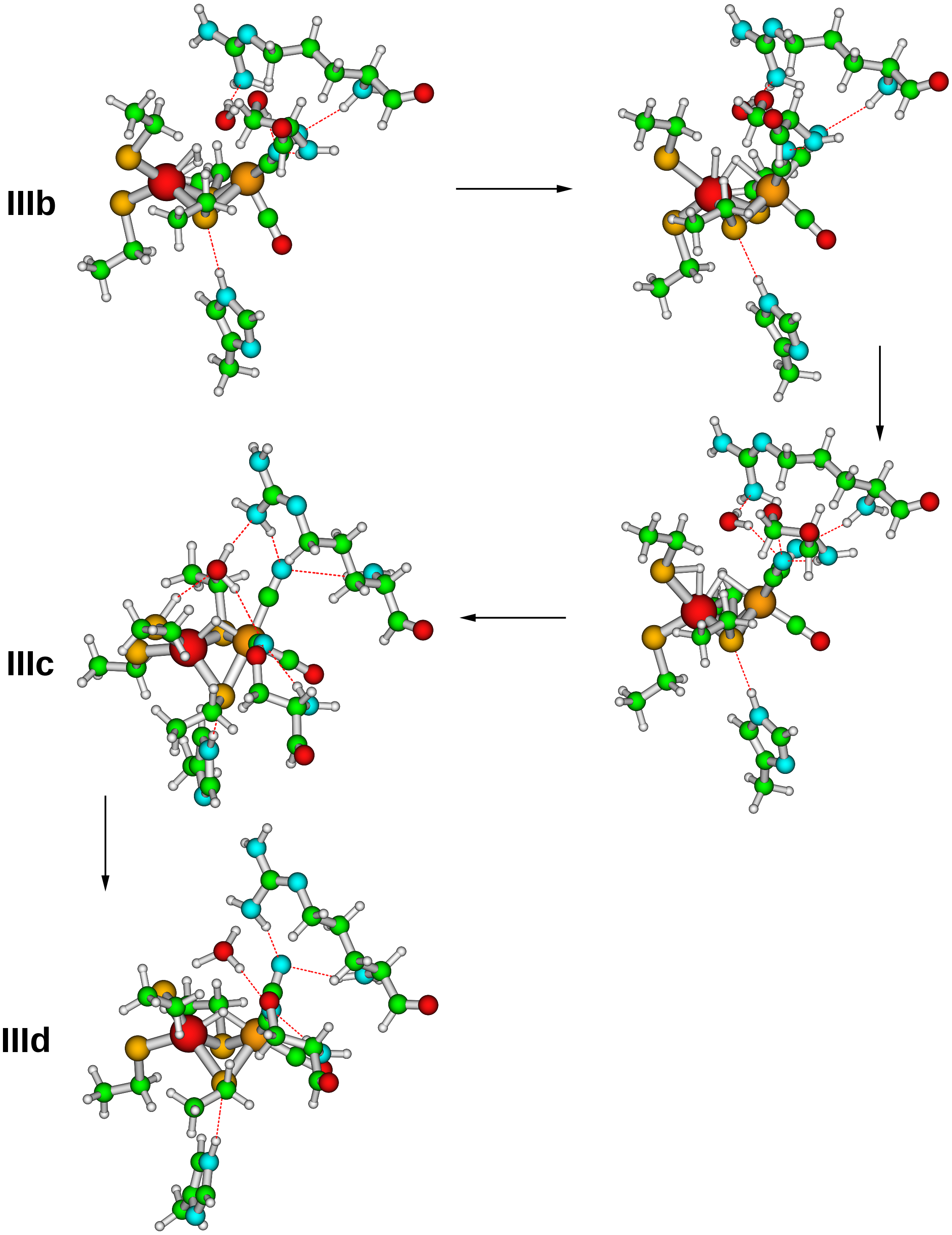

Figure 9.8: Snapshots of the geometry optimizations of the splitting of H_2 by [NiFe] hydrogenase. Top, left: side-on coordination of H_2 (**IIIb**); top, right : splitting of H_2; middle, right: protonation of Cysteine Cys530, middle, left: reorientation of the protonated Cys530 (**IIIc**); bottom: proton transfer to the bridging ligand (**IIId**).

Whereas the overall picture and the reaction products are the same in the two suggested mechanisms with and without the consideration of the coordinating nearby amino acid residues, they strongly differ in the details. In the absence of the protein, the bridging ligand is easily removed and not directly coordinated to the Ni atom. For the substrate, an end-on coordination to the Ni is obtained but no spontaneous dissociation of H_2 is found. The resulting hydride is found to occupy the position of the bridging ligand while H_3O^+ forms hydrogen bonds to the terminal cyanide ligands. The influence of the protein-cofactor interactions is manifested in a tight coordination of the protonated bridging ligand. Arginine Arg463 holds the bridging water molecule in close proximity to the Ni atom. For the substrate a side-on coordination is found. In the reaction cycle, the substrate immediately dissociates and temporarily protonates the terminal cysteine Cys530. This intermediate protonation of the terminal cysteine may explain the higher activity of [NiFeSe] hydrogenases which possess a selenocysteine in the position of Cys530. The role of the arginine residue, again, is to bring the water molecule in close contact with the protonated cysteine and thus finally enable protonation of the water.

The suggested mechanism for the [NiFe] hydrogenase differs in some aspects from those suggested by other authors [71–76]:

- Ni was identified as the active metal site.
- Ni-Si/Ni-C are the catalytically active states.
- The experimentally determined number of electrons and protons that enter the active site was taken into account.
- Experimental data for the paramagnetic states were considered.
- The number of experimentally determined D_2O solvent-exchangeable protons is in agreement with the suggested structures of the paramagnetic states.
- The Ni atom shuttles between formal +III and +II oxidation states.
- The bridging ligand is involved in the activation of the enzyme.
- The Fe atom is not redox active; its role is of structural, not electronic nature.
- Amino acid residues surrounding the active site have an important structural role in retaining the position of the bridging ligand.
- The terminal cysteine and the bridging ligand assist the heterolytic cleavage of H_2.

- A protonation of a cysteine residue is only short-lived and finally the protonated water molecule may receive the proton.

To conclude, the work in this thesis has suggested structural details for the paramagnetic and diamagnetic states of the [NiFe] hydrogenase. In particular, care was taken to assure agreement with a vast amount of experimental data where they were available. Many experimental data could be reproduced within satisfying accuracy. Some experimental findings are predicted and may stimulate further work.

A plausible reaction mechanism which links the well-characterized paramagnetic states via diamagnetic states is proposed. There is ample room to support or contradict the suggested enzymatic mechanism both on the experimental and theoretical side.

The experimental determination of g- and hyperfine tensors in protein single crystals in the Ni-C and Ni-L states will hopefully agree with the suggested g-tensor orientation from relativistic DFT calculations. This work is in progress (S. Foerster, personal communication).

These days, very little is known about the EPR-silent states. Further characterization of these states, e.g. additional parallel-mode detected EPR experiments on the energetic ordering of integer spin states or time-resolved FTIR experiments which lead to more kinetic data would be helpful.

From the theoretical point of view, an efficient and reliable calculation of reaction profiles including second derivatives and transition states on models that consist of 90-100 atoms, when the protein environment is explicitly considered, is required in order to characterize the reaction mechanism. Furthermore, there is a need for methodological extensions for simultaneously considering spin-polarization and spin-orbit coupling in transition metal complexes.

The introduction of a mutagenesis system for the ‘standard hydrogenases’ and site-directed mutations in the proton or electron transfer channels will further help to unravel the catalytic process of [NiFe] hydrogenases.

Chapter 10

Zusammenfassung und Ausblick

In der vorliegenden Arbeit wurden [NiFe]-Hydrogenasen mit Methoden der magnetischen Resonanzspektroskopie (EPR, ENDOR) und der Dichtefunktionaltheorie (DFT) untersucht. Hydrogenasen katalysieren die reversible, heterolytische Oxidation von molekularem Wasserstoff $H_2 \rightleftharpoons H^+ + H^-$.

Das aktive Zentrum in der großen Untereinheit des Enzyms ist ein heterobimetallischer Ni-Fe-Cluster, der von Cysteinaminosäuren koordiniert wird. Drei anorganische Liganden sind zusätzliche terminale Liganden des Eisenatoms. Ein bisher nicht eindeutig identifizierter Ligand verbrückt die beiden Schwermetallatome. Drei Eisen-Schwefelcluster in der kleinen Untereinheit des Proteins sind am Elektronentransfer von und zum aktiven Zentrum beteiligt. In einigen Redoxzuständen weist das aktive Zentrum ungepaarte Elektronen auf und ist deshalb mit der EPR-Spektroskopie und verwandten Methoden untersuchbar.

Ziel dieser Doktorarbeit war es, Einsicht in die Funktionsweise dieses Metalloenzyms über die Charakterisierung der paramagnetischen Intermediate zu erhalten.

Nickelmodellkomplexe

Die beiden anorganischen Modellkomplexe Bis(maleonitrildithiolat)-Nickelat(III) ($\mathrm{Ni(mnt)}_2^-$) und Tricarbonylnickel(I)hydrid ($\mathrm{Ni(CO)_3H}$) weisen gewisse Ähnlichkeiten in der geometrischen und elektronischen Struktur mit den [NiFe]-Hydrogenasen auf. Für diesen beiden Komplexe wurde die Berechnung von $\mathbf{g}$- und $\mathbf{A}$-Tensoren mit dem ZORA-Hamiltonoperator etabliert und kritisch mit vorhandenen experimentellen Ergebnissen verglichen. Ein störungstheoretischer Ansatz wurde als Vergleich ebenfalls verwendet. Der Einfluß skalar-relativistischer Effekte auf die Bindungsparameter wurde diskutiert. Im Detail lassen sich die Einflüsse von skalar-relativistichen Effekten und der Spinbahnkopplung auf die Hyperfeintensoren untersuchen. Die Berücksichtigung der Spinbahnkopplung erweist sich als unverzichtbar, wenn die elektronische Struktur (insbesondere die Hyperfeintensoren) von Übergangsmetallkomplexen mit DFT-Verfahren berechnet werden sollen. Die Übereinstimmung mit experimentellen **g**-Tensoren ist zufriedenstellend. Die Abweichung der berechneten von den experimentellen Daten ist proportional zu der Abweichung der g-Werte von g_e. Für die Hyperfeintensoren ist die Übereinstimmung i.a. sehr gut und die Größe der Abweichung ist wenige Prozent. Experimentelle Uneindeutigkeiten in der Bestimmung der Vorzeichen der Nickel- und Schwefelhyperfeintensoren in $\mathrm{Ni(mnt)}_2^-$ konnten mit Hilfe der Rechnungen behoben werden.

Spindichteverteilung im aktiven Zentrum der [NiFe] Hydrogenase

Für die paramagnetischen Zustände Ni-A, Ni-B und Ni-C war die genaue atomare Struktur des aktiven Zentrum bisher unklar. Insbesondere die Art des Nickel und Eisen verbrückenden Liganden war Gegenstand kontroverser wissenschaftlicher Diskussionen. Es konnte gezeigt werden, daß beste Übereinstimmung mit den Röntgenstrukturdaten der Hydrogenase aus *D. gigas* erzielt werden konnte, wenn der Brückenligand ein O^{2-} oder OH^- war. Der Schwefelligand, der für die Hydrogenase aus *D. vulgaris* Miyazaki F postuliert wurde, konnte nicht durch die Rechnungen bestätigt werden, da die berechneten strukturellen Parameter nicht in gutem Einklang mit experimentellen Ergebnissen der Röntgenstrukturanalyse waren. Die berechnete Verteilung der ungepaarten Spindichte ist in guter Übereinstimmung mit Daten der EPR- und ENDOR-Spektroskopie oder daraus abgeleiteten Ergebnissen. Im Ni-C Zustand konnte gute Übereinstimmung mit der Röntgenstruktur der reduzierten Hydrogenasen aus *D. baculatum* und *D. vulgaris* Miyazaki F erzielt werde, wenn die vakante Position des Brückenliganden in den Röntgenstrukturen durch ein Hydridanion besetzt wurde. Die berechnete Verteilung der ungepaarten Spindichte war ebenfalls in Übereinstimmung mit vorhandenen experimentellen Daten der magnetischen Resonanz. Es konnte gezeigt werde, daß die drei anorganischen, prosthetischen Liganden am Eisenatom des aktiven Zentrums wahrscheinlich zwei Zyanidliganden und ein Kohlenmonoxid sind. Ein für die Hydrogenase aus *D. vulgaris* Miyazaki F postulierter SO-Ligand führte in den Rechnungen zu einer großen Verschiebung der ungepaarten Spindichte. Dieser Ligand erscheint daher wenig wahrscheinlich.

ENDOR-Kristallographie der oxidierten Zustände der [NiFe] Hydrogenase

Proteineinkristalle der [NiFe]-Hydrogenase aus *D. vulgaris* Miyazaki F wurden mit der gepulsten ENDOR-Spektroskopie in den oxidierten Zuständen Ni-A und Ni-B untersucht. Eine Trennung der beiden Spezies und der vier Moleküle in der Einheitszelle (Raumgruppe der Kristalle $P2_12_12_1$) erfolgte durch eine Analyse der rotationswinkelabhängigen EPR-Spektren. Für den Ni-B Zustand konnten drei Hyperfeintensoren aus den winkelabhängigen ENDOR-Spektren analysiert und zugeordnet werden. Die beiden großen Kopplungen wurden β-CH_2 Protonen des verbrückenden Cysteins Cys549 zugeordnet. Für die dritte Kopplung blieben zwei Zuordnungsmöglichkeiten: zu einem Proton am Brückenliganden oder zu einem β-CH_2 Proton des terminalen Cysteins Cys81. DFT Berechnungen der Hyperfeintensoren bestätigten die Zuordnung der beiden großen Hyperfeintensoren und konnten die Uneindeutigkeit bezüglich der dritten Kopplung beseitigen. Die Zuordnung zu einem β-CH_2 Proton des terminalen Cysteins Cys81 erschien am plausibelsten. Der Ni-A Zustand zeichnete sich durch eine Mikroheterogenität der Proteinumgebung aus. Die erhaltenen winkelabhängigen ENDOR-Spektren ließen sich nicht im Detail analysieren. Nichtsdestoweniger konnten die beiden großen Hyperfeinkopplungen, nicht aber die kleinere, dritte Kopplung beobachtet werden. Dieser Befund wurden wiederum unterstützt von DFT Rechnungen.

Relativistische DFT Rechnungen an den paramagnetischen Zuständen der Hydrogenase

In diesem Kapitel konnte erstmals eine Vorstellung der genauen atomaren Zusammensetzung und der elektronischen Struktur der paramagnetischen Zustände Ni-A, Ni-B, Ni-C, Ni-L und Ni-CO der [NiFe]-Hydrogenase gewonnen werden. Im Rahmen des ZORA-Hamiltonoperators wurden eine Vielzahl von möglichen Bindungssituationen berechnet und die erhaltenen Ergebnisse mit experimentellen Daten verglichen. Beste Übereinstimmung bezüglich der Orientierung und Grösse des **g**-Tensors mit den experimentellen Ergebnissen wurde erzielt, wenn der Brückenligand ein OH^- im Ni-B Zustand ist. Die berechneten Hyperfeinwechselwirkungen sind ebenfalls im Einklang mit experimentellen Befunden. Für den Ni-A Zustand (eine O^{2-} Brücke erscheint am plausibelsten) konnte gezeigt werden, daß sich Defizite des ZORA-Hamiltonoperators durch Berücksichtigung von Spinpolarisation im Pauli-Operator teilweise beheben lassen. Für Ni-C wurde beste Übereinstimmung mit experimentellen Ergebnissen erhalten, wenn ein Hydridanion die Bindungsstelle des Brückenliganden einnimmt. Die vorgeschlagene **g**-Tensororientierung wurde später experimentell bestätigt. Nach den Rechnungen geht der Ni-L Zustand aus dem Ni-C Zustand durch Photodissoziation des Bückenliganden hervor. Eine Reduktion zum formalen Ni(I) wird vorgeschlagen. Für alle Zustände (Ni-A, Ni-B, Ni-C, Ni-L) wurden Hyperfeintensoren für ^{61}Ni, ^{57}Fe, ^{33}S, ^{17}O und ^{1}H berechnet und kritisch mit experimentellen Daten verglichen. Das Enzyme wird durch Kohlenmonoxid irreversibel inhibiert. Verschiedene Bindungspositionen für das zusätzliche CO-Molekül wurden untersucht. Beste Übereinstimmung mit experimentellen Ergebnisse wurde für eine axiale Bindung an das aktive Zentrum im Ni-L Zustand erhalten. Zusätzlich wurden ^{14}N Hyperfein- und Quadrupolkopplungen berechnet und diskutiert und der Einfluß der Proteinumgebung auf die elektronische Struktur des aktiven Zentrums untersucht.

Orientierungsselektierte ENDOR-Spektroskopie am Ni-C Zustand

Die regulatorische Hydrogenase (RH) aus *R. eutropha* weist im reduzierten Ni-C Zustand keine Spin-Spin-Kopplung zwischen Elektronenspins des aktiven Zentrums und Fe-S Clustern auf. Dies macht die RH eine ideale Kandidatin für die ENDOR-Charakterisierung des Ni-C Zustandes, die in der Standardhydrogenase aus *D. vulgaris* Miyazaki F aus dem obigen Grund nicht möglich war. In gefrorener Proteinlösung wurde von der Selektivität der Anzahl resonanter Moleküle in Bezug auf das Magnetfeld profitiert. Orientierungsselektierte gepulste ENDOR-Spektren an fünfzehn Feldpositionen wurden so erhalten. Die Analyse der orientierungsselektierten Spektren erfordert eine *a priori* Kenntnis der Lage des $\mathbf{g}$-Tensors in der molekularen Struktur. Diese wurde aus den Rechnungen mit dem ZORA-Hamiltonoperator gewonnen. Zusammen mit den berechneten Größen und Orientierungen der Protonenhyperfeintensoren im Ni-C Zustand konnten insgesamt fünf Protonen zugeordnet werden Vier davon rühren von den beiden β-CH_2 Protonen des terminalen Cysteins Cys530 und des verbrückenden Cysteins Cys549 her. Das fünfte Proton wurde dem verbrückenden Liganden H^- zugeordnet.

Vorschlag eines Reaktionsmechanismus

Die oben erwähnten Einblicke in die verschiedenen paramagnetischen Zustände wurden in diesem Kapitel zusammengefügt, um einen plausible Reaktionsmechanismus des Enzyms vorzuschlagen. Ni-A und Ni-B unterscheiden sich in ihren Aktivierungskinetiken unter reduzierenden Bedingungen. Die Freisetzung des Brückenliganden und die Aufnahme eines Hydridanions in diese Bindungsposition scheinen die Aktivierung des Enzyms darzustellen. Ein plausibler Reaktionsweg, der die gewonnene Einsicht in die paramagnetischen Zustände verbindet mit den Redoxäquivalenten und Protonen, die das aktive Zentrum in jedem Reaktionsschritt aufnimmt, wurde konstruiert. In der Abwesenheit der Proteinumgebung wird ein Modelle für alle Zwischenzustände vorgeschlagen. Das so gewählte Modell ist aber nicht von sich aus katalytisch aktiv, d.h. H_2-Spaltung setzte nicht spontan ein. Erst nach der expliziten Berücksichtigung der Aminosäuren Arginin Arg463, Histidin His72 und Serin Ser486 konnte ein Reaktionszyklus erhalten werden, in dem die heterolytische Dissoziation von H_2 ein spontan ablaufenden Prozeß ist. Das terminale Cystein Cys530 agiert demnach temporär als Base und nimmt das Proton aus der heterolytischen H_2-Spaltung auf. Das Proton wird an den modifizierten Brückenliganden weitergegeben und kann als H_3O^+ oder über einen Protonentransferkanal das aktive Zentrum verlassen. In diesem vorgeschlagenen Mechanismus ist das Nickelatom das katalytisch aktive Metall. Dem Eisenatom und der Proteinumgebung kommen demnach Rollen struktureller Natur zu, z. B. die Positionierung des Brückenliganden, so daß dieser an der Aufnahme des Protons beteiligt werden kann.

Ausblick

In dieser Arbeit konnte Einsicht in die paramagnetischen Zustände und den Reaktionsmechanismus der [NiFe]-Hydrogenase gewonnen werden. Die Resultate können noch viele zukünftige Experimente stimulieren bzw. zur Analyse von experimentellen Befunden beitragen. Die experimentelle Bestimmung der Lage der **g**-Tensoren in den Ni-C und Ni-L Zuständen könnte durch die hier vorgeschlagenen vereinfacht werden. Derzeit wird daran in der AG Lubitz gearbeitet (S. Foerster, persönliche Mitteilung). Verglichen mit den paramagnetischen Zuständen weiß man heute relativ wenig über die diamagnetischen Intermediate. Mit der zeitaufgelöste FTIR-Spektroskopie könnte man wichtige Aussagen über Kinetiken der Zustandsumwandlungen gewinnen. Mit der EPR-Spektroskopie in paralleler Detektion ließen sich noch viele interessante Einzelheiten über diese Zustände hervorbringen, d.h. die energetische Lage von ganzzahligen Spinzuständen könnte bestimmt werden.

Von der theoretischen Seite ist die genaue Berechnung von Reaktionsbarrieren und die Lokalisierung von Übergangszuständen für Systeme von der Grösse von 90-100 Atomen zwingend nötig, um zuverlässige Aussagen über einen möglichen Reaktionsmechanismus machen zu können. Weitere methodische Arbeit ist zur gleichzeitigen Behandlung von Spinbahnkopplung und Spinpolarisation notwendig, um dadurch das Verständnis der elektronischen Struktur von Übergangsmetallkomplexen und -enzymen zu vertiefen.

Bisher existieren nur ungenaue Vorstellungen über einen möglichen Protonen- oder Elektronentransferweg in der [NiFe]-Hydrogenase. Die Etablierung eines Mutagenesesystems für ‘Standardhydrogenasen’ und ortsgerichtete Mutationen im Protonen- oder Elektronentransferweg (Austausch von potentiell am Transfer beteiligten Aminosäuren gegen andere und Beobachtung der Auswirkung der Mutationen auf die Transferraten) wird dazu beitragen, die Spaltung von molekularem Wasserstoff durch dieses Metalloenzym bei Raumtemperatur zu verstehen.

Bibliography

[1] Hoppe-Seyler, F. *Z. Physiol. Chem.* **1887** *11*, 561.

[2] C.Pakes, W. C.; Jollyman, W. H. *J. Chem. Soc.* **1901** *79*, 386.

[3] Harden, A. *J. Chem. Soc.* **1901** *79*, 601.

[4] Stephenson, M.; Stickland, L. H. *Biochem. J.* **1931** *25*, 205.

[5] Tuner, J. A. *Science* **1999** *285*, 687.

[6] Carrette, L.; Collins, J.; Dickinson, A.; Stimming, U. *Bunsen-Magazin* **2000** *2*, 27.

[7] Appleby, A. J. *Scientific American* **1999**, 74.

[8] Cammack, R. *Nature* **1999** *397*, 214.

[9] Maroney, M. J.; Davidson, G.; Allan, C. B.; Figlar, J. *Struct. Bond.* **1998** *92*, 1.

[10] Frausto Da Silva, J. J. R.; Williams, R. J. P. *The Biological Chemistry of the Elements : The Inorganic Chemistry of Life* Clarendon Press, Oxford, UK, 1994.

[11] Fontecilla-Camps, J. C.; Volbeda, A.; Frey, M. *Trends Biotechn.* **1996** *14*, 417.

[12] Albracht, S. P. J. *Biochim. Biophys. Acta* **1994** *1188*, 167.

[13] Adams, M. W. W. *Biochim. Biophys. Acta* **1990** *1020*, 115.

[14] Thauer, R. K.; Klein, A. R.; Hartmann, G. C. *Chem. Rev.* **1996** *96*, 3031.

[15] Voordouw, G. In: *Advances in Inorganic Chemistry Vol. 38*, R. Cammack and A. Sykes (Eds.), Academic Press, London, 1992, pp. 397–422.

[16] Hedderich, R.; Klimmek, O.; Kröger, A.; Dirmeier, R.; Keller, M.; Stetter, K. O. *FEMS Microbiol. Revs.* **1999** *22*, 353.

[17] Adams, M. W. W.; Mortenson, L. E.; Chen, J.-S. *Biochim. Biophys. Acta* **1981** *594*, 105.

[18] Przybyla, A. E.; Robbins, J.; Menon, N.; Peck Jr., H. D. *FEMS Microbiol. Rev.* **1992** *88*, 109.

[19] Wu, L.-F.; Mandrand, M. A. *FEMS Microbiol. Revs.* **1993** *104*, 243.

[20] Rakhely, G.; Colbeau, A.; Garin, J.; Vignais, P. M.; Kovacs, K. L. *J. Bact.* **1998** *180*, 1460.

[21] Dahl, C.; Rakhely, G.; Pott-Sperling, A. S.; Fodor, B.; Takacs, M.; Toth, A.; Kraeling, M.; Györfi, K.; Kovacs, A.; Tusz, J.; Kovacs, K. L. *FEMS Microbiol. Letts.* **1999** *180*, 317.

[22] Volbeda, A.; Fontecilla-Camps, J. C.; Frey, M. *Curr. Op. Struct. Biol.* **1996** *6*, 804.

[23] Ermler, U.; Grabarse, W.; Shima, S.; Goubeaud, M.; Thauer, R. K. *Curr. Op. Struc. Biol.* **1998** *8*, 749.

[24] Ragsdale, S. W. *Curr. Op. Chem. Biol.* **1998** *2*, 208.

[25] Maroney, M. *Curr. Op. Chem. Biol.* **1999** *3*, 188.

[26] Karplus, P. A.; Pearson, M. A.; Hausinger, R. P. *Acc. Chem. Res.* **1997** *30*, 330.

[27] Volbeda, A.; Garcin, E.; Piras, C.; de Lacey, A. L.; Fernandez, V. M.; Hatchikian, E. C.; Frey, M.; Fontecilla-Camps, J. C. *J. Am. Chem. Soc.* **1996** *118*, 12989.

[28] Higuchi, Y.; Yagi, T.; Yasuoka, N. *Structure* **1997** *5*, 1671.

[29] Ermler, U.; Grabarse, W.; Shima, S.; Goubeaud, M.; Thauer, R. K. *Science* **1997** *278*, 829.

[30] Peters, J. W.; Lanzilotta, W. N.; Lemon, B. J.; Seefeldt, L. C. *Science* **1998** *282*, 1853.

[31] Nicolet, Y.; Piras, C.; Legrand, P.; Hatchikian, C. E.; Fontecilla-Camps, J. C. *Structure* **1998** *7*, 13.

[32] Volbeda, A.; Charon, M.-H.; Piras, C.; Hatchikian, E. C.; Frey, M.; Fontecilla-Camps, J. C. *Nature* **1995** *373*, 580.

[33] Fontecilla-Camps, J. C. *J. Biol. Inorg. Chem.* **1996** *1*, 91.

[34] Frey, M. *Structure and Bonding* **1998** *90*, 97.

[35] Garcin, E.; Montet, Y.; Volbeda, A.; Hatchikian, C.; Frey, M.; Fontecilla-Camps, J. C. *Biochm. Soc. Trans.* **1988** *26*, 396.

[36] Rousset, M.; Montet, Y.; Guigliarelli, B.; Forget, N.; Asso, M.; Betrand, P.; Fontecilla-Camps, J. C.; Hatchikian, E. C. *Proc. Natl. Acad. Sci. USA* **1998** *95*, 11625.

[37] Higuchi, Y.; Yasuoka, N.; Kakudo, M.; Katsube, Y.; Yagi, T.; Inokuchi, H. *J. Biol. Chem.* **1987** *262*, 28823.

[38] Higuchi, Y.; Okamoto, T.; Fujimoto, K.; Misaki, S. *Acta Cryst. D* **1994** *50*, 781.

[39] Asso, M.; Guigliarelli, B.; Yagi, T.; Bertrand, P. *Biochim. Biophys. Acta* **1992** *1122*, 50.

[40] Cammack, R.; Patil, D. S.; Hatchikian, E. C.; Fernandez, V. M. *Biochim. Biophys. Acta* **1987** *912*, 98.

[41] Lancaster Jr., J. R. *FEBS Lett.* **1980** *115*, 285.

[42] Graf, E.-G.; Thauer, R. K. *FEBS Lett.* **1981** *136*, 165.

[43] Fernandez, V. M.; Hatchikian, E. C.; Cammack, R. *Biochim. Biophys. Acta* **1985** *832*, 69.

[44] Dole, F.; Fournel, A.; Magro, V.; Hatchikian, E. C.; Bertrand, P.; Guigliarelli, B. *Biochemistry* **1997** *36*, 7847.

[45] Moura, J. J. G.; Moura, I.; Huynh, B. H.; Krüger, H.-J.; Teixeira, M.; DuVarney, R. G.; DerVartanian, D. V.; Ljungdahl, P.; Xavier, A. V.; ad J. LeGall, H. D. P. *Biochem. Biophys. Res. Comm.* **1982** *108*, 1388.

[46] Guigliarelli, B.; More, C.; Fournel, A.; Asso, M.; Hatchikian, E. C.; Williams, R.; Cammack, R.; Bertrand, P. *Biochemistry* **1995** *34*, 4781.

[47] Betrand, P.; Camensuli, P.; More, C.; Guigliarelli, B. *J. Am. Chem. Soc.* **1996** *118*, 1426.

[48] Dole, F.; Medina, M.; More, C.; Cammack, R.; Bertrand, P.; Guigliarelli, B. *Biochemistry* **1996** *35*, 16399.

[49] Bagley, K. A.; Van Garderen, C. J.; Chen, M.; Duin, E. C.; Albracht, S. P. J.; Woodruff, W. H. *Biochemistry* **1994** *33*, 9229.

[50] Bagley, K. A.; Duin, E. C.; Roseboom, W.; Albracht, S. P. J.; Woodruff, W. H. *Biochemistry* **1995** *34*, 5527.

[51] Happe, R. P.; Roseboom, W.; Pierik, A. J.; Albracht, S. P. J. *Nature* **1997** *385*, 126.

[52] Jonas, V.; Thiel, W. *J. Chem. Phys.* **1996** *105*, 3636.

[53] Jensen, F. *Chem. Phys. Lett.* **1990** *169*, 519.

[54] de Lacey, A. L.; Hatchikian, E. C.; Volbeda, A.; Frey, M.; Fontecilla-Camps, J. C.; fernandez, V. M. *J. Am. Chem. Soc.* **1997** *119*, 7181.

[55] Davidson, G.; Choudbury, S. B.; Gu, Z.; Bose, K.; Roseboom, W.; Albracht, S. P. J.; Maroney, M. J. *Biochemistry* **2000** *39*, 7468.

[56] Hsu, H.-F.; Koch, S. A.; Popescu, C. V.; Münck, E. *J. Am. Chem. Soc.* **1997** *119*, 8371.

[57] Coremans, J. M. C. C.; van Garderen, C. J.; Albracht, S. P. J. *Biochim. Biophys. Acta* **1992** *1119*, 148.

[58] Happe, R. H.; Roseboom, W.; Albracht, S. P. J. *Eur. J. Biochem.* **1999** *259*, 602.

[59] Albracht, S. P. J.; Graf, E. G.; Thauer, R. K. *FEBS Letts.* **1982** *140*, 311.

[60] Erkens, A.; Schneider, K.; Müller, A. *J. Biol. Inorg. Chem.* **1996** *1*, 99.

[61] Huyett, J. E.; Carepo, M.; Pamplona, A.; Franco, R.; Moura, I.; Moura, J. J. G.; Hoffman, B. M. *J. Am. Chem. Soc.* **1997** *119*, 9291.

[62] Albracht, S. P. J.; Kröger, A.; der Zwaan, J. W. V.; Unden, G.; Böcher, R.; Mell, H.; Fontijn, R. D. *Biochim. Biophys. Acta* **1986** *874*, 116.

[63] van der Zwaan, J. W.; Coremans, J. M. C. C.; Bouwens, E. C. M.; Albracht, S. P. J. *Biochim. Biophys. Acta* **1990** *1041*, 101.

[64] Lancaster Jr., J. R. *Science* **1982** *216*, 1324.

[65] Lancaster, Jr., J. R., ed. *The Bioinorganic Chemistry of Nickel* VCH, Weinheim, 1988.

[66] Moura, J. J. G.; Teixeira, M.; Moura, I.; LeGall, J. In: *The Bioinorganic Chemistry of Nickel*, J. R. Lancaster, Jr. (Ed.), VCH, Weinheim, 1988, pp. 191–226.

[67] van der Zwaan, J. W.; Albracht, S. P. J.; Fintijn, R. D.; Slater, E. C. *FEBS Lett.* **1985** *179*, 271.

[68] Chapman, A.; Cammack, R.; Hatchikian, E. C.; McCracken, J.; Peisach, J. *FEBS Lett.* **1988** *242*, 134.

[69] Fan, C.; Teixeira, M.; Moura, J.; Moura, I.; Huynh, B.-H.; Gall, J. L.; Peck, H. D. J.; Hoffman, B. M. *J. Am. Chem. Soc.* **1991** *113*, 20.

[70] Whitehead, J. P.; Gurbiel, R. J.; Bagyinka, C.; Hoffman, B. M.; Maroney, M. J. *J. Am. Chem. Soc.* **1993** *115*, 5629.

[71] Pavlov, M.; Siegbahn, P. E. M.; Blomberg, M. R. A.; Crabtree, R. H. *J. Am. Chem. Soc.* **1998** *120*, 548.

[72] Pavlov, M.; Blomberg, M. R. A.; Siegbahn, P. E. M. *Intern. J. Quant. Chem.* **1999** *73*, 197.

[73] DeGioia, L.; Fantucci, P.; Guigliarelli, B.; Bertrand, P. *Inorg. Chem.* **1999** *38*, 2658.

[74] DeGioia, L.; Fantucci, P.; Guigliarelli, B.; Bertrand, P. *Int. J. Quant. Chem.* **1999** *73*, 187.

[75] Niu, S.; Thomson, L. M.; Hall, M. B. *J. Am. Chem. Soc.* **1999** *121*, 4000.

[76] Amara, P.; Volbeda, A.; Fontecilla-Camps, J. C.; Field, M. J. *J. Am. Chem. Soc.* **1999** *121*, 4468.

[77] Atherton, N. M. *Principles of Electron Spin Resonance* Ellis Horwood PTR Prentice Hall, New York, 1993.

[78] Weil, J. A.; Bolton, J. R.; Wertz, J. E. *Electron Paramagnetic Resonance* Wiley and Sons Inc., New York, 1994.

[79] Abragam, A.; Bleaney, B. *Electron Paramagnetic Resonance of Transition Ions* Clarendon Press, Oxford, UK, 1970.

[80] Mabbs, F. E.; Collison, D. *Electron Paramagnetic Resonance of d Transition Metal Compounds* Elsevier, Amsterdam, 1992.

[81] Pilbrow, J. R. *Transition Ion Electron Paramagnetic Resonance* Clarendon Press, Oxford, UK, 1990.

[82] Feher, G. *Phys. Rev.* **1956** *103*, 834.

[83] Schweiger, A. *Angew. Chem. Int. Ed. Engl.* **1991** *30*, 265.

[84] Gemperle, C.; Schweiger, A. *Chem. Rev.* **1991** *91*, 1481.

[85] Kurreck, H.; Kirste, B.; Lubitz, W. *Electron Nuclear Double Resonance Spectroscopy of Radicals in Solution* VCH, Weinheim, Germany, 1988.

[86] McConnell, H. M. *J. Chem. Phys.* **1956** *24*, 764.

[87] Harriman, J. E. *Theoretical Foundations of Electron Spin Resonance* Academic Press Inc., New York, 1978.

[88] Lowe, D. J. *ENDOR and EPR of Metalloproteins* R. G. Landes Co., UK, 1995.

[89] Parr, R.; Yang, W. *Density-Functional Theory of Atoms and Molecules* Oxford University Press, New Yorck, New Yorck, 1989.

[90] Koch, W.; Holthausen, M. C. *A Chemist's Guide to Density Functional Theory* WILEY-VCH, Weinheim, Germany, 2000.

[91] Becke, A. D. *Phys. Rev. A* **1988** *38*, 3098.

[92] Lee, C.; Yang, W.; Parr, R. G. *Phys. Rev. B* **1988** *37*, 785.

[93] Perdew, J. P. *Phys. Rev.* **1986** *B33*, 8822.

[94] Hamprecht, F. A.; Cohen, A. J.; Tozer, D. J.; Handy, N. C. *J. Chem. Phys.* **1998** *109*, 6264.

[95] Becke, A. D. *J. Chem. Phys.* **1993** *98*, 5648.

[96] Stevens, P. J.; Devlin, J. F.; Chabalowski, C. F.; Frisch, M. J. *J. Phys. Chem.* **1994** *98*, 11623.

[97] Ziegler, T. *Chem. Rev.* **1991** *91*, 651.

[98] Ziegler, T. *Can. J. Chem.* **1995** *73*, 743.

[99] Koch, W.; Hertweg, R. H. In: *Encyclopedia of Computational Chemistry*, P. von Ragué Schleyer (Ed.), Wiley and Sons Inc., New York, 1998, pp. 900–920.

[100] C. W. Bauschlicher Jr. In: *Encyclopedia of Computational Chemistry*, P. von Ragué Schleyer (Ed.), Wiley and Sons Inc., New York, 1998, pp. 3084–3094.

[101] Siegbahn, P. E. M. In: *Advances in Chemical Physics Vol. XCIII*, I. Prigogine and S. A. Rice (Eds.), Wiley and Sons Inc., New York, 1996, pp. 333–388.

[102] Jonas, V.; Thiel, W. *J. Chem. Phys.* **1995** *102*, 8474.

[103] Siegbahn, P. E. M.; Blomberg, M. R. A. *Chem. Rev.* **2000** *100*, 421.

[104] Pykkö, P. *Chem. Rev.* **1988** *88*, 563.

[105] Visscher, L.; Aerts, P. J. C.; Nieuwpoort, W. C. *J. Chem. Phys.* **1992** *96*, 2910.

[106] Visscher, L.; Visser, O.; Aerts, P. J. C.; Merenga, H.; Nieuwpoort, W. C. *Comp. Phys. Commun.* **1994** *81*, 120.

[107] van Wüllen, C. *J. Comput. Chem.* **1999** *20*, 51.

[108] Ziegler, T. *J. Chem. Phys.* **1981** *74*, 1271.

[109] Knappe, P.; Rösch, N. *J. Chem. Phys.* **1990** *92*, 1153.

[110] Frenking, G.; Antes, I.; Boehme, M.; Dapprich, S.; Ehlers, A. W.; Jonas, V.; Neuhaus, A.; Otto, M.; Stegmann, R.; Veldkamp, A.; Vyboishchikov, S. In: *Rev. Comp. Chem. Vol. 8*, K. B. Lipkowitz and D. B. Boyd (Eds.), Wiley and Sons Inc., New York, 1996, pp. 63–143.

[111] Cundari, T. R.; Benson, M. T.; Lutz, L.; Sommer, S. O. In: *Rev. Comp. Chem. Vol. 8*, K. B. Lipkowitz and D. B. Boyd (Eds.), Wiley and Sons Inc., New York, 1996, pp. 145–202.

[112] van Lenthe, E.; Baerends, E. J.; Snijders, J. G. *J. Chem. Phys.* **1993** *99*, 4597.

[113] van Lenthe, E.; Baerends, E. J.; Snijders, J. G. *J. Chem. Phys.* **1994** *101*, 9783.

[114] Chang, C.; Pélissier, M.; Durand, P. *Phys. Scr.* **1986** *34*, 394.

[115] Pople, J. A.; Beveridge, D. L.; Dobosh, P. A. *J. Am. Chem. Soc.* **1968** *90*, 4201.

[116] Plato, M.; Tränkle, E.; Lubitz, W.; Lendzian, F.; Möbius, K. *Chem. Phys.* **1986** *107*, 185.

[117] Karna, S. P.; Grein, F.; Engels, B.; Peyerimhoff, S. D. *Int. J. Quant. Chem.* **1989** *36*, 255.

[118] Feller, D.; Davidson, E. R. In: *Theoretical Models of Chemical Bonding Vol. 3*, Z. B. Maksic (Ed), Springer-Verlag, Heidelberg, Germany, 1991, pp. 430–453.

[119] Chipman, D. M. In: *Quantum Mechanical Electronic Structure Calculations with Chemical Accuracy*, S. R. Langhoff (Ed.), Kluwer, Amsterdam, 1995, pp. 109–138.

[120] Eriksson, L. A.; Wang, J.; Boyd, R. J. *Chem. Phys. Letts.* **1993** *211*, 88.

[121] Barone, V.; Adamo, C.; Russo, N. *Chem. Phys. Letts.* **1993** *212*, 5.

[122] Barone, V. In: *Recent Advances in Density Functional Methods Part I*, D. P. Chong (Ed.), World Scientific, Singapore, 1995, pp. 287–304.

[123] Malkin, V. G.; Malkina, O. L.; Eriksson, L. A.; Salahub, D. R. In: *Modern Density Functional Theory: A Tool for Chemistry*, J. M. Seminario and P. Politzer (Eds.), Elsevier, Amsterdam, 1995, pp. 273–347.

[124] Eriksson, L. A. In: *Encyclopedia of Computational Chemistry*, P. von Ragué-Schleyer (Ed.), Wiley and Sons Inc., New York, 1998, pp. 952–958.

[125] Engels, B.; Eriksson, L. A.; Lunell, S. *Adv. Quantum Chem.* **1996** *27*, 297.

[126] Munzarova, M.; Kaupp, M. *J. Phys. Chem A* **1999** *103*, 9966.

[127] Hayes, R. G. *Inorg. Chem.* **2000** *39*, 156.

[128] Belanzoni, P.; Baerends, E. J.; van Asselt, S.; Langewen, P. B. *J. Phys. Chem.* **1995** *99*, 13094.

[129] Belanzoni, P.; Baerends, E. J.; Gribnau, M. *J. Phys. Chem. A* **1999** *103*, 3732.

[130] Swann, J.; Westmoreland, T. D. *Inorg. Chem.* **1997** *36*, 5348.

[131] van Lenthe, E.; van der Avoird, A.; Wormer, P. E. S. *J. Chem. Phys.* **1998** *108*, 4783.

[132] van Lenthe, E.; Snijders, J. G.; Baerends, E. J. *J. Chem. Phys.* **1996** *105*, 6505.

[133] Törring, J. T.; Un, S.; Küpling, M.; Plato, M.; Möbius, K. *J. Chem. Phys.* **1997** *107*, 3905.

[134] Lushington, G. H.; Bundgen, P.; Grein, F. *Int. J. Quant. Chem.* **1995** *55*, 377.

[135] Engström, M.; Minaev, B.; Vahtras, O.; Ågren, H. *Chem. Phys.* **1998** *237*, 149.

[136] Jayatilaka, D. *J. Chem. Phys.* **1998** *108*, 7587.

[137] Tachikawa, H. *Chem. Phys. Lett.* **1996** *260*, 582.

[138] Bruna, P. J.; Grein, F. *J. Chem. Phys.* **1998** *109*, 9439.

[139] Lushington, G. H. *J. Phys. Chem. A* **2000** *104*, 2969.

[140] Vahtras, O.; Minaev, B.; Ågren, H. *Chem. Phys. Lett.* **1997** *281*, 186.

[141] Engström, M.; Himo, F.; Gräslund, A.; Minaev, B.; Vahtras, O.; Agren, H. *J. Phys. Chem. A* **2000** *104*, 5149.

[142] Schreckenbach, G.; Ziegler, T. *J. Phys. Chem. A* **1997** *101*, 3388.

[143] Patchkovskii, S.; Ziegler, T. *J. Chem. Phys.* **1999** *111*, 5730.

[144] Patchkovskii, S.; Ziegler, T. *J. Am. Chem. Soc.* **2000** *122*, 3506.

[145] Schreckenbach, G.; Ziegler, T. *Theor. Chem. Acc.* **1998** *99*, 71.

[146] van Lenthe, E.; Wormer, P. E. S.; van der Avoird, A. *J. Chem. Phys.* **1997** *107*, 2488.

[147] Malkina, O.; Vaara, J.; Schimmelpfennig, B.; Munzarova, M.; Malkin, V. G.; Kaupp, M. *J. Am. Chem. Soc.* **2000** *122*, 9206.

[148] Halcrow, M. A.; Christou, G. *Chem. Rev.* **1994** *94*, 2421.

[149] Maki, A. H.; Edelstein, N.; Davison, A.; Holm, R. H. *J. Am. Chem. Soc.* **1964** *86*, 4580.

[150] Schmitt, R. D.; Maki, A. H. *J. Am. Chem. Soc.* **1968** *90*, 2288.

[151] Huyett, J. E.; Choudhury, S. B.; Eichhorn, D. M.; Bryngelson, P. A.; Maroney, M. J.; Hoffman, B. M. *Inorg. Chem.* **1998** *37*, 1361.

[152] Sano, M.; Adachi, H.; Yamatera, H. *Bull. Chem. Soc. Jpn.* **1981** *54*, 2636.

[153] Kraffert, C.; Walther, D.; Peters, K.; Lindqvist, O.; Langer, V.; Sieler, J.; Reinhold, J.; Hoyer, E. *Z. Anorg. Allg. Chem.* **1990** *588*, 167.

[154] Shiozaki, H.; Nakazumi, H.; Kitao, T. *J. Jpn. Soc. Col. Mat.* **1987** *60*, 415.

[155] Blomberg, M. A.; Wahlgren, U. *Chem. Phys.* **1980** *49*, 117.

[156] Hjalmars, I. F.; Henrickson-Enflo, A. *I. J. Quant. Chem.* **1980** *18*, 409.

[157] Zakharov, I. I.; Startsev, A. N.; Yudanov, I. V.; Zhidomirov, G. M. *J. Struct. Chem.* **1996** *37*, 201.

[158] Arca, M.; Demartin, F.; Devillanova, F. A.; Garau, A.; Isai, F.; Lelj, F.; Lippols, V.; Pedraglio, S.; Verani, G. *J. Chem. Soc. Dalton Trans.* **1998** *22*, 3731.

[159] Morton, J. R.; Preston, K. F. *J. Magn. Res.* **1978** *30*, 577.

[160] Theoretical Chemistry *Amsterdam Density Functional (ADF), Rev. 1999* Vrije Universiteit De Boelelaan 1083, NL-1081 HV Amsterdam, The Netherlands.

[161] te Velde, G.; Baerends, E. J. *Int. J. Quant. Chem.* **1992** *99*, 84.

[162] van Lenthe, E.; Ehlers, A.; Baerends, E. J. *J. Chem. Phys.* **1999** *110*, 8943.

[163] Becke, A. D. *J. Chem. Phys.* **1986** *84*, 4524.

[164] Perdew, J. P. *Phys. Rev.* **1986** *B34*, 7406.

[165] Frisch, M. J.; Trucks, G. W.; Schlegel, H. B.; Gill, P. M. W.; Johnson, B. G.; Robb, M. A.; Cheeseman, J. R.; Keith, T.; Petersson, G. A.; Montgomery, J. A.; Raghavachari, K.; Al-Laham, M. A.; Zakrzewski, V. G.; Ortiz, J. V.; Foresman, J. B.; Cioslowski, J.; Stefanov, B. B.; Nanayakkara, A.; Challacombe, M.; Peng, C. Y.; Ayala, P. Y.; Chen, W.; Wong, M. W.; Andres, J. L.; Replogle, E. S.; Gomperts, R.; Martin, R. L.; Fox, D. J.; Binkley, J. S.; Defrees, D. J.; Baker, J.; Stewart, J. P.; Head-Gordon, M.; Gonzalez, C.; Pople, J. A. *Gaussian94, Revision D.2* Gaussian Inc., Pittsburgh PA **1995**.

[166] Kobayashi, A.; Sasaki, Y. *Bull. Chem. Soc. Jpn.* **1977** *50*, 2650.

[167] Schäfer, A.; Horn, H.; Ahlrichs, R. *J. Chem. Phys.* **1992** *97*, 2571.

[168] W. E. Geiger, J.; Allen, C. S.; Mines, T. E.; Senftleber, F. C. *Inorg. Chem.* **1977** *16*, 2003.

[169] Geßner, C.; Stein, M.; Albracht, S. P. J.; Lubitz, W. *J. Biol. Inorg. Chem.* **1999** *4*, 379.

[170] Morton, J. R.; Preston, K. F. *J. Chem. Phys.* **1984** *81*, 5775.

[171] Volbeda, A.; Charon, M.-H.; Piras, C.; Hatchikian, E. C.; Frey, M.; Fontecilla-Camps, J. C. *Nature* **1995** *373*, 580.

[172] Higuchi, Y.; Yagi, T. *Biochem. Biophys. Res. Com.* **1999** *255*, 295.

[173] Pierik, A. J.; Roseboom, W.; Happe, R. P.; Bagley, K. A.; Albracht, S. P. J. *J. Biol. Chem.* **1999** *274*, 3331.

[174] Higuchi, Y.; Ogata, H.; Miki, K.; Yasuoka, N.; Yagi, T. *Structure* **1999** *7*, 549.

[175] *DGauss4.0* Cray Res. Inc., San Diego **1995**.

[176] Godbout, N.; Salahub, D. R.; Andzelm, J.; Wimmer, E. *Can. J. Chem.* **1992** *70*, 560.

[177] Neese, F.; Kappl, R.; Hüttermann, J.; Zumft, W. G.; Kroneck, P. M. H. *J. Biol. Inorg. Chem.* **1998** *3*, 53.

[178] Barone, V.; Adamo, C. *Intern. J. Quant. Chem.* **1997** *61*, 443.

[179] Geßner, C.; Trofanchuk, O.; Kawagoe, K.; Higuchi, Y.; Yasuoka, N.; Lubitz, W. *Chem. Phys. Lett.* **1996** *256*, 518.

[180] Surerus, K. K.; Chen, M.; der Zwaan, W. V.; Rusnak, F. M.; Kolk, M.; Duin, E. C.; Albracht, S. P. J.; Münck, E. *Biochemistry* **1994** *33*, 4980.

[181] Gu, Z.; Dong, J.; Allen, C. B.; Choudbury, S. B.; Franco, R.; Moura, J. J. G.; Moura, I.; LeGall, J.; Przybyla, A. E.; Roseboom, W.; Albracht, S. P. J.; Axley, M. J.; Scott, R. A.; Maroney, M. J. *J. Am. Chem. Soc.* **1996** *118*, 11155.

[182] Stein, M.; Trofanchuk, O.; Brecht, M.; Lendzian, F.; Bittl, R.; Higuchi, Y.; Lubitz, W. *manuscript in preparation* **2001**.

[183] Trofanchuk, O.; Stein, M.; Geßner, C.; Lendzian, F.; Higuchi, Y.; Lubitz, W. *J. Biol. Inorg. Chem.* **2000** *5*, 36.

[184] Brecht, M.; Stein, M.; Trofanchuk, O.; Lendzian, F.; Bittl, R.; Higuchi, Y.; Lubitz, W. In: *Magnetic Resonance and Related Phenomena Vol. II*, D. Ziessow, F. Lendzian, W. Lubitz (Eds.), TU Berlin, 1998, pp. 818–819.

[185] Garcin, E.; Vernede, X.; Hatchikian, E.; Volbeda, A.; Frey, M.; Fontecilla-Camps, J. C. *Structure* **1999** *7*, 557.

[186] Bagyinka, C.; Whitehead, J. P.; Maroney, M. J. *J. Am. Chem. Soc.* **1993** *115*, 3576.

[187] Rist, G. H.; Hyde, J. S. *J. Chem. Phys.* **1970** *52*, 4633.

[188] Hüttermann, J. In: *Biological Magnetic Resonance Vol. 13*, L. J. Berliner and J. Reuben (Eds.), Plenum Press, New York, 1993, pp. 219–252.

[189] Hoffman, B. M.; DeRose, V. L.; Doan, P. E.; Gurbiel, R. J.; Houseman, A. L. P.; Telser, J. In: *Biological Magnetic Resonance Vol. 13*, L. J. Berliner and J. Reuben (Eds.), Plenum Press, New York, 1993, pp. 151–218.

[190] Trofanchuk, O.; Stein, M.; Gessner, C.; Lendzian, F.; Higuchi, Y.; Lubitz, W. *J. Biol. Inorg. Chem.* **2000** *5*, 36.

[191] Dinse, K. P. In: *Advanced EPR - Applications in Biology and Biochemistry*, A. J. Hoff (Ed.), Elsevier, Amsterdam, 1989, pp. 615–631.

[192] Coremans, J. W. A.; Poluektov, O. G.; Groenen, E. J. J.; Nar, G. W. C. H.; Messerschmidt, A. *J. Am. Chem. Soc.* **1996** *118*, 12141.

[193] Mims, W. B. *Proc. R. Soc. London* **1965** *283*, 452.

[194] Davies, E. R. *Phys. Lett. A* **1974** *47A*, 1.

[195] Doan, P. E.; Fan, C.; Hoffman, B. M. *J. Am. Chem. Soc.* **1994** *116*, 1033.

[196] Geßner, C. *NiFe-Hydrogenasen: Beiträge der EPR-Spektroskopie zur Strukturaufklärung des aktiven Zentrums* Ph.D. thesis Technische Universität Berlin **1996**.

[197] Wachters, A. J. H. *J. Chem. Phys.* **1970** *52*, 1033.

[198] Hay, P. J. *J. Chem. Phys.* **1977** *66*, 4377.

[199] Raghavachari, K.; Truck, G. W. *J. Chem. Phys.* **1989** *91*, 1062.

[200] McLean, A. D.; Chandler, G. S. *J. Chem. Phys.* **1980** *72*, 5639.

[201] Krishnan, R.; Binkley, J. S.; Seeger, R.; Pople, J. A. *J. Chem. Phys.* **1980** *72*, 650.

[202] Frisch, M. J.; Pople, J. A.; Binkley, J. S. *J. Chem. Phys.* **1984** *80*, 3265.

[203] Reed, A. E.; Curtiss, L. A. *Chem. Rev.* **1988** *88*, 899.

[204] Glendening, E. D.; Reed, A. E.; Carpenter, J. E.; Weinhold, F. *NBO Version 3.1*.

[205] BRUKER Analytische Messtechnik In: *Pulsed EPR: A new field of applications*, C. P. Keijzers, E. J. Reijerse and J. Schmidt (Eds.), North Holland, Amsterdam, 1989, pp. 81-88.

[206] Atherton, N. M. *Principles of Electron Spin Resonance* Prentice Hall, New York, 1993.

[207] Mouesca, J.-M.; Rius, G.; Lamotte, B. *J. Am. Chem. Soc.* **1993** *115*, 4714.

[208] Teixera, M.; Moura, I.; Xavier, A. V.; Dervartanian, D. V.; LeGall, J.; Jr., H. D. P.; Huynh, B. H.; Moura, J. G. *Eur. J. Biochem.* **1983** *130*, 481.

[209] Trofanchuk, O. *Catalytic Center of [NiFe] Hydrogenases. EPR, ENDOR and FTIR Studies* Ph.D. thesis TU Berlin **2000**.

[210] Biosym Technologies *Insight II* Version 235 San Diego, 1994.

[211] Pople, J. A.; Gill, P. M. W.; Handy, N. C. *Int. J. Quant. Chem.* **1995** *56*, 303.

[212] Jensen, F. *Introduction to Computational Chemistry* Wiley and Sons Inc., Chichester, UK, 1999.

[213] van der Zwaan, J. W.; Albracht, S. P. J.; Fontijn, R. D.; Roelofs, Y. B. M. *Biochim. Biophys. Acta* **1986** *872*, 208.

[214] van Leeuwen, R.; van Lenthe, E.; Baerends, E. J.; Snijders, J. G. *J. Chem. Phys.* **1994** *101*, 1272.

[215] Sadlej, A. J.; Snijders, J. G.; van Lenthe, E.; Baerends, E. J. *J. Chem. Phys.* **1995** *102*, 1758.

[216] van Lenthe, E.; Baerends, E. J. *J. Chem. Phys.* **2000** *112*, 8279.

[217] Cammack, R.; Fernandez, V. M.; Schneider, K. In: *The Bioinorganic Chemistry of Nickel* J. R. Lancaster, Jr. (Ed.), VCH, Weinheim, 1988, pp. 167–190.

[218] R. Cammack, C. Bagyinka, K. L. K. *Eur. J. Biochem.* **1989** *182*, 357.

[219] Lemon, B. J.; Peters, J. W. *Biochemistry* **1999** *38*, 12969.

[220] Dikanov, S. A.; Patil, D. S.; Bowman, M. K. *J. Inorg. Biochem.* **1997** *67*, 427.

[221] Lenz, O.; Friedrich, B. *Proc. Natl. Acad. Sci. USA* **1998** *95*, 12474.

[222] Kleihues, L.; Lenz, O.; Bernhard, M.; Buhrke, T.; Friedrich, B. *J. Bact.* **2000** *182*, 2716.

[223] Pierik, A. J.; Schmelz, M.; Lenz, O.; Friedrich, B.; Albracht, S. P. J. *FEBS Lett.* **1998** *438*, 231.

[224] Hurst, G. C.; Henderson, T. A.; Kreilick, R. W. *J. Am. Chem. Soc.* **1985** *107*, 7294.

[225] Henderson, T. A.; Hurst, G. C.; Kreilick, R. W. *J. Am. Chem. Soc.* **1985** *107*, 7299.

[226] Kappl, R.; Hüttermann, J. In: *Advanced EPR - Applications in Biology and Biochemistry*, A. J. Hoff (Ed.), Elsevier, Amsterdam, 1989, pp. 501–540.

[227] Hoffman, B. M.; Gurbiel, R. J.; Werst, M. M.; Sivaraja, M. In: *Advanced EPR - Applications in Biology and Biochemistry*, A. J. Hoff (Ed.), Elsevier, Amsterdam, 1989, pp. 541–591.

[228] Mombourquette, M. J.; Weil, J. A. *J. Mag. Res.* **1992** *99*, 37.

[229] Teixeira, M.; Moura, I.; Xavier, A. V.; Huynh, B. H.; DerVartanian, D. V.; Peck Jr., H. D.; LeGall, J.; Moura, J. J. G. *J. Biol. Chem.* **1985** *260*, 8942.

[230] Sorgenfrei, O.; Duin, E. C.; Klein, A.; Albracht, S. P. J. *Eur. J. Biochem.* **1997** *247*, 681.

[231] Montet, Y.; Amara, P.; Volbeda, A.; Vernede, X.; Hatchikian, E. C.; Field, M. J.; Frey, M.; Fontecilla-Camps, J. C. *Nat. Struct. Biol.* **1997** *4*, 523.

Danksagung

Herrn Prof. Dr. Wolfgang Lubitz danke ich für die freundliche Aufnahme in seine Arbeitsgruppe und die Betreuung bei der Bearbeitung eines spannenden Themas übergangsmetallhaltiger Enzymkatalyse. Seine Kritik und Skeptik gegenüber den Aussagen theoretischer Verfahren waren immer eine Herausforderung.

Herr Prof. Dr. Wolfram Koch hat freundlicherweise die Mitbegutachtung der Doktorarbeit übernommen. In der Anfangsphase der Arbeit waren einführende Diskussionen über die elektronische Struktur von Übergangsmetallen sehr hilfreich. Den Mitarbeitern seiner Arbeitsgruppe danke ich für technische Unterstützung mit quantenchemischen Programmen.

I am very grateful to Prof. Dr. Yoshiki Higuchi (University of Kyoto, Japan) for an excellent co-operation. Without his magnificent and beautiful protein single crystals, much of the work in this thesis would not have been possible.

Herrn Dipl.-Chem. Thorsten Buhrke aus der AG von Frau Prof. Dr. Bärbel Friedrich (Humboldt-Universität Berlin) danke ich für die Anzucht, Isolation und Reinigung der regulatorischen Hydrogenase. Thorsten, mein angeheirateter Schwipp-Cousin, wir werden schon noch zusammen alt werden - und sei es auf dem Spielplatz. Unvergessen sind unsere gemeinsamen Pantschereien in Unwissenheit vom 1. Semester an bis zum heutigen Tag.

I enjoyed the co-operation with Prof. Dr. Evert Jan Baerends and Dr. Erik and Lenthe (VU Amsterdam, Netherlands). I happily remember their hospitality during a short stay in Amsterdam. I learned a lot from their carefulness in the interpretation of results from DFT. Erik, you are the most gifted theoretical physicists I have ever met. Before I met you, I always thought relativistic effects were something for anoraks.

Herrn Dr. Thomas Steinke vom Konrad-Zuse-Zentrum für Informationstechnik Berlin (ZIB) bin ich dankbar für Hilfe und Unterstützung mit den Großrechnern am ZIB.

I thank Prof. Dr. Tom Ziegler and Dr. Serguei Patchkovskii (University of Calgary, Canada) for making the QR code by Dr. Georg Schreckenbach available to me. I was allowed to use their impressive Cobalt cluster.

Herrn Dr. Friedhelm Lendzian und Herrn Priv.-Doz. Dr. Robert Bittl danke ich für Tag-und-Nacht Hilfe mit den Spektrometern, wenn es mal nach Ampere riecht. Esc-Esc-Esc-p-p-r-e-i-a.

Den Mitgliedern der H2ase-Combo (Frau Dr. Olga Trofantschuk, Herrn Dipl.-Phys. Marc Brecht und Frau Dipl.-Chem. Stefanie Foerster) verdanke ich eine Menge. Olga, unvergessen bleiben unsere langen Messungen. Hannes, Herr der Pulse, ein Puls geht schon noch rein; was heißt das denn nun biologisch? Stefanie, Frau mit den glücklichen Händchen, behandele die paramagnetischen Proben gut.

Alle Mitarbeiter der AG Lubitz haben eine angenehme, anregende Arbeitsatmosphäre geschaffen.

Dem Fonds der Chemischen Industrie danke ich für ein Chemiefondsstipendium in der Anfangsphase der Promotion.

Die Arbeit wäre niemals vollendet worden ohne den Zuspruch, die Unterstützung und die Ablenkung durch meine Familie. Ich widme Kerstin und Jonas diese Arbeit.

Lebenslauf

Name	Matthias Stein
Geburtsdatum	03.05.1971
Geburtsort	Berlin
Familienstand	verheiratet mit Kerstin Stein, geb. Bethge
seit 21.01.1998	freuen wir uns über unseren Sohn Jonas Paul
Ausbildung	
1977 – 1983	Stechlinsee-Grundschule, Berlin
1983 – 1990	Rheingau-Gymnasium, Berlin
06/1990	Abitur
1990 – 1993	Chemiestudium an der TU Berlin
1992	Vordiplom mit der Note “sehr gut”
1993 – 1994	Auslandsstudienaufenthalt an der University of Manchester, UK
1994	‘Master of Science’ Abschluß der University of Manchester, UK
1994 – 1995	Chemiestudium an der TU Berlin
09/1995	Diplom in Chemie “mit Auszeichnung”
01/1997	Beginn der Dissertation an der TU Berlin
Tätigkeiten	
1995-1996	wissenschaftlicher Mitarbeiter bei Prof. Dr. J. Sauer, Arbeitsgruppe Quantenchemie der Max-Planck-Gesellschaft
1997 – 2000	wissenschaftlicher Mitarbeiter am Max-Volmer-Institut für Biophysikalische Chemie und Biochemie der Technischen Universität Berlin
seit 01.01.2000	Geschäftsführer des Sonderforschungsbereiches 498